OPTICAL AND MECHANICAL CHARACTERIZATION AND ANALYSIS OF NANOSCALE SYSTEMS

by

Daniel N. Lamont

B.S. in Chemistry, University of Pittsburgh, 2004

Submitted to the Graduate Faculty of the

Kenneth P. Dietrich School of Arts and Sciences in partial fulfillment

of the requirements for the degree of

Doctor of Philosophy

University of Pittsburgh

2016

UNIVERSITY OF PITTSBURGH

DIETRICH SCHOOL OF ARTS AND SCIENCES

This dissertation was presented

by

Daniel N. Lamont

It was defended on

August 5, 2016

and approved by

Geoffrey R. Hutchison, PhD, Assistant Professor

Hrvoje Petek, PhD, Professor

Gilbert C. Walker, PhD, Professor

Dissertation Advisor: David H. Waldeck, PhD, Professor

OPTICAL AND MECHANICAL CHARACTERIZATION AND ANALYSIS OF NANOSCALE SYSTEMS

Daniel N. Lamont, Ph.D.

University of Pittsburgh, 2016

This thesis discusses research focused on the analysis and characterization of nanoscale systems. These studies are organized into three sections based on the research topic and methodology: Part I describes research using scanning probe microscopy, Part II describes research using photonic crystals and Part III describes research using spectroscopy. A brief description of the studies contained in each part follows. Part I discusses our work using scanning probe microscopy. In Chapter 3, we present our work using apertureless scanning near-field optical microscopy to study the optical properties of an isolated subwavelength slit in a gold film, while in chapter 4 atomic force microscopy and a three point bending model are used to explore the mechanical properties of individual multiwall boron nitride nanotubes. Part II includes our studies of photonic crystals. In Chapter 6 we discuss the fabrication and characterization of a photonic crystal material that utilizes electrostatic colloidal crystal array self assembly to form a highly ordered, non closed packed template; and in Chapter 7 we discuss the fabrication and characterization of a novel, simple and efficient approach to rapidly fabricate large-area 2D particle arrays on water surfaces. Finally, in Part III we present our spectroscopic studies. In Chapter 9 we use fluorescence quenching and fluorescence lifetime measurements to study electron transfer in aggregates of cadmium selenide and cadmium telluride nanoparticles assemblies. Chapter 10 features our work using the electronic structure of zinc sulfide

semiconductor nanoparticles to sensitize the luminescence of Tb^{3+} and Eu^{3+} lanthanide cations, and Chapter 11 presents our recent work studying photo-induced electron transfer between donor and acceptor moieties attached to a cleft-forming bridge.

TABLE OF CONTENTS

LIST OF TABLES

LIST OF FIGURES

LIST OF EQUATIONS

PREFACE

Acknowledgements

I consider myself extremely fortunate to have received my undergraduate and graduate education at the University of Pittsburgh. I would like to thank the Department of Chemistry for all of the support I received throughout my graduate career.

I am truly grateful for the many people that have made this work possible. I would like to thank David Waldeck for his excellent mentorship and support. Dave is an exceptional scientist, and my development has benefited immensely from his scientific knowledge. I am indebted to Gilbert Walker for the support and encouragement he provided during my early graduate training. Additionally I would like to thank the members of my dissertation committee, Hrvoje Petek and Geoffrey Hutchison, for their feedback, assistance and generously-donated time.

Many thanks to all the current and former members of the Waldeck laboratory for their camaraderie and support. I greatly value the broad and deep knowledge this community possesses. I would especially like to thank Brittney Graff for her exceptional collaboration and expertise. I greatly appreciate her incredible kindness and her friendship. Special thanks to Prasun Mukherjee for his technical guidance and insight. Thanks also to Emil Wierzbinski for his insight and unique perspective.

Many thanks to the staff of the Department of Chemistry, the Dietrich School Machine Shop, and the Peterson Institute for Nanoscience and Engineering. Special thanks to Jay Auses for his advocacy and encouragement.

I dedicate this work to my family. I would like to thank my wife and best friend, Layla Banihashemi, and my wonderful parents, Robert and Cindy Lamont, for everything they have done to make this achievement possible. I profoundly appreciate their unwavering encouragement, multifaceted support and steady guidance.

1.0 INTRODUCTION

This thesis discusses research focused on the analysis and characterization of nanoscale systems. These studies are organized into three sections based on the research topic and methodology: Part I describes research using scanning probe microscopy, Part II describes research using photonic crystals and Part III describes research using spectroscopy. A brief description of the studies contained in each part follows.

Scope of Part I: Scanning Probe Microscopy:

Chapter 3 discusses our work using apertureless scanning near-field optical microscopy to study the optical properties of an isolated subwavelength slit in a gold film. Due to the highly scattering nature of the probe and the sample, near-field images contained significant interference fringe artifacts. A model was developed to explain the origin of this imaging artifact.

In Chapter 4 atomic force microscopy and a three point bending model are used to explore the mechanical properties of individual multiwall boron nitride nanotubes. A force mapping technique is used to collect force curves from various locations along the length of the nanotube. A discussion of the relationship between tube diameter and bending moduli is included.

Scope of Part II: Studies of Photonic Crystals

Chapter 6 describes the fabrication and characterization of a photonic crystal material that utilizes electrostatic colloidal crystal array self assembly to form a highly ordered, non closed packed template. This template is then filled with a hydrogel, which is then cross-linked to form a soft photonic crystal. Silica is then condensed within this soft crystal matrix and after thermal treatment an inverse silica photonic crystal material is created.

In Chapter 7 we have developed a novel, simple and efficient approach to rapidly fabricate large-area 2D particle arrays on water surfaces. These arrays can easily be transferred onto various substrates and functionalized for chemical sensing applications. The degree of ordering of 2D arrays decreases with the particle size. This may be due to the fact that arrays created with the smaller particles are less mechanically stable and may have been disturbed during handling.

Scope of Part III: Spectroscopy Studies.

In Chapter 9 we use fluorescence quenching and fluorescence lifetime measurements to study electron transfer in aggregates of cadmium selenide and cadmium telluride nanoparticles. Electron transfer-induced fluorescence quenching was found to depend on interparticle distance, the energetic alignment of the nanoparticle valence and conduction bands, and the direction of the electric field between the nanoparticles created by their surface charges.

Chapter 10 features our work using the electronic structure of zinc sulfide semiconductor nanoparticles to sensitize the luminescence of Tb^{3+} and Eu^{3+} lanthanide cations. A semiempirical model is used to discuss lanthanide ion sensitization in terms of an energy and charge transfer between trap sites.

Chapter 11 presents our recent work studying photo-induced electron transfer between donor and acceptor moieties attached to a cleft-forming bridge. Here, two different bis-peptide scaffold molecules were used as molecular bridges, which control the spatial position of the electron donor and acceptor groups. Both of these scaffolds form solvent-accessible clefts, allowing us to investigate solvent mediated electron tunneling through non-bonded contacts.

2.0 SCANNING PROBE MICROSCOPY

INTRODUCTION

2.1 PAST, PRESENT, AND FUTURE OF NANOSCOPY.

After Abbe's treatment of the diffraction limit was published, we have taken up the challenge to develop robust and easy to use super-resolution imaging techniques. These efforts have lead to the development of several mature high spatial resolution techniques such as electron microscopy and atomic force microscopies. In recent decades researchers have developed methods for subwavelength spatial resolution in optical microscopy. Below I provide a brief review of the history of microscopy development with enhanced detail on the proximal probe methods, force microscopy and near-field scanning microscopy, that are used in Chapters 3 and 4

2.2 OPTICAL MICROSCOPY

The first optical microscope was developed in 1595 by Hans Janssen, a Dutch eyeglasses polisher. It extended optical observation to the world of micrometer scaled materials. Then, microscopy development stagnated for nearly a hundred years until 1675, when Antonij van Leeuwnehoek discovered how to construct high power simple lenses and began developing microscopy systems commercially. In the late seventeenth century Jan Swammerdam and Robert Hooke built the first multilens microscopes capable of producing optical magnification of several hundred times. This advance allowed exploration of micron-scale details and observation of the "invisible worlds" of bacteria and cells.

By the late nineteenth century, advancements in the fields of photonic and material science facilitated the design and construction of aberration-corrected, compound-lens systems and microscope instrumentation capable of sub-micron resolution.[1] In 1872, with the support of Carl Zeiss, Ernst Abbe commenced research into the mass production of compound objective lenses. These efforts revealed the fundamental relationship between wavelength and diffraction limited resolution.

2.3 ELECTRON MICROSCOPY

At the end of the nineteenth century and early twentieth century the discovery of the electron and the development of quantum mechanics provided the fundamental insights needed to develop the "electron microscope". In 1933 Ernst Ruska developed an electron microscope capable of 50 nm

resolution. In the 1950s lattice scale resolutions of ~ 1 nm were achieved, and in the 1970s atomic resolution was demonstrated for heavy atoms such a thorium or gold. There development coincided with the rise in solid state materials research. Maturation of electron microscopy continued in the 1980s and 1990s, and commercial instrumentation capable of sub-nanometer resolution proliferated. Advancements in aberration correction of electron optics has further extended the resolution limit to sub-angstrom length scales. [5]

2.4 SCANNING PROBE MICROSCOPY

In 1980, adaptations of SEM technologies stimulated the development of probe based microscopy techniques. [7] In probe based microscopies, a probe or detector is moved from point to point scanning a grid along the surface of a sample. Typically, the probe is regulated to maintain a near surface distance separation between the probe and surface. The family of techniques which use this scanning mechanism are called scanning probe microscopies (SPM). The first kind of SPM, the scanning tunneling microscope (STM) was developed in 1981/1982. In STM the probe/surface distance is regulated by measurement of the electron tunneling current between an atomically sharp metal probe and a conductive surface. In atomic force microscopy (AFM) a mechanical probe is used to measure the force between a nanoscale tip and the surface. In scanning near-field optical microscopy (SNOM) an optical detector and nanoscale sized aperture can be used to image an optical near-field with a lateral resolution approaching 20 nm. In all of these methods a near surface interaction mechanism results in a detectable signal which is processed to produce an image of a display interface.

2.5 MOTIVATION FOR MICROSCOPY DEVELOPMENT

Using the cellphone as an example, it is readily apparent that with each successive product generation feature sizes are trending smaller and smaller. Consequently the critical dimensions of the intrinsic design in silicon based structures have become smaller than the wavelengths of visible light. Additionally, with each generation, the number density and architectural complexity of the fundamental elements used to construct higher-level systems has increased. As the critical dimensions of individual components of an emerging technology continue to shrink, characterization at subwavelength length scales becomes an increasingly desired capability, and non-conventional microscopy technology will continue to grow in the coming decades.

Classically, microscopy was used for morphological inspections; however today the challenge of characterizing nanoscale materials and devices has imposed significantly larger demands. Due to its flexibility and broadly ranging contrast motifs, optical microscopy is ubiquitous in nearly every branch of science and applied technology. The critical dimension of biological cells, large biological molecules and many engineered nanostructured materials occurs on length scales ranging from 1 nanometer to 1 micron. The major challenge of optical instrumentation when applied to nano-scale systems stems from the diffraction limit. The characteristics of a microscope suited to nanoscale characterization include sub-100 nm resolution, high chemical specificity, operation in ambient conditions, and possible fluid based observations. Additionally, microscope technology capable of observing the temporal dynamics of scientifically interesting processes is desirable.

Advancements in the fields of photonics and opto-electronics have relied on the ability to observe and characterize electromagnetic fields on nanometer length scales. In many applications it is necessary to conduct quantitative topographical analysis while simultaneously performing electrical, thermal, or optical characterization. Material properties, doping profiles, electrostatic potentials, static electric dipoles, thermal conductivity, stress, forces and light fields must be detected on micro and and nanometer length scales.

The resolution of optical microscopy is limited by the wavelength dependent resolution limit. In SPM, resolution is limited primarily by the probe size and signal to noise ratio. A fundamental requirement for all high resolution SPM techniques is the localized nature of the interaction mechanism between the probe and surface; the probe must interrogate the surface under near-field conditions. The requirements of near-field control can be explained by exploring the classical diffraction limited resolution.

2.6 SUPER-RESOLUTION FRAMEWORK

2.6.1 Limitations of Optics

Light is unable to be confined by a conventional optical system to a linear dimension significantly smaller the $\lambda/2$; referred to as the diffraction limit. This is commonly explained as an extension of Heisenberg's uncertainty principle to the positional uncertainty of a photon with a known momentum; [4] which in one dimension is

$$\Delta x_x \ |p_x| \approx \hbar$$

Equation 2.1

Here, Δx_x and p_x refer to any of the three Cartesian components of the photon displacement and momentum vectors, respectively. In a medium *i*, the three components of the wavevector k must satisfy $k_i^2 = k_x^2 + k_y^2 + k_z^2$ .Where $k_i = 2\pi/\lambda_i = n_i|k_0|$ with k_0, the wavevector in vacuum, n_i, the index of refraction and, λ_i, the wavelength in medium i.

Classic or conventional optical systems can be defined as the interaction between a material and freely propagating photons. A photon is considered freely propagating when all components of its wavevector are real. Consequently, no wavevector component can be larger than k_i. Therefore, the positional uncertainty of a freely propagating photon is greater than or equal to

$$\Delta x_{class} \geq \frac{1}{|k_x|} = \frac{\lambda_i}{2\pi}$$

Equation 2.2

When a freely propagating photon is confined or focused using a classical objective , the smallest resolvable distance, or critical dimension (CD), is defined as $CD = \frac{\kappa_1 \lambda}{NA}$ where λ is the wavelength. NA is the numerical aperture, $NA = n_n \sin\theta$,where θ is the maximal half angle of the cone light that can enter the objective. The constant factor κ_1 depends on the intensity distribution of the incident light and ranges from 0.61 to 0.36. For a typical objective uniformly illuminated with near-UV light, NA = 0.9, κ_1 = 0.61, and λ = 400 nm $CD \approx 140\ nm$. Thus a classical optic is capable of borderline nanometer size resolution.

2.6.2 Near-field Optics

Super-resolution can be achieved when a highly confined non-propagating electromagnetic field, a so called evanescent wave, interacts with a material. The amplitude of an evanescent wave decays rapidly in at least one spatial coordinate, and the wavevector of an evanescent wave is complex. If one wavevector component, typically denoted k_z, has a significant imaginary component then residual components can be larger than $|k_n|$. Consequently the larger wavevector component reduces the spatial extent, Δx.

An evanescent wave can be excited at a boundary between two different media; for example, the total internal reflection at a glass-air interface or the field around a radiating molecular dipole . The amplitude of these fields decays rapidly along the interface normal and the vast majority of the field strength is located near the interface. Consequently, these types of fields are called near-fields. Two defining characteristics of near-fields are that $k_x \geq |k_n|$ and

$\varepsilon > (\frac{8\pi}{c})|\boldsymbol{S}|$. The first relation is the previously described wavevector equality, and the second relation shows that the energy density, ε, is greater than the time-averaged flow of radiation through a volume element determined by the Poynting vector, **S**. The latter expression is an equality for freely propagating waves.

2.7 SPECIFIC SPM TECHNIQUES.

Centuries of research has produced rich insights into the fundamental principles which govern the interaction between electromagnetic fields and matter. Application of this knowledge has allowed the development of a diverse range of spectroscopic techniques, and highly selective techniques have emerged which are capable of interrogating a sample to provide information on the elemental composition, chemical and molecular organization, and higher level structural information. In the fields of localized probe-based microscopy, a wide array of techniques have been developed.

2.8 FORCE-DISTANCE CURVES

Static or contact mode atomic force microscopy (AFM) is used to measure the mechanical properties of a sample and is a well-developed branch of AFM. In contact mode AFM, a mechanical cantilever probe is scanned above a sample while a detector sensitive to probe deflection is used to measure the tip-sample force. This method can probe both attractive and

repulsive forces. Contact mode AFM is typically operated in the repulsive regime, i.e., the cantilever is in contact with the surface and is deflected away from the surface. However, static mode AFM can be operated in both the repulsive and attractive regimes. Static mode is in reference to the fact that the cantilever is not undergoing dynamic oscillating motion.

The standard application of contact AFM is imaging of surface topography using a constant force imaging modality. The tip is in direct contact with surface and the tip-surface interaction is principally a strongly repulsive interaction. Detection of cantilever deflection and a tip-sample interaction force setpoint are used to parameterize an electronic feedback loop used to maintain a constant force between the tip and sample. If the spring constant of the probe is significantly lower than the effective spring constant of the sample atomic bonds, direct determination of the height of the surface is possible. The contact zone between tip and sample is typically understood to consist of many atoms; a contact diameter in the range of 1-10 nm is typical. Long-range attractive tip-sample forces can be imaged using a constant height scanning motif. For example, if a ferromagnetic probe is used, then magnetic forces domain can be sensed from the cantilever deflection observed in constant height mode imaging. Friction Force microscopy is an another static mode AFM technique. By scanning the cantilever sidewise with respect to the cantilever length in constant-force contact mode, the lateral forces caused by torsional bending of the cantilever can be detected. Using this signal, local variations in surface friction can be resolved with nanometer resolution.

Force-distance curves are measured by monotonically decreasing the probe-sample separation while the cantilever deflection is monitored. It is desirable to obtain the tip-sample force, $F_{ts}(d)$, as a function of tip-sample distance, d. What is principally measured during the

collection of a force distance curve is the deflection of the cantilever tip, z_{tip}, as a function of the z-position of the sample. Althought the z_{tip} is proportional to $F_{ts}(d)$, the z-position of the sample is a convolution of the z-motion and the cantilever deflection.

Mechanical properties, such as sample elasticity or maximum tip-sample adhesion force are readily measured using force-distance curves. Additionally, when imaging samples that are sensitive to the applied tip-sample force, such as soft biological samples, a force-distance curve conducted at pre-selected points enables selection of a force setpoint that does not unnecessarily wear and degrade sample integrity.

2.9 APERTURELESS NEAR-FIELD OPTICAL MICROSCOPY

In the original scanning near-field optical microscope (SNOM), the aperture-based SNOM, the optical diffraction limit is surpassed by forcing light through the metallic aperture of an optical fiber-like probe under near-field conditions. By definition, near-field conditions require the probe to be positioned in close proximity to the surface where near-fields, optical or otherwise, have significant amplitude. As has been stated previously, the resolution of the optical near-field scanning probe techniques is limited by the diameter of the probe. Unfortunately, the probe diameter also limits signal-to-noise as the aperture size shrinks and ultimately reduces the light throughput. In aperture-based NSOM, the metalized, tapered glass geometry of the probe must balance miniaturization of the probe dimensions against the photon throughput limitations imposed by the waveguide cutoff effect.

Apetureless near-field scanning optical microscopy (ANSOM) circumvent the aperture-size paradox by leveraging well-known mechanisms of optical field enhancement. Typically, a strongly scattering sharp probe, such as an AFM tip, is placed in the focus of a laser beam allowing field confinement effects to act as the basis of the ultra resolution mechanism. The nano-optical field in the near-field region of the probe apex can be strongly enhanced due to localized surface plasmon resonances or to geometric considerations such as lightning rod and antenna effects.

In general, two classes of ANSOM have emerged. One type is scatter type microscopy (s-SNOM), in which a strongly scattering tip is either polarized by a surface near-field or polarizes a surface near-field.[3] In this method the tip scatters the optical near-field, converting it into a propagating optical signal which can be detected by traditional optical schemes. The second type is tip enhanced microscopy, where a tip enhanced field is used to locally excite a material by a variety of optical mechanisms.[6] Mechanisms include: tip enhanced Raman scattering, tip-enhanced harmonic generation, and tip-enhanced fluorescence. More recently, s-SNOM probes in which single metal particles are attached to dielectric tips have emerged. [2] This probe morphology is both significantly more robust and mechanically superior than the high aspect ratio tip previously used in s-SNOM.

The ANSOM technique used in the studies contained in this thesis are based on sharp tip light scattering. Again, this technique has no wavelength based resolution limit; resolution is nearly entirely determined by the probe radius. Probes with 20 nm radii are common and 10 nm lateral resolutions have been demonstrated.

2.10 FUTURE OF SCANNING PROBE MICROSCOPY (SPM)

Central to all SPM techniques is the use of a mechanical tip. A probe located in the near-field of a sample can sense a diverse spectrum of interaction mechanisms. Simultaneous high resolution measurement of near-field interaction mechanisms and topography is a major advantage of SPM. However, SPM techniques have not been fully developed into user-friendly and robust systems, and are typically limited in scan speed and field of view. Consequently significant efforts need to be made in:

- The use of multi-probe systems. Multi-probe techniques will increase sample acquisition speed and interaction volumes. By using an array of tips, it would be possible to sense different sample properties simultaneously.
- The development of probes which join both sensor and actuator functionality. Possible examples would include nanoscalpels or nanopipettes. Nanoscale detector arrays will allow a diverse range of surface properties to be assessed.
- The integration of SPM into complementary microscopy techniques, such as classical optical microscopes. Integration of SPM, focused ion beam and SEM in a single system would provide characterization and fabrication possibilities relevant to a wide range of fields.

2.11 BIBLIOGRAPHY

[1] **Hughes, A.** (**1956**). *Studies in the history of microscopy. 2. the later history of the achromatic microscope*, Journal of the Royal Microscopical Society 76 : 47-60.

[2] **Kalkbrenner, T.; Håkanson, U.; Schädle, A.; Burger, S.; Henkel, C. and Sandoghdar, V.** (**2005**). *Optical microscopy via spectral modifications of a nanoantenna*, Physical review letters 95 : 200801.

[3] **Knoll, B. and Keilmann, F.** (**1999**). *Near-field probing of vibrational absorption for chemical microscopy*, Nature 399 : 134-137.

[4] Novotny, L. and Hecht, B., **2012**. *Principles of nano-optics*. Cambridge University Press, Cambridge, UK;New York;.

[5] Tendeloo, G. V.; Van Dyck, D. and Pennycook, S. J., **2012**. *Handbook of nanoscopy*. Wiley-VCH, Weinheim, Germany.

[6] **Wessel, J.** (**1985**). *Surface-enhanced optical microscopy*, JOSA B 2 : 1538-1541.

[7] Yablon, D. G., **2013**. *Scanning probe microscopy for industrial applications: nanomechanical characterization*. John Wiley & Sons, Hoboken, New Jersey.

[8] Zayats, A. V. and Richards David, P., **2009**. *Nano-optics and near-field optical microscopy*. Artech House, Boston;London;.

3.0 OBSERVATION AND ANALYSIS OF LOCALIZED OPTICAL SCATTERING WITH NON-PASSIVE PROBES

Author contribution: The author of this dissertation was responsible for all the experiments and prepared the manuscript.

3.1 INTRODUCTION

Nanophotonics have demonstrated promise in a range of applications from integrated optical circuits to medical diagnostics.[12; 13; 19; 55; 72; 77; 79; 84] Often, only a small set of simple, subwavelength structural elements such as concentric circles, slit apertures, and two dimensional aperture arrays are utilized to construct complex nanophotonic devices. [12; 13; 17; 19; 24; 46; 47; 56] The increasing sophistication of nanophotonics depends on an acute understanding of the interaction between electromagnetic radiation and these subwavelength optical elements. Direct observation of this interaction is possible with the use of a near-field scanning microscope. Near-field scanning microscopy is capable of resolving electromagnetic phenomenon at length scales below the diffraction limit.[3; 5; 23; 27; 29; 31; 32; 35-38; 42; 43; 58; 66; 68; 78; 81; 86] However, several

well documented experimental challenges, convolute the signal response of near-field microscopes.[8; 23; 29; 35; 42; 54; 58; 66] In this work, transmission mode apertureless near-field scanning optical microscopy is employed to study localized optical scattering above a subwavelength aperture. This document will address complexities arising from the interaction of propagating radiation with a polarizable probe-sample interface.

The term scanning near-field optical microscope (NSOM) is used to describe members of a family of instruments capable of resolving electromagnetic field distributions at length scales significantly smaller than the diffraction limit. The maximum resolution of traditional optical microscopes utilizing diffraction limited optics approaches λ/2, where λ is the wavelength of illumination.[67] NSOM studies regularly demonstrate resolutions of λ/10 and λ/60 resolution has been reported.[61]

The NSOM was first proposed in 1928 by E.H. Synge.[74] In a brief series of papers and private correspondences exploring the feasibility of sub-wavelength resolution, Synge proposed a mechanism of image formation using an optical probe consisting of a sub-wavelength circular aperture in an opaque screen or a quartz cone with a metal coating everywhere except the apex. Illumination of these sub-wavelength apertures generates an electromagnetic near-field containing high spatial frequency components. Placing a sample surface into the generated near-field facilitates scattering of high spatial frequency fields by sub-wavelength size surface elements. Scanning the aperture in a plane parallel to the sample surface and collecting scattered light with diffractive optics generates a super-resolved image. Spatial resolution is due to the localized nature of the electromagnetic near-field. Efficient near-field to far-field conversion is possible only when the separation between aperture and sample is less than the wavelength of the incident field. When optical frequency illumination sources are used, nanometer scale resolution

may be obtained; however, distance regulation on the order of several 10s of angstroms is required. The significant technological challenges imposed by nanometer scale scanning resulted in a significant delay before Synge's hypothesis was verified at optical frequencies. By 1984, rapid development of piezoelectric crystal fabrication and scanning probe microscopy (SPM) techniques such as scanning tunneling microscopy and atomic force microscopy (AFM) facilitated experimental verification of NSOM in the visible spectrum.[61] More recently, several research groups have obtained sub-wavelength resolved images by scattering high spatial frequency fields with a subwavelength spherical probe.[7; 32; 86] Near-field scanning techniques based on this approach are generally referred to as apertureless NSOM or ANSOM. Several review articles focusing on aperture based NSOM [10; 16], ANSOM [31; 33; 58], and optical near-field theories [21; 60] demonstrate the development this field.

ANSOM overcomes several significant experimental limitations of aperture based NSOM such as:

- Skin depth limited resolution
  - In visible spectrum NSOM, maximum resolution approaches 20 nm due to the skin depth of metals used to define the aperture boundary.
- Low signal sensitivity
  - Small signal levels are due to inherently small light throughput of the aperture.
- Low incident power
  - Near-field illumination intensity is limited by thermal damage mechanisms present at probe apertures
- Waveguide cut off

- NSOM probes are typically constructed by from elongated optical waveguides. Consequently, the utility of aperture NSOM is limited to wavelengths below the cut-off frequency.[3; 9; 23; 25-29; 32-34; 54; 65; 85]

In ANSOM, near-field resolution is proportional to the spatial profile of the probe. The radius of curvature at the apex of commercially available SPM probes commonly approach 5 nm. ANSOM signal sensitivity can be enhanced by utilizing probe materials with large scattering or absorption cross section. Metal coated probes have radius of curvature approaching 25nm. A single ANSOM system may be utilized across broad spectral range.[29] The widespread availability of commercial probes and probe positioning equipment significantly enhances the accessibility of ANSOM as a common laboratory instrument.

As with all scanning probe technologies, the key physical principles involved are localized in the region surrounding the probe. Of primary importance is the physics of probe-sample optical coupling. In ANSOM experiments, sensitivity and resolution critically depend on the ability of the probe-sample systems to localize and scatter electromagnetic fields with large spatial wavevectors, k_{sp}. Typically, an ANSOM probe is placed between one and several hundred nanometers above the sample surface. At this length scale, theoretical calculations predict enhancement of incident electromagnetic fields at optical frequencies for many materials. Additional field enhancement is expected for systems which support surface active electromagnetic resonance modes such as plasmons or phonons.[4; 30; 40; 63] Also, the "lightning rod effect," present in all geometrically constrained conductive systems, plays a role in localized field enhancement.[11; 18; 50; 62]

Theoretical probe-sample coupling studies have been reported using a multitude of techniques. These techniques include the multiple-multipole method [11; 53; 56; 63], the Green dyadic technique[21; 22; 40; 59], the Finite Difference Time Doman [51] , and rigorous electromagnetic treatments [6; 15; 62; 78] .

A primary challenge of ANSOM experiments arises from the need to isolate true optical near-field signals, which contributes a small fraction to the total collected signal. Background contributions from light reflected, scattered, or diffracted by nearby sample structures often masks the localized probe-sample coupling and diminishes resolution. Two techniques, Lock-in amplification [43; 78] and high harmonic demodulation [29; 39; 42; 70] are often used to overcome this issue. These techniques may be implemented via harmonic modulation of the probe sample separation. In ANSOM experiments, probe-sample distances are frequently regulated by an AFM controller capable of performing non-contact or “tapping mode” (TM) imaging [10; 64].

This work reports the characterization of near-field optical properties of elementary structures. Apertureless scanning near-field optical microscopy (ANSOM) enables observation of optical properties below the diffraction limit; however, data collected by this technique may contain more than near-field contributions. In this work, transmission mode ANSOM is used to study optical properties of an isolated subwavelength slit. Constant-height mode ANSOM images reveal fringe patterns on both sides of a slit aperture. Fringe patterns are sensitive to the relative positions of the ANSOM detection optics and the slit. Fringes result from a superposition of probe scattered fields and the average wavevector of collected light. Analysis confirms the existence of two families of scattered fields which are directed parallel to the sample plane and

propagate in opposite directions away from the slit. Data collected using different probe geometries reveal the existence of a homodyning field comprised of fields transmitted through the slit and scattered by the ANSOM probe body.

3.2 EXPERIMENTAL DETAILS

3.2.1 Deposition of Metal Film

An Electron-beam evaporation system (Thermionics model VE 180) was used to evaporate a 200nm thick Au film over a 5 nm layer of Ti on a quartz substrate. Prior to metal film deposition, the substrate was cleaned in argon plasma.

3.2.2 Fabrication of Nanoslits

A focused ion/electron dual beam system (JEOL model SMI-3050SE) was used to mill apertures into the metal film. An ion beam with 100 pA current was used. The minimum ion dose required to completely mill through the metal film was determined by milling and cross-sectioning several test structures in a manner similar to that recently reported.[57]

3.2.3 Near-field Microscopy

In order to study sub-wavelength resolved optical fields localized near the surface of isolated apertures, an ANSOM was designed and constructed. The ANSOM was constructed by integrating a sample illumination pathway and a homebuilt optical microscope into a commercial SPM platform (Veeco Instruments, Dimension 3100). A brief description of the experimental apparatus follows.

Direct backside illumination of sample structures was achieved with a sample excitation pathway and a custom SPM sample stage (Figure 3.1). A single mode, polarization maintaining optical fiber coupled 532 nm light from frequency doubled Nd:YVO4 laser into the excitation pathway. Fiber optic output was collimated by an aspherical lens and passed through a linear polarizer. Incident field polarization angle was set by rotating the major axes of the fiber and the polarizer. The electric component of the incident field was polarized perpendicular to the long axis of the slit. A reversed telescope expanded the collimated beam diameter to match the input iris of a condenser lens. A 45 degree mirror directed the focused Gaussian beam onto the backside of the patterned metal film. A portion of the fields transmitted and diffracted by the slit aperture were scattered by an oscillating probe and collected using 10x long working distance objective lens, NA = .23, elevated approximately 15 degrees above the x-y sample plane. The objective was focused onto the SPM probe/nanoaperture interaction zone. A dielectric filter separated incident illumination and 670 nm wavelength SPM feedback illumination. An adjustable aperture placed in a confocal plane helped limit collected scattering to a region several microns wide centered near the probe apex. Light passing through the aperture impinged onto a photon multiplier tube (Hamamatsu 1P28). PMT signals were passed to an impendence matched

input of a lock-in amplifier (Stanford Research SR844). Cantilever-probe oscillation frequencies, obtained from the SPM controller electronics, provided the lock-in reference signal. Demodulated optical signals were routed to the SPM controller, synchronized to SPM topography and stored.

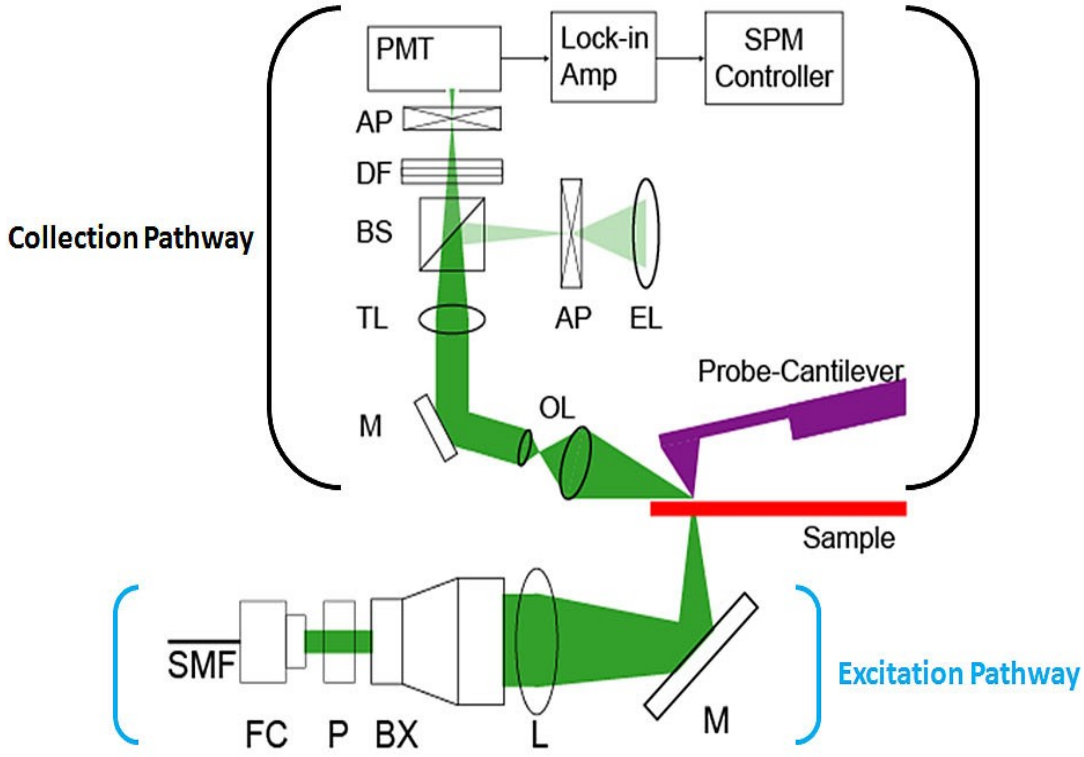

Figure 3.1: Instrument schematic

The elements of excitation pathway are: single mode fiber, SMF, fiber collimation lens, FC, linear polarizer, P, beam expander, BX, positive lens, L, and mirror, M. The elements of the collection pathway: objective lens, OL, tube lens, TL, beam splitter, BS, dielectric filter, DF, aperture, AP, eye-piece lens, EL, and photon multiplier tube, PMT.

ANSOM images were collected by laterally scanning a SPM probe regulated by TM feedback. In order to minimize optical-topographical coupling, ANSOM data was collected at a constant height above the average sample plane. [42] PtIr5 coated conductive SPM probes with an approximate force constant between 42-45 N/m, were used in all studies. Peak to center probe oscillation amplitude was set to approximately 85nm. Two different apertureless probe geometries were utilized in this study. Scaled drawings of the traditional geometry (Nanosensors PPP-NCHPt) and extended geometry (Nanosensors ATEC-NPt) probes used in this study are depicted in (Figure 3.2).

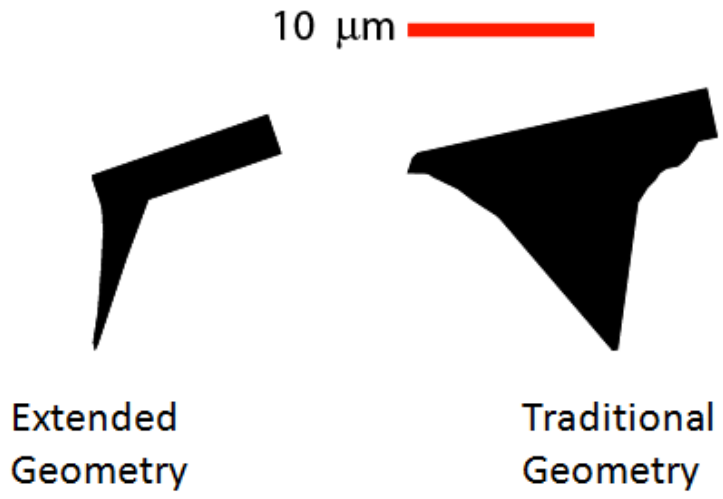

Figure 3.2: ANSOM probe drawings

Scaled drawings of ANSOM probes Extended Geometry: (Nanosensors ATEC-NPt) Traditional Geometry: (Nanosensors PPP-NCHPt)

3.3 RESULTS AND DISCUSSION

3.3.1 Lateral ANSOM Images of a Single Metallic Nanoslit

We present three cases where changes in the relative orientations of the detector and probe-cantilever system with respect to a slit aperture affect fringe patterns observed in ANSOM images. In (Figure 3.3), panels A, C, and E display topography of an isolated slit aperture in opaque gold film. Panels B, D, and F display constant height *n f* demodulated optical signals. Approximate slit locations are marked by a dashed line. On the left hand side of this figure, relative orientations of the SPM cantilever and detector with respect to the long slit axis are represented schematically. In the schematics, the smaller rectangle represents the free end of the cantilever.

In the first case, (Figure 3.3 A, B) the detector is parallel to the slit, looking down the long slit axis, and tilted 15degrees above the sample plane. The fringe pattern observed in the 2f demodulated optical signal makes angles of +/- 45 degrees from the long slit axis, with the fringes on either side of the slit being perpendicular to each other. The demodulated optical image shows a clear asymmetry in the field amplitudes on each side of the slit, with the fringes on the left side being far more pronounced than those on the right. Preliminary results, discussed in a subsequent section, suggest that this asymmetry arises from the cantilever's orientation with respect to the slit.

In the second case, (Figure 3.3 C, D) the slit remains in roughly the same orientation as the first case, but the detector is now rotated clockwise by 45 degrees. The fringe pattern observed in the 1f demodulated signal also appears to rotate clockwise relative to the first case, with the fringes on either side remaining mutually orthogonal. Again, asymmetric intensity distribution on either side of the slit is observed. However in this case, the gain on the detector was increased making the fringes on the right hand side more apparent and in turn causing detector saturation in higher intensity regions.

In the third case, (Figure 3.3 E, F), the sample and SPM scan angle are rotated 90 degrees in the laboratory frame. These rotations produce qualitatively similar topography as compared to the previous cases, but the key difference here being the slit is now oriented perpendicular to the detector. Fringing is exclusively observed on one side of the slit.

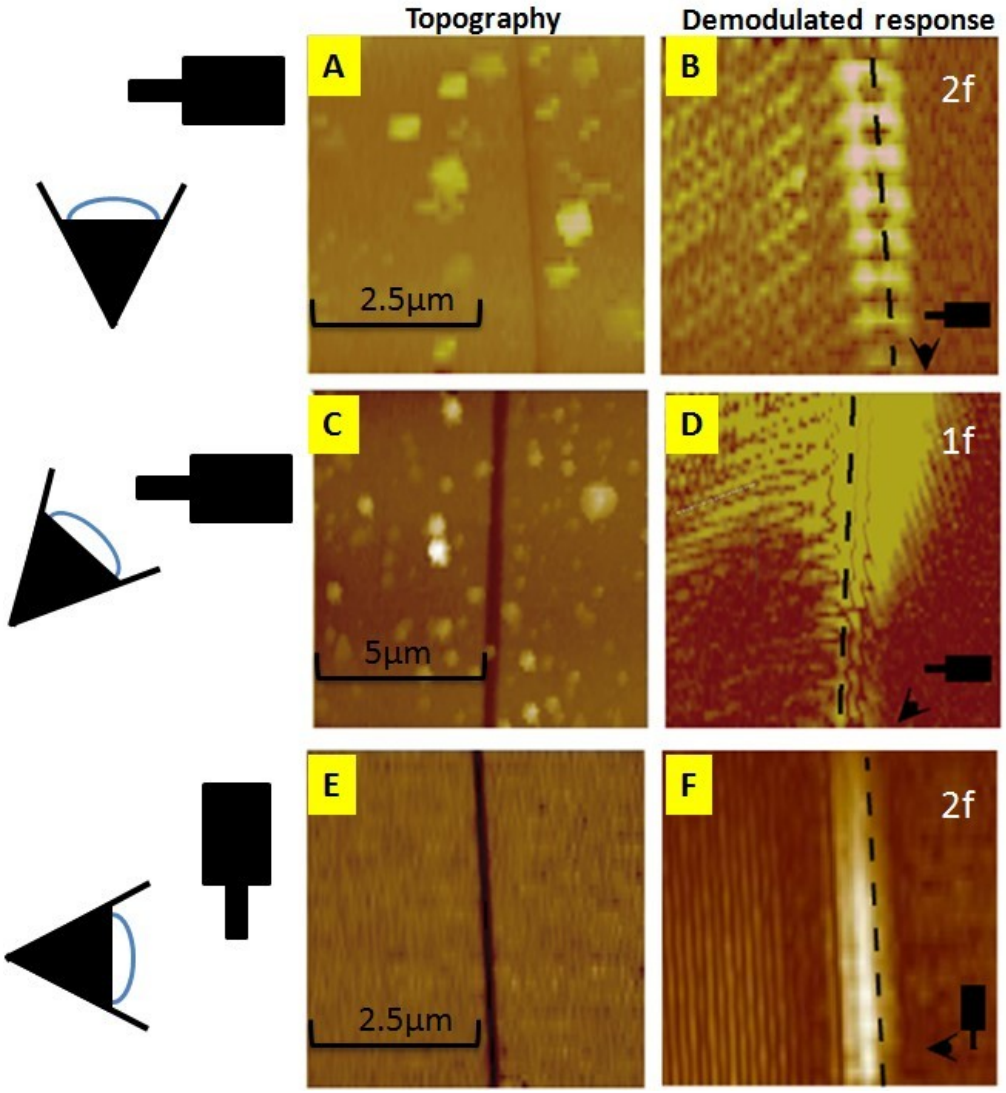

Figure 3.3: Lateral ANSOM imaging with extended probe

Panels A, C, and E: topography of an isolated slit apertures in opaque gold film. Panels B, D, and F: nf demodulated optical signal. Approximate slit locations are marked by a dashed line Left hand side: Schematic representation of relative orientations of SPM cantilever and detector with respect to the long slit axis. In the schematics, the smaller rectangle represents the free end of the cantilever.

3.3.2 Model: Superposition of Background and Probe Scattered Fields

In this section a model based on the approach of Aubert [5] is expanded and utilized to explain interference patterns observed in lateral ANSOM images. This model accurately predicts observed fringe periodicity and two-dimensional interference profiles.

Illumination of a stationary nanoslit milled in an optically thick metal screen leads to diffraction causing a static background field. When losses due to specular scattering by the metal film and material absorption are neglected this field can be expressed as

$$\overrightarrow{E_{diff}} = |E_{diff}|\exp(i\varphi_{diff})$$

Equation 3.1

where φ_{diff} is the phase of the diffracted reference field. A conductive spherical probe scanned a distance z above the x-y sample plane scatters a portion of the diffracted field. The field scattered by a harmonically oscillating probe is given by

$$\vec{E}_t = |E_t|\exp(i\varphi_t(x,y,t))$$

Equation 3.2

where φ_t is the position-sensitive phase of the scattered field. Field perturbations due to probe motion along the z-axis may be neglected if the probe is smaller than the incident wavelength and the distance between the sample and probe is constant [42]. Setting the reference signal of a lock-in amplifier to the probe oscillation frequency facilitates detection of probe modulated fields. Elimination of non-modulated intensity products of $\left(\vec{E}_t + \vec{E}_{diff}\right)^2$ allows the intensity to be expressed as

$$I(x,y,t) = \left|E_t\right|^2 + 2\left|E_{diff}\,E_t\right| \cos\left(\varphi_t(x,y) + \varphi_{diff}\right)$$

Equation 3.3

Theoretical [2; 14; 20; 41; 42; 44; 45; 48; 49; 52; 69; 75; 76; 80; 82] and experimental [1; 2; 20; 73; 80; 83] studies have suggested that the edges of a sub-wavelength slit transform incident fields into transmitted fields containing wavevector components parallel to the metal film output surface. In this case, transmitted fields propagate away from the center of the slit, and the plane containing the long slit axis and the z-axis forms a plane of symmetry. φ_t may be expressed as

$$\varphi_t(x,y) = k_{diff} \cdot \left(x\,\hat{X} + y\,\hat{Y}\right) - k_{det} \cdot \left(x\,\hat{X} + y\,\hat{Y}\right)$$

Equation 3.4

where k_{diff} is the wavevector of the diffracted portion of the transmitted field, and k_{det} is the average wavevector admitted by the objective lens. $\hat{X}$ and $\hat{Y}$ are Cartesian unit vectors which describe the sample plane. Only the components of the k_{diff} and k_{det} parallel to the sample surface are included in Equation 3.4. In order to account for the proposed diffraction symmetry, Equation 3.4 is re-expressed as

$$\varphi_t(x,y) = (-1)^{\zeta} k_{diff}\left[x\cos\left(\theta_s - \frac{\pi}{2}\right) + y\sin\left(\theta_s - \frac{\pi}{2}\right)\right] - k_{det}\cdot\left(x\hat{X} + y\hat{Y}\right)$$

Equation 3.5

with

$$\zeta = \begin{Bmatrix} 0 \text{ if } angle(x,y) < \theta_s \\ 1 \text{ if } angle(x,y) > \theta_s \end{Bmatrix}$$

Equation 3.6

The function “angle(x,y)” returns the angle from the x-axis to a line containing the origin and the probe location. Probe coordinates directly overlapping the slit aperture are neglected. Inserting Equation 3.5 into Equation 3.3 permits calculation of two dimensional, probe-position dependent interference plots.

This model predicts that the direction of the fringe pattern can be controlled by either rotating the detector relative to the diffracted field, or vice versa. Namely, it is the direction of the average detected wavevector, k_{det}, relative to the diffracted wavevector, k_{diff}, that determines

the angle of the fringes through Equation 3.5. In order for the fringes on the left and right to remain orthogonal to each other during rotation of the detector, they must result from the superposition of wavevectors with identical magnitudes.

Simulated phases corresponding to the three case geometries discussed were calculated and are presented in (Figure 3.4 B, D, F). The directions of k_{det} and k_{diff} used in these simulations are indicated by white vectors. Simulated interference patterns are consistent with the collected demodulated optical scattering images shown in (Figure 3.4 A, C, E). Simulated fringe patterns were calculated by assuming diffracted wavevectors possess significant projections along plane of the metal film and, on each side of the aperture, diffracted fields propagate in opposite directions. In the first two cases, panels A-B and C-D, fringes on either side of the slit are perpendicular to each other. In the third case (Figure 3.4 E, F), where the slit is perpendicular to the detector, the model predicts the absence of fringes, right hand side of panel F, due to antiparallel alignment of detected wavevectors.

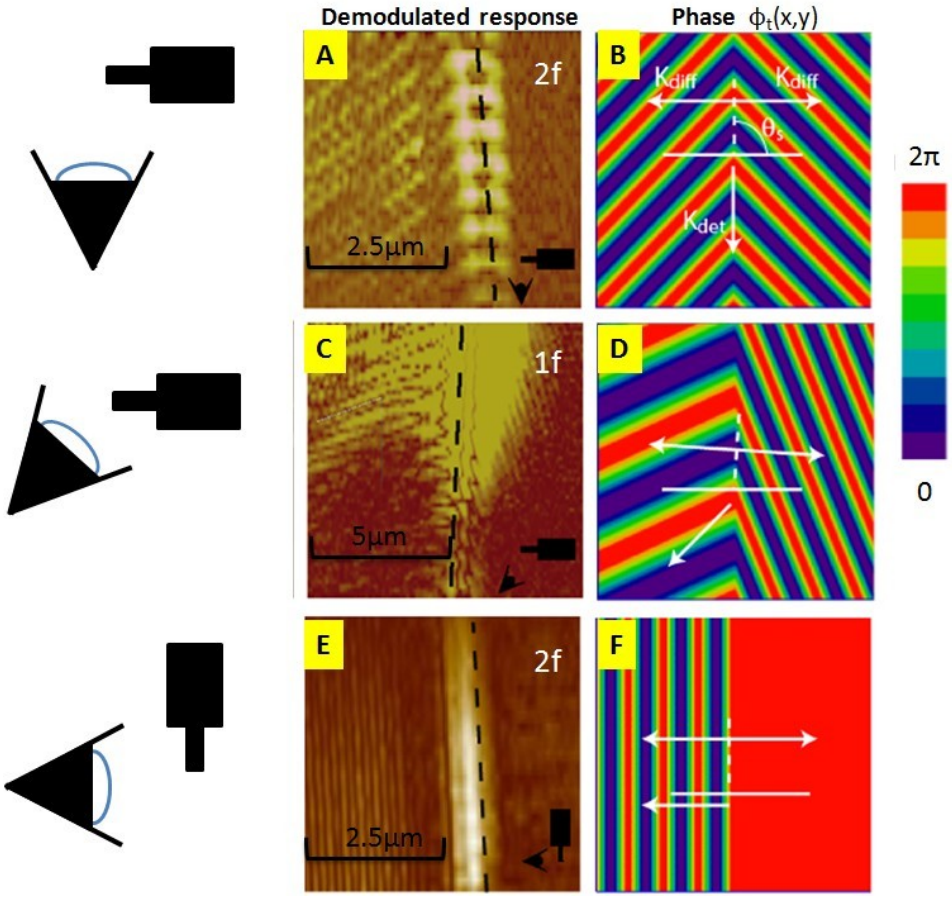

Figure 3.4: Simulated phase calculation.

Panels A, C, and E: nf demodulated optical signal. Approximate slit locations are marked by a dashed line Panels B, D, and F: simulated phases. The directions of k det and kdiff used in during calculation are indicated by white vectors.

This model fails to address origins of the asymmetry observed in the measured field intensities on the two sides of the slit. This is because the interference model only accounts for probe position and does not consider complex probe shape. A comparison of ANSOM images collected with different styles of SPM probe geometries sheds light upon the origin of asymmetric intensity.

ANSOM images presented in (Figure 3.5) were collected with traditional geometry probes whereas the images contained in (Figure 3.4) were collected using extended geometry probes. When a traditional probe is scanned on the right side of the slit, propagating light transmitted directly through the apertures is reflected off of the base of the probe and the end of the cantilever, creating a strong self-homodyning field [71]. In panel B of (Figure 3.5), this constructive interference results in the high intensity vertical band located to the right of the slit. On the other hand, when the probe is scanned over the left side of the slit, the transmitted field is reflected weakly off of the base of the cantilever resulting in a smaller homodyned field. Increasing detector gain allows observation of scattered field on the left side (data not shown) at the expense of detector saturation. A comparison of the adjacent scattering surfaces available when a probe is located on left and right hand sides of the slit is illustrated in (Figure 3.6).

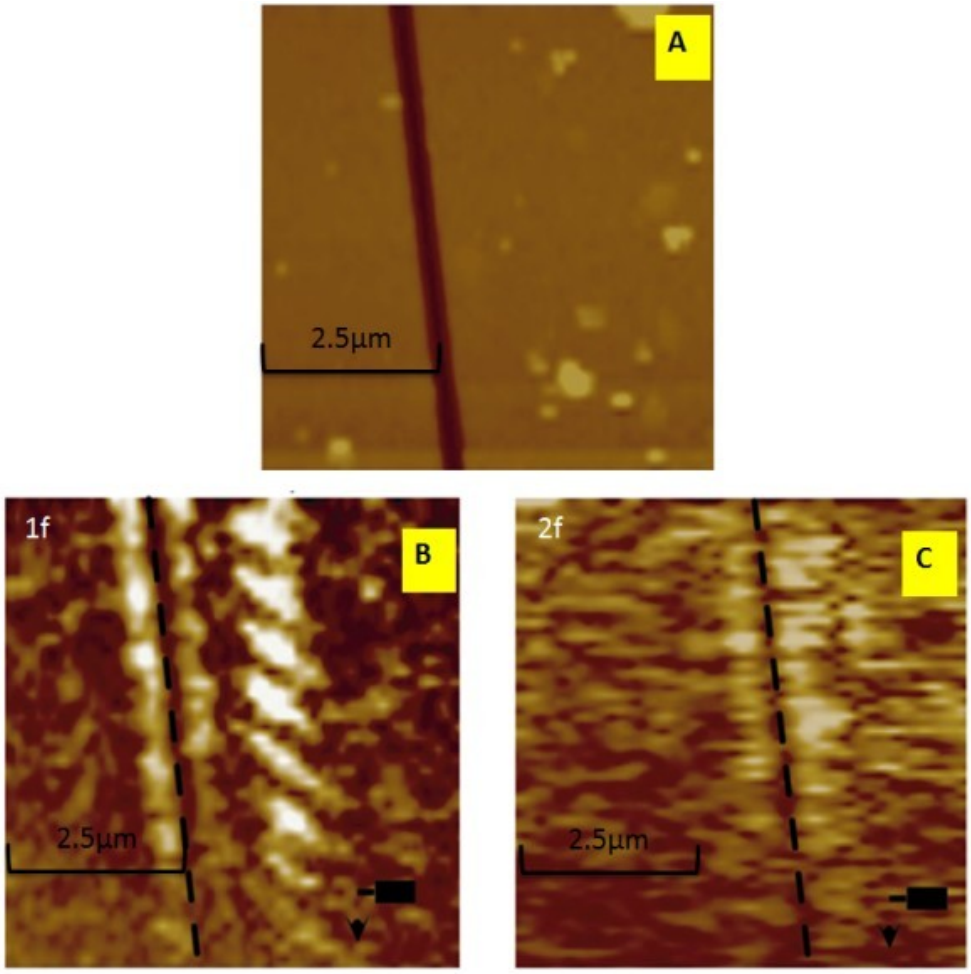

Figure 3.5: ANSOM imaging with traditional probe

Panel A: topography signal Panel B: 1f demodulated optical signal Panel C: 2f demodulated optical signal In these images, the relative orientation of SPM cantilever and detector with respect to the long slit axis is comparable to the experimental geometry depicted in (Figure 8 A,B).

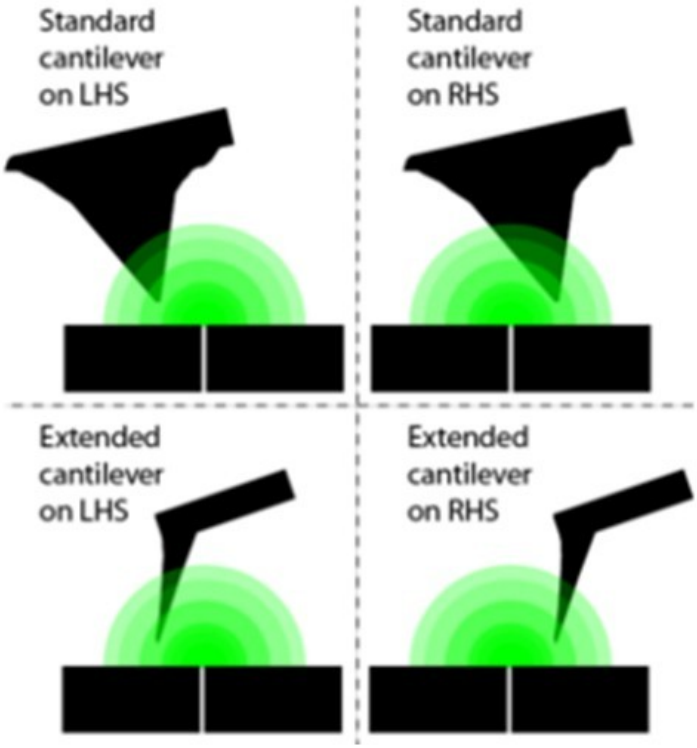

Figure 3.6: Scattering surfaces

Replacement of a traditional geometry probe with an extended geometry probe requires an increase in the detector gain. In the images collected with the extended probe, (Figure 3.4), fringes are predominantly observed left of the slit. Additional increases in detector gain allow observation of fringes on the right side while saturating the detector elsewhere. When the extended probe is on the left side, reflection of transmitted fields is qualitatively similar to the situation in which the traditional probe is located left of the slit. Compared to traditional probes, extended probes posses smaller surface area which may explain the increased detector gain. Extended probe bodies weakly scatter the transmitted fields and produce a relatively weak self-homodyning field.

When the extended probe is located right the slit, there is a low probability that the cantilever body or tip base can scatter transmitted light, and detector gain must be significantly increased to observe fringing right of the slit. For traditional tips located right of the aperture, portions of tip base and cantilever body protrude towards the slit. This may be the cause of the high intensity strip observed right of the slit in (Figure 3.5 B).

At 2f demodulation, (Figure 3.5 C), fringe patterns were diminished and intensity more localized near slit edges than in the 1f demodulation image (Figure 3.5 B). 2f demodulated signals are more sensitive to surface bound fields [29]; this suggests a majority of the light exiting the slit apertures is weakly bound to the sample surface.

The experimentally observed interference originates from variations in optical path length between the probe and detector. The existence of fringes in regions several wavelengths away from the aperture edges suggests the presence of freely propagating background fields. The ratio of scattered far-fields to scattered near-fields, e.g. fields localized along the edges of the slit, is large. Consequently, resolution of near-fields launched and scattered by the subwavelength

dimensionality of this aperture requires a higher degree of far-field discrimination than was achieved in this study. Improvements in near-field to far-field scattering ratio can be obtained several ways. Demodulation at frequencies greater than *2f* would result in images containing higher concentration of localized fields; however, advantages of higher harmonic demodulation are partially offset by decreases in overall signal intensity. Because the slit aperture utilized in this study was not strictly sub-wavelength, a non-negligible portion of incident field was able to propagate through the aperture. Fabrication of apertures with larger depth to width aspect ratios, possible with lower ion beam currents, or illumination with longer wavelength incident fields would significantly decrease contributions of this field to the total signal. Additionally, with the probe's apex near the surface, a large number of scattering centers along the base of the tip and cantilever body exist outside of the near-field intensity region. The scattering contributions of these centers likely originate in the far-field and do not enhance image resolution. The surface of an ideally suited probe would be optically passive at every except at the apex. Selective etching or deposition of conductive SPM probes may provide additional signal to noise enhancement.

3.4 SUMMARY AND CONCLUSIONS

We demonstrated ANSOM images of a nanoslit aperture contain interference fringes which result from superposition of the average detected wavevector and components of the field scattered by the nanoslit. Analysis confirms that such a slit generates two scattered orders launched perpendicular to the slit. Furthermore, fringe patterns can be controlled by changing the orientation of the slit, and thus the direction of the two scattered orders, with respect to the

detector or vice versa. The model originally developed by Aubert et al. was extended to account for the two scattered orders present in our system. The resulting calculated fields agreed well with the ANSOM data in several different detector/slit orientations.

Additionally, probe geometry and probe position relative to the slit strongly affect the magnitude of self-homodyning fields exhibited in ANSOM images. For a single slit aperture, sources of homodyning fields include a propagating field transmitted through the slit and reflected by the probe base and/or cantilever body. Sensitivity of self-homodyne amplification to probe geometry suggests that portions of the probe base and cantilever body scatter significant transmitted optical fields.

3.5 BIBLIOGRAPHY

[1] **Aigouy, L.; Lalanne, P.; Hugonin, J. P.; Julie, G.; Mathet, V. and Mortier, M.** (**2007**). *Near-Field analysis of surface waves launched at nanoslit apertures*, Physical Review Letters 98 : 153902/1-153902/4.

[2] **Akarca-Biyikli, S. S.; Bulu, I. and Ozbay, E.** (**2004**). *Enhanced transmission of microwave radiation in one-dimensional metallic gratings with subwavelength aperture*, Applied Physics Letters 85 : 1098-1100.

[3] **Akhremitchev, B. B.; Pollack, S. and Walker, G. C.** (**2001**). *Apertureless scanning near-field infrared microscopy of a rough polymeric surface*, Langmuir 17 : 2774-2781.

[4] **Ashino, M. and Ohtsu, M.** (**1998**). *Fabrication and evaluation of a localized plasmon resonance probe for near-field optical microscopy/spectroscopy*, Applied Physics Letters 72 : 1299-1301.

[5] **Aubert, S.; Bruyant, A.; Blaize, S.; Bachelot, R.; Lerondel, G.; Hudlet, S. and Royer, P.** (**2003**). *Analysis of the interferometric effect of the background light in apertureless scanning near-field optical microscopy*, Journal of the Optical Society of America B 20 : 2117-2124.

[6] **Averbukh, I. S.; Chernobrod, B. M.; Sedletsky, O. A. and Prior, Y.** (**2000**). *Coherent near field optical microscopy*, Optics Communications 174 : 33-41.

[7] **Bachelot, R.; Gleyzes, P. and Boccara, A. C.** (**1995**). *Near-field optical microscope based on local perturbation of a diffraction spot*, Opt. Lett 20 : 1924-1926.

[8] **Barchiesi, D.** (**2006**). *Scanning near-field optical data contrast measurement: a tomographylike near-field reconstruction*, Appl Opt FIELD Full Journal Title:Applied optics 45 : 7597-601.

[9] **Bek, A.; Vogelgesang, R. and Kern, K.** (**2006**). *Apertureless scanning near field optical microscope with sub-10 nm resolution*, Review of Scientific Instruments 77 : 043703.

[10] **Betzig, E. and Trautman, J. K.** (**1992**). *Near-field optics: microscopy, spectroscopy, and surface modification beyond the diffraction limit*, Science (Washington, DC, United States) 257 : 189-95.

[11] **Bohn, J. L.; Nesbitt, D. J. and Gallagher, A.** (**2001**). *Field enhancement in apertureless near-field scanning optical microscopy*, J. Opt. Soc. Am. A 18 : 2998-3006.

[12] **Bonod, N.; Popov, E.; Li, L. and Chernov, B.** (**2007**). *Unidirectional excitation of surface plasmons by slanted gratings*, Optics Express 15 : 11427-11432.

[13] **Bozhevolnyi, S. I.; Volkov, V. S.; Devaux, E.; Laluet, J.-Y. and Ebbesen, T. W.** (**2006**). *Channel plasmon subwavelength waveguide components including interferometers and ring resonators*, Nature (London, United Kingdom) 440 : 508-511.

[14] **Bravo-Abad, J.; Martín-Moreno, L. and García-Vidal, F. J.** (**2004**). *Transmission properties of a single metallic slit: From the subwavelength regime to the geometrical-optics limit*, Physical Review E 69 : 26601.

[15] **Calander, N. and Willander, M.** (**2002**). *Theory of surface-plasmon resonance optical-field enhancement at prolate spheroids*, Journal of Applied Physics 92 : 4878-4884.

[16] **Dunn, R. C.** (**1999**). *Near-Field scanning optical microscopy*, Chemical Reviews (Washington, D. C.) 99 : 2891-2927.

[17] **Egorov, D.; Dennis, B. S.; Blumberg, G. and Haftel, M. I.** (**2004**). *Two-dimensional control of surface plasmons and directional beaming from arrays of subwavelength apertures*, Phys. Rev. B 70 : 033404.

[18] **Furukawa, H. and Kawata, S.** (**1996**). *Analysis of image formation in a near-field scanning optical microscope: effects of multiple scattering*, Optics Communications 132 : 170-178.

[19] **Gan, Q.; Guo, B.; Song, G.; Chen, L.; Fu, Z.; Ding, Y. J. and Bartoli, F. J.** (**2007**). *Plasmonic surface-wave splitter*, Applied Physics Letters 90 : 161130/1-161130/3.

[20] **Garcia-Vidal, F. J.; Lezec, H. J.; Ebbesen, T. W. and Martin-Moreno, L.** (**2003**). *Multiple paths to enhance optical transmission through a subwavelength slit*, Phys. Rev. Lett. 90 : 213901.

[21] **Girard, C. and Dereux, A.** (**1996**). *Near-field optics theories*, Reports on Progress in Physics 59 : 657-699.

[22] **Girard, C.; Martin, O. J. F. and Dereux, A.** (**1995**). *Molecular lifetime changes induced by nanometer scale optical fields*, Physical Review Letters 75 : 3098.

[23] **Gomez, L.; Bachelot, R.; Bouhelier, A.; Wiederrecht, G. P.; Chang, S.-h.; Gray, S. K.; Hua, F.; Jeon, S.; Rogers, J. A.; Castro, M. E.; Blaize, S.; Stefanon, I.; Lerondel, G. and Royer, P.** (**2006**). *Apertureless scanning near-field optical microscopy: a comparison between homodyne and heterodyne approaches*, Journal of the Optical Society of America B: Optical Physics 23 : 823-833.

[24] **Gonzalez, M. U.; Weeber, J. C.; Baudrion, A. L.; Dereux, A.; Stepanov, A. L.; Krenn, J. R.; Devaux, E. and Ebbesen, T. W.** (**2006**). *Design, near-field characterization, and modeling of 45 degree surface-plasmon Bragg mirrors*, Physical Review B: Condensed Matter and Materials Physics 73 : 155416/1-155416/13.

[25] **Hayazawa, N.; Inouye, Y. and Kawata, S.** (**1999**). *Evanescent field excitation and measurement of dye fluorescence in a metallic probe near-field scanning optical microscope*, Journal of Microscopy (Oxford) 194 : 472-476.

[26] **Hayazawa, N.; Inouye, Y.; Sekkat, Z. and Kawata, S.** (**2000**). *Metallized tip amplification of near-field Raman scattering*, Optics Communications 183 : 333-336.

[27] **Hecht, B.; Bielefeldt, H.; Inouye, Y. and Pohl, D. W.** (**1997**). *Facts and artifacts in near-field optical microscopy*, Journal of Applied Physics 81 : 2492-2498.

[28] **Hillenbrand, R. and Keilmann, F.** (**2002**). *Material-specific mapping of metal/semiconductor/dielectric nanosystems at 10 nm resolution by backscattering near-field optical microscopy*, Applied Physics Letters 80 : 25-27.

[29] **Hillenbrand, R.; Knoll, B. and Keilmann, F.** (**2001**). *Pure optical contrast in scattering-type scanning near-field microscopy*, Journal of Microscopy (Oxford, United Kingdom) 202 : 77-83.

[30] **Hillenbrand, R.; Taubner, T. and Keilmann, F.** (**2002**). *Phonon-enhanced light-matter interaction at the nanometre scale*, Nature (London, United Kingdom) 418 : 159-162.

[31] **Inouye, Y.** (**2001**). *Apertureless metallic probes for near-field microscopy*, Topics in Applied Physics 81 : 29-48.

[32] **Inouye, Y. and Kawata, S.** (**1994**). *Near-field scanning optical microscope with a metallic probe tip*, Opt. Lett 19 : 159-161.

[33] **Kawata, S.** (**2001**). *Near-field microscope probes utilizing surface plasmon polaritons*, Topics in Applied Physics 81 : 15-27.

[34] **Kawata, S. and Inouye, Y.** (**1995**). *Scanning probe optical microscopy using a metallic probe tip*, Ultramicroscopy 57 : 313.

[35] **Keilmann, F.** (**2004**). *Scattering-type near-field optical microscopy*, Journal of Electron Microscopy 53 : 187-192.

[36] **Kim, Z. H.; Liu, B. and Leone, S. R.** (**2005**). *Nanometer-scale optical imaging of epitaxially grown GaN and InN islands using apertureless near-field microscopy*, Journal of Physical Chemistry B 109 : 8503-8508.

[37] **Knoll, B. and Keilmann, F.** (**1999**). *Near-field probing of vibrational absorption for chemical microscopy*, Nature (London) 399 : 134-137.

[38] **Knoll, B. and Keilmann, F.** (**2000**). *Enhanced dielectric contrast in scattering-type scanning near-field optical microscopy*, Optics Communications 182 : 321-328.

[39] **Konopsky, V. N.** (**2000**). *Operation of scanning plasmon near-field microscope with gold and silver tips in tapping mode: demonstration of subtip resolution*, Optics Communications 185 : 83-93.

[40] **Kottmann, J. P.; Martin, O. J. F.; Smith, D. R. and Schultz, S.** (**2001**). *Dramatic localized electromagnetic enhancement in plasmon resonant nanowires*, Chemical Physics Letters 341 : 1-6.

[41] **Kukhlevsky, S. V.; Mechler, M.; Samek, O. and Janssens, K.** (**2006**). *Analytical model of the enhanced light transmission through subwavelength metal slits: Green's function formalism versus Rayleigh's expansion*, Applied Physics B: Lasers and Optics 84 : 19-24.

[42] **Labardi, M.; Patane, S. and Allegrini, M.** (**2000**). *Artifact-free near-field optical imaging by apertureless microscopy*, Applied Physics Letters 77 : 621-623.

[43] **Laddada, R.; Benrezzak, S.; Adam, P. M.; Viardot, G.; Bijeon, J. L. and Royer, P.** (**1999**). *Detection of an evanescent field scattered by silicon tips in an apertureless scanning near-field optical microscope*, European Physical Journal: Applied Physics 6 : 171-178.

[44] **Lalanne, P.; Hugonin, J. P. and Rodier, J. C.** (**2005**). *Theory of surface plasmon generation at nanoslit apertures*, Physical Review Letters 95 : 263902.

[45] **Lalanne, P.; Hugonin, J. P. and Rodier, J. C.** (**2006**). *Approximate model for surface-plasmon generation at slit apertures*, J. Opt. Soc. Am. A 23 : 1608-1615.

[46] **Laux, E.; Genet, C.; Skauli, T. and Ebbesen, T. W.** (**2008**). *Plasmonic photon sorters for spectral and polarimetric imaging*, Nat Photon 2 : 161-164.

[47] **Lezec, H. J.** (**2002**). *Beaming light from a subwavelength aperture*, Science 297 : 820.

[48] **Lezec, H. J. and Thio, T.** (**2004**). *Diffracted evanescent wave model for enhanced and suppressed optical transmission through subwavelength hole arrays*, OPTICS EXPRESS 12 : 3629-3651.

[49] **Lindberg, J.; Lindfors, K.; Setälä, T.; Kaivola, M. and Friberg, A.** (**2004**). *Spectral analysis of resonant transmission of light through a single sub-wavelength slit*, Opt. Express 12 : 623-632.

[50] **Martin, O. J. F. and Girard, C.** (**1997**). *Controlling and tuning strong optical field gradients at a local probe microscope tip apex*, Applied Physics Letters 70 : 705-707.

[51] **Martin, Y. C.; Hamann, H. F. and Wickramasinghe, H. K.** (**2001**). *Strength of the electric field in apertureless near-field optical microscopy*, Journal of Applied Physics 89 : 5774.

[52] **Mechler, M.; Samek, O. and Kukhlevsky, S. V.** (**2007**). *Enhanced transmission and reflection of few-cycle pulses by a single slit*, Physical Review Letters 98 : 163901-4.

[53] **Novotny, L.** (**1996**). *Single molecule fluorescence in inhomogeneous environments*, Applied Physics Letters 69 : 3806-3808.

[54] **Novotny, L. and Stranick, S. J.** (**2006**). *Near-field optical microscopy and spectroscopy with pointed probes*, Annual Review of Physical Chemistry 57 : 303-331.

[55] **Ohtsu, M.; Kobayashi, K.; Kawazoe, T.; Sangu, S. and Yatsui, T.** (**2002**). *Nanophotonics: Design, fabrication, and operation of nanometric devices using optical near fields*, IEEE Journal of Selected Topics in Quantum Electronics 8 : 839-862.

[56] **Pacifici, D.; Lezec, H. J. and Atwater, H. A.** (**2007**). *All-optical modulation by plasmonic excitation of CdSe quantum dots*, Nat Photon 1 : 402-406.

[57] **Pang, Y.; Genet, C. and Ebbesen, T. W.** (**2007**). *Optical transmission through subwavelength slit apertures in metallic films*, Optics Communications 280 : 10-15.

[58] **Patanè, S.; Gucciardi, P. G.; Labardi, M. and Allegrini, M.** (**2004**). *Apertureless near-field optical microscopy*, RIVISTA DEL NUOVO CIMENTO 27.

[59] **Pieruccini, M.; Savasta, S.; Girlanda, R.; Iotti, R. C. and Rossi, F.** (**2003**). *Near-field light emission from nano- and micrometric complex structures*, Applied Physics Letters 83 : 2480-2482.

[60] **Pohl, D. W.** (**2001**). *Near-field optics and the surface plasmon polariton*, Topics in Applied Physics 81 : 1-13.

[61] **Pohl, D. W.; Denk, W. and Lanz, M.** (**1984**). *Optical stethoscopy: Image recording with resolution lambda/20*, Applied Physics Letters 44 : 651-653.

[62] **Porto, J. A.; Carminati, R. and Greffet, J. J.** (**2000**). *Theory of electromagnetic field imaging and spectroscopy in scanning near-field optical microscopy*, Journal of Applied Physics 88 : 4845-4850.

[63] **Porto, J. A.; Johansson, P.; Apell, S. P. and López-Ríos, T.** (**2003**). *Resonance shift effects in apertureless scanning near-field optical microscopy*, Physical Review B 67 : 085409.

[64] **Putman, C. A. J.; Van der Werf, K. O.; De Grooth, B. G.; Van Hulst, N. F. and Greve, J.** (**1994**). *Tapping mode atomic force microscopy in liquid*, Applied Physics Letters 64 : 2454-2456.

[65] **Raschke, M. B.; Molina, L.; Elsaesser, T.; Kim, D. H.; Knoll, W. and Hinrichs, K.** (**2005**). *Apertureless Near-Field Vibrational Imaging of Block-Copolymer Nanostructures with Ultrahigh Spatial Resolution*, CHEMPHYSCHEM-WEINHEIM- 6 : 2197.

[66] **Rasmussen, A. and Deckert, V.** (**2005**). *New dimension in nano-imaging: breaking through the diffraction limit with scanning near-field optical microscopy*, Analytical and Bioanalytical Chemistry 381 : 165-172.

[67] Saleh, B. E. A. and Teich, M. C., **1991**. *Fundamentals of Photonics*. John Wiley & Sons, Inc., .

[68] **Sasaki, H. and Sasaki, Y.** (**2006**). *Imaging of refractive index change by the reflection-mode scattering-type scanning near-field optical microscope: Simulation and observations*, Journal of Applied Physics 85 : 2026-2030.

[69] **Schouten, H. F.; Visser, T. D.; Lenstra, D. and Blok, H.** (**2003**). *Light transmission through a subwavelength slit: Waveguiding and optical vortices*, Physical Review E 67 : 036608.

[70] **Stark, R. W. and Heckl, W. M.** (**2003**). *Higher harmonics imaging in tapping-mode atomic-force microscopy*, Review of Scientific Instruments 74 : 5111-5114.

[71] **Stebounova, L.; Akhremitchev, B. B. and Walker, G. C.** (**2003**). *Enhancement of the weak scattered signal in apertureless near-field scanning infrared microscopy*, Review of Scientific Instruments 74 : 3670-3674.

[72] **Stuart, D. A.; Haes, A. J.; Yonzon, C. R.; Hicks, E. M. and Van Duyne, R. P.** (**2005**). *Biological applications of localised surface plasmonic phenomenae*, Nanobiotechnology, IEE Proceedings - 152 : 13-32.

[73] **Suckling, J. R.; Sambles, J. R. and Lawrence, C. R.** (**2005**). *Remarkable zeroth-order resonant transmission of microwaves through a single subwavelength metal slit*, Physical Review Letters 95 : 187407-4.

[74] **Synge, E. H.** (**1928**). *A suggested method for extending microscopic resolution into the ultra-microscopic region*, Phil. Mag 6 : 1.

[75] **Takakura, Y.** (**2001**). *Optical resonance in a narrow slit in a thick metallic screen*, Phys. Rev. Lett. 86 : 5601.

[76] **Thomas, D. A. and Hughes, H. P.** (**2004**). *Enhanced optical transmission through a subwavelength 1D aperture*, Solid State Communications 129 : 519-524.

[77] **Volkov, V. S.; Bozhevolnyi, S. I.; Devaux, E.; Laluet, J.-Y. and Ebbesen, T. W.** (**2007**). *Wavelength selective nanophotonic components utilizing channel plasmon polaritons*, Nano Letters 7 : 880-884.

[78] **Walford, J. N.; Porto, J. A.; Carminati, R.; Greffet, J. J.; Adam, P. M.; Hudlet, S.; Bijeon, J. L.; Stashkevich, A. and Royer, P.** (**2001**). *Influence of tip modulation on image formation in scanning near-field optical microscopy*, Journal of Applied Physics 89 : 5159-5169.

[79] **Weeber, J.-C.; Lacroute, Y.; Dereux, A.; Devaux, E.; Ebbesen, T.; Girard, C.; Gonzalez, M. U. and Baudrion, A.-L.** (**2004**). *Near-field characterization of Bragg mirrors engraved in surface plasmon waveguides*, Physical Review B: Condensed Matter and Materials Physics 70 : 235406/1-235406/12.

[80] **Wei, P.-K.; Chou, H.-L. and Fann, W.-S.** (**2002**). *Optical near field in nanometallic slits*, Opt. Express 10 : 1418-1424.

[81] **Wurtz, G.; Bachelot, R. and Royer, P.** (**1999**). *Imaging a GaAlAs laser diode in operation using apertureless scanning near-field optical microscopy*, Eur. Phys. J. AP 5 : 269-275.

[82] **Xie, Y.; Zakharian, A. R.; Moloney, J. V. and Mansuripur, M.** (**2004**). *Transmission of light through slit apertures in metallic films*, Opt. Express 12 : 6106.

[83] **Yang, F. and Sambles, J. R.** (**2002**). *Resonant Transmission of Microwaves through a Narrow Metallic Slit*, Physical Review Letters 89 : 063901.

[84] **Yin, L.; Vlasko-Vlasov, V. K.; Pearson, J.; Hiller, J. M.; Hua, J.; Welp, U.; Brown, D. E. and Kimball, C. W.** (**2005**). *Subwavelength focusing and guiding of surface plasmons*, Nano Letters 5 : 1399-1402.

[85] **Zenhausern, F.; Martin, Y. and Wickramasinghe, H. K.** (**1995**). *Scanning interferometric apertureless microscopy: Optical imaging at 10 angstrom resolution*, Science 269 : 1083.

[86] **Zenhausern, F.; O'Boyle, M. P. and Wickramasinghe, H. K.** (**1994**). *Apertureless near-field optical microscope*, Applied Physics Letters 65 : 1623-1625.

4.0 DIAMETER-DEPENDENT BENDING MODULUS OF INDIVIDUAL MULTIWALL BORON NITRIDE NANOTUBES

List of authors: Adrienne E. Tanur, Jiesheng Wang, Arava L. M. Reddy, Daniel N. Lamont, Yoke Khin Yap, and Gilbert C. Walker

Author contribution: The author of this dissertation contributed to the characterization of the boron nitride nanotubes, providing interpretation of the results and preparation of the manuscript. This work has been published as *J. Phys. Chem. B* **2013**, 117, 4618

4.1 INTRODUCTION

Boron nitride nanotubes (BNNTs), first predicted in 1994 [5; 51] and synthesized in 1995, [12] have attracted increasing attention in recent years due to their unusual properties. Although structurally similar to carbon nanotubes (CNTs), BNNTs have significantly different optical and electronic properties. BNNTs are much more insulating than CNTs, with a band gap of 5–6 eV which is largely independent of tube chirality or diameter.[5] Theoretical studies

have indicated that the axial Young's modulus of single wall BNNTs (SWBNNTs) is of the same order as that of carbon nanotubes (~1 TPa).[28; 65] BNNTs' mechanical properties, together with their high aspect ratio, high thermal conductivity,[4] optical transparency, electrically insulating character, and high resistance to oxidation (up to 1100 °C),[10] make them ideal fillers for technologically relevant composite materials such as seals and encapsulants[3; 11; 49; 70] and biomaterials.[36] In addition, BNNTs show promise for a diverse range of other applications, including hydrogen storage,[44; 50] targeted drug delivery,[15] and optoelectronic devices such as lasers and light emitting diodes.[32; 39]

For BNNTs to be successfully employed in the aforementioned applications, a better understanding of their mechanical properties is required. This is particularly important for applications which rely on the mechanical properties of individual tubes, such as resonators and sensors,[14] and microtubule mimics.[47] In contrast to CNTs, only a handful of experimental studies have been conducted on BNNTs to determine their Young's modulus. Chopra and Zettl[13] used the resonance technique of Treacy et al.[64] to determine that an arc-discharge multiwall BNNT (MWBNNT) (3.5 nm outer diameter) had a modulus of ~1.22 TPa. Electric-field-induced resonance experiments by Suryavanshi et al.[61] yielded moduli of 505–1031 GPa for a set of 18 tubes, with outer diameters ranging from 34 to 94 nm. Golberg et al.[23] determined moduli of 0.5–0.6 TPa (40 and 100 nm outer diameter tubes) *via* in situ bending experiments using an atomic force microscope (AFM) setup within a transmission electron microscope (TEM). Using a similar setup, Ghassemi et al.[22] measured five MWBNNTs with outer diameters of 38–51 nm, and found that the average modulus was ~0.5 TPa. Depending on the choice of shell thickness, the Young's modulus of a 1.9 nm diameter

SWBNNT was found to range from 0.87 to 1.11 TPa.[1] The wide range of moduli observed indicates a need for further study in order to elucidate the influence of factors such as the synthesis technique, nanotube structure, and morphology on the Young's modulus.

Three-point bending tests conducted with AFM have been used to characterize the modulus of a variety of high aspect ratio structures, including CNTs,[38; 52; 54] nanowires,[45; 67] and electrospun polymers.[59] Typically, the nanotubes or wires are deposited onto a stiff substrate with a topographical pattern, such as polished porous Al_2O_3 membranes or Si gratings patterned with trenches. The tubes occasionally lie over pores or trenches, and the midpoint of the suspended portion is subjected to a downward force applied by the AFM tip. Force–displacement curves are obtained, and the bending modulus can be calculated directly from the slope of the force curve together with the geometrical parameters of the tube's diameter and suspended length. In most studies, the supported beam ends are assumed to have clamped boundary conditions due to the adhesion between the nanomaterial and the substrate. However, this assumption can be unfounded and can be a source of systematic error in the determination of the bending modulus. Other beam end boundary conditions include simply supported and mixed support in which one end is clamped and the other end is simply supported. Depending on the support conditions, the solution of the Euler–Bernoulli beam equation takes on different forms, yielding different expressions for the bending modulus. The appropriate boundary conditions for an individual tube can be determined if multiple locations along the length of the suspended tube are probed. This allows for a more accurate determination of the modulus value, as demonstrated by Shanmugham et al.,[57] Chen et al.,[9] Kluge et al., [35] and Gangadean et al.[20]

In this study, we use AFM to measure the bending modulus E_B of MWBNNTs synthesized by a growth-vapor-trapping chemical vapor deposition (GVT-CVD) technique.[37] A force mapping technique is used in order to collect force curves from various locations along the length of the suspended tube. We show that for our sample the majority of tubes possess simply supported ends instead of clamped ends. On the basis of these boundary conditions, we calculate the bending moduli for tubes of various diameters, and we present a discussion about the diameter dependence that is observed.

4.2 EXPERIMENTAL METHODS

MWBNNTs were synthesized *via* the growth-vapor-trapping chemical vapor deposition technique previously described by Lee and co-workers.[37] The MWBNNTs were collected on Si substrates and sonicated in ethanol to form a MWBNNT suspension.

The MWBNNTs were characterized with scanning electron microscopy (SEM), low and high resolution transmission electron microscopy (TEM, HR-TEM), and Fourier transform infrared spectroscopy (FTIR). The morphology of the as-synthesized MWBNNTs was characterized with SEM (S-4700, Hitachi, Japan). For the TEM measurements, the MWBNNT suspension was dropped onto a holey carbon TEM grid and allowed to dry. Bright-field low resolution TEM images were acquired at 30 kV, 17.5 μA emission current (S-5200, Hitachi, Japan). Bright-field HR-TEM images were acquired at 200 kV, 39 μA emission current (HD-2000, Hitachi, Japan). FTIR spectra were taken using an attenuated total internal reflection (ATR) setup. The MWBNNT suspension was dropped onto a ZnSe ATR crystal and allowed to

dry. For comparison purposes, hexagonal boron nitride (*h*-BN) nanoparticles (MK-hBN-N70, MK Impex Canada, Mississauga, Ontario) were also characterized by FTIR. Spectra were recorded on a FTIR spectrometer (Spectrum BX, Perkin-Elmer, Waltham, MA) at a resolution of 1 cm^{-1}.

For the AFM sample preparation, the MWBNNT suspension was dropped onto clean Si substrates patterned with trenches 400 nm wide and 200 nm deep (LightSmyth Technologies, Eugene OR) and was allowed to dry. AFM height images of the tubes on the patterned substrate were acquired in air under ambient conditions using AC (intermittent contact) mode (MFP-3D, Asylum Research, Santa Barbara CA). Si probes (NCH, Nano World, Neuchâtel Switzerland) with tip radii of ∼20 nm were used. The optical lever sensitivity of the cantilevers was calibrated by acquiring force curves in contact mode on a clean Si substrate. The spring constant of each cantilever used was determined by the thermal method and found to range from 33 to 46 N/m. [30] A discussion of the applicability of the thermal method for high spring constant cantilevers is presented in the Supporting Information. AFM force maps (typically 2 μm × 0.5 μm with 32 × 16 points) were obtained of MWBNNTs spanning trenches. A force curve (applied force F versus tip–sample separation) was collected at each point on the map. The force curves corresponding to the points along the suspended portion of the tube (as determined from the height map and the force curves themselves) were analyzed to extract the effective tube stiffness, k_{eff}, by a linear fit to the slope of the force curve. A more detailed description of the force mapping method is given in the Supporting Information.

The suspended length L for a given tube was determined from the AFM height map as well as from higher-resolution AFM height images acquired in tapping mode. The lateral dimension of the pixels making up the force map was used to estimate the errors associated with the values of position (a, b) and suspended length. The tube diameter was determined by the height of the tube on the substrate from the tapping mode height images.

4.3 RESULTS AND DISCUSSION

4.3.1 Characterization of MWBNNTs

Electron microscopy images of the MWBNNTs produced by the GVT-CVD method are shown in Figure 4.1. The scanning electron microscope (SEM) image in Figure 4.1a shows straight fibers with diameters ranging from ~15 to 60 nm. Figure 4.1b depicts a low resolution bright field TEM image of the as-synthesized MWBNNTs, and confirms the hollow tubular nature of the fibers. A high resolution TEM image of a dark region in a tube wall is shown in Figure 4.1c. The layers appear crystalline with an interlayer spacing of ~0.34 nm, as determined from the (002) diffraction spots in the fast Fourier transform for this region (not shown). This spacing is consistent with the crystal structure of hexagonal boron nitride and BNNTs.[22; 37]

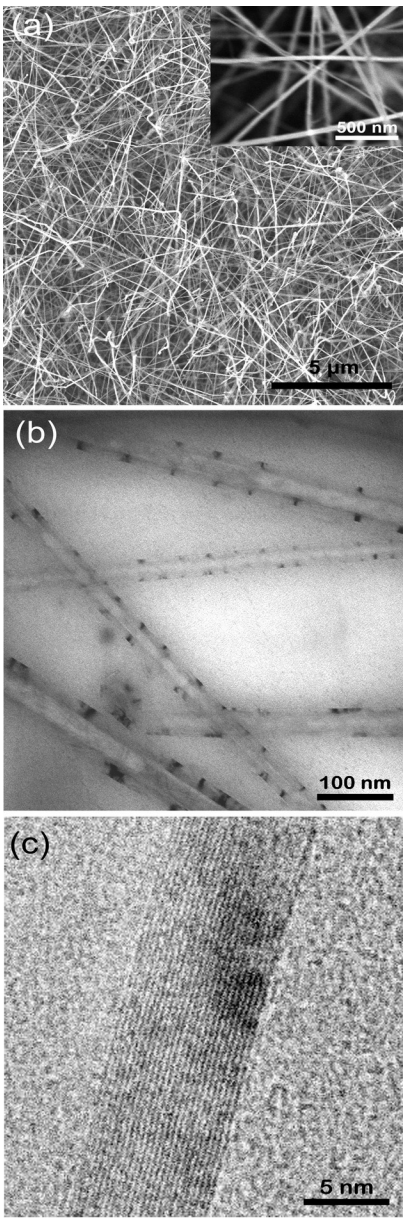

Figure 4.1: SEM image of MWBNNTs

(a) SEM image of MWBNNTs. Inset: Higher magnification SEM image showing straight, slender fibers 15–60 nm in diameter. (b) Low resolution TEM image of MWBNNTs. (c) High resolution TEM image of a MWBNNT wall near a typical dark spot shown in part b.

The FTIR spectrum of the MWBNNTs is shown in Figure 4.2. For comparison, the spectrum for commercially available hexagonal BN (*h*-BN) nanoparticles is also given. The broadness of the *h*-BN peaks is likely due to due to both size distribution as well as defects within the crystal structure, predominantly on the edges of the nanoparticles. The MWBNNT spectrum exhibits peaks at ~1368 and ~1510 cm^{-1}, which correspond to the in-plane transverse optical (TO) and longitudinal optical (LO) E_{1u} modes of *h*-BN. The TO E_{1u} mode is a stretching mode along the tube axis, while the LO E_{1u} mode is a stretching mode along the tube circumference. A weak feature at around 800 cm^{-1} is shown enlarged in the inset ofFigure 4.2. A shoulder is visible at ~819 cm^{-1} and a peak at ~806 cm^{-1}. These spectral features correspond to the out-of-plane TO and LO A_{2u} modes of *h*-BN. [22; 68]

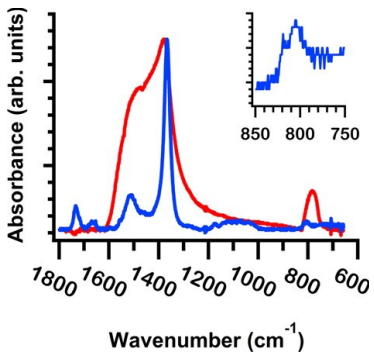

Figure 4.2: FTIR spectrum of MWBNNTs

. FTIR spectrum of MWBNNTs (blue line). The FTIR spectrum of h-BN nanoparticles (red line) is also shown for comparison.

4.3.2 AFM Three-Point Bending

In three-point bending experiments, slender wires can be modeled as an elastic string (pure stretching), a stiff beam (pure bending), or a combination of the two. Heidelberg et al.[27] presented a generalized approximation for these behaviors, in which a force F is applied to the midpoint of the suspended wire and the wire ends are assumed to be clamped:

$$F_{center} = \frac{192\,E_B I}{L^3}\delta_{center}\left(1+\frac{A}{24\,I}\delta_{center}^2\right)$$

Equation 4.1

In the above expression, δ is the deflection of the wire, E_B is the bending modulus, A is the cross-sectional area of the wire, and I is the second moment of area. At small displacements, the wire undergoes pure bending which is described by the first linear term. At large displacements, axial tensile stresses are induced as the wire stretches which are described by the cubic second term ($F \propto \delta^3$). In this study, only pure bending is considered because the experiments are conducted within the small deflection regime, in which the maximum deflection does not exceed the radius of the wire.

To model the MWBNNTs in this study as stiff beams undergoing pure bending, Euler–Bernoulli beam theory was employed. It should be noted that this theory assumes a homogeneous isotropic material, which is not the case for multiwall nanotubes. Nevertheless,

simulations indicate that this approximation offers an adequate description of nanotube bending mechanics prior to buckling.[31] As a result, this approach has been widely used in AFM bending experiments on nanowires and nanotubes.[38; 45; 52; 54; 59] Unique solutions to the beam equation depend on the boundary conditions of the beam ends, which can be considered to be clamped (no deflection or slope at beam end) or simply supported (no deflection or bending moment at beam end). Beam schematics are presented in Figure 4.3, which summarize the three models considered in this work: simply supported beam model (a, SSBM), double clamped beam model (b, DCBM), and mixed support beam model (c, MSBM).[29]

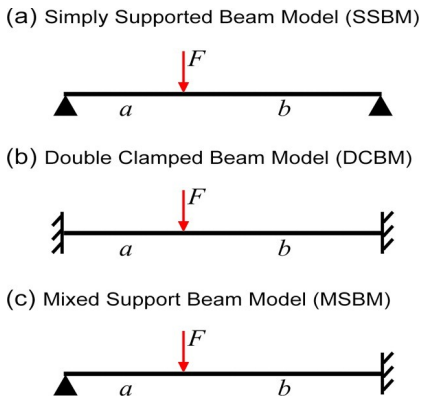

Figure 4.3: Beam schematics

Beam schematics describing beam bending boundary conditions.

The corresponding equations are as follows:

$$\text{SSBM:} \quad F = \frac{3 L E_B I}{a^2 b^2} \delta$$

Equation 4.2

$$\text{DCBM:} \quad F = \frac{3 L^3 E_B I}{a^3 b^3} \delta$$

Equation 4.3

$$\text{MSBM:} \quad F = \frac{12 L^3 E_B I}{a^2 b^3 (3L + a)} \delta$$

Equation 4.4

In these equations, L is the suspended length of the beam and a and b are the suspended lengths on both sides of the applied force F, where $a + b = L$. I, the second moment of area, is taken to be $I = \pi D^4/64$ which is defined for a solid cylindrical wire with a circular cross section, where D is the diameter. Hence, in this approximation of the multiwall nanotube beam, only the outer diameter is taken into account and not the inner diameter. In order to determine the appropriate boundary conditions for each tube, the AFM tip is used to apply a force at different positions

along the suspended tube, not just at the midpoint. Therefore, AFM force curves (plots of F versus the tip–sample separation (=beam deflection, δ)) are collected at multiple locations along the tube. The linear slope of a force curve directly yields the effective tube stiffness, $k_{eff} = F/\delta$. The boundary conditions for the tube are determined by plotting k_{eff} versus the position along the tube (a/L) and performing fits to the various beam models (Equations 4.2-4.4). The bending modulus E_B is then determined using the appropriate beam model.

Figure 4.4 shows SEM (a) and AFM images (b–d) of suspended MWBNNTs on patterned Si trenches (400 nm wide and 200 nm deep). An AFM height image of a typical MWBNNT spanning a trench is shown in Figure 4.4b. The height image is subsequently divided up into pixels (typically 32 × 16 or 64 × 32) by the AFM software, and force curves are collected at each point (pixel) during the force mapping procedure. The corresponding AFM height map image illustrating the spatial location (x, y) of each of the force measurements is shown in Figure 4.4c. The height in each pixel is determined from the Z range distance at which the tip first engages the sample during the extend portion of the force curve. Figure 4.4d shows the AFM height image of the MWBNNT after the force map was performed, and its similarity to Figure 4.4b indicates that the tube did not shift or deform as a result of the force measurements. Typical force curves collected from different locations on a MWBNNT are shown in Figure 4.5. The red dotted line corresponds to a force curve obtained from a location where the tube is supported by the Si substrate (red “x” in Figure 4.4c, illustrative purpose only), while the blue solid line corresponds to a force curve obtained from a position where the tube is suspended over a trench (blue “x” in Figure 4.4c, illustrative purpose only). The slope of the blue solid line in Figure 4.5 is equivalent to k_{eff}, as shown

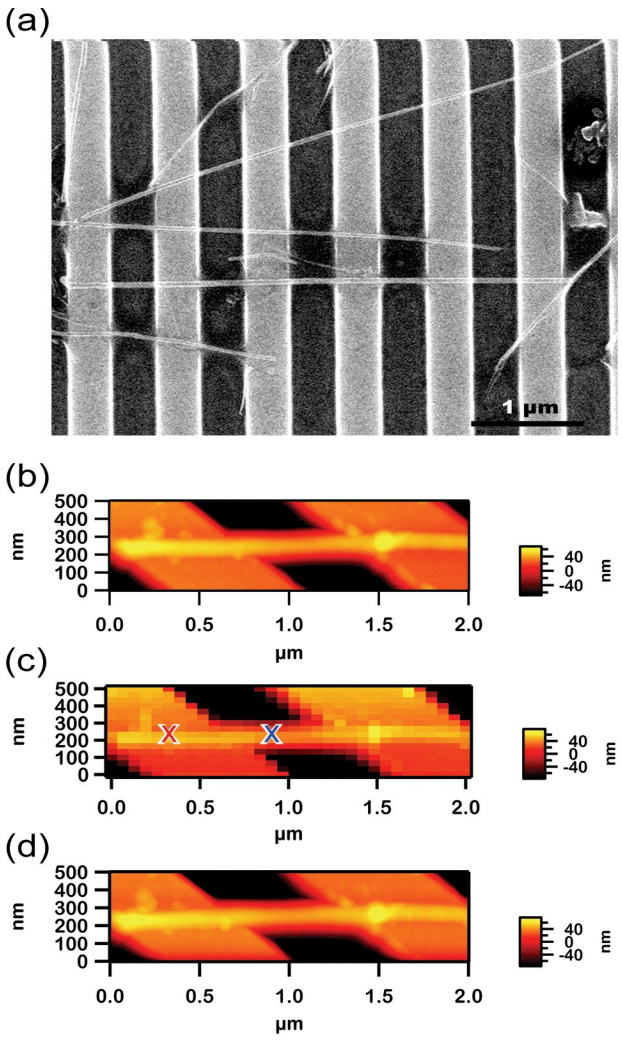

Figure 4.4: SEM image of MWBNNTs

(a) SEM image of MWBNNTs on patterned Si substrate. (b) AFM height image before force mapping was performed. (c) Height map image corresponding to a force map acquired at a deflection trigger of 1 nm. (d) AFM height image after a force map was acquired.

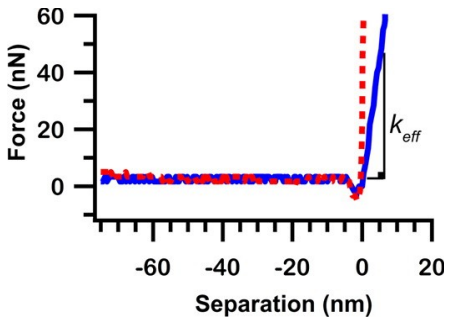

Figure 4.5: Force curve

(Red dotted line) Force curve obtained from a point on a tube supported by substrate. (Blue solid line) Force curve obtained from a point on a tube suspended over a trench.

Plots of the effective tube stiffness (k_{eff}) versus position along the suspended tube (a/L) fitted with Equations 4.2-4.4 corresponding to SSBM, DCBM, and MSBM are given in Figure 4.6. The values of k_{eff} located near the ends ($a/L < 0.2$, $a/L > 0.8$) of the suspended tubes were not included in the fits, because of the large error associated with fitting force curves with large slopes (theoretically, at the ends, k_{eff} approaches infinity). Figure 4.6a shows that SSBM fits the data better than DCBM, signifying that the MWBNNT is an example of a simply supported tube. On the other hand, the data in Figure 4.6b fits the MSBM model well and is therefore an example of a tube which is fixed on one end (its left side) and simply supported on the opposite end (its right side). Despite the fact that all of the tubes examined were on the same sample, various support conditions were observed which demonstrate the importance of determining the boundary conditions for each individual tube.

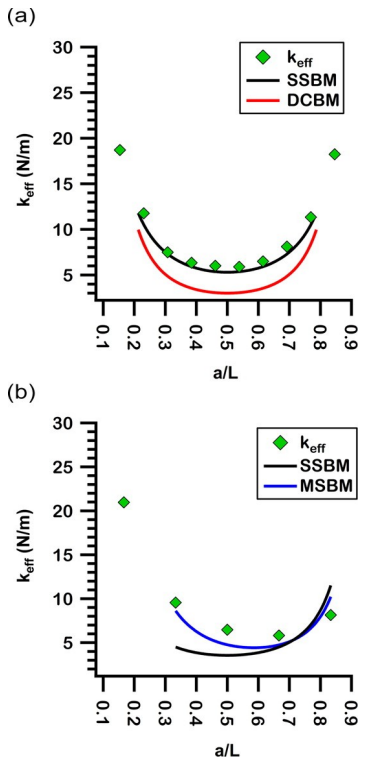

Figure 4.6: Tube effective stiffness (k_{eff}) vs position

Tube effective stiffness (k_{eff}) vs position along suspended tube (a/L). (a) A simply supported tube.

(b) A mixed support tube, with the left side fixed and the right side simply supported.

4.3.3 Elastic Properties

The bending moduli EB determined for 20 tubes with diameters ranging from 18 to 55 nm are shown in Figure 4.7. EB ranged from 100 ± 20 to 1800 ± 300 GPa, with an average of 760 ± 30 GPa. The error in EB was determined via error propagation, using an error of 10% for the tube outer diameter D, half the lateral pixel width in the force map for the tube length L and lengths on each side of the loading position (a, b), and an error of 20% for the effective spring constant of the tube keff.

It is worth noting that there is the possibility that the calculated bending moduli may be underestimated due to inaccurate assumptions about the cross-sectional geometry. The nanotubes were approximated to be solid wires, with a solid circular cross section. This model was chosen because it was not possible for us to determine the inner diameter of the nanotubes we probed with AFM, given that we deposited the tubes on a substrate that is not amenable to TEM analysis. A more accurate model would be a hollow cylinder, with an inner diameter D_i and an outer diameter D_o, which results in a second moment of area expression of $I = \pi/64(D_o^4 - D_i^4)$. Modeling the tube as a solid wire as opposed to a hollow cylinder underestimates the modulus; however, in the most extreme case (i.e., very large diameter tube with only a few walls), the underestimation is on the order of 30%. On the basis of the range of D_i/D_o ratios observed in TEM data for 24 tubes in the same MWBNNT production batch as the tubes used in the bending experiments (presented in the Supporting Information), the underestimation is closer to 10% for our particular sample.

The Young's modulus of nanotubes and nanowires made of homogeneous isotropic materials such as B and B_4C are typically comparable to the Young's modulus of the bulk material.[18; 40; 62] However, for highly anisotropic nanomaterials including CNTs and BNNTs, the Young's modulus should theoretically approach an upper limit defined by the in-plane elastic constant of graphite and *h*-BN, respectively, which exceeds the Young's moduli of the bulk materials by 2 orders of magnitude.[28; 56] For *h*-BN single crystals, this constant was measured to be c_{11} = 811 GPa,[6] while, for single crystal graphite, c_{11} = 1109 GPa.[28; 56] These measurements correlate well with various theoretical calculations.[24; 46] This limit is expected to apply to MWBNNTs as well, because the modulus depends mainly on intrawall bonds. Simulations suggest that the Young's modulus of a MWCNT is slightly higher than that of a SWCNT, for the same outer diameter, due to the effect of interwall van der Waals forces in MWCNTs.[42]

From the plot of E_B versus tube outer diameter shown in Figure 4.7, it is evident that there is a decreasing trend for the bending modulus with increasing tube diameter. The average E_B of the MWBNNTs studied in the present investigation matches the c_{11} elastic constant of *h*-BN quite closely; however, the origin of the wide range of bending moduli and the diameter dependence requires further analysis.

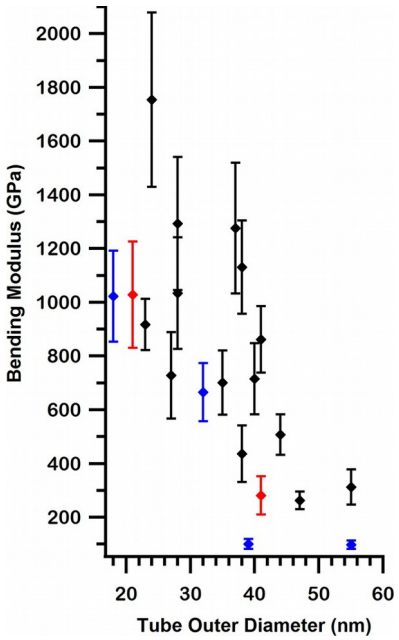

Figure 4.7: Bending modulus vs tube outer diameter.

Bending modulus vs tube outer diameter. The beam model used for calculating E_B is denoted by black (SSBM), blue (MSBM), and red (DCBM).

In experimental studies of multiwall nanotubes, a wide range of modulus values has been measured. For MWCNTs, Treacy et al.[64] were first to show that CNTs have Young's moduli in the TPa range, using a thermal excitation method. They found that arc-discharge MWCNTs with outer diameters ranging from 5.4 to 24.8 nm had Young's moduli of 0.4 to 4.15 TPa. A number of other studies have also produced Young's moduli in the TPa range, for arc-discharge MWCNTs.[48; 52; 54; 69] Within these studies, despite the focus on the ~1 TPa measurements as validation of the superior mechanical properties of CNTs, there are many instances of tubes with lower moduli, on the order of tens to hundreds of GPa. In the work of Salvetat et al.,[54] catalytic CVD MWCNTs were also studied and found to have an average modulus of 27 GPa, which is dramatically lower than the average modulus of 810 GPa measured for arc-discharge MWCNTs. Additional studies also observe lower moduli for catalytic CVD and pyrolytic MWCNTs, in certain cases as low as tens of GPa.[19; 21; 43] Typically, catalytic CVD and pyrolysis synthesis methods produce tubes with defective structures compared with the highly crystalline tubes synthesized by arc-discharge. While point defects do not affect the modulus by more than a few percent,[55] extended defects can cause the modulus to drop by as much as 2 orders of magnitude.[21; 54]

In some studies, within sample sets of nanotubes produced under the same conditions, the modulus is observed to drop with increasing tube diameter. This diameter dependence can be attributed to three possibilities, namely, the probing of an elastic rippling mode in bending experiments,[48] the presence of defects,[38; 43] or shear effects. Because of the highly anisotropic nature of the BNNTs, we do not consider surface stress effects which are known to give rise to diameter dependent moduli in relatively isotropic nanowires and nanotubes.[16] Due to the linearity of the force curves obtained in the present study, it is unlikely that rippling

modes are the cause of the low moduli measurements observed for larger tubes. Although it was not rare to acquire force curves which exhibited kinks, potentially due to tube buckling or tip slipping events, fits were only made to the initial linear portion of the force curves (for deflections less than 10 nm) after contact. In terms of defects, the low resolution TEM image (Figure 4.1b) shows long, straight nanotubes with uniform diameters. The high resolution TEM image (Figure 4.1c) shows that the dark spots present in the tube walls in Figure 4.1b are crystalline. The MWBNNTs do not appear to exhibit the type of pronounced structural defects that were found to affect the modulus of catalytic or pyrolytic MWCNTs, as discussed above. In beam bending experiments, shear must always be considered for short, stocky beams—those which have a length-to-diameter ratio of $L/D < 10$. The length-to-diameter ratio L/D was measured to be greater than 10 for all tubes in this study, which indicates that, if shear effects are present, they are not a result of the experimental geometry. Rather, they can be an indication of a material's anisotropy.[33; 38]

If shear effects are present, then the bending modulus is not equivalent to the Young's modulus. In order to determine whether the Young's modulus of the MWBNNTs is diameter dependent, the contribution of shear deflection to the total deflection in the bending experiment must be quantified. This approach follows Salvetat and co-workers' bending and shear analysis of single-wall CNT ropes.[53]

The bending modulus is related to the Young's modulus E_Y and the shear modulus G using the following relationship, determined by Timoshenko beam theory:[34; 38; 53; 63]

$$\frac{1}{E_B} = \frac{1}{E_y} + \gamma \frac{f_s}{G}\left(\frac{D^2}{L^2}\right)$$

Equation 4.5

In this expression, f_s is a shape factor which has a value of 10/9 for a cylindrical beam and γ is a shear term coefficient with values of 3, 1.715, and 0.75 for DCBM, MSBM, and SSBM, respectively. The Timoshenko beam theory converges to the Euler–Bernoulli beam theory when the beam is rigid in shear ($G \rightarrow \infty$). In this case, the bending modulus is equal to the Young modulus and is not diameter dependent (which is not the case here). E_Y and G in our case can be estimated by plotting $1/E_B$ against (D^2/L^2), as shown in Figure 4.8. A linear fit weight by the error in $1/E_B$ was obatined for a trimmed sata set of 16 tubes. The shear coefficient was taken as γ = 1.152, determined by the number of tubes exhibiting each type of boundary condition (16 tubes total = 12 simply supported tubes + 2 mixed support tubes + 2 doubly clamped tubes). E_Y and G were determined to be 1800 ± 300 and 7 ± 1 GPa, respectively. The expected shear modulus for a MWBNNT should be on the order of several hundred GPa, based on the calculations for MWCNTs[42; 58] which find that $G_{MWCNT} \sim 500$ GPa. This value is on the order of the intralayer shear modulus. However, the value of G that we determined for MWBNNTs is much lower than this, and is close to the value of the c_{44} elastic constant of *h*-BN, c_{44} = 7.7 ± 5, measured by Bosak et al.[6] This elastic constant is equivalent to the interlayer shear modulus

of *h*-BN, and describes the shear between basal planes. In the case of the MWBNNT structure, this corresponds to shearing between tube walls, which can only occur if there are discontinuities due to the presence of extended defects within the tube walls.e

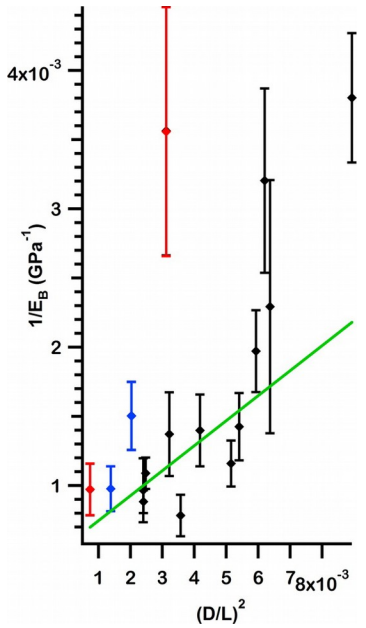

Figure 4.8: Determination of the Young's modulus and shear modulus

Determination of the Young's modulus and shear modulus via a fit to a plot of $1/E_B$ *vs* $(D/L)^2$*. The beam model used for calculating* $1/E_B$ *is denoted by black (SSBM), blue (MSBM), and red (DCBM). The equation used for the fit is* $1/E_B = 1/E_Y + 1.139 f_s/G\,(D^2/L^2)$*.*

Although no extensive defects are apparent from the TEM characterization of the MWBNNTs, as discussed above, the dark spots within the tube walls in the low resolution TEM image (Figure 4.1b) and their somewhat regular pattern within a given tube warrant additional consideration. A detailed electron diffraction study by Celik-Aktas et al.[7] determined that the dark spots can be attributed to a helical nanotube structure in which the tube is comprised of two or more helices (each comprised of multiple walls) which wrap to form the entire nanotube. In this structure, the dark spots correspond to a strongly diffracting helix, which is locally highly crystalline. The highly crystalline regions are joined together by line defects which result in a faceted helix. The lighter regions of the tube wall form the other helix, which possesses the conventional nested coaxial cylindrical structure expected for multiwall nanotubes. On the basis of this multihelix nanotube structure, it is conceivable that the line defects within the faceted helix as well as the interface between faceted and cylindrical helices make interwall shearing a possibility. Therefore, as our analysis of the bending data suggests, shear cannot be ignored in the calculation of the elastic modulus, and shear effects arise from nanotube anisotropy ($G \ll E_Y$) and the presence of defects within the nanotubes, and not from the experimental geometry.

Our finding that the shear modulus of MWBNNTs is orders of magnitude smaller than the Young's modulus indicates that the existing theoretical models are not sufficient in predicting the mechanical properties of such extremely anisotropic structures, particularly when structural defects are present.[42] Experiments performed on MWCNTs support this assertion. Guhados et al.[25] determined that $E_Y = 350 \pm 110$ GPa and $G = 1.4 \pm 0.3$ GPa for 13 MWCNTs grown by a CVD method, while Wei et al.[66] found that E_Y ranged from 300 to 900 GPa while G ranged from 30 to 800 MPa, for a sample of eight tubes. Both studies attribute the low shear modulus to defects in the structure of the nanotubes. There are several possible benefits of

having a low shear modulus: (1) Taking advantage of its high melting temperature, the shear modulus of MWBNNTs cast within metals or ceramics would enable damping of vibrations. This could result in quieter, more durable materials.[2; 17; 60] (2) Local distortions allowed due to the low shear modulus could enable MWBNNTs to adapt to local structure variations while maintaining rigidity on long length scales (longitudinal distortions), imparting toughness to otherwise brittle composite materials.[69] (3) The mutual compensation of shear modulus and Young's modulus, whereby tubes of different diameters have similar bending stiffness, could allow for lower purity BNNT materials in BNNT coated interfaces for release applications.[26; 41] (4) With a shear modulus on the order of the value for *h*-BN, MWBNNTs can be used as a high-temperature solid lubricant additive in industrially relevant composites. [8] The nanotube structures would have the added advantages of enabling more efficient heat transport on longitudinal length scales,[4] and increasing the wear resistance of the composite due to reinforcement of the matrix.[71]

4.4 CONCLUSIONS

The bending modulus of individual multiwall boron nitride nanotubes (MWBNNTs) was measured *via* AFM bending experiments. Boundary conditions for the beam bending model were determined by using a force mapping technique. MWBNNTs were found to have excellent mechanical properties, with an average bending modulus of 760 ± 30 GPa, which is consistent with the theoretically predicted value for BNNTs. Shear effects were found to be non-negligible, and the Young's modulus and shear modulus were determined to be 1800 ± 300 and 7 ± 1 GPa,

respectively. The experimental geometry and the dimensions of the nanotubes were not major contributors to the shear effects; rather, it is likely that interwall shearing occurred between crystalline and faceted cylindrical helices in these MWBNNTs.

4.5 BIBLIOGRAPHY

[1] **Arenal, R.; Golberg, D.; Wang, M.-S.; Xu, Z. and Loiseau, A.** (**2011**). , Nanotechnology 22 : 265704.

[2] **Balani, K. and Agarwal, A.** (**2008**). , J. Appl. Phys. 104 : 063517.

[3] **Bando, Y.; Golberg, D.; Tang, C.; Terao, T. and Zhi, C. Y.** (**2010**). , Pure Appl. Chem. 82 : 2175.

[4] **Bando, Y.; Golberg, D.; Tang, C.; Zhang, J.; Ding, X.; Fan, S. and Liu, C.** (**2006**). , J. Phys. Chem. B 110 : 10354.

[5] **Blase, X.** (**1994**). , Europhys. Lett. 28 : 335.

[6] **Bosak, A.; Serrano, J.; Krisch, M.; Watanabe, K.; Taniguchi, T. and Kanda, H.** (**2006**). , Phys. Rev. B 73 : 041402.

[7] **Celik-Aktas, A.; Zuo, J. M.; Stubbins, J. F.; Tang, C. C. and Bando, Y.** (**2005**). , Acta Crystallogr., Sect. A 61 : 533.

[8] **Chen, W.; Gao, Y.; Chen, C. and Xing, J.** (**2010**). , Wear 269 : 241.

[9] **Chen, Y.; Dorgan, B. L.; McIlroy, D. N. and Aston, D. E.** (**2006**). , J. Appl. Phys. 100 : 104301.

[10] **Chen, Y.; Zou, J.; Campbell, S. J. and Caer, G. L.** (**2004**). , Appl. Phys. Lett. 84 : 2430.

[11] **Choi, S. R.; Bansal, N. P. and Garg, A.** (**2007**). , Mater. Sci. Eng., A 460-461 : 509.

[12] **Chopra, N. G.; Luyken, R. J.; Cherrey, K.; Crespi, V. H.; Cohen, M. L.; Louie, S. G. and Zettl, A.** (**1995**). , Science 269 : 966.

[13] **Chopra, N. G. and Zettl, A.** (**1998**). , Solid State Commun. 105 : 297.

[14] **Chowdhury, R. and Adhikari, S.** (**2011**). , IEEE Trans. Nanotechnol. 10 : 659.

[15] **Ciofani, G.; Raffa, V.; Yu, J.; Chen, Y.; Obata, Y.; Takeoka, S.; Menciassi, A. and Cuschieri, A.** (**2009**). , Curr. Nanosci. 5 : 33.

[16] **Cuenot, S.; Frétigny, C.; Demoustier-Champagne, S. and Nysten, B.** (**2004**). , Phys. Rev. B 69 : 165410.

[17] **Deng, C. F.; Wang, D. Z.; Zhang, X. X. and Ma, Y. X.** (**2007**). , Mater. Lett. 61 : 3229.

[18] **Ding, W.; Calabri, L.; Chen, X.; Kohlhaas, K. M. and Ruoff, R. S.** (**2006**). , Compos. Sci. Technol. 66 : 1112.

[19] **Gaillard, J.; Skove, M. and Rao, A. M.** (**2005**). , Appl. Phys. Lett. 86 : 233109.

[20] **Gangadean, D.; David, N. M.; Brian, E. F. and Aston, D. E.** (**2010**). , Nanotechnology 21 : 225704.

[21] **Gao, R. P.; Wang, Z. L.; Bai, Z. G.; de Heer, W. A.; Dai, L. M. and Gao, M.** (**2000**). , Phys. Rev. Lett. 85 : 622.

[22] **Ghassemi, H. M.; Lee, C. H.; Yap, Y. K. and Yassar, R. S.** (**2010**). , J. Appl. Phys. 108 : 024314.

[23] **Golberg, D.; Costa, P. M. F. J.; Lourie, O.; Mitome, M.; Bai, X.; Kurashima, K.; Zhi, C.; Tang, C. and Bando, Y.** (**2007**). , Nano Lett. 7 : 2146.

[24] **Green, J. F.; Bolland, T. K. and Bolland, J. W.** (**1976**). , J. Chem. Phys. 64 : 656.

[25] **Guhados, G.; Wan, W.; Sun, X. and Hutter, J. L.** (**2007**). , J. Appl. Phys. 101 : 033514.

[26] Haubner, R.; Wilhelm, M.; Weissenbacher, R.; Lux, B. and Jansen, M., **2002**. *High Performance Non-Oxide Ceramics II*. , .

[27] **Heidelberg, A.; Ngo, L. T.; Wu, B.; Phillips, M. A.; Sharma, S.; Kamins, T. I.; Sader, J. E. and Boland, J. J.** (**2006**). , Nano Lett. 6 : 1101.

[28] **Hernandez, E.; Goze, C.; Bernier, P. and Rubio, A.** (**1999**). , Appl. Phys. A: Mater. Sci. Process. 68 : 287.

[29] Hsu, T. H., **1988**. *Structural Engineering and Applied Mechanics Data Handbook*. , .

[30] **Hutter, J. L. and Bechhoefer, J.** (**1993**). , Rev. Sci. Instrum. 64 : 1868.

[31] **Iijima, S.; Brabec, C.; Maiti, A. and Bernholc, J.** (**1996**). , J. Chem. Phys. 104 : 2089.

[32] **Jaffrennou, P.; Barjon, J.; Lauret, J. S.; Maguer, A.; Golberg, D.; Attal-Tretout, B.; Ducastelle, F. and Loiseau, A.** (**2007**). , Phys. Status Solidi B 244 : 4147.

[33] **Kaplan-Ashiri, I.; Cohen, S. R.; Apter, N.; Wang, Y.; Seifert, G.; Wagner, H. D. and Tenne, R.** (**2007**). , J. Phys. Chem. C 111 : 8432.

[34] **Kis, A.; Mihailovic, D.; Remskar, M.; Mrzel, A.; Jesih, A.; Piwonski, I.; Kulik, A. J.; Benoit, W. and Forro, L.** (**2003**). , Adv. Mater. 15 : 733.

[35] **Kluge, D.; Abraham, F.; Schmidt, S.; Schmidt, H.-W. and Fery, A.** (**2010**). , Langmuir 26 : 3020.

[36] **Lahiri, D.; Singh, V.; Benaduce, A. P.; Seal, S.; Kos, L. and Agarwal, A.** (**2011**). , J. Mech. Behav. Biomed. Mater. 4 : 44.

[37] **Lee, C. H.; Wang, J. S.; Kayatsha, V. K.; Huang, J. Y. and Yap, Y. K.** (**2008**). , Nanotechnology 19 : 455605.

[38] **Lee, K.; Lukić, B.; Magrez, A.; Seo, J. W.; Briggs, G. A. D.; Kulik, A. J. and Forró, L.** (**2007**). , Nano Lett. 7 : 1598.

[39] **Li, L. H.; Chen, Y.; Lin, M. Y.; Glushenkov, A. M.; Cheng, B. M. and Yu, J.** (**2010**). , Appl. Phys. Lett. 97 : 141104.

[40] **Lin, C.-H.; Ni, H.; Wang, X.; Chang, M.; Chao, Y. J.; Deka, J. R. and Li, X.** (**2010**). , Small 6 : 927.

[41] **Lipp, A.; Schwetz, K. A. and Hunold, K.** (**1989**). , J. Eur. Ceram. Soc. 5 : 3.

[42] **Lu, J. P.** (**1997**). , Phys. Rev. Lett. 79 : 1297.

[43] **Lukic, B.; Forro, L.; Seo, J. W.; Bacsa, R. R.; Delpeux, S.; Beguin, F.; Bister, G.; Fonseca, A.; Nagy, J. B. and Kis, A.** (**2005**). , Nano Lett. 5 : 2074.

[44] **Ma, R. Z.; Bando, Y.; Zhu, H. W.; Sato, T.; Xu, C. L. and Wu, D. H.** (**2002**). , J. Am. Chem. Soc. 124 : 7672.

[45] **Ni, H.; Li, X. D. and Gao, H. S.** (**2006**). , Appl. Phys. Lett. 88 : 043108.

[46] **Ohba, N.; Miwa, K.; Nagasako, N. and Fukumoto, A.** (**2001**). , Phys. Rev. B 63 : 115207.

[47] **Pampaloni, F. and Florin, E.-L.** (**2008**). , Trends Biotechnol. 26 : 302.

[48] **Poncharal, P.; Wang, Z. L.; Ugarte, D. and de Heer, W. A.** (**1999**). , Science 283 : 1513.

[49] **Ravichandran, J.; Manoj, A. G.; Liu, J.; Manna, I. and Carroll, D. L.** (**2008**). , Nanotechnology 19 : 085712.

[50] **Reddy, A. L. M.; Tanur, A. E. and Walker, G. C.** (**2010**). , Int. J. Hydrogen Energy 35 : 4138.

[51] **Rubio, A.; Corkill, J. L. and Cohen, M. L.** (**1994**). , Phys. Rev. B 49 : 5081.

[52] **Salvetat, J. P.; Bonard, J. M.; Thomson, N. H.; Kulik, A. J.; Forro, L.; Benoit, W. and Zuppiroli, L.** (**1999**). , Appl. Phys. A: Mater. Sci. Process. 69 : 255.

[53] **Salvetat, J. P.; Briggs, G. A. D.; Bonard, J. M.; Bacsa, R. R.; Kulik, A. J.; Stockli, T.; Burnham, N. A. and Forro, L.** (**1999**). , Phys. Rev. Lett. 82 : 944.

[54] **Salvetat, J. P.; Kulik, A. J.; Bonard, J. M.; Briggs, G. A. D.; Stockli, T.; Metenier, K.; Bonnamy, S.; Beguin, F.; Burnham, N. A. and Forro, L.** (**1999**). , Adv. Mater. 11 : 161.

[55] **Sammalkorpi, M.; Krasheninnikov, A.; Kuronen, A.; Nordlund, K. and Kaski, K.** (**2004**). , Phys. Rev. B 70 : 245416.

[56] **Santosh, M.; Maiti, P. K. and Sood, A. K.** (**2009**). , J. Nanosci. Nanotechnol. 9 : 5425.

[57] **Shanmugham, S.; Jeong, J.; Alkhateeb, A. and Aston, D. E.** (**2005**). , Langmuir 21 : 10214.

[58] **Shen, L. and Li, J.** (**2005**). , Phys. Rev. B 71 : 035412.

[59] **Shin, M. K.; Kim, S. I.; Kim, S. J.; Kim, S. K.; Lee, H. and Spinks, G. M.** (**2006**). , Appl. Phys. Lett. 89 : 231929.

[60] **Sueyoshi, H.; Rochman, N. T. and Kawano, S.** (**2003**). , J. Alloys Compd. 355 : 120.

[61] **Suryavanshi, A. P.; Yu, M. F.; Wen, J. G.; Tang, C. C. and Bando, Y.** (**2004**). , Appl. Phys. Lett. 84 : 2527.

[62] **Tao, X.; Dong, L.; Wang, X.; Zhang, W.; Nelson, B. J. and Li, X.** (**2010**). , Adv. Mater. 22 : 2055.

[63] Timoshenko, S., **1955**. *Strength of materials*. , .

[64] **Treacy, M. M. J.; Ebbesen, T. W. and Gibson, J. M.** (**1996**). , Nature 381 : 678.

[65] **Verma, V.; Jindal, V. K. and Dharamvir, K.** (**2007**). , Nanotechnology 18 : 435711.

[66] **Wei, X.-L.; Liu, Y.; Chen, Q.; Wang, M.-S. and Peng, L.-M.** (**2008**). , Adv. Funct. Mater. 18 : 1555.

[67] **Wen, B. M.; Sader, J. E. and Boland, J. J.** (**2008**). , Phys. Rev. Lett. 101 : 175502.

[68] **Wirtz, L. and Rubio, A.** (**2003**). , IEEE Trans. Nanotechnol. 2 : 341.

[69] **Wong, E. W.; Sheehan, P. E. and Lieber, C. M.** (**1997**). , Science 277 : 1971.

[70] **Zhi, C. Y.; Bando, Y.; Wang, W. L. L.; Tang, C. C. C.; Kuwahara, H. and Golberg, D.** (**2008**). , J. Nanomater. : 642036.

[71] **Zhou, S.-m.; Zhang, X.-b.; Ding, Z.-p.; Min, C.-y.; Xu, G.-l. and Zhu, W.-m.** (**2007**). , Composites, Part A 38 : 301.

5.0 PHOTONIC CRYSTALS INTRODUCTION

Advances in imaging, communication, sensing and other applications have been driven over the past fifty years through advances in laser technology, non-linear optics and imaging optics. However, advances in nanoscale optics and nanophotonics have yet to have their full impact on society. The foundational science underling nanophotonics in particular, plasmonics and photonic crystals, has been laid in the past few decades. [3; 5; 6]

Photonic crystals, which are discussed in this section, are commonly defined as a class of materials which possess significantly strong periodic modulation of refractive index on the order of the optical wavelength, typically 100 to 1000 nm. These materials exhibit wavelength selective light reflection and other diffraction related phenomena arising from a photonic band gap. A photon band gap is the range of photon energies for which light cannot propagate in a material. Photonic crystals have been designed with photonic band gaps that prohibit photon propagation in one or more wavelength bands.

The origin of a photonic crystal's properties can be understood by consideration of the light wave's interference in the material. In analogy to the interference of electron waves and electron band gap theory explaining many of the electrical properties of semiconductors, periodicity is responsibly for the photonic band gap effect. Below I explain how this effect arises for a one-dimensional photonic bandgap. The two and three dimensional photonic band gap

materials, which are described in Chapters 6 and 7, can be understood by extending the one-dimensional Bragg refraction framework to include Bragg diffraction of waves propagating in any direction.

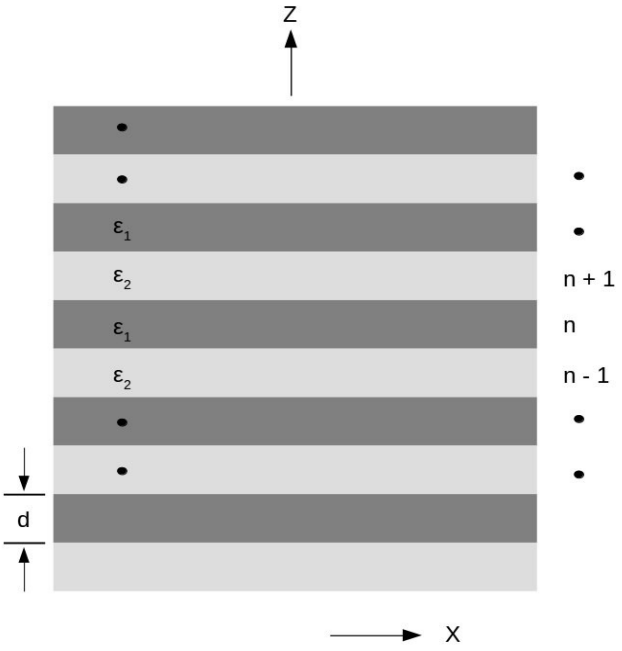

Figure 5.1: Schematic of 1D photonic crystal

(see text for details)

5.1 THE PHOTONIC BAND GAP

Consider a system composed of an infinite number of planar layers of thickness d; assume that the layers are oriented perpendicular to the z direction, and that the dielectric constant of the layers alternates between the values ε_1 and ε_2, (see Figure 5.1). The optical wavevector inside the material is given by $\mathbf{k} = (k_x, k_y, k_z)$. In addition, consider the system non-magnetic, $\mu_1 = \mu_2 = 1$ and, lossless. In this approximation, two classes of electronic field modes can be defined, **TE** modes, where the electric field vector is parallel to the layer boundaries, and **TM** modes, where the magnetic field vector is parallel to the layer boundaries. Using the typical separation of variables method allows the **TE** and **TM** modes to be expressed by,

$$\boldsymbol{TE}: \quad \boldsymbol{E}(\boldsymbol{r}) = E(z)e^{i(k_x x + k_y y)}\boldsymbol{n}_{\boldsymbol{x}}$$

Equation 5.1

$$\boldsymbol{TM}: \quad \boldsymbol{H}(\boldsymbol{r}) = H(z)e^{i(k_x x + k_y y)}\boldsymbol{n}_{\boldsymbol{x}}$$

Equation 5.2

In each layer n, the z dependent component of the **E(r)** and **H(r)** may be expressed as a superposition of a forward and a backward propagating wave with the form,

$$\boldsymbol{TE}: \quad E_{n,j}(z) = a_{n,j}e^{ik_{zj}(z-nd)} + b_{n,j}e^{-ik_{zj}(z-nd)}$$

Equation 5.3

$$\boldsymbol{TM}: \quad H_{n,j}(z) = a_{n,j}e^{ik_{zj}(z-nd)} + b_{n,j}e^{-ik_{zj}(z-nd)}$$

Equation 5.4

where $a_{n,j}$ and $b_{n,j}$ are constants which depend on the layer number, n, and the medium dielectric constant, ε_j. In the exponential terms, the longitudinal wavenumber k_{zj} is given by,

$$k_{zj} = \sqrt{\frac{\omega^2}{c^2}\epsilon_j - k_{||}^2}$$

in which $k_{||} = \sqrt{k_x^2 + k_y^2}$ is the wavevector component parallel to the material interfaces.

Constraining the solutions with the boundary condition, $z = z_n = nd$ between the n^{th} and the $(n+1)^{th}$ layers, and utilizing Maxwell's equations,

$$\nabla \times \boldsymbol{E} = i\omega\mu_0 \boldsymbol{H} \text{ and } \nabla \times \boldsymbol{H} = -i\omega\epsilon_0\epsilon \boldsymbol{H}$$

allows the pre-exponential constants to be determined as follows,

$$\textbf{TM}: \quad H_{n,1}(z_n) = H_{n+1,2}(z_n),$$
$$\frac{1}{\epsilon_1}\frac{d}{dz}H_{n,1}(z_n) = \frac{1}{\epsilon_2}\frac{d}{dz}E_{n+1,2}(z_n)$$

Equation 5.5

$$\textbf{TM}: \quad H_{n,1}(z_n) = H_{n+1,2}(z_n),$$
$$\frac{1}{\epsilon_1}\frac{d}{dz}H_{n,1}(z_n) = \frac{1}{\epsilon_2}\frac{d}{dz}H_{n+1,2}(z_n)$$

Equation 5.6

Substitution of the superposition wave forms of Equations 5.3 and 5.4 into Equations 5.5 and 5.6 gives,

$$a_{n,1} + b_{n,1} = a_{n+1,2}e^{-ik_{z2}d} + b_{n+1,2}e^{ik_{z2}d}$$
$$a_{n,1} - b_{n,1} = p_m\left[a_{n+1,2}e^{-ik_{z2}d} - b_{n+1,2}e^{ikz2d}\right]$$

where $p_m \in \{p_{TE}, p_{TM}\}$ is a polarization dependent factor which is defined for **TE** modes as $p_{TE} = \frac{k_{z2}}{k_{z1}}$ and for **TM** modes as $p_{TM} = \frac{k_{z2}}{k_{z1}}\frac{\epsilon_1}{\epsilon_2}$. As developed, this model has two equations and four unknowns, $a_{n,1}, b_{n,1}, a_{n+1,2}, b_{n+1,2}$ for each mode type. Evaluating the boundary conditions at the interface $z = z_{n-1} = (n-1)d$, located between the (n-1)th and nth layers lead to,

$$a_{n-1,2}+b_{n-1,2}=a_{n,1}e^{-ik_{z1}d}+b_{n,1}e^{ik_{z1}d},$$
$$a_{n-1,2}-b_{n-1,2}=\frac{1}{p_m}\left[a_{n,1}e^{-ik_{z1}d}-b_{n,1}e^{ik_{z1}d}\right]$$

which results in each mode type having four equations with a total of six unknown constants. Utilizing the Floquet-Bloch theorem, which states that if E is a field located in a periodic medium with periodicity 2d, the equality $E(z+2d)=e^{ik_{B1}2d}E(z)$ must be true. The wavevector k_{B1} is the Bloch wavevector, and a complementary expression exists for the magnetic field component. Application of the Floquet-Bloch theorem results in,

$$\left[a_{n+1,2}+b_{n+1,1}e^{-2ik_{z2}[z-(n-1)d]}\right]=e^{ik_{B1}2d}\left[a_{n-1,2}+b_{n-1,2}e^{-2ik_{z2}[z-(n-1)d]}\right]$$

This equality must hold for any position z; therefore it is required that,

$$a_{n+1,2}=a_{n-1,2}e^{ik_{B1}2d},$$
$$b_{n+1,2}=b_{n-1,2}e^{ik_{B1}2d},$$

reducing the number of unknowns from six to four, and allowing the homogeneous system of equations to be solved. Using standard methods to solve this system of equations returns the following characteristic equation,

$$\cos(2k_{B1}d)=\cos(k_{z1}d)\cos(k_{z2}d)-\frac{1}{2}\left[p_m+\frac{1}{p_m}\right]\sin(k_{z1}d)\sin(k_{z2}d).$$

Because the left-hand side of the above equation must be in the range [-1 … 1], the absolute value of right-hand side cannot be larger than unity. This conclusion gives rise to the formation of band gaps. For example, at normal incidence,

$$k_{z1}=\sqrt{\epsilon_1}\frac{\omega}{c},\qquad k_{z2}=\sqrt{\epsilon_2}\frac{\omega}{c}$$
$$\epsilon_1=2.25,\qquad \epsilon_2=9$$

a wave with λ = 12d can propagate, but a wave with λ = 9d cannot.

5.2 DEFECTS AND DISORDER IN PHOTONIC CRYSTALS

When defects or disorder interrupt the dielectric periodicity of photonic crystals the photonic band gap can be affected, and even destroyed. Photons with energies within the photonic band gap cannot propagate through photonic crystals. Research efforts have been conducted on photonic crystal waveguide structures created by the introduction of line defects into a two dimensional photonic crystal.[1; 2; 4; 6] When a line of defects are introduced, photons with frequencies within the band gap can propagate through the crystal using the line defect as a waveguide. This approach has been used to create waveguide structures capable of guiding light around sharp bends via narrow channels with minimal losses. Photonic crystal-based waveguides provide a basis for the construction of photonic circuitry components. Tactical introduction of defects in photonic crystals can be used to localize or guide light; i.e., selective destruction of photonic crystal order is often desirable. Thus understanding and quantifying defects and disorder in a photonic band gap material is important.

Disorder in photonic crystals degrades the magnitude and increases the width of Bragg diffraction peaks. Fabrication of photonic crystals with well-defined band gaps requires highly ordered and long-range crystal structures. The optical properties of photonic crystals are most often characterized using UV-Vis spectroscopy and refractometry. Angle-resolved, UV-Vis measurements of photonic crystals enable comparison to theoretically predicted Bragg diffraction. Electron microscopies are typically used to assess crystal morphology and allow quantification of crystal ordering.

The pair correlation function g(r) can be used to quantify the probability of finding the center of a particle at a given distance from the center of another particle relative to that of a completely homogeneous distribution. The function g(r) is defined as:

$$g(r) = \frac{1}{\langle p \rangle} \frac{dn(r, r+dr)}{da(r, r+dr)}$$

Here the pair correlation function is normalized by the average particle number density <ρ>. In two dimensional space, n(r,r+dr) is the number of particles located within a circular ring with a radius of r and a width of dr. As r increases, g(r) probes the long-range particle ordering. Pair correlation functions of highly ordered systems are characterized by a series of peaks. The average nearest neighbor distance is given by the location of the first peak, while peak widths can be used to describe the deviation from an ideal lattice. Comparing the pair correlations of disordered photonic crystals to idealized models can reveal underlying lattice structures.

Chapters 6 and 7 include a discussion of a method used to calculate and quantify the pair correlations of self-assembled photonic crystals. In these works, a custom image analysis toolbox was used to pre-process SEM micrographs prior to calculating pair correlation.

Photonic band gap materials facilitate the control of photons on nanometer length scales. Waveguides and optical cavities can be engineered with nanoscale dimensions. Photonic crystals have already found applications in integrated photonic circuits; and current research trends suggest increasing integration of photonic circuits featuring photonic crystals. Characterization of photonic crystals is a prerequisite to further development of integrated photonic circuits. Consequently, in band gap dependent applications, material order must be controlled and quantified.

5.3 BIBLIOGRAPHY

[1] **Baba, T.; Fukaya, N. and Yonekura, J.** (**1999**). *Observation of light propagation in photonic crystal optical waveguides with bends*, ELECTRONICS LETTERS-IEE 35 : 654-654.

[2] **Busch, K.; Lölkes, S.; Wehrspohn, R. B. and Föll, H.** (**2004**). *Photonic crystals*, New York: Willey : 241-247.

[3] Di Bartolo, B.; Collins, J. and Silvestri, L., **2013**. *Nano-optics for enhancing light-matter interactions on a molecular scale: plasmonics, photonic materials and sub-wavelength resolution*. Springer, Dordrecht.

[4] Joannopoulos, J. D.; Johnson, S. G.; Winn, J. N. and Meade, R. D., **2011**. *Photonic crystals: molding the flow of light*. Princeton university press, .

[5] Novotny, L. and Hecht, B., **2012**. *Principles of nano-optics*. Cambridge University Press, Cambridge, UK;New York;.

[6] Soukoulis, C. M., **2012**. *Photonic crystals and light localization in the 21st century*. Springer Science & Business Media, .

6.0 CHARGE STABILIZED CRYSTALLINE COLLOIDAL ARRAYS AS TEMPLATES FOR FABRICATION OF NON-CLOSE-PACKED INVERTED PHOTONIC CRYSTALS

Author list: Justin J. Bohn, Matti Ben-Moshe, Alexander Tikhonov, Dan Qu, Daniel N. Lamont, and Sanford A. Asher

Author contribution: The author of this dissertation was responsible for characterizing the degree of order of the photonic crystals, providing interpretation of the results and contributing to the preparation of the manuscript. This work has been publish as *Journal of Colloid and Interface Science* ***2010****, 344, 298*

6.1 INTRODUCTION

The last two decades has seen the emergence of the important field of photonic crystals. The name photonic crystals was coined to describe materials which control light propagation through periodic variations in their optical dielectric constants.[29; 31; 72]

Photonic crystal materials are of major technological significance in areas such as optical computing and communications where photonic devices are being developed to replace electronic devices.[3; 27; 29; 30; 40; 49; 61] Photonic crystal materials also offer the possibility to fabricate complete 3-D photonic bandgap materials which exclude electromagnetic radiation (including the vacuum field) within its finite spectral bandgap.[10; 48] Phenomena such as spontaneous emission are suppressed in these materials.[47; 72]

Lithography is the most straightforward method to fabricate two and three dimensional photonic crystal materials for photonic applications.[1; 14-17; 26; 38; 50; 60] This top down fabrication methodology is highly successful in fabricating complex photonic crystal materials. These fabricated structures are extremely useful in demonstrating proof of concept for photonic crystal devices. However, lithographic processes are expensive, and this cost is likely to prevent commercialization of many photonic crystal devices.

Thus, much of the recent work in photonic crystal fabrication has utilized colloidal particle self assembly. The utility of colloidal particle self assembly is evident from the photonic crystal materials found in nature. For example, earth mined opals are photonic crystals formed from the close packed self assembly of silica colloidal particles.[56] The first work fabricating artificial opals used gravity sedimentation to obtain photonic crystal periodic structures.[19; 44; 63]

Much of the recent colloidal particle self assembly work has emphasized methods that form close packed photonic crystal materials. These methods utilize variances of vertical colloidal particle deposition methods.[28; 36; 64; 67; 73] Surprisingly, many of these close packed assembly methods claim formation of fcc crystals[25; 37; 59; 63] which require that the self assembly select for the fcc crystal form, rather than the random stacked

crystal forms, which would normally result from simple hard sphere interparticle interactions; the fcc crystal assembly process requires long range interparticle interactions that select for fcc ABCABC layer packing.

A major limitation of close packed photonic crystal systems is that their ordering, and therefore their photonic crystal properties depend upon the colloidal particle size polydispersity. Clearly, increasing size polydispersity will degrade ordering.[55] Further, charge polydispersity will degrade ordering to the extent that electrostatic interactions are involved in the close packing mechanism. Disorder in the photonic crystals degrade the magnitude and increase the widths of the Bragg diffraction peaks.[39; 55; 62]

Fabrication of a complete 3-D photonic bandgap material requires specific crystal structures and a very large periodic variation in its optical dielectric constant. The most straightforward approach to forming a complete 3-D photonic bandgap crystal would utilize an inverse opal fcc crystal structure that requires a minimum refractive index ratio of 2.8.[12] The inverse opal structure is formed within an fcc photonic crystal by infiltrating an fcc photonic crystal structure with a high refractive index material, and then removing the original fcc spheres, leaving an inverse fcc lattice of air holes with a refractive index of n=1.

Optimization of the inverse opal crystal structure would permit decreasing the required refractive index modulation. For example, it was recently found that an inverted non close packed fcc lattice shows a wider photonic band gap (10 %) than does a close packed inverted fcc crystal structure with the same lattice constant.[20; 23]

The recent work which has attempted to generate non close packed photonic crystals has utilized thermal sintering and etching of close packed colloidal crystals.[21; 42; 43] This work has also employed conformally backfilling[23; 35; 45] these close packed colloidal crystals. It should be noted that the resulting photonic crystal materials retain the disorder present in the original close packed crystals.

In the work here we demonstrate a straightforward method to form *non close-packed* highly ordered fcc direct and inverse opal silica photonic crystals materials. We show that size and charge polydispersity has surprisingly little impact on ordering for colloidal particle systems that are formed through electrostatic self assembly. Our group has utilized the high ordering of electrostatically self assembled crystalline colloidal array (CCA) photonic crystal materials since the mid-1980's. [4; 5; 7; 13; 22]

More recently we polymerized a hydrogel around electrostatically self assembled CCA to form a polymerized CCA (PCCA). This PCCA is a responsive photonic crystal material[8] which proved useful for chemical sensing [24; 34; 52; 58; 65; 70], as well as for sensing temperature.[54; 66] We also developed magnetically responsive superparamagnetic and ferrimagnetic photonic crystal materials [68; 69; 71], as well as, photonic crystals that respond to light as optical switching materials.[6; 32; 33; 41; 51]

Electrostatic CCA self assembly relies on the electrostatic repulsions between colloidal particles of like charge. For the systems used here the colloidal particle surface groups are strong acid sulfonic acids which ionize in aqueous environments. For low ionic strength aqueous solutions the electrostatic interactions are large and occur over long distances (~1 μm) which enable formation of macroscopic fcc CCA crystals. The ordering appears superior to that which

can occur for close packed crystals because the soft electrostatic potentials avoid glass formation, they allow crystal annealing and they should ameliorate the disorder penalty for particle size and charge polydispersity.

Here we describe the fabrication of new highly ordered photonic crystal materials that utilize electrostatic CCA self assembly to form a highly ordered template. We then form a soft photonic crystal material where we lightly crosslink a hydrogel around the CCA template. We then condense solid silica within the PCCA hydrogel. This allows us to control the photonic crystal periodicity independently from the diameter of the colloidal particles making up the fcc crystal. This also allows us to tune the form of the dielectric constant modulation of the photonic crystal separate from its periodicity. We also demonstrate that we can remove the organic polymer and form an inverse opal structure. Thus, we can independently vary the periodicity and the silica wall thickness.

We show that our simple, electrostatic self assembly process gives rise to a photonic crystal with higher ordering compared to typical close-packed photonic crystal structure. We use DLVO theory to model interparticle interactions to gain insight into why electrostatic self assembly results in high order.

6.2 EXPERIMENTAL METHODS

6.2.1 Materials

2, 2-diethoxyacetophenone (DEAP, 98%, Acros Organics), polyethylene glycol dimethacrylate 200 (Polysciences Inc.), 2-hydroxyethyl acrylate (98%, Polysciences Inc.), diethylene glycol (Sigma), anhydrous ethyl alcohol (Pharmco Inc.) and tetraethyl ortho silicate (TEOS, Fluka) were used as received. Figure 6.1 shows our synthetic scheme for fabricating an inverted photonic crystal (IPC) structure by using a CCA template.

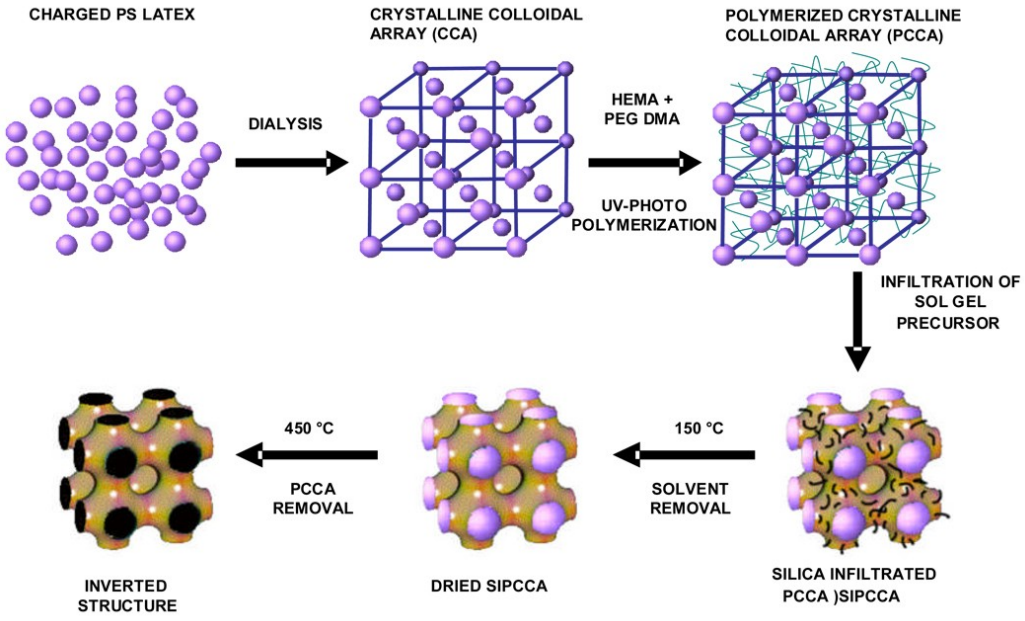

Figure 6.1: Synthetic scheme for fabricating an inverted photonic crystal. Charged polystyrene colloidal particles are dialyzed. Non ionic monomers are added. The system electrostatically self assembles into an fcc CCA which is UV-photopolymerized to fabricate a PCCA. A TEOS precursor is infiltrated into the hydrogel network and silica is condensed within the PCCA. The newly formed siPCCA is then heat treated to remove solvent and organic polymer forming the inverted structure.

6.2.2 Preparation of PCCA

The highly-charged, non-cross-linked, monodisperse polystyrene colloids (Figure 6.1) used to fabricate the siPCCA were prepared by emulsion polymerization.[53] The colloidal particle size as measured by TEM is 180 nm ± 4nm. The colloidal particles were cleaned by dialysis against deionized water followed by shaking with mixed bed ion-exchange resin (Bio-Rad AG501-X8 (D)) In a typical PCCA recipe 2,2-hydroxyethyl methacrylate (6 g, 4.6×10^{-2} mol, Polysciences) and polyethylene glycol dimethacrylate (0.174 g, 5.3×10^{-4} mol, Polysciences) were mixed together in a 2 dram vial. Aluminum oxide was added to remove the inhibitor contained in the monomer solutions. The solutions were centrifuged for 5 min to remove the aluminum oxide. 0.5 g of the deinhibited monomer solution supernatant was added to 2 g of the cleaned, highly charged colloidal particle dispersion.

The resulting mixture was shaken for 30 sec. 10% diethoxyacetophenone (DEAP; 10 µL, 3.84 µmol; Aldrich) was added to the mixture which was then vortexed for 30 sec. The mixture was injected between two quartz plates separated by a 125 µm Parafilm spacer. UV-photopolymerization was performed by using two UV mercury lamps (Black Ray) for 13 min. The PCCA film was removed from the quartz cell and equilibrated in a deionized water bath.

6.2.3 Infiltration of Sol-gel Precursor

A silica sol-gel precursor solution was prepared using a 1:1:3 molar ratio of TEOS/EtOH/water adjusted to a pH of 2 with concentrated HCl. The fabricated PCCA film template was immersed into two ml of the precursor solution.

Polymerization and condensation of the TEOS occurred around and within the PCCA hydrogel matrix over the course of 5 days, generating an alcogel within the PCCA template. The silica network was allowed to age and strengthen for an additional five days before further processing.

6.2.4 Solvent Removal

The silica sol-gel infiltrated PCCA was solvent-exchanged for one week in ethanol. This ethanol-containing, silica-infiltrated PCCA (siPCCA) was then heated at 85 °C for 1 day, followed by heating to 150 °C for 5 hrs to remove all solvent.

6.2.5 Polymer Removal

After solvent removal, the temperature was increased to 250 °C and held for 6 hours to melt the polystyrene colloidal particles as shown in iFigure 6.2. Higher temperature treatment at 450 °C removed all organic polymer materials, leaving behind only the infiltrated silica.[57] Upon firing the sample cracked into small fragments consisting of monoliths approximately 2 mm on a side.

6.2.6 Physical Measurements

Transmission electron microscopy was used to measure particle size. We used a Phillips FEG XL-30 FESEM operating in the ranges of 10–50 KeV to image the inverted structures. Diffraction spectra were obtained at room temperature using an Ocean Optics USB2000 spectrophotometer with a six-around-one reflectance probe. Solvent refractive indices were measured by using a Bausch & Lomb refractometer.

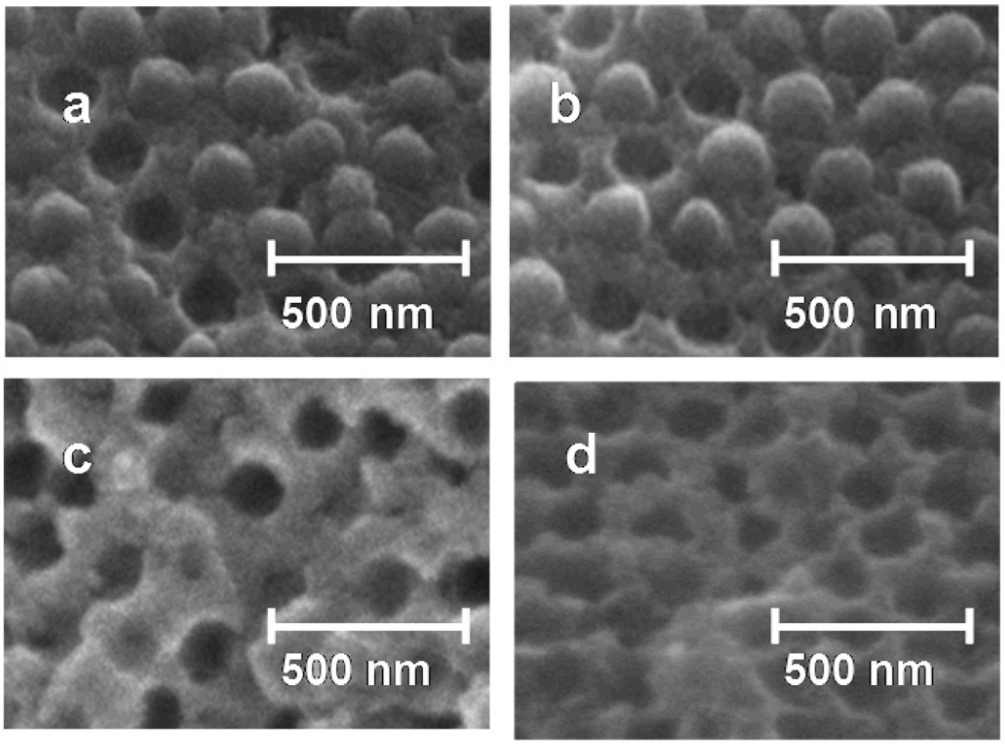

Figure 6.2: Melting polystyrene colloidal particles.

SEM images of a room temperature cleaved siPCCA showing its evolution through the heat treatment process. a. At 85 °C the colloidal particle lattice remains intact. b. After 150 °C heat treatment little deformation of polystyrene colloidal particles is evident. c. 250 °C heat treatment melts the colloidal particles leaving some polymer behind. d. The 450 °C heat treatment removes all of the organic polymer material leaving behind a highly ordered inverted opal of pure silica.

6.3 RESULTS AND DISCUSSION

6.3.1 Photonic Crystal Structure

Figure 6.2 shows four positions on a cleaved (111) surface of a silica filled PCCA (siPCCA) sample at room temperature after heat treatments at 85 °C, 150 °C, 250 °C, and 450 °C. This siPCCA was formed as shown in Figure 6.1 by polymerizing a hydrogel around a CCA, which self-assembled due to the electrostatic repulsions between colloidal particles. The CCA generally forms as a face centered cubic (fcc) lattice with a spacing determined by the particle number density.

The hydrogel polymerizes around the fcc lattice without altering the CCA order. TEOS was then infiltrated and condensed into the PCCA. Figure 6.2 a and bshow that the PCCA colloidal lattice remains intact upon condensation of silica within the PCCA hydrogel matrix. Some polystyrene particles have fallen out of the surface which proves that the PCCA hydrogel embeds the CCA lattice and does not covalently attach to the colloidal particles.

Figure 6.2c shows the siPCCA after heat treatment at 250 °C, which exceeds the 240 °C melting point of the non-cross-linked polystyrene.[74] The colloidal particles appear to have significantly melted, leaving holes in the surface. The siPCCA at this stage turned brown indicating that polymer degradation occurred. Energy dispersive x-ray analysis of the wall space shows both silicon and carbon peaks indicating the presence of both organic material and the infused silica.

Heat treatment at 450 °C (Figure 6.2d) removed the brown color of the siPCCA. Energy dispersive x-ray analysis shows the absence of a carbon peak in the wall space. The organic polymer material has burnt out during this heat treatment, leaving a pristine *non-close-packed* silica inverted opal structure. Thermogravimetric analysis shows a decreasing mass as the structure is heated from 150 °C to 450 °C. However, it was impossible to measure the relative organic polymer loss because of a pure silica coat of unknown thickness formed around the siPCCA during the condensation of the TEOS precursor solution within the PCCA.

Figure 6.3 shows the SEM image of a different siPCCA sample, where a razor blade was used to abrade the (111) surface. We used these SEM images to determine the siPCCA in-plane spacing of the 85 °C, 150 °C, 250 °C and 450 °C heat-treated samples. These in plane spacings were used to calculate the fcc (111) lattice plane spacing, d_{111}:

$$d_{hkl} = \frac{\sqrt{2}D}{\sqrt{h^2+k^2+l^2}}$$

Equation 6.1

where D is the nearest neighbor spacing observed in the Figure 6.2 SEM, and h, k, and l are the Miller indices of the presumed face-centered-cubic crystal.

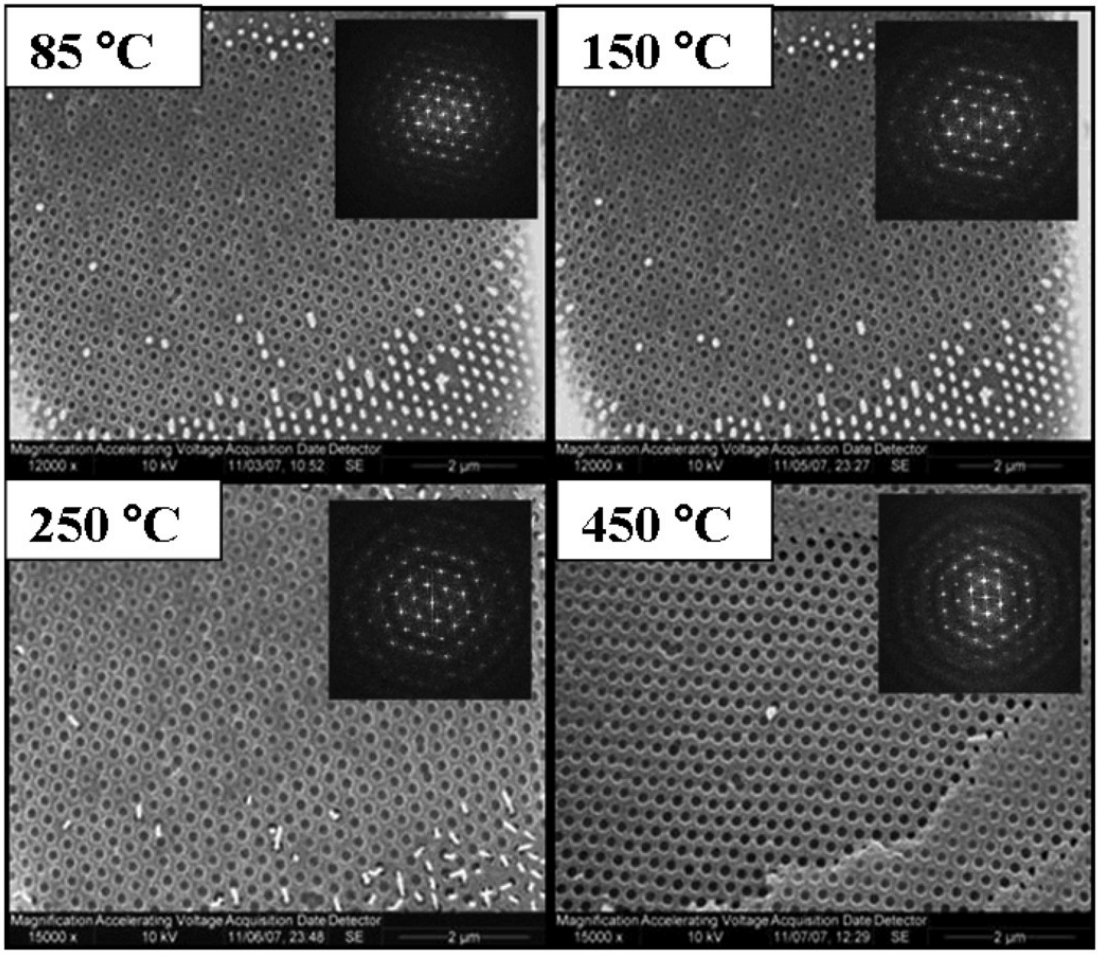

Figure 6.3: Heat treatment of the siPCCA

SEM images of the (111) plane obtained by abraiding the surface of the siPCCA. The 450 °C sample needed to be reabraided because the palladium sputter coating had fallen off. Insets: Fourier transforms show the high ordering within the (111) plane.

Abrasion of the siPCCA sample removes the silica coat as well as latex spheres. The SEM derived (111) lattice plane spacing for the 85 °C and 150 °C heated samples were essentially identical at 245±4 nm and 245±4 nm (mean ± SD) which indicates no decrease in lattice constant upon heating. A slight decrease was calculated for the (111) lattice plane spacing for the 250 °C (238±4 nm) and 450 °C (224±5 nm) heat treated samples. The ordering and interparticle spacing which originated from the electrostatic formation of the original CCA lattice, which was rigidified by formation of the PCCA and was set by the silica condensation, is maintained throughout the heat treatment process.

Figure 6.4 shows the room temperature spectrum of the 180° back diffracted light for light incident normal to the (111) surface of the heat treated siPCCA sample. The diffraction of the siPCCA blue-shifts as the treatment temperature increases above 150 °C. Bragg's law (Equation 6.2) indicates that at a constant incident glancing angle a decrease in diffraction wavelength requires a decrease in the average material refractive index, n_{avg}, or the d_{111} lattice plane spacing, or both

$$m\lambda = 2 d_{111} n_{avg} \sin\theta$$

Equation 6.2

where m is the order of diffraction, λ is the diffracted wavelength in air and θ is the glancing angle of incidence. The average refractive index, n_{avg}, is approximately equal to the refractive indices of the components, n_i, weighted by their volume fractions, φ_i.

$$n_{avg} = \sum n_i \varphi_i$$

Equation 6.3

Substituting the SEM calculated d_{111} and the diffracted wavelength in Bragg's law we can calculate n_{avg} for each treated sample (Table 1). Clearly, the average refractive index decreases at heat treatments of greater than 150 °C, indicating removal of the organic material.

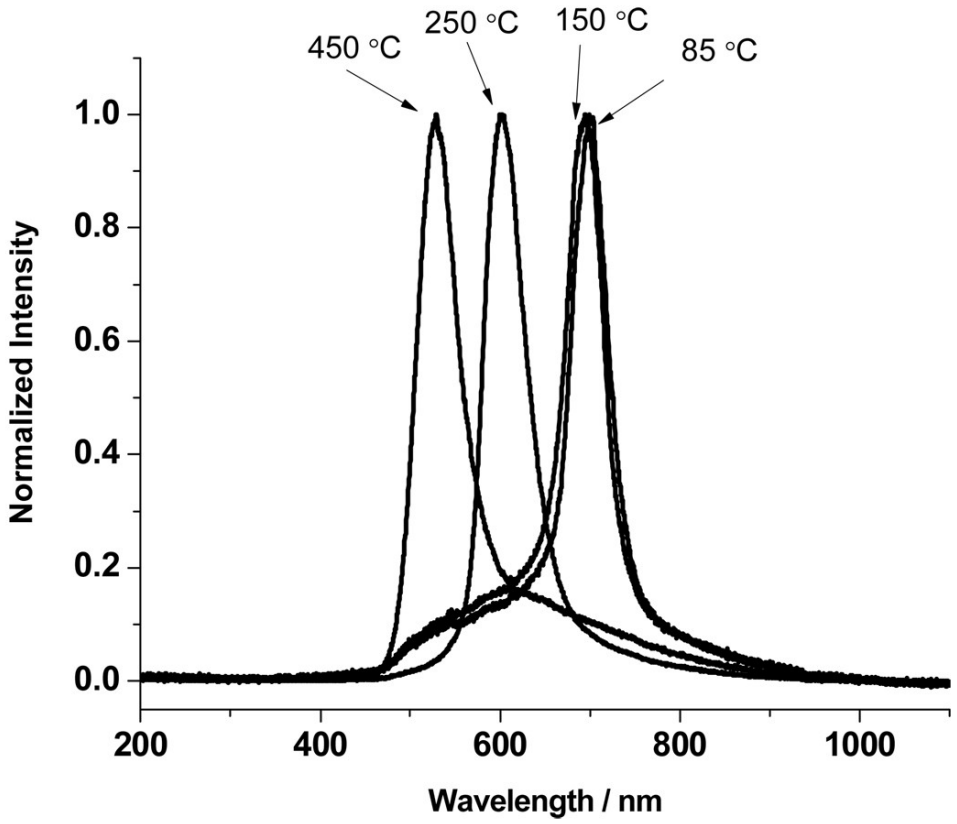

Figure 6.4: Diffraction spectra of siPCCA

Room temperature diffraction spectra for light incident normal to the (111) planes of the siPCCA measured after heat treatments of 85, 150, 250 °C, and 450 °C. As discussed in the text, the blue-shift in diffraction is due to the refractive index decrease which results from the loss of polymeric material during the heat-treatment

Table 1: Polymer heat treatment

Temp	**N_{avg}**	**D_{111}**	**φ_{silica}**	**Φ_{void}**	**$\Phi_{organic}$**
85 ˚C	1.42	245	0.2	0.2	0.6
150 ˚C	1.42	245	0.2	0.2	0.6
250 ˚C	1.27	236	0.22	0.47	0.31
450 ˚C	1.12	224	0.26	0.74	0

Increasing heat treatment temperatures vaporize the polymer decreasing n_{avg} and slightly decreasing the nearest neighbor spacing. Removal of the organic material increases the void space.

At 450 °C the inverted photonic crystal contains only silica and void space so that the relative volume fractions of each, φ_{silica} and φ_{void}, can be calculated from the values of n_{avg} and n_{silica}

$$n_{avg\ 450^{o}C} = \varphi_{silica}\, n_{silica} + \varphi_{void}\, n_{void}$$

Equation 6.4

The refractive index of silica in the inverted photonic crystal was determined by infusing solvents[11] into the 450 °C pure silica sample in order to refractive index match the silica which causes the diffraction to disappear (Figure 6.5a). For this experiment, an inverted siPCCA was heat treated to 450 °C and the diffraction from a single region was monitored. We infused the solvents for 24 hrs to achieve equilibrium. The diffraction disappears upon infiltration of chloroform indicating that n_{silica}~1.45, the refractive index of $CHCl_3$. Thus, using Equation 6.4, we calculate φ_{silica} = 26% for the 450 °C heat treated sample, giving a void volume fraction of φ_{void} = 0.74.

Table 1 shows that n_{avg} decreases for the 250 °C sample, indicating loss of organic polymer. Given a constant φ_{silica} we can calculate the polymer and void volume fraction for all of the samples by using Equation 6.5.

$$n_{avg} = \varphi_{silica} n_{silica} + \varphi_{void} n_{void} + \varphi_{polymer} n_{polymer}$$

Equation 6.5

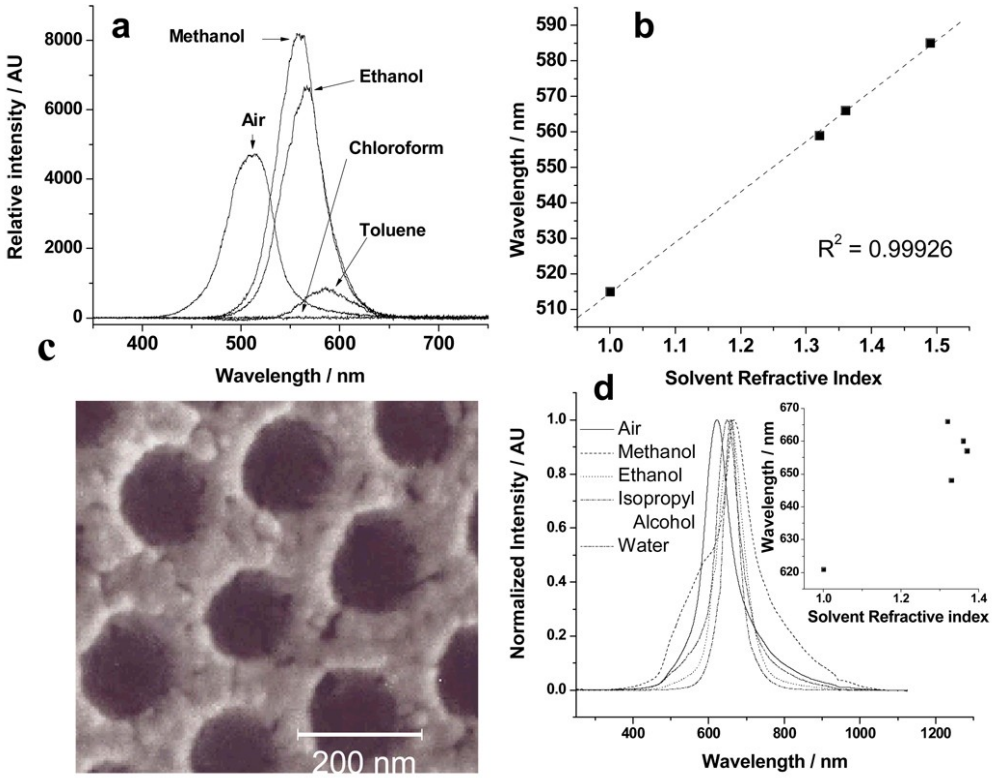

Figure 6.5: Void volume of siPCCA

Study of void volume of siPCCA. a. Diffraction spectra obtained from the 450 °C heat treated siPCCA in air and with solvent infiltrations of methanol, ethanol, chloroform, and toluene. b. Linear best fit of the diffraction maxima of the 450 °C solvent infiltration data of a versus solvent refractive index. c. SEM image showing wall porosity of siPCCA after 450 °C heat treatment. d. Diffraction dependence on solvent refractive index for 250 °C heat treated sample

By assuming that the remaining polymer composition is identical to that of the original PCCA we can estimate a volume average polymer refractive index, $n_{polymer}$ ~ 1.55. Table 1 shows that the 85 °C heat treated siPCCA has a $\phi_{polymer}$=0.6, which is ~50% greater than that of the originally prepared PCCA. This occurs because, although the original PCCA swells after exposure to the silica precursor solution, it then dramatically shrinks as the silica condenses within the PCCA.

Table 1 shows that there is no loss of polymer for the 150 °C heat treated sample, but almost half of the polymer is lost for the 250 °C heat treated sample. We calculate that the void volume fraction of 20 % of the 85 and 150 °C heat treated samples almost doubles for the 250 °C heat treated sample. The void volume fraction maximizes at 74% for the 250 °C heat treated sample. It should be noted that we find a 20 % void volume fraction for the 85 °C heat treated sample that results from evaporation of the solvent in the original silica condensed siPCCA. The increased silica volume fraction for the 250 °C heat treated sample results from the volume decrease of the siPCCA evident from the observed SEM decreased in-plane spacing as discussed above. Our calculations of the volume fractions at the lower heat treatment temperatures took cognizance of the calculated decrease in the (111) lattice plane spacing calculated from the SEM data. We account for the change in silica volume fraction through the proportionality $\varphi silicaV=\varphi'silicaV'$, where V is the original siPCCA volume and φ'_{silica} and V' are the silica volume fraction and unit cell volume after heat treatment.

We can independently determine ϕ_{silica} at 450 °C from a plot of the dependence of the diffraction wavelength for normal incidence upon the refractive index of the infiltrated solvent (Figure 6.5b). The slope of Equation 6.6 can be used to calculate ϕ_{void} and the intercept to calculate ϕ_{silica}.

$$\lambda = 2 d_{111} n_{silica} \varphi_{silica} + 2 d_{111} n_{solvent} \varphi_{void}$$

Equation 6.6

Utilizing the derived (111) lattice plane spacing and the slope we determined a silica filling fraction of φ_{silica} = 17%, indicating a lower φ_{silica} than calculated from the excellent assumption that the diffraction wavelength in air can be simply related to the average siPCCA refractive index given the SEM determined lattice spacing.

We conclude that the decreased slope calculated from Equation 6.6 results from sealed voids which are inaccessible to the solvent. The SEM in Figure 6.5c shows the complex morphology of the walls of the siPCCA. Obviously, the silica has condensed as particles which are closely packed. It would not be surprising that part of the voids would be sealed off from solvent infiltration.

To calculate the void volume inaccessible to solvent we can rewrite

$$\lambda = 2d_{111} n_{silica} \varphi_{silica} + 2d_{111} n_{solvent} \varphi_{accvoid} + 2d_{111} n_{air} \varphi_{inaccvoid}$$

Equation 6.7

where the total void volume is partitioned into inaccessible and accessible voids. From this expression we calculate a 9% unfillable void space located in the silica wall space giving the silica wall a ~35% porosity.

Figure 6.5d shows the results of solvent infiltrations into the 250 °C heat treated siPCCA where some, but not all, of the polymer was removed. The diffraction spectrum in air is broad and not symmetric and shows shoulders on both sides indicating a relatively inhomogeneous siPCCA, in contrast to that of the Figure 6.5a 450 °C heat treated siPCCA. Infiltration of methanol results in a very complex bandshape indicating a variable accessibility into this siPCCA. In contrast, the bandshapes of the ethanol, isopropanol and water infiltrations are more symmetric which indicates a chemical selectivity for solvent accessibility in the presence of organic polymers. Peculiarly, the largest red-shift in diffraction results from methanol (shoulder), which has the lowest refractive index. Obviously, there is some interesting interfacial chemical selectivity present.

6.3.2 Wall Spacing and Periodicity of siPCCA, Surface Morphology

The use of CCA electrostatic self-assembly enables the fabrication of fcc photonic crystal materials where the nearest neighbor spacing can be defined independently of the interparticle spacing. For inverse opal fcc crystals this allows us to independently control the fcc sphere void spacing and the wall thickness as shown in Figure 6.6a and b which show two different siPCCA's made from identical colloidal particles, but where the lattice constant is varied by changing the CCA particle number density. The decreased particle number density increases the wall thickness and the silica wall volume fraction.

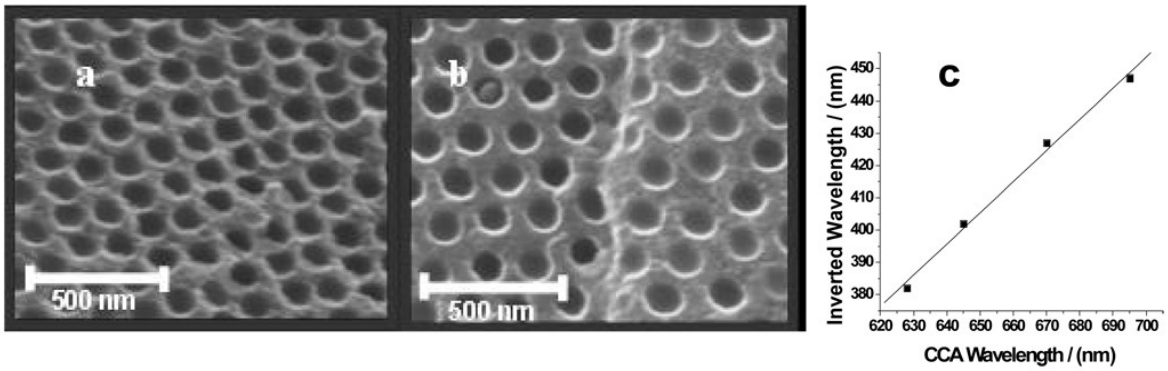

Figure 6.6: 450 °C heat treated siPCCA

a. SEM of 450 °C heat treated siPCCA prepared from 186 nm diameter 18 wt% CCA (1.5×10^{14} particles/cm^3) and b. 12 wt% CCA (9.9×10^{13} particles/cm^3) CCA A smaller particle number density increases the nearest-neighbor spacing. c. Linear correlation between CCA diffraction and diffraction of 450 °C heat treated siPCCA.

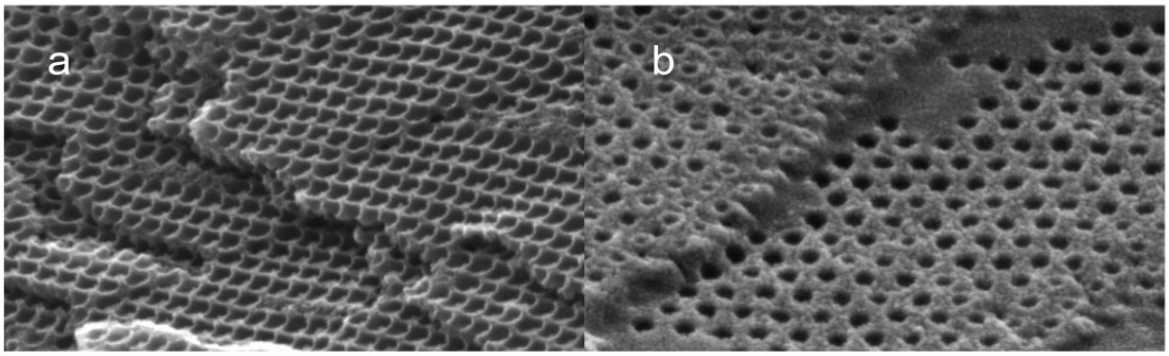

Figure 6.7: siPCCA plateau regions

SEM measured at a 50° angle to a 450 °C heat treated cleaved siPCCA formed with a. 1.5×10^{14} particles/cm^3 and b. 9.9×10^{13} particles/cm^3 particle number densities. The high particle number density siPCCA wall morphology shows clear ridges between nearest neighbors. The siPCCA made with low particle number density show smooth plateau regions between sphere holes.

Figure 6.6c, which demonstrates proportionality between the CCA diffraction and that of the 450 °C heat treated siPCCA demonstrates that the original template CCA determines the inverted siPCCA structure and spacing. In summary, the results above demonstrate that we have developed a simple scalable, inexpensive process to create highly ordered photonic crystal materials. We use electrostatically stabilized CCA as a template to form highly ordered siPCCA and inverse opal silica photonic crystals, where the spacing and wall thickness can be independently varied.

The Figure 6.7 SEM of inverted siPCCA inverse opal samples at high and low particle density show clear differences in morphology of the cleaved surfaces. In contrast to the low particle density surface which has plateaus between holes, the high particle number density surface shows ridges between the originally close packed particles giving a hexagonal array of bowl shaped cavities which may prove useful for future applications.

6.3.3 Ordering

As shown in the SEM photographs above and in Figure 6.8 the siPCCA and the inverse opal photonic crystal materials are highly ordered over long ranges. Figure 6.8 shows an siPCCA cleaved mainly along the 100 plane surfaces. The ordering of the SEM visually suggests high order, possibly higher than that of the more typically studied close packed photonic crystal materials made from colloidal particles with similar particle size monodispersities. The presumed increased ordering of the siPCCA compared to close packed photonic crystals is expected from the superior ordering of the original CCA template. The ordering of the CCA derives from soft electrostatic repulsions between colloidal particles. Because of the soft repulsive interactions,

colloidal particle polydispersity should have less impact on the ordering of electrostatically stabilized CCA than would occur for hard sphere-interacting close packed systems, as shown below.

This phenomenon is evident from Figure 6.9 which shows the disorder induced by the inclusions of ~4-fold and ~2-fold larger particles in the original CCA template. The deformation in the crystal lattice anneals out within approximately two particle layers, due to the CCA soft electrostatic interparticle potential.

To quantitatively analyze the Figure 6.9a ordering of our inverse opal siPCCA we calculated the two dimensional pair correlation function (PCF), g(r) of the area enclosed by the white circle

$$g(r) = \frac{1}{\langle \rho \rangle} \frac{dn(r, r+dr)}{da(r, r+dr)}$$

Equation 6.8

We calculated the number of spheres, *dn*, which lie at a radius of r from the defined origin within a circular ring of width *dr*. As r increases g(r) probes the long range particle ordering within the (111) plane. We repeated this calculation for multiple origins within the lattice (white colored centers). The average of the g(r) values was normalized by the average particle number density and the area of the circular ring $da=2\pi rdr$.

For well ordered crystals g(r) will be large for r values corresponding to multiples of the in-plane (111) lattice constants. In contrast, g(r) will be small for intermediate r values. Colvin *et al* recently showed highly ordered photonic crystal lattices generate g(r) showing many peaks over large values of r which clearly indicate good long range ordering.[55]

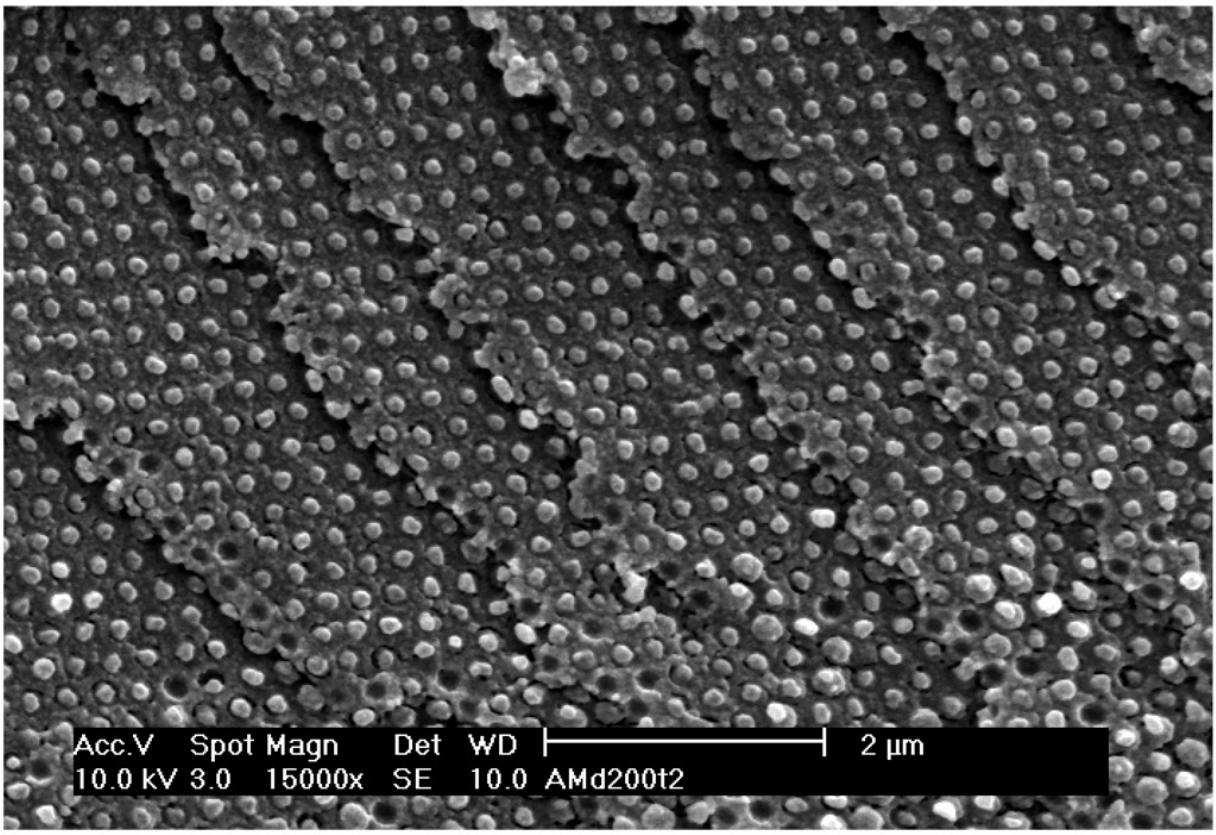

Figure 6.8: siPCCA 100 planes

SEM of cleaved cross-section of low particle density siPCCA showing exposed 100 planes.

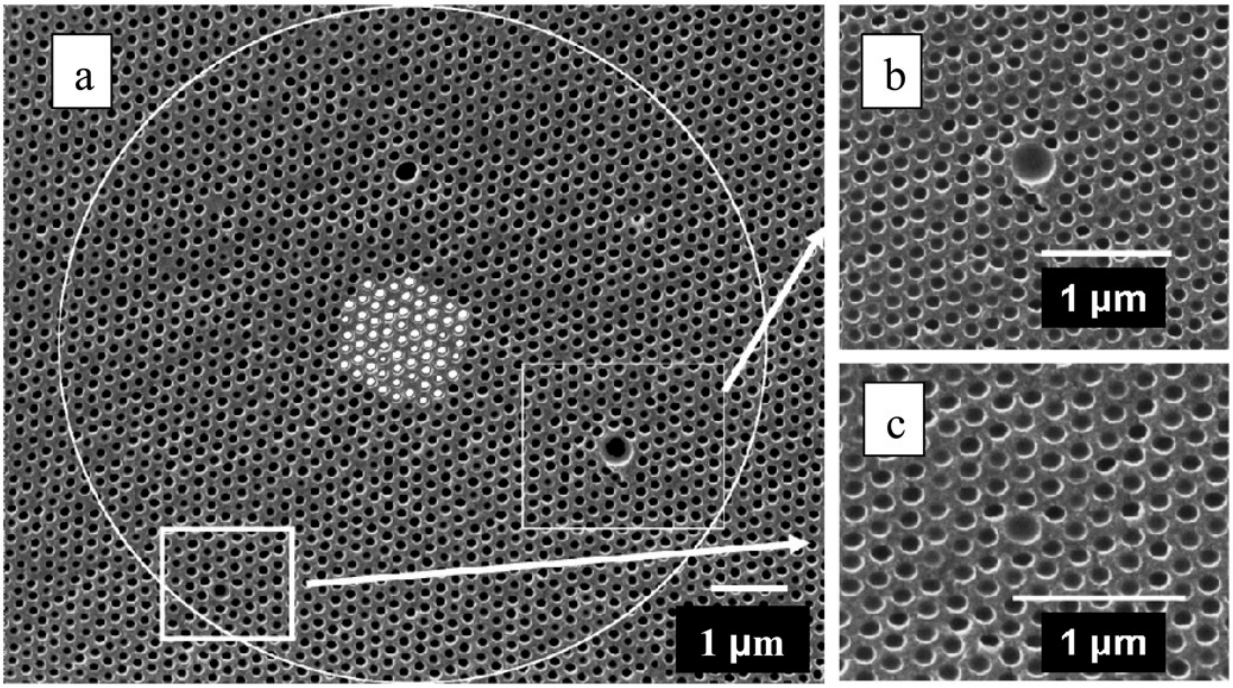

Figure 6.9: siPCCA 111 planes

a. SEM image showing the (111) plane surface of a silica inverse opal photonic crystal which was heat treated to 450 °C. The white circle encloses the area used to calculate the pair correlation function (PCF). The small white circles at the center of the image shows the different origins used for the PCF. b. Expanded images showing impact of a 4-fold and c. 2-fold larger colloidal particles on the ordering. The strains in the periodic order of the lattice anneal over approximately two particles layers.

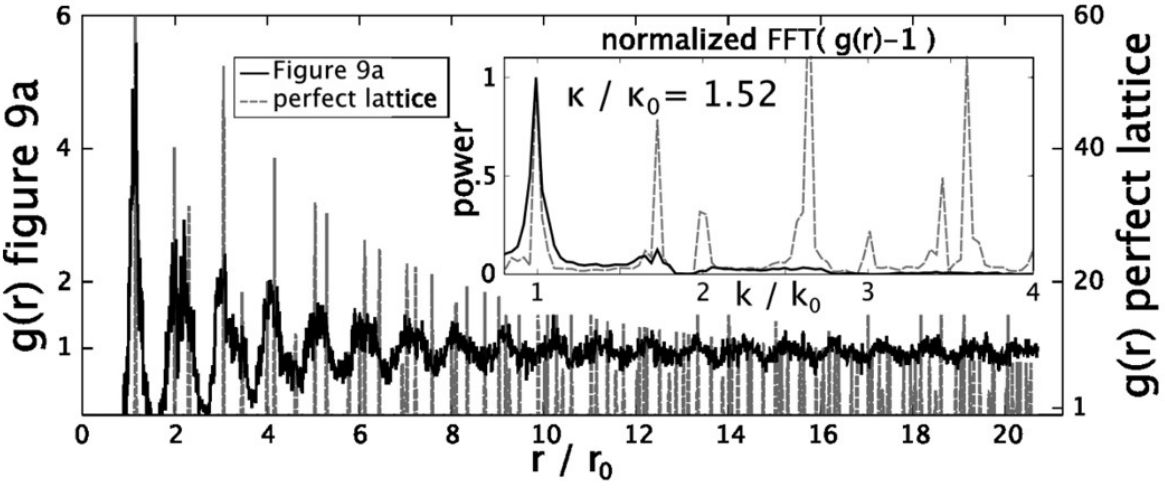

Figure 6.10: Pair correlation function

Calculated pair correlation function (PCF) from sample shown in Figure 6.9a and PCF for a perfect lattice (vertical dashed lines) as a function of r/r_o, where r_o is the mean near neighbor center to center spacing. The inset shows the Fourier Transforms (FT) of both PCF where the dotted lines show the FT of the perfect lattice.

Figure 6.10 compares g(r) for the Figure 6.9a area within the white circle to g(r) of a perfect (111) plane with the same average in-plane spacing and area. g(r) shows peaks out to $r/r_o > 20$ that coincide with those calculated for a perfect lattice, however, the g(r) siPCCA peak amplitudes are smaller indicating a decreased ordering compared to the perfect lattice. The Figure 6.10 inset shows the FT of g(r)-1 for the Figure 6.9 image. We calculate that $\kappa/\kappa_o = 1.52$ demonstrating that our siPCCA is highly ordered. This high order occurs in spite of the presence of multiple point defects. This ordering which results from simple CCA self assembly favorably compares very favorably to the ordering found for convective self-assembled close-packed photonic crystals.[55] Rengarajan et al [55] samples formed by convective self assembly of 3 to 4 % colloidal size distributions have average $\kappa/\kappa_o \sim 1.5$, a value essentially identical to what we obtained through electrostatic self assembly of the template.

We can qualitatively understand the decreased impact of particle polydispersity on CCA ordering compared to that of close-packed particles by examining the interparticle repulsive interactions. At present the electrostatic interaction between charged particles is modeled by using DLVO theory.[9] We are aware that this is only a rough approximation since it is well known that DLVO theory fails to describe particle repulsion for particles with high charge.[46] Further the effective particle charge must be renormalized to significantly decrease the charge density so that DLVO theory can successfully model electrostatic interactions for real colloidal dispersions.[2]

The DLVO interaction potential, $U_{DLVO}(r)$ between particles with different sizes and charges is:

$$U_{DLVO}(r) = \frac{Z_1^* Z_2^* e^2}{\epsilon}\left[e^{\frac{\kappa a_1}{1+\kappa a_1}}\right]\left[e^{\frac{\kappa a_2}{1+\kappa a_2}}\right]\frac{e^{-\kappa r}}{r}$$

Equation 6.9

where Z^*_1 and Z^*_2 are the renormalized charges on two particles of radius a_1 and a_2. e is the fundamental electronic charge, ε is the static dielectric constant of the medium and r is the interparticle separation distance.[18] The Debye length, 1/κ, is given by

$$1/\kappa = \sqrt{\frac{4\pi e^2}{\epsilon k_B T}[n_p Z^* + n_i]}$$

Equation 6.10

where k_B is Boltzmann's constant, n_p is the particle number density and n_i is the ionic impurity concentration. We presume that the system contains no added impurities, so that n_i = 0. For the discussion below we assume that a 10% variation in a single particle diameter and/or single particle charge results in a negligible change in the Debye length of the system.

The discussion below assumes a nominal colloidal particle diameter of 130 nm and a renormalized charge of Z=1000. This charge renormalization corrects for extra charge screening not included in DLVO theory. We choose for discussion a CCA nearest neighbor distance of 250 nm between particles, giving a particle number density of 1.613×10^{14} particles/cm^3. We calculate $1/\kappa$ for our system to be 10.4 nm.

Figure 6.11 shows that for this distance separation there is a negligible difference in the DLVO potential in response to a 10 % increase in particle charge. Thus, changes in particle charge must negligibly impact the CCA ordering at these nearest-neighbor distances.

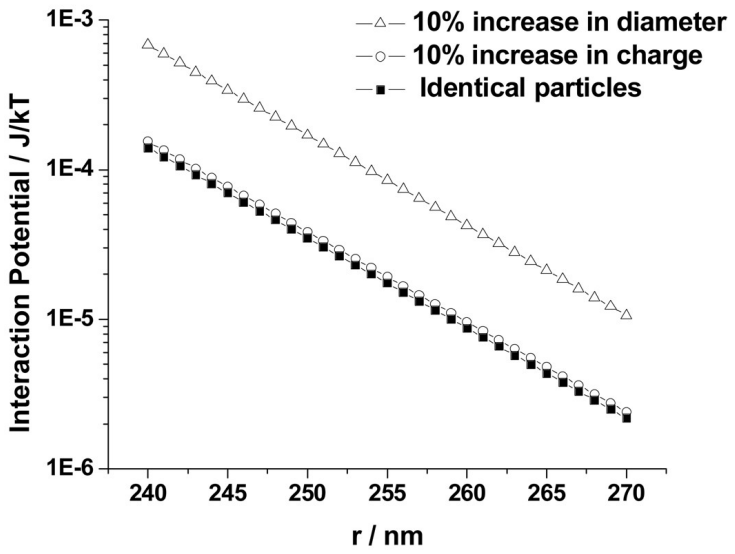

Figure 6.11: Dependence of $U_{DLVO}(r)$ upon interparticle distance

Dependence of $U_{DLVO}(r)$ upon interparticle distance between (■) two identical particles of 130 nm diameter with a renormalized charge of 1000; (○) between two identical particles of diameter 130 nm, where one particle has a renormalized charge of 1000 and the other 1100; (△) between a particle of diameter 130 nm and one 10% larger, both with a renormalized charge of 1000.

In contrast, Figure 6.11 shows that DLVO theory predicts a ~10 % increase in repulsive interactions with a 10 % increase in the particle diameter. However, the porential energy difference at the same interparticel spacing of 250nm is quite small, ~ 2 x 10^{-3} k_BT per particle

This soft electrostatic repulsive potential prevents defect particles from significantly impacting CCA ordering. We can roughly model the change which occurs in the interparticle spacing brought on by a single defect particle with a 10 % increased particle diameter by modeling the forces in a one dimensional array of particles that spans the characteristic photonic crystal macroscopic size (Figure 6.12). We calculate the forces between particles, neglecting all but nearest neighbor interactions, from the derivative of the DLVO potential with respect to interparticle distance, r.

$$F(r) = \frac{0 Z_1 e Z_2 e}{\epsilon}\left[\frac{e^{\kappa a_1}}{1+\kappa a_1}\right]\left[\frac{e^{\kappa a_2}}{1+\kappa a_2}\right]\left[\frac{1+\kappa r}{r^2}\right]e^{-kr}$$

Equation 6.11

We assume a linear array of N particles. We compare the distance between particles for an array of N identical particles which is x= L/ (N+1). When a single particle is replaced with a defect particle having a 10% increase in diameter the particles expand around the defect particle and contract around the other particles until the forces balance. This would result in a negligible average particle spacing decrease for the other particles since this spacing difference would be distributed over the other particles in the array.

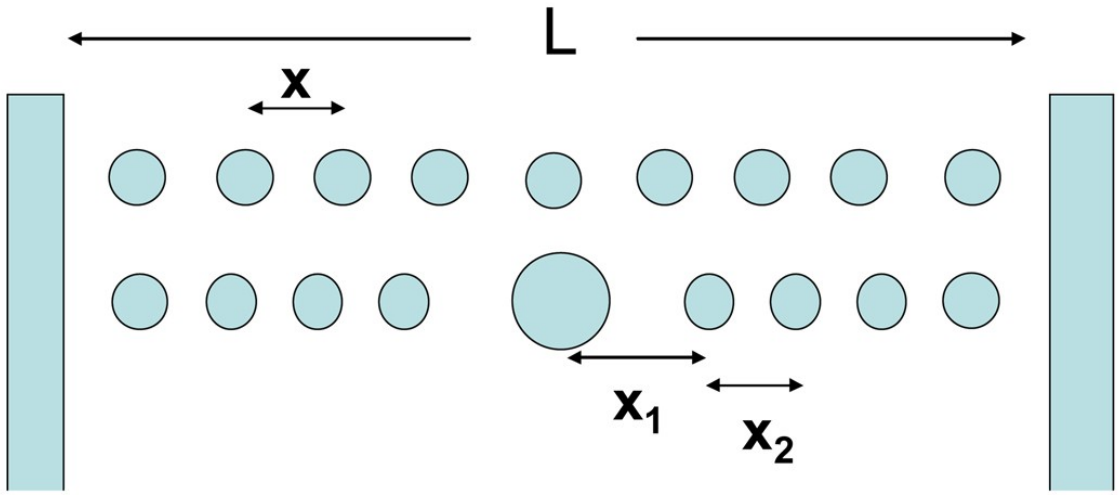

Figure 6.12: Model for response of one dimensional array of N particles to a single defect particle

Model for response of one dimensional array of N particles to a single defect particle of increased diameter. The N particles are arrayed along a cell of length L. In the top array the particle diameters are identical and the system self assembles such that the spacings between particles are identical at $x = L / (N + 1)$*. In the bottom array one particle is replaced with a particle of larger diameter. The distance between the larger diameter particle and the adjacent particle is* $x_1 = x + \delta$*, while the distance between the other identical particles is* $x_2 = L - 2x_1 / (N - 1)$*.* δ *is determined by the equilibrium between forces.*

We can look at this issue more quantitatively by equilibrating the forces between particles. Equation 6.12 and Equation 6.13 show that $F(x_1)$ defines the force between the defect particle and its nearest neighbor while $F(x_2)$ defines the force between the remaining identical particles. We assume that the length of the particle array is constant at 250 µm

$$F(x_1) = \frac{-(Z_1 \cdot e)^2}{\epsilon}\left[\frac{e^{\kappa a_1}}{1+\kappa a_1}\right]\left[\frac{e^{\kappa a_2}}{1+\kappa a_2}\right]\left[\frac{1+\kappa x_1}{x_1^2}\right]e^{-\kappa x_1}$$

Equation 6.12

$$F(x_2) = \frac{-(Z_1 \cdot e)^2}{\epsilon}\left[\frac{e^{\kappa a_1}}{1+\kappa a_1}\right]\left[\frac{e^{\kappa a_2}}{1+\kappa a_2}\right]\left[\frac{1+\kappa x_2}{x_2^2}\right]e^{-\kappa x_2}$$

Equation 6.13

which represents the smallest dimension common to our CCA films. The nearest neighbor spacing of this system before the addition of a particle defect is x = 250 nm. Therefore N = 999 particles.

Addition of a 10% increased particle diameter to the array changes the spacing between the defect and its nearest neighbor to a $x_1 = x + \delta$, where δ is the added spacing gained by the equilibration of force between the defect and its nearest neighbor, $x_2 = (L\text{-}2 (x + \delta)) / (N - 1)$

By equilibrating the forces in Equation 6.12 and Equation 6.13 we calculate δ = 5.7 nm for a 10% increased particle size. The separation between all other particles is very small:

$$x_2 = \frac{L-2(x+\delta)}{N-1} = \frac{x\cdot(N+1)-2x-2\delta}{N-1} = \frac{x(N-1)-2\delta}{N-1} = x-\frac{2\delta}{N-1}$$

Equation 6.14

For the typical large values of N there is negligible change in the interparticle spacings x_2 except exactly around the defect particle. In contrast for a close-packed system, a 10% change in particle size generates a 10 % change in local spacing which disorders the system locally over the distance that dislocations continue to disorder the system macroscopically.

6.4 CONCLUSIONS

We developed a simple, straightforward method to form *non close-packed* ultra-highly ordered fcc direct and inverse opal silica photonic crystals. We utilize a self assembled electrostatically stabilized crystalline colloidal array (CCA) template prepared from monodisperse, highly charged polystyrene colloidal particles. We then polymerize a hydrogel around the CCA (PCCA) and then condense silica within the PCCA to form a highly ordered siPCCA photonic crystal. Heating at 450 °C removes the organic polymer leaving the inverse opal structure.

This approach allows us to independently control the photonic crystal periodicity and size of the basis of the fcc unit cell. We select the fcc lattice constant by defining the particle number density of this electrostatically self assembled structure. Thus, we independently control the spacing between particles. The particle diameter used determines the wall spacing of the inverse opal photonic crystal and determines the shape of the photonic crystal dielectric constant modulation. This allows us to optimize the diffraction of our photonic crystal structures.

These fcc photonic crystals simply and spontaneously self assemble due to their soft electrostatic repulsion potentials. They show ordering as good or possibly better than close-packed photonic crystals formed by convective assembly. We show that colloidal particle size polydispersity has less impact on photonic crystal electrostatic ordering than occurs for ordering of close-packed crystals. Point defect induced crystal strains in electrostatically stabilized CCA anneal within ~two particle layers. We also show that charge polydispersity has only a small impact on crystal ordering and that the strains due to defect particles of different charge also anneal out over ~two particle layers.

6.5 BIBLIOGRAPHY

[1] **Akahane, Y.; Asano, T.; Song, B.-S. and Noda, S.** (**2003**). *High-Q photonic nanocavity in a two-dimensional photonic crystal*, Nature 425 : 944-947.

[2] **Alexander, S.; Chaikin, P.; Grant, P.; Morales, G.; Pincus, P. and Hone, D.** (**1984**). *Charge renormalization, osmostic pressure, and bulk modulus of colloidal crystals: Theory*, The Journal of Chemical Physics 80 : 5776-5781.

[3] **Arsenault, A.; Fournier-Bidoz, S.; Hatton, B.; Míguez, H.; Tétreault, N.; Vekris, E.; Wong, S.; Yang, S.; Kitaev, V. and Ozin, G.** (**2004**). *Towards the synthetic all-optical computer: Science fiction or reality?*, Journal of Materials Chemistry 14 : 781-794.

[4] Asher, S. (**1986**). *US Patent 4,627,689*.

[5] Asher, S. (**1994**). *US Patent 5,281,370*.

[6] Asher, S. (**1995**). *US Patent 5,452,123*.

[7] **Asher, S.; Flaugh, P. and Washinger, G.** (**1986**). *Crystalline colloidal Bragg diffraction devices: The basis for a new generation of Raman instrumentation*, Spectroscopy 1.

[8] **Asher, S.; Holtz, J.; Liu, L. and Wu, Z.** (**1994**). *Self-assembly motif for creating submicron periodic materials. Polymerized crystalline colloidal arrays*, Journal of the American Chemical Society 116 : 4997-4998.

[9] **Belloni, L.** (**2000**). *Colloidal interactions*, Journal of Physics Condensed Matter 12 : R549-R587.

[10] **Blanco, A.; Chomski, E.; Grabtchak, S.; Ibisate, M.; John, S.; Leonard, S.; Lopez, C.; Meseguer, F.; Miguez, H.; Mondla, J.; Ozin, G.; Toader, O. and Van Driel, H.** (**2000**). *Large-scale synthesis of a silicon photonic crystal with a complete three-dimensional bandgap near 1.5 micrometres*, Nature 405 : 437-440.

[11] **Blanford, C.; Schroden, R.; Al-Daous, M. and Stein, A.** (**2001**). *Tuning solvent-dependent color changes of three-dimensionally ordered macroporous (3DOM) materials through compositional and geometric modifications*, Advanced Materials 13 : 26-29.

[12] **Busch, K. and John, S.** (**1998**). *Photonic band gap formation in certain self-organizing systems*, Physical Review E - Statistical Physics, Plasmas, Fluids, and Related Interdisciplinary Topics 58 : 3896-3908.

[13] **Carlson, R. J. and Asher, S. A.** (**1984**). *Characterization of optical diffraction and crystal structure in monodisperse polystyrene colloids.*, Applied Spectroscopy 38 : 297-304.

[14] **Cheng, C. and Scherer, A.** (**1995**). *Fabrication of photonic band-gap crystals*, Journal of Vacuum Science and Technology B: Microelectronics and Nanometer Structures 13 : 2696-2700.

[15] **Chow, E.; Lin, S.; Johnson, S.; Villeneuve, P.; Joannopoulos, J.; Wendt, J.; Vawter, G.; Zubrzycki, W.; Hou, H. and Alleman, A.** (**2000**). *Three-dimensional control of light in a two-dimensional photonic crystal slab*, Nature 407 : 983-986.

[16] **Christodoulides, D.; Lederer, F. and Silberberg, Y.** (**2003**). *Discretizing light behaviour in linear and nonlinear waveguide lattices*, Nature 424 : 817-823.

[17] **Chutinan, A.; John, S. and Toader, O.** (**2003**). *Diffractionless flow of light in all-optical microchips*, Physical Review Letters 90 : 123901/1-123901/4.

[18] **Crocker, J. and Grier, D.** (**1996**). *When like charges attract: The effects of geometrical confinement on long-range colloidal interactions*, Physical Review Letters 77 : 1897-1900.

[19] **Davis, K.; Russel, W. and Glantschnig, W.** (**1991**). *Settling suspensions of colloidal silica: Observations and X-ray measurements*, Journal of the Chemical Society, Faraday Transactions 87 : 411-424.

[20] **Doosje, M.; Hoenders, B. and Knoester, J.** (**2000**). *Photonic bandgap optimization in inverted fee photonic crystals*, Journal of the Optical Society of America B: Optical Physics 17 : 600-606.

[21] **Fenollosa, R. and Meseguer, F.** (**2003**). *Non-close-packed artificial opals*, Advanced Materials 15 : 1282-1285.

[22] **Flaugh, P. L.; O'Donnell, S. E. and Asher, S. A.** (**1984**). *Development of a new optical wavelength rejection filter: Demonstration of its utility in raman spectroscopy.*, Applied Spectroscopy 38 : 847-850.

[23] **Graugnard, E.; King, J.; Gaillot, D. and Summers, C.** (**2006**). *Sacrificial-layer atomic layer deposition for fabrication of non-close-packed inverse-opal photonic crystals*, Advanced Functional Materials 16 : 1187-1196.

[24] **Holtz, J. and Asher, S.** (**1997**). *Polymerized colloidal crystal hydrogel films as intelligent chemical sensing materials*, Nature 389 : 829-832.

[25] **Hoogenboom, J.; Derks, D.; Vergeer, P. and Van Blaaderen, A.** (**2002**). *Stacking faults in colloidal crystals grown by sedimentation*, Journal of Chemical Physics 117 : 11320-11328.

[26] **Imada, M.; Chutinan, A.; Noda, S. and Mochizuki, M.** (**2002**). *Multidirectionally distributed feedback photonic crystal lasers*, Physical Review B - Condensed Matter and Materials Physics 65 : 1953061-1953068.

[27] **Imada, M.; Lee, L.; Okano, M.; Kawashima, S. and Noda, S.** (**2006**). *Development of three-dimensional photonic-crystal waveguides at optical-communication wavelengths*, Applied Physics Letters 88.

[28] **Jiang, P.; Bertone, J.; Hwang, K. and Colvin, V.** (**1999**). *Single-crystal colloidal multilayers of controlled thickness*, Chemistry of Materials 11 : 2132-2140.

[29] **Joannopoulos, J.; Meade, R. and Winn, J.** (**1995**). , Photonic crystals: Molding the flow of light .

[30] **Joannopoulos, J.; Villeneuve, P. and Fan, S.** (**1997**). *Photonic crystals: Putting a new twist on light*, Nature 386 : 143-149.

[31] **John, S.** (**1987**). *Strong localization of photons in certain disordered dielectric superlattices*, Physical Review Letters 58 : 2486-2489.

[32] **Kesavamoorthy, G. and Asher, S.** (**1997**). *Optically nonlinear Bragg diffracting nanosecond optical switches*, Physical Review Letters 78 : 3860-3863.

[33] **Kesavamoorthy, R.; Super, M. and Asher, S.** (**1992**). *Nanosecond photothermal dynamics in colloidal suspension*, Journal of Applied Physics 71 : 1116-1123.

[34] **Kimble, K.; Walker, J.; Finegold, D. and Asher, S.** (**2006**). *Progress toward the development of a point-of-care photonic crystal ammonia sensor*, Analytical and Bioanalytical Chemistry 385 : 678-685.

[35] **King, J.; Galliot, D.; Graugnard, E. and Summers, C.** (**2006**). *Conformally back-filled, non-close-packed inverse-opal photonic crystals*, Advanced Materials 18 : 1063-1067.

[36] **Kitaev, V. and Ozin, G.** (**2003**). *Self-assembled surface patterns of binary colloidal crystals*, Advanced Materials 15 : 75-78.

[37] **Koh, Y. and Wong, C.** (**2006**). *In situ monitoring of structural changes during colloidal self-assembly*, Langmuir 22 : 897-900.

[38] **Krauss, T.; Song, Y.; Thoms, S.; Wilkinson, C. and DelaRue, R.** (**1994**). *Fabrication of 2-D photonic bandgap structures in GaAs/AlGaAs*, Electronics Letters 30 : 1444-1446.

[39] **Li, Z.-Y. and Zhang, Z.-Q.** (**2000**). *Fragility of photonic band gaps in inverse-opal photonic crystals*, Physical Review B - Condensed Matter and Materials Physics 62 : 1516-1519.

[40] **López, C.** (**2003**). *Materials aspects of photonic crystals*, Advanced Materials 15 : 1679-1704.

[41] **Maurer, M.; Lednev, I. and Asher, S.** (**2005**). *Photoswitchable spirobenzopyran-based photochemically controlled photonic crystals*, Advanced Functional Materials 15 : 1401-1406.

[42] **Meseguer, F.** (**2005**). *Colloidal crystals as photonic crystals*, Colloids and Surfaces A: Physicochemical and Engineering Aspects 270-271 : 1-7.

[43] **Meseguer, F. and Fenollosa, R.** (**2005**). *Non-close packed colloidal crystals*, Journal of Materials Chemistry 15 : 4577-4580.

[44] **Míguez, H.; López, C.; Meseguer, F.; Blanco, A.; Vázquez, L.; Mayoral, R.; Ocaña, M.; Fornés, V. and Mifsud, A.** (**1997**). *Photonic crystal properties of packed submicrometric SiO2 spheres*, Applied Physics Letters 71 : 1148-1150.

[45] **Míguez, H.; Tétreault, N.; Yang, S.; Kitaev, V. and Ozin, G.** (**2003**). *A new synthetic approach to silicon colloidal photonic crystals with a novel topology and an omni-directional photonic bandgap: Micromolding in Inverse Silica Opal (MISO)*, Advanced Materials 15 : 597-600.

[46] **Naji, A.; Jungblut, S.; Moreira, A. and Netz, R.** (**2005**). *Electrostatic interactions in strongly coupled soft matter*, Physica A: Statistical Mechanics and its Applications 352 : 131-170.

[47] **Noda, S.; Fujita, M. and Asano, T.** (**2007**). *Spontaneous-emission control by photonic crystals and nanocavities*, Nature Photonics 1 : 449-458.

[48] **Noda, S.; Tomoda, K.; Yamamoto, N. and Chutinan, A.** (**2000**). *Full three-dimensional photonic bandgap crystals at near-infrared wavelengths*, Science 289 : 604-606.

[49] **Norris, D.** (**2007**). *Photonic crystals: A view of the future*, Nature Materials 6 : 177-178.

[50] **Painter, O.; Lee, R.; Scherer, A.; Yariv, A.; O'Brien, J.; Dapkus, P. and Kim, I.** (**1999**). *Two-dimensional photonic band-gap defect mode laser*, Science 284 : 1819-1821.

[51] **Pan, G.; Kesavamoorthy, R. and Asher, S.** (**1998**). *Nanosecond switchable polymerized crystalline colloidal array bragg diffracting materials*, Journal of the American Chemical Society 120 : 6525-6530.

[52] **Reese, C.; Baltusavich, M.; Keim, J. and Asher, S.** (**2001**). *Development of an intelligent polymerized crystalline colloidal array colorimetric reagent*, Analytical Chemistry 73 : 5038-5042.

[53] **Reese, C.; Guerrero, C.; Weissman, J.; Lee, K. and Asher, S.** (**2000**). *Synthesis of highly charged, monodisperse polystyrene colloidal particles for the fabrication of photonic crystals*, Journal of Colloid and Interface Science 232 : 76-80.

[54] **Reese, C.; Mikhonin, A.; Kamenjicki, M.; Tikhonov, A. and Asher, S.** (**2004**). *Nanogel nanosecond photonic crystal optical switching*, Journal of the American Chemical Society 126 : 1493-1496.

[55] **Rengarajan, R.; Mittleman, D.; Rich, C. and Colvin, V.** (**2005**). *Effect of disorder on the optical properties of colloidal crystals*, Physical Review E - Statistical, Nonlinear, and Soft Matter Physics 71.

[56] **Sanders, J.** (**1964**). *Colour of precious opal*, Nature 204 : 1151-1153.

[57] **Sen, T.; Tiddy, G.; Casci, J. and Anderson, M.** (**2003**). *One-pot synthesis of hierarchically ordered porous-silica materials with three orders of length scale*, Angewandte Chemie - International Edition 42 : 4649-4653.

[58] **Sharma, A.; Jana, T.; Kesavamoorthy, R.; Shi, L.; Virji, M.; Finegold, D. and Asher, S.** (**2004**). *A general photonic crystal sensing motif: Creatinine in bodily fluids*, Journal of the American Chemical Society 126 : 2971-2977.

[59] **Sirota, E.; Ou-Yang, H.; Sinha, S.; Chaikin, P.; Axe, J. and Fujii, Y.** (**1989**). *Complete phase diagram of a charged colloidal system: A synchro- tron x-ray scattering study*, Physical Review Letters 62 : 1524-1527.

[60] **Song, B.-S.; Noda, S.; Asano, T. and Akahane, Y.** (**2005**). *Ultra-high-Q photonic double-heterostructure nanocavity*, Nature Materials 4 : 207-210.

[61] **Takeda, H.; Chutinan, A. and John, S.** (**2006**). *Localized light orbitals: Basis states for three-dimensional photonic crystal microscale circuits*, Physical Review B - Condensed Matter and Materials Physics 74.

[62] **Tikhonov, A.; Coalson, R. and Asher, S.** (**2008**). *Light diffraction from colloidal crystals with low dielectric constant modulation: Simulations using single-scattering theory*, Physical Review B - Condensed Matter and Materials Physics 77.

[63] **Van Blaaderen, A. and Wiltzius, P.** (**1997**). *Growing large, well-oriented colloidal crystals*, Advanced Materials 9 : 833-835.

[64] **Vlasov, Y.; Bo, X.-Z.; Sturm, J. and Norris, D.** (**2001**). *On-chip natural assembly of silicon photonic bandgap crystals*, Nature 414 : 289-293.

[65] **Walker, J. and Asher, S.** (**2005**). *Acetylcholinesterase-based organophosphate nerve agent sensing photonic crystal*, Analytical Chemistry 77 : 1596-1600.

[66] **Weissman, J.; Sunkara, H.; Tse, A. and Asher, S.** (**1996**). *Thermally switchable periodicities and diffraction from mesoscopically ordered materials*, Science 274 : 959-960.

[67] **Xia, Y.; Gates, B.; Yin, Y. and Lu, Y.** (**2000**). *Monodispersed colloidal spheres: Old materials with new applications*, Advanced Materials 12 : 693-713.

[68] **Xu, X.; Friedman, G.; Humfeld, K.; Majetich, S. and Asher, S.** (**2001**). *Superparamagnetic photonic crystals*, Advanced Materials 13 : 1681-1684.

[69] **Xu, X.; Friedman, G.; Humfeld, K.; Majetich, S. and Asher, S.** (**2002**). *Synthesis and utilization of monodisperse superparamagnetic colloidal particles for magnetically controllable photonic crystals*, Chemistry of Materials 14 : 1249-1256.

[70] **Xu, X.; Goponenko, A. and Asher, S.** (**2008**). *Polymerized polyHEMA photonic crystals: pH and ethanol sensor materials*, Journal of the American Chemical Society 130 : 3113-3119.

[71] **Xu, X.; Majetich, S. and Asher, S.** (**2002**). *Mesoscopic monodisperse ferromagnetic colloids enable magnetically controlled photonic crystals*, Journal of the American Chemical Society 124 : 13864-13868.

[72] **Yablonovitch, E.** (**1987**). , J. Phys., Colloq. C5.

[73] **Zheng, Z.; Liu, X.; Luo, Y.; Cheng, B.; Zhang, D.; Meng, Q. and Wang, Y.** (**2007**). *Pressure controlled self-assembly of high quality three-dimensional colloidal photonic crystals*, Applied Physics Letters 90.

[74] Dean, J. A. (Ed.), **1973**. *Lange's Handbook of Chemistry*. McGraw-Hill, .

7.0 FABRICATION OF LARGE-AREA TWO-DIMENSIONAL COLLOIDAL CRYSTALS

Author list: Jian-Tao Zhang, Luling Wang, Daniel N. Lamont, Sachin S. Velankar, and Sanford A. Asher

Author Contribution: The author of this dissertation was responsible for characterizing the degree of order of the photonic crystals, providing interpretation of the results and contributing to the preparation of the manuscript. This work has been published as *Angew Chem. Int. ed.* ***2012****, 51, 6117*

7.1 INTRODUCTION

Two-dimensional crystalline colloidal arrays (CCAs) have numerous applications, such as photonic crystal materials and sensors[11-13; 22; 23; 26; 28; 29]. Recently, numerous methods have been developed to prepare well-ordered 2D assemblies.[4; 6-8; 10; 24; 25] , These methods include spin coating,[6] dip coating,[7] and electrophoretic deposition [24] of colloidal particles on planar substrates to form 2D nanoparticle arrays. Particle assembly at interfaces can also be used to form 2D CCA

monolayers.[4; 8; 10; 25] 2D particle arrays have previously been prepared on water surfaces.[9; 14; 17; 19; 27] For example, Giersig and co-workers reported on the self-assembly of polystyrene (PS) latex particles on a water surface by applying a particle suspension to a clean silicon wafer, immersing the silicon wafer in water, and then consolidating the particle array by addition of surfactant. Through this method a few square centimeter 2D arrays were obtained.[19] Retsch et al. used a similar approach to prepare close-packed 2D colloidal crystals by floating and re-depositing colloidal monolayers at the air/water interface.[17] Qi and co-workers modified this approach by dropping an aqueous ethanol particle suspension onto a solid substrate that was surrounded by water. [9] The dispersion spread on the water surface, resulting in monolayer 2D films up to about 16 cm^2 in the area.[9] Pan et al. developed a method to fabricate close-packed monolayer arrays of latex particles on a stirred water surface. Then they transferred the arrays onto a substrate.[14] The maximum sizes of the 2D array developed by the above methods appear limited to tens of square centimeters. There is a need to develop methods to prepare 2D arrays of larger sizes.

For example, Jeong et al. reported a method to form large-area 2D arrays based on a wire-wound rod coating method.[5] Recently, Vogel et al. presented a method to produce close-packed monolayers by using a glass slide to add colloid suspensions to the air–water interface. Close-packed monolayer patches crystallize upon spreading of an ethanolic PS colloid dispersion. Upon further addition of colloid, the patches eventually assemble into a monolayer covering the complete water surface.[21] Our group fabricated large 2D arrays by spreading alcohol/water solutions of colloidal particles on top of mercury surfaces.[30; 31] We obtained well-ordered 2D arrays by self-assembly of colloidal particles on mercury as the solvent

evaporated. These 2D arrays could easily be attached to hydrogel films.[30; 31] Although this method was very successful in preparing large-area 2D arrays, the use of mercury as a substrate is undesirable because of its toxicity.

Here, we report on fast fabrication of large 2D arrays of colloidal particles at the air/water interface by a needle tip flow method. The preparation of the 2D monolayer CCAs by this approach is illustrated in Figure 7.1a. The tip of a sharpened injection needle was positioned to be just in contact with the water surface. The suspension was slowly and smoothly layered onto the top of the water surface to form monolayer particle arrays. The spreading force of the suspension drives the freshly formed particle array radially away from the needle tip to the outer edge of the dish. A beautiful continuous 2D array monolayer filled the entire water surface (>280 cm^2 in the current study, Equation 7.1b) in 2 min. The area of the resulting 2D arrays was as large as the area of the water surface used. Many 2D array applications will benefit from the ability to prepare large-area 2D arrays.

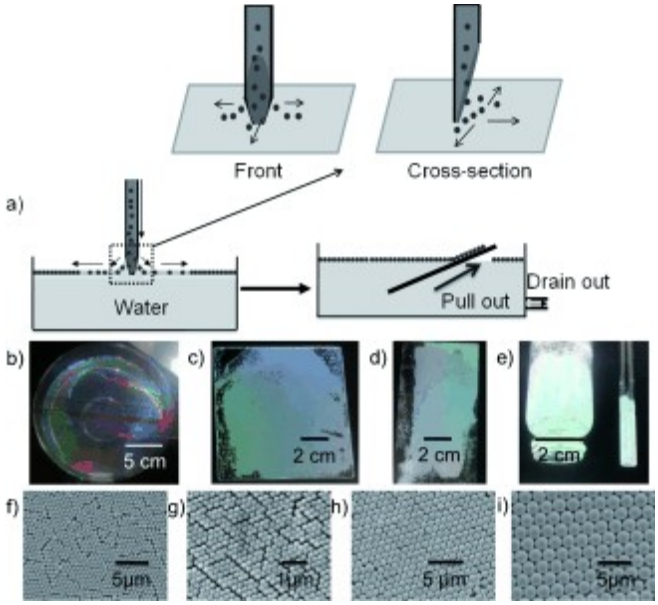

Figure 7.1: Fabrication of a 2D PS particle array by the needle tip flow technique

a) Fabrication of a 2D PS particle array by the needle tip flow technique. The transfer of the 2D arrays onto a substrate is shown by draining out the water or by lifting the array on a substrate. b) Photograph of 580 nm PS 2D array on the water surface in a glass dish 19 cm in diameter. 580 nm diameter PS 2D crystal arrays transferred onto c) flat glass, d) a plastic sheet, and e) a curved glass. SEM images of 2D arrays of f) 580 nm, g) 235 nm, h) 1 μm, and i) 2 μm PS particles.

7.2 RESULTS AND DISCUSSION

The spreading of the particle suspension uses the Marangoni effect in which a surface tension gradient causes the liquid surface to be pushed away from the regions of low surface tension. In the present case the Marangoni flow induced by adding the alcohol-containing colloidal dispersion onto the water surface causes the colloidal particle dispersion to rapidly spread outwards, thus covering the surface with particles.[3; 20]

The position of the needle tip is critically important for the formation of a 2D array on the water surface. The contact of the needle tip with the water surface forms a meniscus structure along the needle tip wall (Figure 7.1a). This meniscus damps the vertical flow forces to prevent breaking of the water surface to enable the layering of the colloid dispersion on the water surface.

As shown in Figure 7.1a we can transfer the floating 2D array onto a substrate by either draining the water and settling the 2D array on the substrate, or by lifting the substrate and depositing the 2D array on the substrate. Figure 7.1c-e show examples of 580 nm diameter PS 2D crystal arrays transferred onto a flat glass slide, a flat plastic sheet, and curved glass substrates. Scanning electron microscopy (SEM) images show that the 2D arrays are hexagonally close-packed. The arrays form hexagonal multi-domains of areas larger than 20 μm^2 (Figure 7.1f). Figure 7.1g, h, and i shows SEM images of 2D PS arrays with particle sizes ranging from 235 nm to 2 μm.

We conducted a quantitative analysis of the ordering of the 2D arrays shown in the SEM images (Figure 7.1) by calculating the 2D pair correlation function, $g(r)$ [1; 2; 16] , given in Equation 7.1,

$$g(r) = \frac{1}{\langle p \rangle} \frac{dn(r, r+dr)}{da(r, r+dr)}$$

Equation 7.1

where a is the shell area and $n(r,r+dr)$ is the number of particles that lie within the shell considered. A SEM micrograph was first converted into a binary image, and then the MATLAB image processing toolbox was used to locate the centroid of each particle. The bulk particle density was calculated by dividing the total number of particles by the area of the polygon formed by the particles inside the edges of the image boundaries. The curves of $g(r)$ were calculated between r=0.05 R_0 to r=30 R_0 using shell thicknesses of 0.016 R_0, where R_0 is the particle radius and r is the distance from the origin of the radial distribution function and $g(r)$ is the calculated distance. To properly accommodate particles near the boundaries, a sub-routine was used to determine the fraction of each $g(r)$ integration shell within the image boundaries.

As previously reported, [2; 16] ,a quantitative measure of ordering is obtained from the ratio of the full width at half maximum (FWHM), κ, of the first peak in the Fourier transform of the function $g(r)-1$ to that of a perfectly ordered array, κ_0. The ratio of κ/κ_0=1 indicates a 2D colloidal crystal that is essentially perfect in 2D structural ordering, whereas $\kappa/\kappa_0 \leq 1.5$ suggests a

very highly ordered 2D structure; κ/κ_0>1.5 indicates significant disordering.[16] Each SEM image was measured against a perfect array with comparable period, image resolution, and number of particles.

As shown in Figure 7.2a, $g(r)$ shows a series of broad peaks that coincide with those calculated for a perfect array. The peak intensities of $g(r)$ decrease with the shell radius, $r/2R_0$, which indicates that the 2D ordering decreases over long distances. The 2 and 1 μm PS arrays exhibit significant correlation beyond the tenth normalized distance, $r/2R_0$. For the 235 nm PS array, the correlation is not evident for $r/2R_0$>5. The κ/κ_0 values, calculated for 2 μm, 1 μm, 580 nm and 235 nm PS arrays, are 1.01, 1.32, 1.70, and 2.59, respectively (Figure 7.2b), which indicates that the 2 μm PS array is nearly perfectly ordered, and the 1 μm array is highly ordered.

The ordering of 2D arrays decreases with the particle size. This is probably due to the fact that the thinner particle arrays are less robust. The ordering of the small size particle 2D arrays may have been disturbed by sample handling.

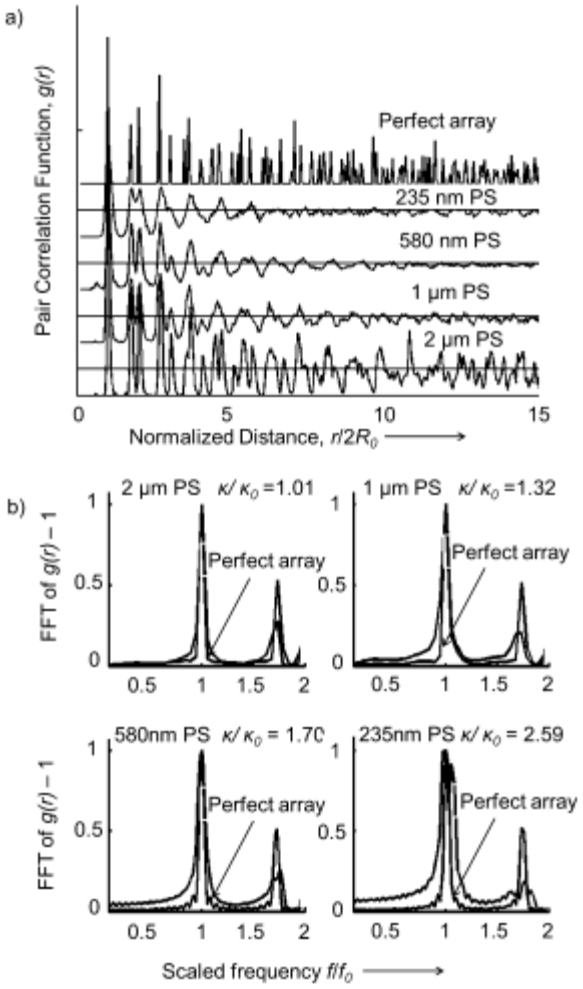

Figure 7.2: Pair correlation function.

a) Curves of g(r) calculated for 235 nm, 580 nm, 1 μm, and 2 μm PS particle arrays shown in Figure 7.1. Horizontal black lines indicate g(r)=1. b) Single-sided power spectra Fourier transforms (FT) of g(r) compared to FT of the corresponding perfectly ordered arrays. The power spectra were scaled to have identical maxima at $f/f_0=1$.

We modified our method to form 2D arrays on thin water films with the needle tip flow technique (Figure 7.3a). After removing the water layer between the 2D array and the substrate, the 2D array can be easily transferred onto a substrate. Figure 7.3 b and c shows photographs of the 580 nm PS 2D arrays prepared on top of a glass and a plastic sheet. SEM images show that the arrangement of 2D particles was also hexagonally close-packed and consisted of multi-domains (Figure 7.3 d and e), which are similar to the morphology of the 2D arrays prepared on bulk water and then transferred onto substrates (Figure 7.1f).

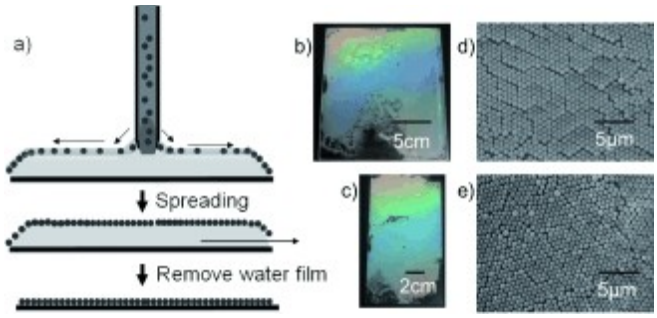

Figure 7.3: Fabrication with substrate transfer

a) Fabrication of a 2D array on a flat substrate coated with a thin layer of water. Photographs of thus prepared 2D 580 nm PS arrays on b) a glass and c) a plastic sheet. SEM images of 580 nm PS 2D arrays on d) a glass and e) a plastic sheet.

Using this approach, we fabricated 2D array patterns that contained patches of particles of different sizes (Figure 7.4). We prepared a 490 nm PS 2D array patch first through the needle tip flow method (Figure 7.4a) and then we used a dispersion of larger PS particles of 580 nm in diameter to form a patch with a larger spacing in the middle (Figure 7.4b). These two particle arrays display different diffraction colors (Figure 7.4d). We can imagine writing patterns of 2D arrays for particular applications in displays, for chemical separations, and sensing.

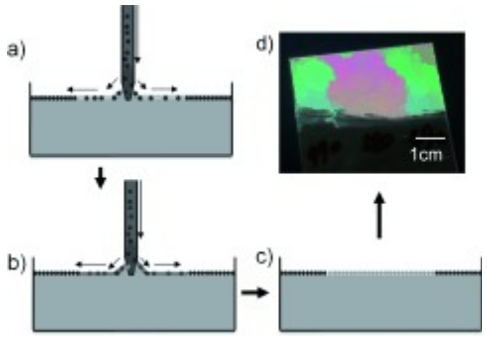

Figure 7.4: Fabrication with two particle diameters.

Fabrication of a 2D array pattern formed with patches of two different particle diameters. a) Spreading of a first particle array on water. b) Spreading of a second particle array. c) Resulting 2D array patterns on water. d) Visually observed diffraction of transferred 2D array pattern on a glass substrate.

Our 2D particle arrays on substrates can be further functionalized and used for sensing applications to visually detect analytes. As shown in Figure 7.5a we fabricated a thin hydrogel film of 2D particles for pH sensing by depositing chitosan (CS, 2 wt %) that is dissolved in a 1 wt % acetic acid aqueous solution on a 2D particle array on a glass slide. We then evaporated the solvents, washed the CS film with a 0.4 M aqueous NaOH solution to neutralize the acid, and cross-linked the hydrogel in 0.5 wt % glutaraldehyde solution for 10 s. After washing with water, we obtained a pH-sensitive 2D PS array hydrogel film (Figure 7.5b). Figure 7.5c shows the SEM image of the 2D particles embedded in the dried CS hydrogel film.

We measured the diffraction in the Littrow configuration by using a six around one reflection probe where we excite with white light the surrounding six fibers and collect the diffracted light with the central fiber. The angle between the probe and the normal to the 2D array sensor was about 32°. Figure 7.5d shows the diffraction spectrum of the 2D array CS films at pH 7 (in pure water) and at pH 5 (in 2-(*N*-morpholino)ethanesulfonic acid, MES buffer solution). At pH 7 diffraction is observed at 535 nm, whereas at pH 5 diffraction occurs at 645 nm. The CS hydrogel swells because of the protonation of its NH_2 groups at pH 5.[18] The CS hydrogel film swelling increases the particle lattice spacing of the 2D array, which red-shifts the diffracted light. Figure 7.5e shows a photograph of the 2D array CS hydrogel film sensors on a mirror surface that reflects the diffracted light.[31] The photograph clearly shows the green and red colors of the diffracted light.

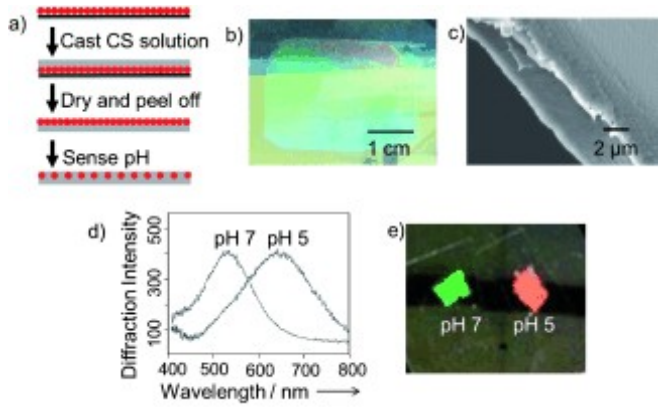

Figure 7.5: pH sensing

a) Preparation of a 2D array CS hydrogel film for pH sensing. The CS solution was poured on the 2D array on a glass slide, followed by drying in air. The 2D array CS hydrogel was peeled off the glass slide, washed with 0.4 M NaOH and water, and then cross-linked. The 2D array hydrogel sensed pH values by swelling and shifting the diffracted light wavelength. b) Photograph of a 2D array CS hydrogel in water. c) SEM image of a 2D array CS hydrogel film. d) Diffraction of a 2D array CS hydrogel film at pH 7 and 5. The measurement was carried out in a Littrow configuration with a measurement angle of about 32° between the probe and the normal to the 2D array. e) Photograph taken at an angle of 32° to the 2D array normal showing the 2D PS array CS hydrogel colors at pH 7 and 5. The 2D array hydrogels were placed on an Al mirror.

In conclusion, we have developed a novel, simple, and efficient approach to rapidly fabricate large-area 2D particle arrays on water surfaces. These arrays can easily be transferred onto various substrates and functionalized for chemical sensing applications.

7.3 EXPERIMENTAL SECTION

Polystyrene (PS) particles with diameters of 490 and 580 nm were synthesized according to a previously reported method.[15] The concentrations of 490 nm PS and 580 nm PS are 15 and 20 wt %, respectively, in water. The PS dispersion and propanol were mixed at a ratio of 2:1 in volume and the mixture was vortexed for 1 min. Then the PS suspension was layered onto a water surface using a syringe pump (Razel A99-FM, Razel Scientific Instruments, Inc.). To transfer the 2D array onto a substrate, we lifted up the pre-placed substrate or drained the water in the container.

The arrangement and morphology of the array was observed by using a scanning electron microscope (SEM, Joel JSM6390LV) after sputter coating a thin layer of Au. Diffraction measurements were conducted at a fixed angle using an Ocean Optics USB2000-UV-VIS spectrometer, a LS-1 Tungsten Halogen Light Source and an R-series Fiber Optic Reflection Probe. The hydrogels were equilibrated in water (pH 7) or in MES buffer solution (pH 5) and then were put onto an Al glass mirror for diffraction measurements. The measurement was carried out in the Littrow configuration with a measurement angle of about 32° between the probe and the normal to the 2D array.

7.4 BIBLIOGRAPHY

[1] Allen, S. and Thomas, E., (**1999)**. *The Structure of Materials.* Wiley.

[2] **Bohn, J.; Ben-Moshe, M.; Tikhonov, A.; Qu, D.; Lamont, D. and Asher, S.** (**2010**). *Charge stabilized crystalline colloidal arrays as templates for fabrication of non-close-packed inverted photonic crystals*, Journal of Colloid and Interface Science 344 : 298-307.

[3] **Cai, Y. and Zhang Newby, B.-M.** (**2010**). *Polymeric microstructure arrays consequence of Marangoni flow-induced water droplets*, Applied Physics A: Materials Science and Processing 100 : 1221-1229.

[4] **Dimitrov, A.; Dushkin, G.; Yoshimura, H. and Nagayama, K.** (**1994**). *Observations of latex particle two-dimensional-crystal nucleation in wetting films on mercury, glass, and mica*, Langmuir 10 : 432-440.

[5] **Jeong, S.; Hu, L.; Lee, H.; Garnett, E.; Choi, J. and Cui, Y.** (**2010**). *Fast and scalable printing of large area monolayer nanoparticles for nanotexturing applications*, Nano Letters 10 : 2989-2994.

[6] **Jiang, P. and McFarland, M.** (**2004**). *Large-scale fabrication of wafer-size colloidal crystals, macroporous polymers and nanocomposites by spin-coating*, Journal of the American Chemical Society 126 : 13778-13786.

[7] **Kim, M.; Im, S. and Park, O.** (**2005**). *Fabrication and structural analysis of binary colloidal crystals with two-dimensional superlattices*, Advanced Materials 17 : 2501-2505.

[8] **Kondo, M.; Shinozaki, K.; Bergstroem, L. and Mizutani, N.** (**1995**). *Preparation of colloidal monolayers of alkoxylated silica particles at the air-liquid interface*, Langmuir 11 : 394-397.

[9] **Li, C.; Hong, G. and Qi, L.** (**2010**). *Nanosphere lithography at the gas/liquid interface: A general approach toward free-standing high-quality nanonets*, Chemistry of Materials 22 : 476-481.

[10] **Li, C.; Hong, G.; Wang, P.; Yu, D. and Qi, L.** (**2009**). *Wet chemical approaches to patterned arrays of well-aligned ZnO nanopillars assisted by monolayer colloidal crystals*, Chemistry of Materials 21 : 891-897.

[11] **Li, F.; Josephson, D. and Stein, A.** (**2011**). *Colloidal assembly: The road from particles to colloidal molecules and crystals*, Angewandte Chemie - International Edition 50 : 360-388.

[12] **Li, F.; Josephson, D. and Stein, A.** (**2011**). , Angew. Chem. 123 : 378-409.

[13] **Li, Y.; Koshizaki, N. and Cai, W.** (**2011**). *Periodic one-dimensional nanostructured arrays based on colloidal templates, applications, and devices*, Coordination Chemistry Reviews 255 : 357-373.

[14] **Pan, F.; Zhang, J.; Cai, C. and Wang, T.** (**2006**). *Rapid fabrication of large-area colloidal crystal monolayers by a vortical surface method*, Langmuir 22 : 7101-7104.

[15] **Reese, C. and Asher, S.** (**2002**). *Emulsifier-free emulsion polymerization produces highly charged, monodisperse particles for near infrared photonic crystals*, Journal of Colloid and Interface Science 248 : 41-46.

[16] **Rengarajan, R.; Mittleman, D.; Rich, C. and Colvin, V.** (**2005**). *Effect of disorder on the optical properties of colloidal crystals*, Physical Review E - Statistical, Nonlinear, and Soft Matter Physics 71.

[17] **Retsch, M.; Zhou, Z.; Rivera, S.; Kappl, M.; Zhao, X.; Jonas, U. and Qin, L.** (**2009**). *Fabrication of large-area, transferable colloidal monolayers utilizing self-assembly at the air/water interface*, Macromolecular Chemistry and Physics 210 : 230-241.

[18] Ruel-Gariépy, E. and Leroux, J. (**2006**). *12*. In: (Ed.), *Chitosan: A Natural Polycation with Multiple Applications*, American Chemical Society.

[19] **Rybczynski, J.; Ebels, U. and Giersig, M.** (**2003**). *Large-scale, 2D arrays of magnetic nanoparticles*, Colloids and Surfaces A: Physicochemical and Engineering Aspects 219 : 1-6.

[20] **Scriven, L. and Sternling, C.** (**1960**). *The Marangoni effects*, Nature 187 : 186-188.

[21] **Vogel, N.; Goerres, S.; Landfester, K. and Weiss, C.** (**2011**). *A convenient method to produce close- and non-close-packed monolayers using direct assembly at the air-water interface and subsequent plasma-induced size reduction*, Macromolecular Chemistry and Physics 212 : 1719-1734.

[22] **Xia, D.; Ku, Z.; Lee, S. and Brueck, S.** (**2011**). *Nanostructures and functional materials fabricated by interferometric lithography*, Advanced Materials 23 : 147-179.

[23] **Xia, Y.; Gates, B.; Yin, Y. and Lu, Y.** (**2000**). *Monodispersed colloidal spheres: Old materials with new applications*, Advanced Materials 12 : 693-713.

[24] **Xie, R. and Liu, X.-Y.** (**2008**). *Electrically directed on-chip reversible patterning of two-dimensional tunable colloidal structures*, Advanced Functional Materials 18 : 802-809.

[25] **Yamaki, M.; Matsubara, K. and Nagayama, K.** (**1993**). *A thin liquid layer on the surface of mercury as a matrix of a flow-mediated two-dimensional assembly of proteins*, Langmuir 9 : 3154-3158.

[26] **Yang, S.-M.; Jang, S.; Choi, D.-G.; Kim, S. and Yu, H.** (**2006**). *Nanomachining by colloidal lithography*, Small 2 : 458-475.

[27] **Yu, J.; Yan, Q. and Shen, D.** (**2010**). *Co-self-assembly of binary colloidal crystals at the air - Water interface*, ACS Applied Materials and Interfaces 2 : 1922-1926.

[28] **Zhang, J.; Li, Y.; Zhang, X. and Yang, B.** (**2010**). *Colloidal self-assembly meets nanofabrication: From two-dimensional colloidal crystals to nanostructure arrays*, Advanced Materials 22 : 4249-4269.

[29] **Zhang, J. and Yang, B.** (**2010**). *Patterning colloidal crystals and nanostructure arrays by soft lithography*, Advanced Functional Materials 20 : 3411-3424.

[30] **Zhang, J.-T.; Wang, L.; Chao, X. and Asher, S.** (**2011**). *Periodicity-controlled two-dimensional crystalline colloidal arrays*, Langmuir 27 : 15230-15235.

[31] **Zhang, J.-T.; Wang, L.; Luo, J.; Tikhonov, A.; Kornienko, N. and Asher, S.** (**2011**). *2-D array photonic crystal sensing motif*, Journal of the American Chemical Society 133 : 9152-9155.

8.0 SPECTROSCOPY INTRODUCTION

8.1 INTRODUCTION

Fluorescence spectroscopy and related techniques are pervasive in many branches of science and are applicable to many different types of chemical systems. Fluorescence measurements can provide a wide range of information and insight into molecular processes, including solvent-solute interaction, and the energetics of donor-acceptor systems. Steady-state and time-resolved spectroscopy play a principle role in the investigations included in Chapters 9, 10 and 11. This chapter presents a brief framework of the fundamental principles of fluorescence spectroscopy.

8.2 STEADY-STATE AND TIME-RESOLVED FLUORESCENCE

Fluorescence measurements can be classified into a steady-state and time-resolved dichotomy. In steady-state techniques a sample is illuminated with a constant illumination source and emission intensity as a function of wavelength or spectrum, is detected. In time-resolved measurements a pulsed light source allows the decay of fluorescence intensity to be recorded. Because fluorescence processes typically occur on the nanosecond time scale, high-speed detection systems and timing electronics are required in time-resolved measurements.

As noted by Lakowicz [2], steady-state observation records an average of the time-resolved phenomena over the intensity decay of a sample, and much of the molecular information is lost during this averaging process. However, many characteristics of a fluorophore can be deduced from features in the steady-state fluorescence. For example, the sensitivity of a fluorophore to solvent polarity can be determined from the Stoke shifts, which are more pronounced in polar solvents.

Time-resolved measurements provide many types of molecular information. For example, macromolecules can exist in more than a single conformation, and the decay time of a bound probe may depend on conformation, with different decay times indicating different conformations. When energy transfer is possible, the relative orientations of energy donors and acceptors can be inferred.

8.3 FLUORESCENCE LIFETIMES AND QUANTUM YIELDS

The fluorescence lifetime and quantum yield are arguably the two most important characteristic parameters for any type of fluorophore. The quantum yield is defined as the number of photons emitted versus the number of photons absorbed; consequently, the brightest fluorophores have quantum yields that approach unity. The fluorescence lifetime is a measure of the amount of time a molecule spends in an excited state before returning to a ground state. Generally, fluorescence lifetimes are on the order of 10 ns. Fluorescence emission is a stochastic process and can be characterized by a radiate rate constant, Γ. The quantum yield and lifetime can be modified by nonradiative processes, k_{nr}, that affect the overall lifetime and quantum yield.

In fluorescence experiments the number of excited molecules, n(t), is not directly measured, but rather fluorescence intensity, which is proportional to n(t), is recorded. Assuming the most elementary case, in which excited state decay processes are first order in the population of the excited state, the decay of the excited state population is given by

$$\frac{dn(t)}{dt} = (\Gamma + k_{nr})n(t)$$

Assuming that Γ and k_{nr} are time independent rate constants, the population of excited state molecules, n(t), decays as $n(t) = \exp(-t/\tau)$ where τ is the fluorescent lifetime and is given by $\tau = (\Gamma + k_{nr})^{-1}$. Because the excited state decay is proportional to the intensity, we can write $I(t) = I_0 \exp(-t/\tau)$, where I_0 is the intensity at time 0. For a single exponential decay, the

lifetime can be directly related to the average time a fluorophore spends in the excited state; however, decays with complex or multi-exponential decay characteristics can be significantly more difficult to interpret.

8.4 FLUORESCENCE QUENCHING

Any process that causes a decrease in fluorescent intensity can be considered a type of quenching. Intensity of fluorescence can be decreased by a variety of mechanisms. One type of quenching is collisional quenching. In this quenching mode, an excited-state fluorophore returns to a ground state during a diffusive encounter with a quenching moiety; however, the fluorophore is not chemically altered during this process. The decrease in fluorescent intensity due to collisional quenching is describe using the Stern-Volmer equation:

$$\frac{F_0}{F} = 1 + K[Q] = 1 + k_q \tau_0 [Q]$$

where K is the Stern-Volmer quenching constant, k_q is the biomolecular quenching constant, τ_0 is the unquenched lifetime, and [Q] is the quencher concentration.

In addition to collisional quenching, a variety of other processes can reduce fluorescence intensity. In static quenching fluorophores may form nonfluorescent complexes with quencher molecules. Quenching can also be due to the attenuation of incident light either by excessive

fluorophore concentration or the presence of an additional absorbing moiety. Additionally, excited state reaction, molecular rearrangements and energy transfer are other mechanisms that produce quenching.

Static and dynamic quenching require the fluorophore and quencher to be in direct physical contact. In collisional quenching, contact between a quencher and a fluorophore in an excited state returns the fluorophore to the ground state via a non-radiative process. In static quenching a nonfluorescent complex is formed between a quencher and fluorophore. Excited state stabilization due to the formation of charge-transfer complexes has been studied extensively. Nonpolar solvents can enhance fluorescent emission intensity from excited charge-transfer complexes called an exciplexs. In a polar solvent, exciplex emission is quenched due to stabilization of the exciplex, which lowers the excited state energy. Model systems in which an electron donor and electron acceptor are connected by a molecular bridge have been particularly useful in understanding the dynamics of charge transfer. In Chapter 11 synthetic control of stereo-centers allows modification of the donor-acceptor geometry in order to explore the role solvents play in an electron transfer reaction.

8.5 RESONANCE ENERGY TRANSFER

In contrast to dynamic quenching and complex formation, which require close proximity between a fluorophore and a quenching moiety, resonance energy transfer (RET) is a through-space interaction that can occur over longer distances. RET mechanisms decrease intensity of a “donor” chromophore by transferring excited state energy to an “acceptor” moiety, which would then undergo its own excited state relaxation processes. This process intrinsically involves an

excited state. A prerequisite of RET is some degree of spectral overlap between the emission spectrum of an energy donor and the absorption spectrum of an energy acceptor. There is no intermediate photon in RET. Donor photons do not participate in RET, as this process is not dependent on the absorption of donor photons by the acceptor. The rate of energy transfer, k_t, between donor and acceptor is determined by the donor-acceptor spectral overlap and distance. The rate is described by

$$k_t = \frac{1}{\tau_d}\left(\frac{R_0}{r}\right)^6$$

where r is the donor to acceptor distance, R_0 is the Förster distance, and τ_d is the lifetime of the donor in the absence of energy transfer. Förster distances typically range from 15 to 60 Å and are determined, in part, by the spectral overlap. The extent of donor quenching can be used to determine donor to acceptor distance.

8.6 TIME-RESOLVED LIFETIME MEASUREMENTS

Time-resolved measurements frequently provide information that is not available in steady-state measurements. An often cited example is RET between a donor-accept system in which the donor emission is observed to be quenched 50%. It is impossible to tell from the steady-state spectra if this level of quenching is due to half of the donor being completely quenched, all of the donor being quenched 50%, or some combination of these two extremes. These cases are easily distinguished by measurement of the donor lifetime. The time-resolved measurements presented

in the following works (Chapters 9, 10 and 11) are based on the time-domain method. In this method a short pulse of light, significantly shorter than the fluorescent lifetimes to be measured, is used to excite a sample. The time-dependent intensity profile is measured using fast photon counting electronics, which are synchronized to the excitation pulse. Fluorophores emit at random times during the intensity decay. Some fluorophores emit quickly following the excitation pulse while others emit after a significantly longer time delay. The intensity decay is formed by collecting a statistical average of many photon emissions. Fitting the intensity decay to an exponential allows determination of the excited state lifetime. However, care must be taken when interpreting intensity decays that exhibit multi-exponential decay, as the amplitude and lifetime fitting parameters are interconnected with many possible solutions capable of satisfactorily fitting experimental data .

When conducting time-resolved fluorescence measurements, significant effort must be made in the fitting of intensity decay to lifetime models. Elucidation of this point is facilitated by examining the nature of the time-resolved intensity signal.

8.6.1 Intensity Decay Laws

Since the 1970s, maturation of time-resolved fluorescence techniques has included numerous methods of data analysis. An early analysis method that is still widely used today is the nonlinear least squares procedure (NLLS). In NLLS the level of consistency of a model function, typically composed of 1-3 exponentially decaying components, to experimental data is quantified. If the model function is found to be satisfactorily consistent with the experimental data, best estimates

for parameter values are assigned. More recently algorithms using method-of-moments (MEM) analysis have been deployed, which allow complex decay profiles to be fit to distributions of lifetimes.[1; 3-5]

8.6.2 Multi-Exponential Decay

By far the most common model used in fitting simple to moderately complex fluorescence decays is the multi-exponential model. This model has the form

$$I(t) = \sum_{i=1}^{n} \alpha_i \exp(-t/\tau_i)$$

where τ_i and α_i represent the decay times and amplitude components respectively. The physical meaning of the model parameters depends on the system. In Chapter 11 an n = 2 model can be used to relate this equation to the forward and backward charge transfer rate constants. When applied to a mixture of single lifetime fluorophores each τ_i corresponds to the lifetime of an individual component.

8.6.3 Lifetime Distributions

For some systems, the intensity decay profile observed is the result of a distribution of lifetime components, not a combination of discrete lifetimes. For example, fluorophores in a mixed solvent system may be exposed to a range of solvent environments. Variability in the number of polar solvent molecules in the immediate fluorophore environment may result in different decay

intensities. Additionally, due to the uncertainty in estimated parameter values, NLLS is not suited to the analysis of multi-exponential decays containing closely spaced decay times. As is demonstrated in Chapter 11, lifetime distribution fitting procedures can be used to partially recover these closely spaced lifetimes.

8.7 APPLICATION OF FLUORESCENCE

Lanthanide metal ions display well-defined spectral emission lines that have long emission lifetimes in aqueous solutions. The lanthanide emission results from nominally forbidden transitions from the 4f orbitals; consequently, the emissive rate is very low, resulting in long emission lifetimes typically in the range of 0.5 to 3 ms, and absorption coefficients are very low, less than 10 $M^{-1}cm^{-1}$. Despite these limitations lanthanides are attractive fluorophores for detection applications because the lanthanide emission has an extremely narrow line spectral profile. In most applications, the low absorption cross-section requires lanthanides to be complexed with some type of sensitizer. In Chapter 10 we show that ZnS nanoparticles can act as an excitation antenna for a variety of different lanthanides that can be doped into the material.

Inorganic semiconductor nanoparticles (NP) exhibit a range of interesting material characteristics. The bandgap can be tuned by varying the NP size. The net charge and solubility can be modified by exchanging the surface capping ligands used to stabilize the inorganic core of the NP. In Chapter 9, by studying the fluorescence quenching, we show that the direction of the electric field created by electrostatic assemblies of oppositely charged cadmium selenide and cadmium telluride nanoparticles can significantly alter the rate of photo-induced charge transfer between the donor and acceptor nanoparticles.

In Chapter 11, photo-induced electron transfer is studied using bis-peptide molecules as semi-rigid donor-bridge-acceptor scaffolds. Here, the importance of electron tunneling through non-bonded contact is examined using steady-state fluorescence and lifetime distribution analysis.

8.8 BIBLIOGRAPHY

[1] **Dudewicz, E. J. and Van Der Meulen, E. C.** (**1981**). *Entropy-based tests of uniformity*, Journal of the American Statistical Association 76 : 967-974.

[2] Lakowicz, J. R., **2007**. *Principles of Fluorescence Spectroscopy*. Springer US, .

[3] **Livesey, A. and Brochon, J.** (**1987**). *Analyzing the distribution of decay constants in pulse-fluorimetry using the maximum entropy method*, Biophysical Journal 52 : 693.

[4] **Merola, F.; Rigler, R.; Holmgren, A. and Brochon, J. C.** (**1989**). *Picosecond tryptophan fluorescence of thioredoxin: evidence for discrete species in slow exchange*, Biochemistry 28 : 3383-3398.

[5] **Vincent, M.; Brochon, J. C.; Merola, F.; Jordi, W. and Gallay, J.** (**1988**). *Nanosecond dynamics of horse heart apocytochrome c in aqueous solution as studied by time-resolved fluorescence of the single tryptophan residue (Trp-59)*, Biochemistry 27 : 8752-8761.

9.0 ELECTRON TRANSFER AND FLUORESCENCE QUENCHING OF NANOPARTICLE ASSEMBLIES

Author list: Mingyan Wu, Prasun Mukherjee, Daniel N. Lamont and David H. Waldeck

Author contribution: The author of this dissertation contributed to the photophysical characterization of the assemblies, interpretation of the results and the preparation of the manuscript. This work has been published as *J. Phys. Chem. C* ***2010*** *114, 5751*

9.1 INTRODUCTION

Motivated by the increasing worldwide demand for clean energy resources, an effort is being made to develop relatively cheap and highly efficient solar cells.[7; 33] Bulk heterojunction (BHJ) solar cells, which are formed by the nanoscale phase separation of organic materials, are one promising new platform for the development of low-cost photovoltaic (PV) technology;[25; 51; 77] however, the power conversion efficiency of BHJ solar cells is low compared to that of silicon-based p−n junction solar cells. The highest certified efficiency for BHJ solar cells is now in the range of 6−7%, whereas the suggested maximum efficiency is in the range of 10−12%.[22; 61] Improved efficiencies should be realized by better optimizing

energy levels of the donor and acceptor materials, improving the charge transport in the donor−acceptor blend, improving charge separation yields at the phase boundaries, and better limiting recombination losses.[61] The formation of composites of organic conductors with inorganic nanoparticles (NPs) is one possible solution to this challenge. Because of their size-dependent electronic and optical properties,[3; 11] inorganic semiconductor NPs have shown great promise for many applications such as photovoltaic cells,[43; 44; 59; 66] bioimaging,[1; 10; 14; 48] sensing/detection,[20; 28] light-emitting diodes (LEDs), [62; 65] lasers,[6; 35] etc. The worldwide scientific research in this area has grown exponentially because the chemical synthesis of nanometer-sized crystals with controlled size and shape is relatively simple and inexpensive,[53; 57; 76] and the NPs are amenable to further synthetic modification. Thus, they can serve as building blocks to prepare larger and more complex architectures, e.g., NP molecules, two-dimensional arrays, and three-dimensional assemblies. The properties of these nanoscale and larger assemblies depend on the properties of the individual NPs and on the chemical, electronic, and magnetic coupling between them.[49; 63; 69; 71; 78]

Controlling the charge transfer between semiconductor NPs in assemblies[16; 26] is essential for improving the performance of photovoltaic cells[46] and LEDs.[27] For example, CdS,[36] CdSe,[56] and PbS[54] NPs, among others, have been used as light-absorbing sensitizers for large band gap metal oxide materials (TiO_2, SnO_2). These semiconductor NPs have been shown to enhance the metal oxide's photoelectrochemical and photocatalytic activities by absorbing visible photons and injecting electrons (or holes) into the metal oxide. Recent reports of multiple exciton generation (MEG) by one absorbed photon, in some NPs, is one exciting new phenomenon that is unique to these nanomaterials and offers a

mechanism for dramatically improving the efficiency of NP-based solar cells.[18; 60] Efficient charge transfer requires strong electronic coupling between the semiconductor NPs and the metal oxide, and efficient charge separation requires favorable energetics (band alignment) to inhibit back electron transfer.[21; 47; 50; 70; 74] Generally, closely packed assemblies of NPs may be obtained in different ways, covalently or noncovalently, including drop-casting,[5; 49] Langmuir methods,[24] cross-linking precipitation,[12; 38] and stepwise self-assembly.[9; 41] The exploitation of electrostatic interactions has proved to be a simple, effective approach for generating organized assemblies of charged NPs,[23; 31] and this latter approach is used here.

Interfacial photoinduced charge transfer to metal NPs[32; 80] or dye/chromophore molecules to semiconductor NPs has been extensively investigated.[26; 58; 64] Except for the previously mentioned sensitization of TiO_2 by NPs,[36; 54; 56] core−shell materials, [34] and nanorod heterostructure materials,[17; 42] the charge transfer between semiconductor NPs has drawn little attention, especially CdSe and CdTe, which are otherwise extensively studied. Recently, Gross et al. studied the charge separation between thioglycolic acid (TGA) capped CdTe and CdSe NP aggregates, achieved by the incorporation of divalent Ca^{2+} ions between them.[23] Like that work, this study investigates charge transfer between CdSe and CdTe NPs that have a type II band alignment. Instead of inducing association of similarly charged NPs with divalent Ca^{2+} ions, the charge transfer assembly is formed by the spontaneous self-assembly of the two oppositely charged NPs and can be manipulated by variation of their surface charge. The NP compositions and sizes are chosen so that energy transfer quenching is minimized and the charge transfer can be followed by the

photoluminescence (PL) quenching and lifetime shortening of the CdTe NPs by the CdSe NPs. The magnitude of the PL quenching and lifetime shortening was found to depend on the interparticle distance, relative NP sizes, and direction of the electric field created by the surface charges.

9.2 EXPERIMENTAL DETAILS

9.2.1 Materials and Methods

Selenium powder (99.999%), tellurium powder (99.999%), cadmium chloride ($CdCl_2$; 99%), sodium borohydride ($NaBH_4$; 98%), hexadecylamine (HDA; 99%), trioctylphosphine (TOP; 97%), trioctylphosphine oxide (TOPO; 90%), CdO (99.999%), 3-mercaptopropionic acid (MPA; 97%), *N*,*N*-dimethyl-2-aminoethanethiol hydrochloride (DEA; 95%), *N*,*N*,*N*-trimethyl-1-dodecylammonium chloride (TDA; 99%), and *N*,*N*,*N*-trimethyl-2-aminoethane chloride (CEA; 99%) were purchased from Aldrich. *N*,*N*,*N*-trimethyl(11-mercaptoundecyl)ammonium chloride (TMA; 98%) was purchased from ProChimia Surfaces (www.prochimia.com). See Figure 9.1 for the structures of these compounds. All reagents and solvents were used as received. Water used in all experiments was purified by a Barnstead Nanopure system, and its resistance was 18.2 MΩ-cm at 25 °C.

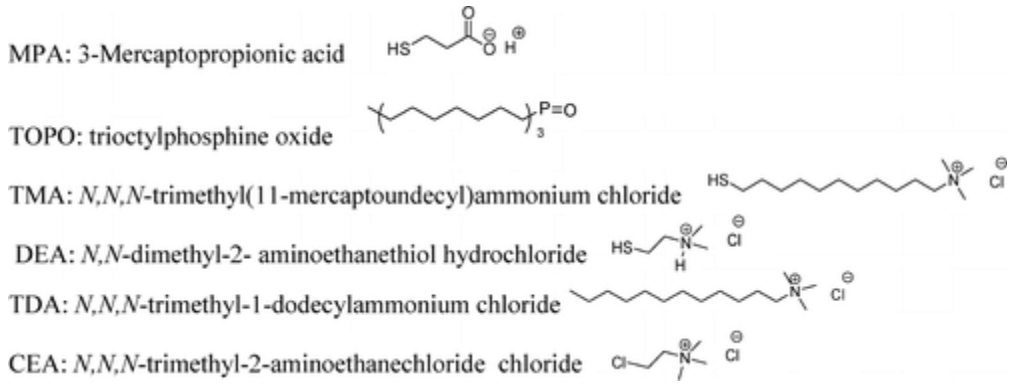

Figure 9.1: Abbreviations, definitions, and structures

9.2.2 CdSe NP Synthesis and Ligand Exchange

TOPO-capped CdSe nanoparticles were prepared in a manner similar to a previously published procedure.[53; 55] For a typical synthesis of CdSe nanoparticles, 0.0514 g (0.40 mmol) of CdO, 0.1929 g (0.80 mmol) of HDA, and 3.8668 g (10.0 mmol) of TOPO were loaded into a 25 mL three-neck round-bottom flask. The mixture was heated to 300 °C under an Ar flow until CdO was dissolved. A selenium stock solution (0.0787 g/1.0 mmol of selenium powder dissolved in 4 mL of TOP) was then swiftly injected into the reaction flask. After the injection, nanocrystals were allowed to grow at 280 °C until they reached the desired size. Highly luminescent TOPO-capped CdSe NPs in a nonaqueous medium can be readily transferred to water by the following procedure.[52; 68] About 20 mg of freshly prepared CdSe nanocrystals was precipitated from toluene solution by adding methanol and then isolated by centrifugation. The collected NPs were redissolved in chloroform. For preparing TMA-CdSe

NPs, 2 mg of TMA was dissolved in 3 mL of chloroform and then added to the TOPO-CdSe solution and the resulting solution stirred at room temperature in the dark for 1 h. The TMA-CdSe NPs were gradually precipitated out of solution and then redispersed in water, providing a clear homogeneous dispersion of NPs. The dispersion was purified by using three cycles of concentration/dilution with an Ultrafree centrifugal filtration device (Millipore, MWCO 10,000). These procedures should eliminate soluble organics and excess free ligands from the solution and provide homogeneous aggregate-free NP dispersions that are ready for further use. To obtain DEA-CdSe NPs, 50 mg of DEA was dissolved in 50 μL of water and added into the TOPO-CdSe chloroform solution and the resulting solution stirred at room temperature in the dark for 1 h. The surface-modified CdSe NPs were transferred into water and subsequently purified in a manner similar to that used for the TMA-CdSe NPs. For preparing MPA-CdSe NPs, 20 mg of TOPO-CdSe NPs and 100 μL of MPA were added into 3 mL of DMF. The mixture was heated to ~60 °C in an oil bath for 2 h under an inert atmosphere to get a clear solution. Potassium *tert*-butoxide (~2 wt %) in DMF was added into the mixture to precipitate MPA-CdSe NPs. The obtained CdSe NPs were collected by centrifugation and purified by ultrafiltration.

9.2.3 CdTe NP Synthesis

CdTe NPs were synthesized in aqueous solution, as described in a previously published procedure.[57; 75] The surface charges were controlled to be either negative, by using MPA as the capping ligand, or positive, by using DEA as the capping ligand. For example, MPA-CdTe NPs, typically, were prepared as follows. First, 50.8 mg (0.4 mmol) of tellurium powder and 37.8 mg (1 mmol) of $NaBH_4$ were loaded into a 25 mL two-necked flask and connected to a Schlenk

line. Air was pumped off and replaced with Ar. A 10 mL volume of distilled water was added through a syringe, and the reaction mixture was heated at 80 °C for 30 min to get a deep red clear NaHTe solution. Then an aqueous solution containing 0.2 mmol of $CdCl_2$ and 0.34 mmol of MPA was adjusted to pH 11.9 by adding 0.1 M NaOH solution dropwise. This solution was put into a three-neck flask with a condenser attached and connected to the Schlenk line. Air was pumped off and replaced with Ar, and freshly prepared NaHTe solution (0.01 mmol) was injected through a syringe at room temperature. The reaction mixture was heated to reflux (100 °C), and the timing was started when the temperature reached 100 °C. Both types of modified NPs were purified by ultrafiltration in a manner similar to that used for the CdSe Nps.

The spectroscopic information for the CdTe and CdSe NPs used in this study is summarized in Table 2.

Table 2: First excitonic Peak and PL Peak of NPs

Sample	**1st excitonic peak in UV-vis (nm)**	**PL peak (nm)**
MPA-CdTe-1	579	638
DEA-CdSe-1	519	Quenched
TMA-CdSe	524	Quenched
MPA-CdTe-2	660	732
DEA-CdSe-2	456	Quenched
DEA-CdTe	575	610
MPA-CdSe	520	Quenched

Note that the the postfix numbers 1 and 2 in the first column of table 1 are used to distinguish NPs of the same composition but different sizes.

9.2.4 Steady-State Spectroscopy

Steady-state absorption spectra were measured on an Agilent 8453 spectrometer, and the steady-state emission spectra were measured on a Horiba J-Y Fluoromax 3 fluorescence spectrophotometer.

9.2.5 Time-Dependent Fluorescence Spectroscopy

The time-resolved fluorescence data were collected using the time-correlated single photon counting (TCSPC) method.[39] The instrument response function was measured using a sample of colloidal $BaSO_4$. The samples were excited at 440 nm using a diode laser (PIL043, ALS GmbH) and/or a 585 nm synchronously pumped dye laser at a 1 MHz repetition rate, and 6000 counts in the peak channel were collected for each sample. Experiments were also performed with a 300 kHz repetition rate. Lifetime values were found to be nearly identical to those collected at a 1 MHz repetition rate in all the systems studied. The fluorescence decay curves were fit to a sum of exponentials by a convolution and compare method using IBH-DAS6 analysis software.[40]

9.2.6 Dynamic Light Scattering (DLS) and ζ Potential Measurements

DLS measurements were performed at room temperature in a 90° geometry and analyzed by using particle sizing software with a 532 nm laser (Brookhaven Instrument Co.). The electrophoretic mobility measurements were performed on the same instrument at room temperature with an electrical field strength of 10 V/cm by using a Zeta Plus ζ potential analyzer.

9.3 RESULTS AND DISCUSSION

9.3.1 Formation of Aggregates Through Electrostatic Interaction

As shown in Figure 9.2, MPA-capped CdTe NPs in water show a first excitonic peak at 579 nm (implying a size of about 3.5 nm in diameter[12] and the corresponding PL peak occurs at 638 nm (excitation wavelength at 400 nm). TOPO-capped CdSe NPs, which do not dissolve in water, show a first excitonic peak at 518 nm in toluene (implying a size of about 2.5 nm in diameter) and a corresponding photoluminescence peak at 531 nm.[12] After ligand exchange with TMA or DEA, the CdSe NPs can be completely transferred into water and the absorbance maximum shifts from 518 to 524 nm for TMA and from 518 to 519 nm for DEA. Other than this shift, the spectra do not change significantly. The photoluminescence of the TMA-CdSe and the DEA-CdSe NPs in water is strongly quenched, as compared to that for the TOPO-capped NPs in toluene. The quenching is attributed to trapping states created during the ligand exchange process

of CdSe NPs with thiol molecules, as has been reported previously.[2] The absorption spectrum of CdSe shows a very small overlap with the photoluminescence spectrum of the CdTe, so that electronic energy transfer from the CdTe NPs to the CdSe NPs is negligible (see the Supporting Information [75]).

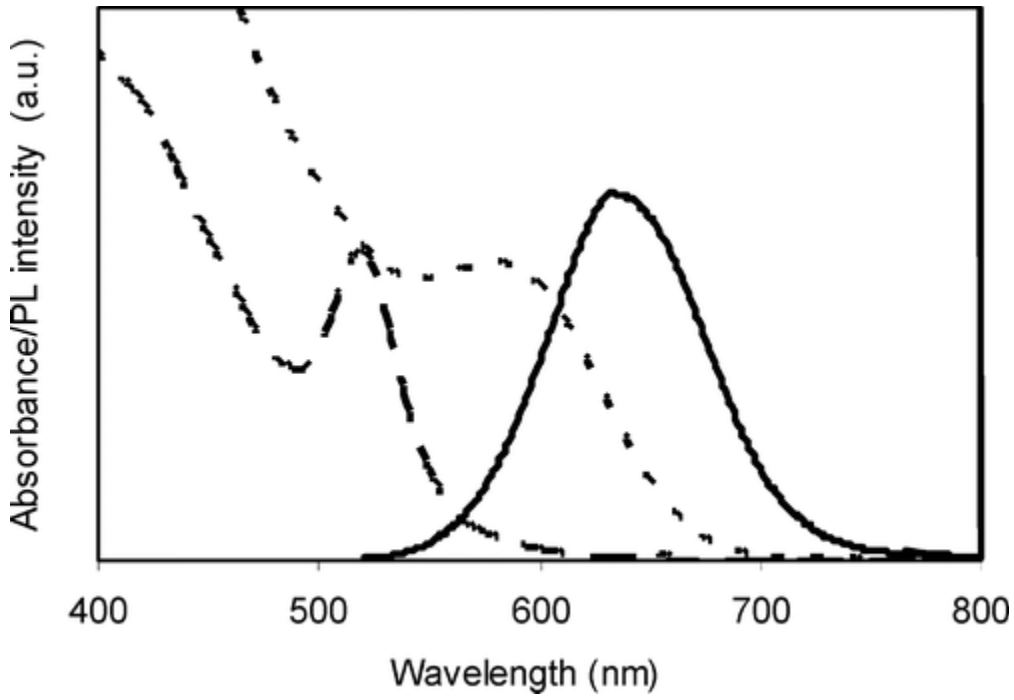

Figure 9.2: Absorption and PL spectra of MPA-capped CdTe and TMA-capped CdSe NPs

Representative absorption and PL spectra of MPA-capped CdTe and TMA-capped CdSe NPs used in this work: from left to right, CdSe absorbance in water after ligand exchange with TMA (− − −), CdTe absorption in water (---), CdTe fluorescence in water (—). The quenched CdSe PL is not shown.

Because of mutual electrostatic attraction, the negatively charged MPA-CdTe NPs and positively charged TMA-CdSe NPs are expected to form aggregates under the appropriate electrolyte solution conditions. The pK_a value of DEA is about 10.5, so that the DEA-capped CdSe is expected to be positively charged in aerated water (pH 6.6), and it can electrostatically interact with the negatively charged MPA-CdTe. The aggregation was quantified by titrating the positively charged TMA- or DEA-capped CdSe NPs into aqueous solutions of negatively charged MPA-capped CdTe NPs, for which the CdTe final concentration was fixed at 0.9×10^{-6} M. Absorption spectra of these solutions show excitonic peaks of both CdSe and CdTe NPs and are a superposition of the individual nanoparticle spectra, indicating that the electronic transitions of the NPs remain isolated on the individual particles after mixing. DLS experiments confirmed the presence of aggregates upon addition of TMA-CdSe (or DEA-CdSe) NPs to the CdTe NP solutions. With increasing concentration of CdSe, the average diameters of the aggregates grew from below 10 nm to on the order of 100 nm and reached a size on the order of 1−2 μm as the molar ratio of CdSe to CdTe approached 0.5 for the larger TMA-CdSe NPs and 1 for the smaller DEA-CdSe NPs. With a further increase in the concentration of positively charged CdSe NPs, the aggregate size decreases to about 100 nm. See the Supporting Information [75] for these data in tabular form.

ζ potential measurements (Figure 9.3) corroborate the DLS results. The initial ζ potential for a solution of negatively charged MPA-CdTe NPs was about −21 mV. As the concentration of TMA-CdSe NPs increased the ζ potential increased to about +1.1 mV at a CdSe/CdTe molar ratio of 0.5 and then to about +28 mV at a molar ratio of 3. The addition of DEA-CdSe NPs to CdTe NP solutions causes a similar trend but has a less sharp transition and asymptotes toward a smaller positive potential.

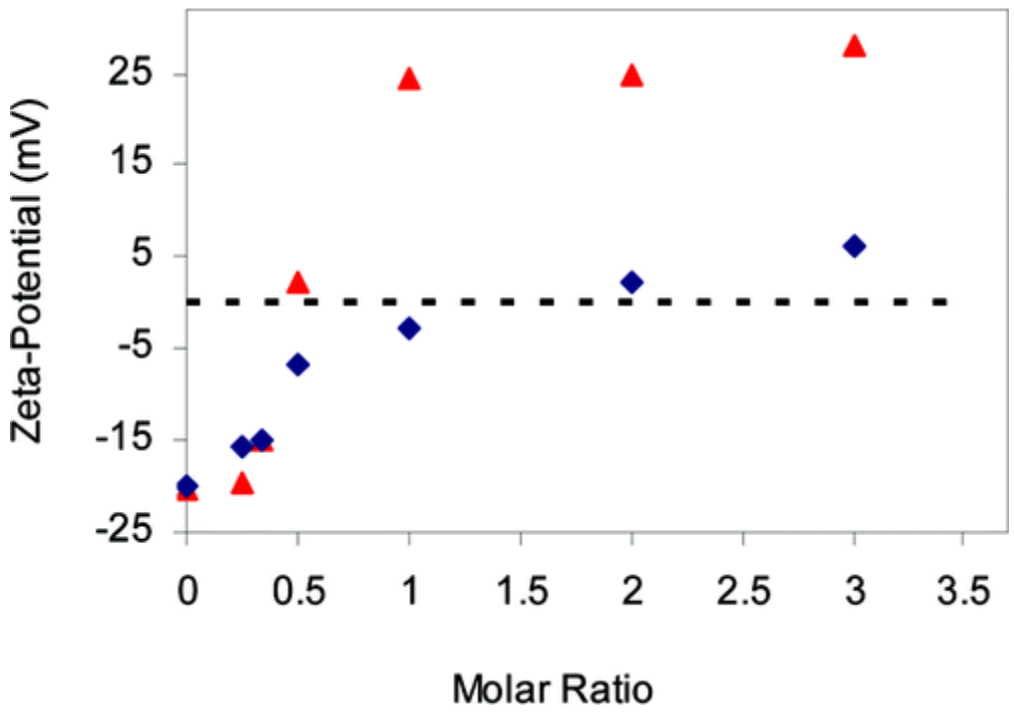

Figure 9.3: ζ potential measurements of assemblies of CdSe/CdTe

ζ potential measurements of assemblies of CdSe/CdTe with increasing concentration of positively charged TMA-CdSe (red ▲) or DEA-CdSe (blue ◆). The dotted line indicates 0 mV. The concentration of the MPA-CdTe NP is fixed at 0.9 μM.

These data indicate that as the proportion of positively charged TMA-CdSe NPs to negatively charged MPA-CdTe NPs increases, aggregates form in the solution and the ζ potential approaches zero. The concentration at which the aggregates are close to being neutral corresponds to the concentration at which DLS gave the largest sizes. As the CdSe NP concentration increases beyond this “isoelectric” point, the size decreases again because the aggregates again have a net charge (albeit of opposite sign) that acts to inhibit the stability of large aggregates. At a molar ratio of 3, the DLS results give an effective diameter of ∼130 nm for the TMA-CdSe aggregates and ∼80 nm for the DEA-CdSe aggregates. The sharper ζ potential change that is observed for TMA-CdSe may occur because more TMA ligands can be loaded onto the CdSe NP surface as compared to DEA (because the longer TMA ligands reduce electrostatic repulsion between neighboring ligands). This explanation can be rationalized from the ζ potential values of pure TMA-CdSe NP solutions, +27 mV, and pure DEA-CdSe NP solutions, about +13 mV.

9.3.2 Aggregation-Induced Self-Quenching Due to Interparticle Interaction

Although the poor spectral overlap inhibits energy transfer quenching of CdTe NPs by CdSe NPs, self-quenching of CdTe NPs can occur. Self-quenching is well-known for NP systems where assembly in solution or the formation of a solid NP film from solution takes place, and it can be attributed to electronic energy transfer from the smaller NPs to the larger NPs in the NP size distribution.[15; 30; 37; 67] For a self-quenching NP solution, a red shift and quenching of the photoluminescence can be observed as the NPs aggregate. To test for the

importance of self-quenching, the surfactant TDA, which has a positive headgroup and a length similar to that of the TMA coating on the CdSe NPs, was titrated with a solution of the negatively charged MPA-CdTe NPs. A 0.9×10^{-6} M solution of MPA-CdTe NPs in water exhibits a strong photoluminescence peak around 638 nm; as TDA surfactant is added to the solution, the emission peak red shifts to 672 nm. Furthermore, the photoluminescence intensity quenches by a factor of 2 as the TDA/CdTe molar ratio increases from 0 to about 1 (assuming there are about 350 MPA ligands per CdTe NP) and is saturated at this value for higher molar ratios (see Figure 9.4b).[45] See the Supporting Information [75] for PL spectra. A similar phenomenon is observed if the CdTe NP solution is titrated with TMA-capped CdSe NPs; the emission's peak wavelength red shifts and saturates at a value of 665 nm at high molar ratios (see Figure 9.4a). We note that the red shift first appears to reach 671 nm at an intermediate mole ratio (1:3 and 1:2 CdSe/CdTe) and then blue shifts back to 665 nm for a CdSe/CdTe molar ratio of 3. Figure 9.4b shows that the final photoluminescence intensity quenches by a factor of about 2. The similarity of the red shift and PL quenching of the CdTe emission by the TMA-CdSe NPs and TDA molecules indicates that the changes observed in the emission spectra arise from the same self-quenching mechanism and is caused by interparticle interactions between CdTe NPs. [15; 30; 37; 67] Other than driving the aggregation of CdTe NPs, the presence of TMA-CdSe NPs does not provide a significant new nonradiative pathway for quenching.

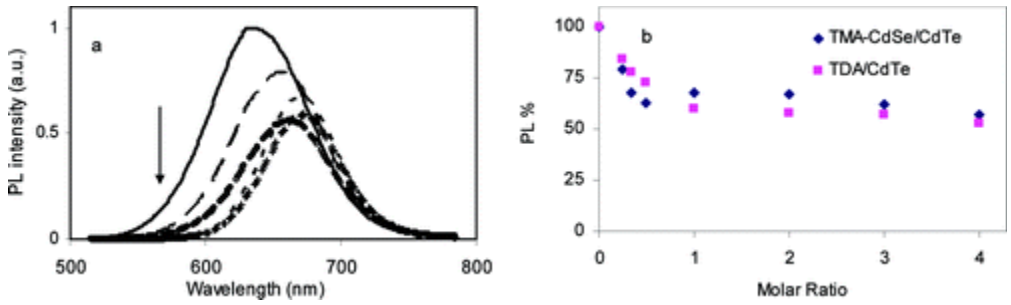

Figure 9.4: PL spectra and relative PL intensity of MPA-CdTe assemblies with increasing concentration of TMA-CdSe

(a) PL spectra of assemblies of MPA-CdTe in water with increasing concentration of TMA-CdSe, as compared to the pure MPA-CdTe NP concentration (0.9×10^{-6} M). The traces are pure MPA-CdTe NP solution (—) and TMA-CdSe/MPA-CdTe at molar ratios of 1:4 (− − −), 1:3 (---), 1:2 (+ + +), and 3:1 (○○○). The cases of 1:1 and 2:1 molar ratios are not shown for clarity. (b) Relative photoluminescence intensity of MPA-CdTe NP aggregates as a function of increasing molar ratio of TMA-CdSe/MPA-CdTe and TDA/MPA-CdTe. Error bars are small and not shown.

9.3.3 Charge Transfer Process from CdTe to CdSe NPs

As shown above, the TMA-CdSe NPs, with their 11-methylene-thick surface coating, behave as a surfactant that induces aggregation and self-quenching (a factor of 2) of the MPA-CdTe NPs. Here we explore how the photoluminescence quenching of the MPA-CdTe NPs depends on the thickness of the organic surface coating of the CdSe NPs, the relative energetics of the NPs, and the direction of the interparticle electric field.

9.3.4 Interparticle Distance Dependence

In contrast to the weak (<50%) photoluminescence quenching of the MPA-CdTe NPs by TMA-CdSe NPs, aggregates of MPA-CdTe NPs with DEA-CdSe NPs (containing only two methylenes) give rise to a very significant (>98%) quenching (see Figure 9.5). For a molar ratio of DEA-CdSe to MPA-CdTe that is less than 1, the PL intensity is quenched by about 30−40% and the peak position is only slightly red-shifted. As the molar ratio increases to 2, the PL intensity is quenched by more than 75% and the peak red shifts to 665 nm, and when the molar ratio increases to 3 or larger, the PL intensity is quenched by more than 90% and the peak emission wavelength shifts back to 656 nm.

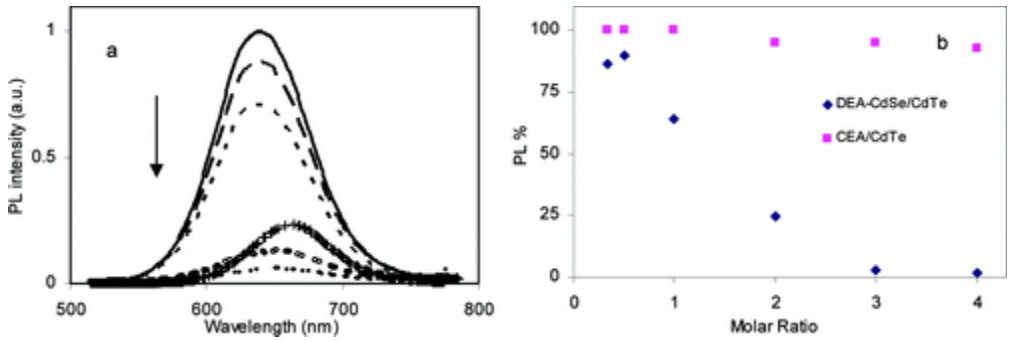

Figure 9.5: PL spectra of MPA-CdTe NPs in water with increasing DEA-CdSe concentration (a) Photoluminescence spectra of MPA-CdTe NPs in water with increasing DEA-CdSe/MPA-CdTe ratio, compared to the pure MPA-CdTe NP solutions (0.9×10^{-6} M). From top to bottom, the traces are pure MPA-CdTe NP solution (—) and DEA-CdSe/MPA-CdTe at molar ratios of 1:2 (− − −), 1:1 (---), 2:1 (+++), 3:1 (○○○), and 4:1 (◇◇◇). The intensity of the 3:1 and 4:1 spectra has been magnified by 5- and 4-fold, respectively, for clarity. (b) Relative photoluminescence intensity of MPA-CdTe NPs with increasing molar ratio of DEA-CdSe/MPA-CdTe and CEA/MPA-CdTe. Error bars are small and not shown.

The quenching of MPA-CdTe NP photoluminescence by DEA-CdSe NPs was found to be reversible. If 0.5 M NaCl was added to a solution of MPA-CdTe NPs, the PL peak remained in the same spectral position as the original peak and a small amount of quenching (~30%) was observed (Figure 9.6a). Subsequent addition of DEA-CdSe NPs, to create a molar ratio of 4:1 with MPA-CdTe, did not induce more significant changes. Similarly if a high concentration of NaCl is added into a solution of DEA-CdSe/MPA-CdTe, the emission's peak wavelength blue shifts back to the original CdTe peak position and the PL intensity recovers to the value found for a NaCl containing solution of MPA-CdTe. These results imply that the NPs do not degrade upon DEA-CdSe addition, nor do they cluster nonspecifically as a result of a high ionic strength of the solution. In addition, this experiment confirms that the close proximity of DEA-CdSe is driven by electrostatic attraction and is required for efficient photoluminescence quenching.

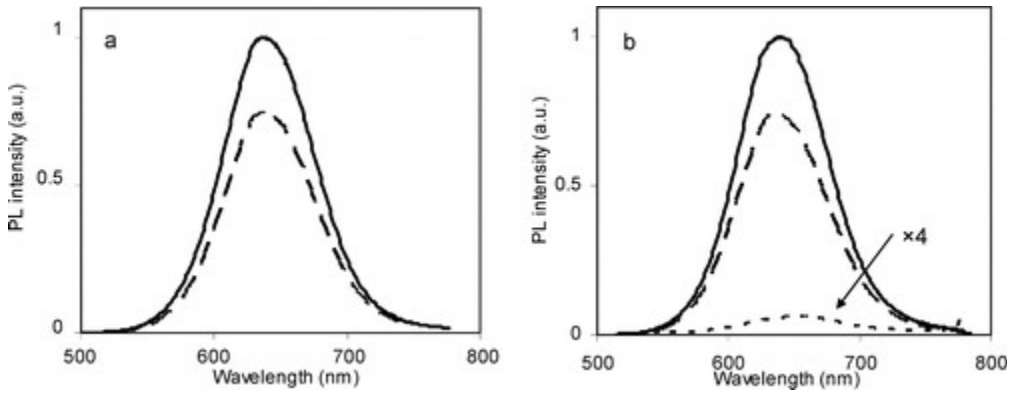

Figure 9.6: PL spectra of MPA-CdTe NP with the addition of quencher NPs

(a) Photoluminescence spectra for a pure MPA-CdTe NP solution (0.9×10^{-6} M) (—) and MPA-CdTe NPs in 0.5 M NaCl solution (− − −). (b) Photoluminescence spectra of a pure MPA-CdTe NP solution (0.9×10^{-6}M) (—), of DEA-CdSe/MPA-CdTe at a molar ratio of 4:1 in 0.5 M NaCl solution (− − −), and of DEA-CdSe/MPA-CdTe aggregates at a molar ratio of 4:1 in water (---). The intensity of CdSe/CdTe at a molar ratio of 4:1 is magnified by 4-fold for clarity.

As a control experiment MPA-CdTe NPs were titrated by CEA, which has a chain length similar to that of DEA and a positive headgroup like that of DEA. This experiment showed that the photoluminescence spectra of CEA/MPA-CdTe do not change significantly (see the Supporting Information [75]). A plot of the relative PL intensities of DEA-CdSe/MPA-CdTe NPs and CEA/MPA-CdTe NPs (see Figure 9.5b) reveals the dramatic difference in quenching efficiencies. The extent of aggregation and ζ potential changes in CEA/MPA-CdTe NP solutions are very small. Clearly, the DEA-CdSe NPs are necessary to observe significant PL quenching, and CEA molecules do not play a role in either inducing the aggregates or PL quenching.

In another control experiment the dendrimer PAMAM 2G (Dendritech, Inc.), which has no visible chromophore, was used to induce aggregates of MPA-CdTe NPs. PAMAM 2G is 2.9 nm in diameter and has 16 NH_2 surface groups which should be protonated in water at pH 6.6. For a molar ratio of 3:1 (PAMAM 2G/MPA-CdTe), aggregates of several hundreds of nanometers diameter were formed and the accompanying ζ potential changed from −21 to +36 mV. The PL peak red shifts to ∼670 nm, and the intensity quenches by 30−40% (see the UV−vis and PL spectra in the Supporting Information [75]).

These experiments indicate that the DEA-CdSe NPs both enhance aggregate formation, as evidenced by a more significant red shift in PL than the case of CEA ligands only, and cause much stronger quenching, as compared to the PAMAM-2G dendrimer systems, which induce aggregates of a size similar to those found for DEA-CdSe. The red shift for the DEA-CdSe/MPA-CdTe NP solution is less than that observed for the TMA-CdSe/MPA-CdTe NP solution (TMA-CdSe/MPA-CdTe red-shifted from 638 to 665 nm, and DEA-CdSe/MPA-CdTe red-shifted from 638 to 656 nm), which indicates less self-quenching of MPA-CdTe NPs even though they may be closer together, on average. Thus, the enhanced quenching of the MPA-CdTe

NP photoluminescence and its weaker spectral shift indicate that a new nonradiative pathway is created by the proximity of DEA-CdSe NPs and that this nonradiative pathway is more rapid than the self-quenching of the MPA-CdTe Nps.

We postulate that electron transfer from the MPA-CdTe to the DEA-CdSe NPs is the new nonradiative relaxation pathway, i.e., quenching mechanism. This mechanism is postulated because of the staggered type II band gap alignment of the CdTe and CdSe NPs, in which both the conduction band and the valence band of CdTe NPs are energetically higher than the corresponding band positions of the CdSe NPs (Figure 9.7 a). In the DEA-CdSe/MPA-CdTe NP assemblies, a lower bound on the interparticle distance is determined by the length of the capping ligand molecules and is close to 1 nm, so that the excited electrons from the conduction band of CdTe can tunnel through the organic ligand barrier to the conduction band of the CdSe. In agreement with the data, this mechanism predicts a much weaker quenching for the TMA-CdSe/MPA-CdTe aggregates than that of DEA-CdSe/MPA-CdTe because of the longer distance (ca. 2 nm) between the NPs in the aggregates (compare Figure 9.4 and Figure 9.5)

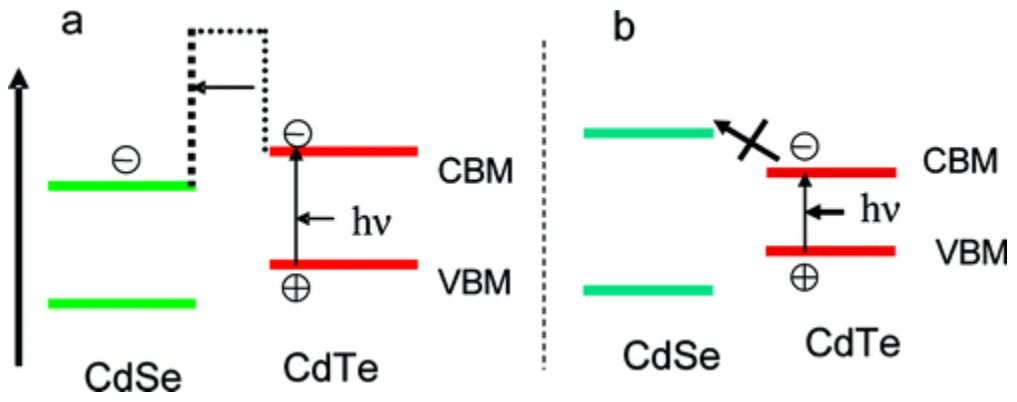

Figure 9.7: Drawing of type II and type I staggered band gap alignment

Schematic Drawing of Type II Staggered Band Gap Alignment of Appropriately Sized CdTe and CdSe NPs (a) and Type I Band Gap Alignment of Larger Sized CdTe and Smaller Sized CdSe NPs (b)

9.3.5 Surface Charge Dependence

The type II band alignment in Figure 9.7a implies that the electron transfer mechanism places an extra negative charge on the CdSe NP and a consequent extra positive charge on the CdTe NP. Given that the CdSe NP surface is positively charged and the CdTe NP surface is negatively charged, the net charge separation between the two types of NPs is decreased by the electron transfer. In contrast, one might expect that the transfer of an electron to a negatively charged CdSe NP from a positively charged CdTe NP might be less facile because of the increase in electrostatic energy, i.e., more net charge separation. This aspect of the electron transfer quenching mechanism was explored by switching the capping ligands and thereby changing the sign of the NP surface charges. DEA-CdTe NPs were synthesized by using a protocol similar to that for the MPA-CdTe NP preparation, and the size was controlled in a similar manner.[19; 81] The first excitonic peak of the DEA-CdTe NPs occurs near 575 nm, and the photoluminescence peak occurs near 610 nm. The MPA-CdSe NPs were prepared from the same TOPO-CdSe NPs that have their first excitonic peak at 518 nm; upon ligand exchange with MPA it shifted to 520 nm (see Figure 9.8).

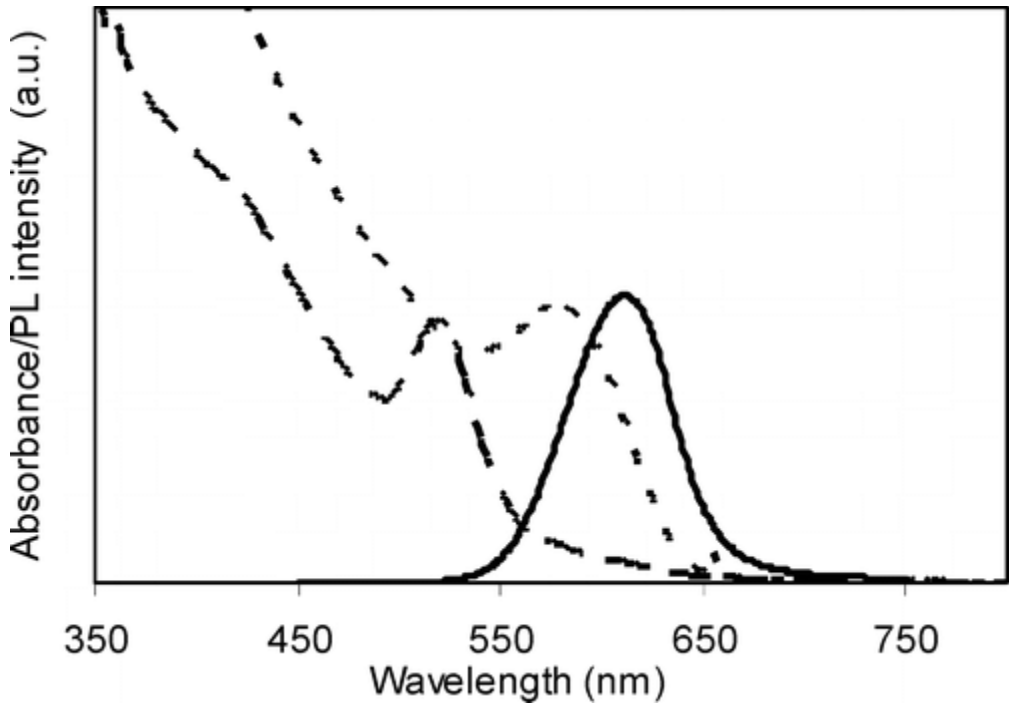

Figure 9.8: Absorption and PL spectra of NPs used in surface charge dependence experiments

Representative absorption and photoluminescence spectra of DEA-CdTe and MPA-CdSe NPs used in surface charge dependence experiments: from left to right, MPA-CdSe NP absorbance in water (− − −), DEA-CdTe NP absorbance in water (---), and DEA-CdTe fluorescence in water (—).

A solution of MPA-CdSe and DEA-CdTe at a molar ratio of 3:1 showed both excitonic peaks of CdTe and CdSe NPs in absorption spectra but did not show a significant quenching effect, as compared to a solution of DEA-CdTe (the PL spectrum of the assembly is similar and not shown). DLS experiments gave aggregate sizes of several tens of nanometers, and ζ potential measurements showed that the potential changed from about +14 mV for the original DEA-CdTe to about −8 mV for MPA-CdSe/DEA-CdTe at a molar ratio of 3:1. Thus, the aggregation properties are similar to those for the other aggregate type (negatively charged CdTe and positively charged CdSe). The inefficient self-quenching of DEA-CdTe compared to the MPA-CdTe systems may reflect the narrower size distribution of interaction energies (fwhm = 1652 $cm^{-1}$for DEA-CdTe as opposed to 2038 cm^{-1} for MPA-CdTe; see the Supporting Information [75]) as well as the shortening of the average fluorescence lifetime (14.1 ns for DEA-CdSe as compared to 39.0 ns for MPA-CdTe). These findings show that the direction of the interparticle electric field changes the photoluminescence quenching efficiency; a finding that is consistent with charge transfer but not with energy transfer.

9.3.6 Kinetic Measurements

Time-resolved photoluminescence measurements, using the TCSPC method, were performed to validate the steady-state measurements and quantify the relevant time scales for the quenching. A diode laser at 440 nm and a dye laser at 585 nm were used as excitation sources, and the emission was collected at the PL peak wavelength. None of the samples showed an excitation wavelength dependence; therefore, only lifetime parameters from the 585 nm excitation are presented here (Table 3 and Figure 9.9). Studies were performed for samples with molar ratios at

which the most pronounced difference in steady-state photoluminescence measurements were observed. Table 3 summarizes the findings by presenting the parameters for a best fit of the data to a sum of exponentials; the quantity ⟨τ⟩ is the average lifetime.

The lifetime data corroborate the steady-state emission data. The photoluminescence decay of the pure MPA-CdTe NP solution could be fit by a biexponential decay law with decay times that are tens of nanoseconds, giving an average lifetime of 39.0 ns. This value is consistent with typical thiol-capped CdTe NP emission lifetimes reported in the literature.[57; 76; 79] Typically, the shorter lifetime is attributed to the intrinsic recombination of initially populated core states, and the longer lifetime reflects the charge trapping kinetics of surface states via a delayed fluorescence mechanism.[4; 8; 13; 29; 72; 73] The amplitude a_2 of the longer lifetime component accounts for nearly 80% of the total PL decay and indicates good surface reconstruction with few recombination centers created during the sample growth process.[72; 79] The TDA/MPA-CdTe and TMA-CdSe/MPA-CdTe NP solutions showed very similar PL decay characteristics with an average lifetime of 24 ns. As discussed above these solutions show steady-state emission quenching of about a factor of 2, and it is attributed to aggregation-induced self-quenching of the CdTe NPs; the ratio of average lifetimes is consistent with the steady-state PL measurement. The decay parameters show that both time constants decrease but only by 10−20%. In contrast, the DEA-CdSe/MPA-CdTe solution showed a dramatic lifetime shortening for both components with an average lifetime of 3.8 ns. This observation is consistent with the steady-state studies and strongly suggests that interparticle separation in the aggregates changes the relative importance of nonradiative decay pathways.

Lastly, a solution of MPA-CdSe/DEA-CdTe which inverts the NP surface charges, hence the sign of the interparticle electric field, has an average lifetime similar to that of the pure solution of DEA-CdTe. These data corroborate the steady-state measurements and their interpretation.

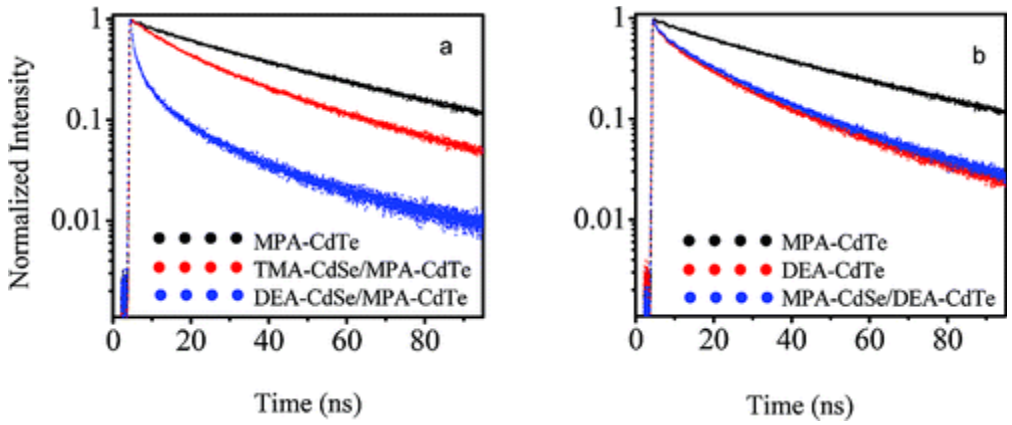

Figure 9.9: Time-Resolved PL decays of NP assemblies

(a) Representative time-resolved PL decays of MPA-CdTe, TMA-CdSe/MPA-CdTe at a 3:1 molar ratio, and DEA-CdSe/MPA-CdTe at a 3:1 molar ratio in water. (b) Representative time-resolved PL decays of MPA-CdTe, DEA-CdTe, and MPA-CdSe/DEA-CdTe at a 3:1 molar ratio in water. The MPA-CdTe data were included in both panels for better comparison.

Table 3: Time-resolved PL decay parameters

System	a_1	τ_1	a_2	τ_2	a_3	τ_3	$\langle\tau\rangle$
MPA-CdTe	0.21	11.4	0.79	46.3			39.0
TDA/ MPA-CdTe	0.56	10.0	0.44	38.4			22.6
CEA/MPA-CdTe	0.21	12.1	0.79	47.4			40.0
TMA-CdSe/ MPA-CdTe	0.52	10.4	0.48	38.0			23.6
DEA-CdSe/ MPA-CdTe	0.65	0.66	0.24	4.2	0.11	21.8	3.8
DEA-CdTe	0.32	1.23	0.41	11.0	0.27	33.5	13.9
MPA-CdSe/ DEA-CdTe	0.35	0.56	0.36	10.3	0.29	33.0	13.5

In Table 2, time-resolved PL was collected with λex = 585 nm and λem ≈ peak maximum. The average lifetime is given by

$\langle\tau\rangle = \sum_i a_i \tau_i$ *. The χ2 for all fits was less than 1.4.*

9.4 SUMMARY AND CONCLUSIONS

An electron transfer quenching mechanism provides a consistent understanding of the photoluminescence quenching of the CdSe/CdTe NP aggregates studied here. When TMA-CdSe NPs are mixed with MPA-CdTe NPs, the interparticle distance in the aggregates is about 2 nm (determined by the length of the capping ligands; see Figure 9.10), and this inhibits electron transfer because the electron tunneling probability through methylene films decays exponentially with the distance, with a typical decay length of 10 per nanometer. Although energy transfer of the CdTe is weak, some self-quenching can be observed in the aggregates.

When DEA-CdSe NPs are mixed with MPA-CdTe NPs, the interparticle distance in the aggregates is only about 1 nm, which is about half that of the TMA-CdSe/MPA-CdTe aggregates. If the tunneling probability through a methylene chain is taken to be proportional to $\exp(-d)$ (d in angstroms), then the shorter distance means that the electron tunneling probability is about 20,000 times more probable, making electron transfer a more facile nonradiative decay pathway. Thus, the quenching and lifetime shortening observed in these assemblies are attributed to electron transfer from CdTe to CdSe through the interparticle barrier (see Figure 9.11).

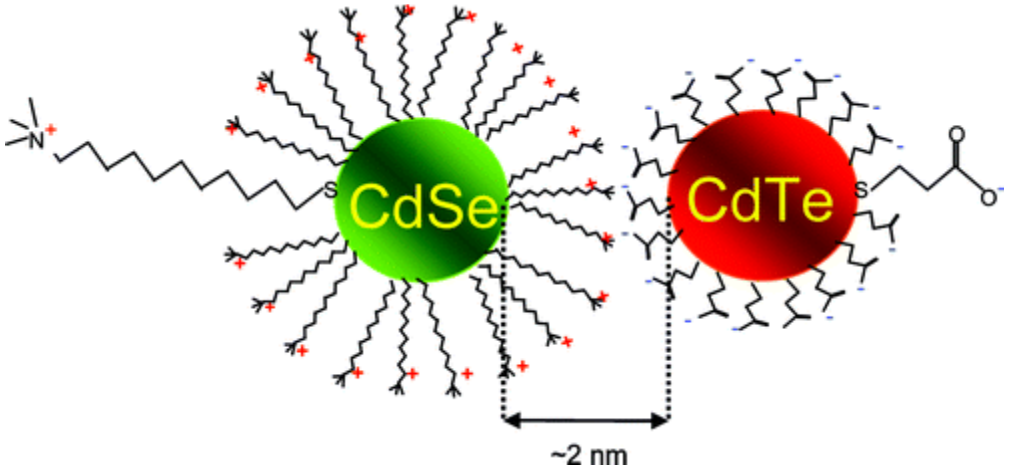

Figure 9.10: Schematic drawing of assemblies formed between TMA-CdSe and MPA-CdTe

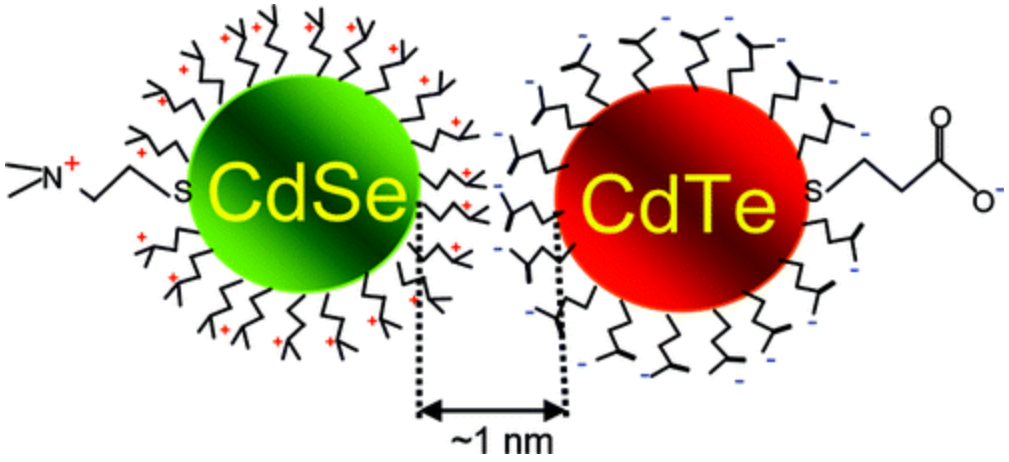

Figure 9.11: Schematic drawing of assemblies formed between DEA-CdSe and MPA-CdTe

The assignment of the quenching mechanism to electron transfer was supported by studies that inverted the surface charge on the NPs in the aggregates; in particular, CdTe was capped with positively charged DEA, and CdSe was capped with negatively charged MPA. Thus, the direction of the electric field between the two types of NPs was inverted (see Figure 9.12). Although the optical properties and the aggregation properties of the NPs did not change significantly with this change in surface ligand, the photoluminescence quenching of their aggregates changed dramatically. Whether the change in rate with the field direction is caused by a change in the tunneling probability and/or the relative energetics of the donor and accepting states of the NPs is not yet known.

In conclusion, this study demonstrates that electron transfer and photoluminescence quenching in CdSe/CdTe NP assemblies can be controlled through the interparticle distance, energetics, electric field created by the surface capping group, and particle size. Time-resolved studies indicate that the electron transfer process may involve surface-localized states. The inhibition of electron transfer by the interparticle electric field is significant and may provide an avenue for inhibiting back electron transfer. These findings should be useful for understanding and controlling charge transfer in nanocrystal-based solar cells.

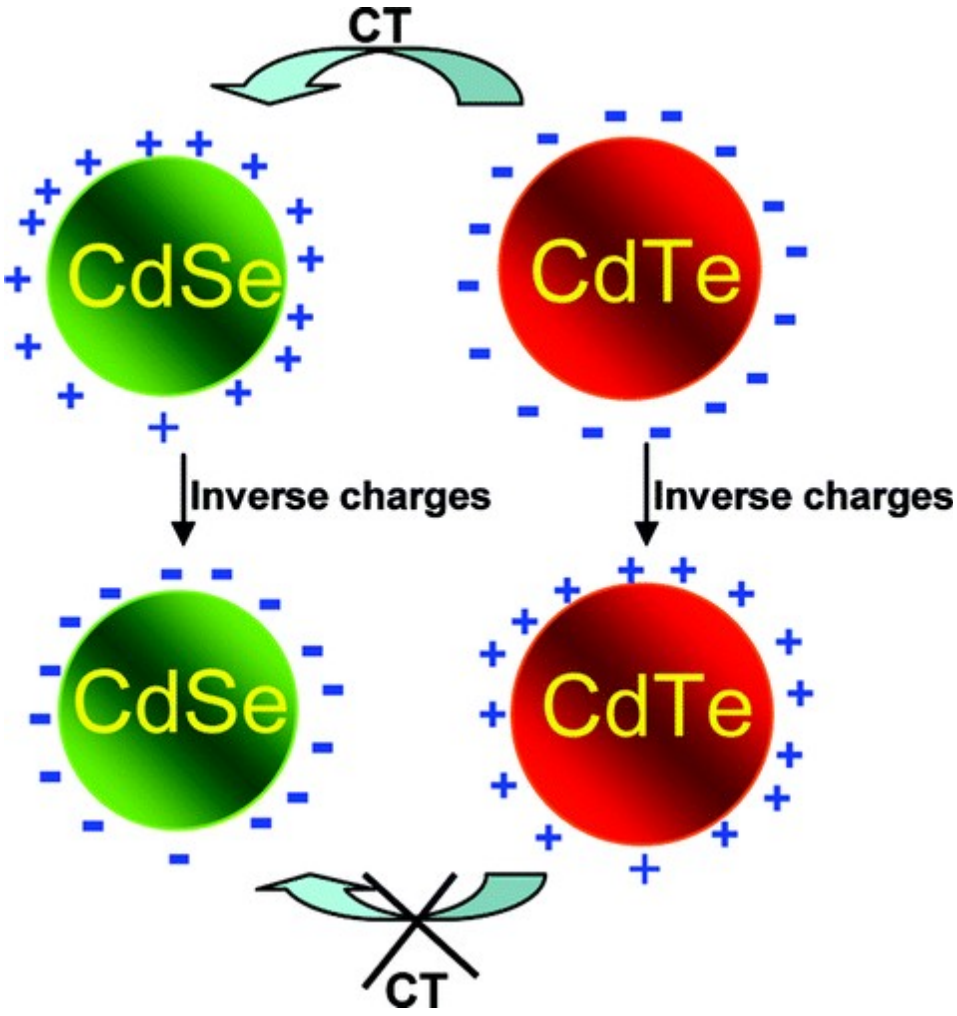

Figure 9.12: Schematic drawing of assemblies formed between MPA-CdSe and DEA-CdTe after inverse charges

9.5 BIBLIOGRAPHY

[1] **Akerman M., E.; Chan W. C., W.; Laakkonen, P.; Bhatia S., N. and Ruoslahti, E.** (**2002**). , Proc. Natl. Acad. Sci. U.S.A. 99 : 12617.

[2] **Aldana, J.; Wang Y., A. and Peng, X.** (**2001**). , J. Am. Chem. Soc. 123 : 8844.

[3] **Alivisatos A., P.** (**1996**). , Science 271 : 933.

[4] **Alivisatos A., P.; Harris A., L.; Levinos N., J.; Steigerwald M., L. and Brus L., E.** (**1988**). , J. Chem. Phys. 89 : 4001.

[5] **Andres R., P.; Bielefeld J., D.; Henderson J., I.; Janes D., B.; Kolagunta V., R.; Kubiak C., P.; Mahoney W., J. and Osifchin R., G.** (**1996**). , Science 273 : 1690.

[6] **Artemyev, M.; Woggon, U.; Wannemacher, R.; Jaschinski, H. and Langbein, W.** (**2001**). , Nano Lett. 1 : 309.

[7] **Barnham K. W., J.; Mazzer, M. and Clive, B.** (**2006**). , Nat. Mater. 5 : 161.

[8] **Bawendi M., G.; Carroll P., J.; Wilson W., L. and Brus L., E.** (**1992**). , J. Chem. Phys. 96 : 946.

[9] **Bethell D. B., M.; Schiffrin D., J. and Kiely, C.** (**1996**). , J. Electroanal. Chem. 409 : 137.

[10] **Bruchez, M.; Moronne, M.; Gin, P.; Weiss, S. and Alivisatos P., A.** (**1998**). , Science 281 : 2013.

[11] **Brus L., E.** (**1986**). , J. Chem. Phys. 90 : 2555.

[12] **Brust, M.; Schiffrin D., J.; Bethell, D. and Kiely C., J.** (**1995**). , Adv. Mater. 7 : 795.

[13] **Byrne S., J.; Corr S., A.; Rakovich T., Y.; Gun'ko Y., K.; Rakovich Y., P.; Donegan J., F.; Mitchell, S. and Volkov, Y.** (**2006**). , J. Mater. Chem. 16 : 2896.

[14] **Chan W. C., W. and Nie, S.** (**1998**). , Science 281 : 2016.

[15] **Crooker S., A.; Hollingsworth J., A.; Tretiak, S. and Klimov V., I.** (**2002**). , Phys. Rev. Lett. 89 : 186802/1.

[16] **Dimitrijevic N., M.; Saponjic Z., V.; Rabatic B., M. and Rajh, T.** (**2005**). , J. Am. Chem. Soc. 127 : 1344.

[17] **Dooley C., J.; Dimitrov S., D. and Fiebig, T.** (**2008**). , J. Phys. Chem. C 112 : 12074.

[18] **Ellingson R., J.; Beard M., C.; Johnson J., C.; Yu, P.; Micic O., I.; Nozik A., J.; Shabaev, A. and Efros A., L.** (**2005**). , Nano Lett. 5 : 865.

[19] **Gaponik, N.; Talapin D., V.; Rogach A., L.; Hoppe, K.; Shevchenko E., V.; Kornowski, A.; Eychmu1ller, A. and Weller, H.** (**2002**). , J. Phys. Chem. B 106 : 7177.

[20] **Goldman E., R.; Clapp A., R.; Anderson G., P.; Uyeda H., T.; Mauro J., M.; Medintz I., L. and Mattoussi, H.** (**2004**). , Anal. Chem. 76 : 684.

[21] **Gopidas K., R.; Bohorquez, M. and Kamat P., V.** (**1990**). , J. Phys. Chem. 94 : 6435.

[22] **Green M., A.; Emery, K.; King D., L.; Igari, S. and Warta, W.** (**2001**). , Prog. Photovoltaics 9 : 287.

[23] **Gross, D.; Susha A., S.; Klar T., A.; Como E., D.; Rogach A., L. and Feldmann, J.** (**2008**). , Nano Lett. 8 : 1482.

[24] **Heath J., R.; Knobler C., M. and Leff D., V.** (**1997**). , J. Phys. Chem. B 101 : 189.

[25] **Huynh W., U.; Dittmer J., K. and Alivisatos A., P.** (**2002**). , Science 295 : 2425.

[26] **Issac, A.; Jin, S. and Lian, T.** (**2008**). , J. Am. Chem. Soc. 130 : 11280.

[27] **J.-W., H. and Bai S., J.** (**2005**). , Nanotechnology 16 : 1406.

[28] **Jin W., J.; Fernandez-Arguelles M., T.; Costa-Fernandez J., M.; Pereiro, R. and Sanz-Medel, A.** (**2005**). , Chem. Commun. : 883.

[29] **Jones, M.; Lo S., S. and Scholes G., D.** (**2009**). , Proc. Natl. Acad. Sci. U.S.A. 106 : 3011.

[30] **Kagan C., R.; Murray C., B.; Nirmal, M. and Bawendi M., G.** (**1996**). , Phys. Rev. Lett. 76 : 1517.

[31] **Kalsin A., M.; Fialkowski, M.; Paszewski, M.; Smoukov S., K.; Bishop K. J., M. and Grzybowski B., A.** (**2006**). , Science 312 : 420.

[32] **Kamat P., V.** (**2002**). , J. Phys. Chem. B 106 : 7729.

[33] **Kamat P., V.** (**2007**). , J. Phys. Chem. C 111 : 2834.

[34] **Kim, S.; Fisher, B.; H.-J., E. and Bawendi, M.** (**2003**). , J. Am. Chem. Soc. 125 : 11466.

[35] **Klimov V., I.; Mikhailovsky A., A.; Xu, S.; Malko, A.; Hollingsworth J., A.; Leatherdale C., A.; Eisler H., J. and Bawendi M., G.** (**2000**). , Science 290 : 314.

[36] **Kohtani, S.; Kudo, A. and Sakata, T.** (**1993**). , Chem. Phys. Lett. 206 : 166.

[37] **Koole, R.; Liljeroth, P.; De Mello Donega, C.; Vanmaekelbergh, D. and Meijerink, A.** (**2006**). , J. Am. Chem. Soc. 128 : 10436.

[38] **Leibowitz F., L.; Zheng, W.; Maye M., M. and Zhong C., J.** (**1999**). , Anal. Chem. 71 : 5076.

[39] **Liu, M.; Kaur, P.; Waldeck D., H.; Xue, C. and Liu, H.** (**2005**). , Langmuir 21 : 1687.

[40] **Liu, M.; Waldeck D., H.; Oliver A., M.; Head N., J. and Paddon-Row M., N.** (**2004**). , J. Am. Chem. Soc. 126 : 10778.

[41] **Liu, Y.; Wang, Y. and Claus R., O.** (**1998**). , Chem. Phys. Lett. 298 : 315.

[42] **Lo S., S.; Khan, Y.; Jones, M. and Scholes G., D.** (**2009**). , J. Chem. Phys. 131 : 084714.

[43] **Mahawela, P.; Jeedigunta, S.; Vakkalanka, S.; Ferekides C., S. and Morel D., L.** (**2005**). , Thin Solid Films 466 : 480.

[44] **Maheshwari, V. and Saraf R., F.** (**2006**). , Science 312 : 1501.

[45] **Mayilo, S.; Hilhorst, J.; Susha A., S.; Hohl, C.; Franzl, T.; Klar T., A.; Rogach A., L. and Feldmann, J.** (**2008**). , J. Phys. Chem. C 112 : 14589.

[46] **McFarland E., W. and Tang, J.** (**2003**). , Nature 421 : 616.

[47] **Mews, A.; Kadavanich A., V.; Banin, U. and Alivisatos A., P.** (**1996**). , Phys. Rev. B 53 : 13242.

[48] **Michalet, X.; Pinaud F., F.; Bentolila L., A.; Tsay J., M.; Doose, S.; Li J., J.; Sundaresan, G.; Wu A., M.; Gambhir S., S. and Weiss, S.** (**2005**). , Science 307 : 538.

[49] **Murray C., B.; Kagan C., R. and Bawendi M., G.** (**2000**). , Annu. Rev. Mater. Sci. 30 : 545.

[50] **Nasr, C.; Hotchandani, S.; Kim W., Y.; Schmehl R., H. and Kamat P., V.** (**1997**). , J. Phys. Chem. B 101 : 7480.

[51] **Park S., H.; Roy, A.; Beaupré, S.; Cho, S.; Coates, N.; Moon J., S.; Moses, D.; Leclerc, M.; Lee, K. and Heeger A., J.** (**2009**). , Nat. Photon 3 : 297.

[52] **Pathak, S.; Choi S., K.; Arnheim, N. and Thompson M., E.** (**2001**). , J. Am. Chem. Soc. 123 : 4103.

[53] **Peng Z., A. and Peng, X.** (**2001**). , J. Am. Chem. Soc. 123 : 183.

[54] **Plass, R.; Pelet, S.; Krueger, J.; Gratzel, M. and Bach, U.** (**2002**). , J. Phys. Chem. B 106 : 7578.

[55] **Qu, L.; Peng Z., A. and Peng, X.** (**2001**). , Nano Lett. 1 : 333.

[56] **Robel, I.; Subramanian, V.; Kuno, M. and Kamat P., V.** (**2006**). , J. Am. Chem. Soc. 128 : 2385.

[57] **Rogach A., L.; Franzl, T.; Klar T., A.; Feldmann, J.; Gaponik, N.; Lesnyak, V.; Shavel, A.; Eychmuller, A.; Rakovich Y., P. and Donegan J., F.** (**2007**). , J. Phys. Chem. C 111 : 14628.

[58] **S.-C., C.; Tachikawa, T.; Fujitsuka, M. and Majima, T.** (**2008**). , J. Phys. Chem. C 112 : 19625.

[59] **Sapsford K., E.; Medintz I., L.; Golden J., P.; Deschamps J., R.; Uyeda H., T. and Mattoussi, H.** (**2004**). , Langmuir 20 : 7720.

[60] **Schaller R., D.; Sykora, M.; Pietryga J., M. and Klimov V., I.** (**2006**). , Nano Lett. 6 : 424.

[61] **Scharber M., C.; Muhlbacher, D.; Koppe, M.; Denk, P.; Waldauf, C.; Heeger A., J. and Brabec C., J.** (**2006**). , Adv. Mater. 18 : 789.

[62] **Schlamp M., C.; Peng X., G. and Alivisatos A., P.** (**1997**). , J. Appl. Phys. 82 : 5837.

[63] **Skolnick M., S. and Mowbray D., J.** (**2004**). , Annu. Rev. Mater. Res. 34 : 181.

[64] **Sudeep P., K.; Takechi, K. and Kamat P., V.** (**2007**). , J. Phys. Chem. C 111 : 488.

[65] **Sundar V., C.; Lee, J.; Heine J., R.; Bawendi M., G. and Jensen K., F.** (**2000**). , Adv. Mater. 12 : 1102.

[66] **Talapin D., V. and Murray C., B.** (**2005**). , Science 310 : 86.

[67] **Tang, Z.; Zhang, Z.; Wang, Y.; Glotzer S., C. and Kotov N., A.** (**2006**). , Science 314 : 274.

[68] **Uyeda H., T.; Medintz I., L.; Jaiswal J., K.; Simon S., M. and Mattoussi, H.** (**2005**). , J. Am. Chem. Soc. 127 : 3870.

[69] **Vanmaekelbergh, D.I. and Liljeroth, P.** (**2005**). , Chem. Soc. Rev. 34 : 299.

[70] **Vinodgopal, K.; Bedja, I. and Kamat P., V.** (**1996**). , Chem. Mater. 8 : 2180.

[71] **Wang, L.; Rastelli, A.; Kiravittaya, S.; Benyoucef, M. and Schmidt O., G.** (**2009**). , Adv. Mater. 21 : 2601.

[72] **Wang, X.; Qu, L.; Zhang, J.; Peng, X. and Xiao, M.** (**2003**). , Nano Lett. 3 : 1103.

[73] **Wehrenberg B., L.; Wang, C. and Guyot-Sionnest P., J.** (**2002**). , J. Phys. Chem. B 106 : 10634.

[74] **Willner, I. and Eichen, Y.** (**1987**). , J. Am. Chem. Soc. 109 : 6862.

[75] **Wu, M.; Mukherjee, P.; Lamont, D. N. and Waldeck, D. H.** (**2010**). *Electron Transfer and Fluorescence Quenching of Nanoparticle Assemblies*, The Journal of Physical Chemistry C 114 : 5751-5759.

[76] **Wuister S., F.; Swart, I.; Van Driel, F.; Hickey S., G. and De Mello Donega, C.** (**2003**). , Nano Lett. 3 : 503.

[77] **Yu, G.; Gao, J.; Hemmelen J., C.; Wudl, F. and Heeger A., J.** (**1995**). , Science 270 : 1789.

[78] **Zabet-Khosousi, A. and A.-A., D.** (**2008**). , Chem. Rev. 108 : 4072.

[79] **Zhao, K.; Li, J.; Wang, H.; Zhuang, J. and Yang, W.** (**2007**). , J. Phys. Chem. C 111 : 5618.

[80] **Zhou, Q.; Li, X.; Fan, Q.; Zhang, X. and Zheng, J.** (**2006**). , Angew. Chem., Int. Ed. 45 : 3970.

[81] **Zou, L.; Gu, Z.; Zhang, N.; Zhang, Y.; Fang, Z.; Zhu, W. and Zhong, X.** (**2008**). , J. Mater. Chem. 18 : 2807.

10.0 LANTHANIDE SENSITIZATION IN II−VI SEMICONDUCTOR MATERIALS: A CASE STUDY WITH TERBIUM(III) AND EUROPIUM(III) IN ZINC SULFIDE NANOPARTICLES

Author list: Prasun Mukherjee, Chad M. Shade, Adrienne M. Yingling, Daniel N. Lamont, David H. Waldeck, and Stéphane Petoud

Author contribution: The author of this dissertation contributed to the photophysical characterization of the nanoparticles, interpretation of the results and the preparation of the manuscript. This work has been published as *J. Phys. Chem. A* ***2011*** *115, 4031*

10.1 INTRODUCTION

Historically, luminescent lanthanides have been extensively used as phosphors, and more recently, they have attracted interest as a new class of luminescent probes and sensors for biological applications.[5; 9; 35; 49; 50; 61; 74] Lanthanides have a number of luminescence properties that make them an attractive alternative to organic fluorophores in

bioanalytical applications and biological imaging. Whereas typical organic fluorophores are prone to photobleaching mechanisms, lanthanide luminescence is highly resistant to photobleaching and, hence, allows longer experiment times or their repetition. The sharp atom like lanthanide emission bands and the negligible overlap between the bands of different lanthanide ions makes them promising candidates for multiplex biological assays through spectral discrimination or for barcode types of applications.[81] Moreover, the long lanthanide luminescence lifetimes (millisecond time range for lanthanide emitting in the visible) allows their signal to be distinguished from the background autofluorescence of biological media (nanosecond time range) through temporal discrimination for improved detection sensitivity.

A major requirement for the use of lanthanides as biological imaging agents is the detection sensitivity they can provide, which includes the emission of a sufficient number of photons to obtain good detection sensitivity. The direct excitation of lanthanides is inefficient because most of the interesting f−f transitions are Laporte-forbidden.[10; 29] As a consequence, the molar extinction coefficients of lanthanide ions are very low[11] ($\leq$10 M^{-1} cm^{-1}, as opposed to 10^4–10^5 M^{-1} cm^{-1} for typical organic fluorophores). The low number of absorbed photons will result in a low number of emitted photons. To overcome this limitation, the concept of sensitization through an antenna effect has been established.[2; 4; 7; 17; 41; 42; 50; 53; 63; 64; 83; 84] In this process, photons from the excitation light are absorbed by a chromophore with high extinction coefficient that transfers the energy to the accepting levels of the lanthanide ions, thus creating a high population of electronically excited lanthanide ions and enhancing the amount of luminescent photons. In addition to efficient energy pumping by this antenna effect, it is also important to prevent the quenching of lanthanide ion

excited states by nonradiative energy transfer to the overtones of high frequency vibrational modes, such as −OH, −NH, and −CH.[3] For applications under biological conditions, it is especially important to protect the lanthanide ions from water molecules.

Semiconductor nanoparticles that contain lanthanide ions are advantageous for biological applications over the undoped nanoparticles because the sharp emission signal corresponding to each lanthanide ion has a unique spectroscopic signature for spectral identification and unambiguous identification. Depending on the lanthanide cations, there is a broad choice of emission wavelength throughout the entire visible and near-IR spectral regions. The near-IR luminescence of lanthanide cations is of special benefit for biological applications because (i) there is an absence of native autofluorescence of tissues in the near−IR region; therefore, a good signal-to-noise ratio is obtained for more sensitive detection, and (ii) near-IR photons can cross significant depths of tissues for potential noninvasive investigation.

Recently, Chengelis et al. reported on the incorporation of terbium ions (Tb^{3+}) in CdSe nanoparticles.[19] Although Tb^{3+} luminescence sensitization was observed for the CdSe/Tb^{3+} system, its emission was obscured by the more intense CdSe bandgap emission in steady-state mode, and a time-gated method was required to specifically identify the Tb^{3+} luminescence. From the excitation spectrum, collected upon monitoring the 545 nm centered Tb^{3+} emission signal, it is evident that part of the excitation energy is transferred from the CdSe nanoparticle states to the accepting energy levels of Tb^{3+} ions, demonstrating that the electronic structure of the nanoparticle can act as an antenna.

Although the CdSe/Tb^{3+} system demonstrates the use of the nanoparticles as an antenna, it has intrinsic limitations; namely, the efficiency of CdSe in sensitizing Tb^{3+} luminescence was low, and the Cd and Se components of the nanoparticles are toxic, thus limiting their applicability for studying biological systems and for diagnostic purposes. To overcome these two drawbacks, we have created a ZnS/Tb^{3+} nanoparticle system, in which the individual constituents are nontoxic or less toxic and more environmentally friendly. Moreover, because the bulk band gap of ZnS is larger than that of CdSe (3.6 eV as opposed to 1.7 eV),[66] the electronic structure of ZnS is expected to sensitize lanthanides more efficiently than CdSe because it ensures a more favorable match of lanthanide acceptor energy levels with respect to the nanoparticle donating energy levels.[27]

This work reports results on ZnS nanoparticles containing three different lanthanides: two visible-emitting lanthanides, Tb^{3+} and Eu^{3+} in ZnS nanoparticles, and corresponding control experiments with Gd^{3+} (which does not have accepting electronic levels in the relevant energy range). ZnS nanoparticle systems without lanthanides were also studied for comparison. Both steady-state and time-resolved luminescence measurements demonstrate that ZnS acts as an efficient antenna to sensitize Tb^{3+} and Eu^{3+} luminescence. A comparison with other II−VI materials (namely, Tb^{3+} incorporated in CdSe, CdS, and ZnSe) is made to elucidate the energy transfer mechanism between the lanthanide and the nanoparticle host.

Understanding the mechanism of lanthanide luminescence sensitization is of main importance for controlling the performance and properties of novel optical materials. Because lanthanide ions behave as hard acids, they bind strongly to hard bases, following the preference order O > N > S. Various researchers have devoted considerable effort to understanding and

exploiting the mechanisms for the luminescence sensitization of lanthanide ions in semiconductor materials. Some of the discussed mechanisms are based on a defect-related Auger transition model,[1; 31; 86] a resonant energy transfer model,[44] bound exciton models, [53; 79] and shallow donor (or acceptor) models.[34] It is generally believed that exciton recombination plays a key role in the luminescence sensitization of lanthanide cations.

Although a number of researchers have discussed lanthanide luminescence in bulk semiconductors[18; 32; 33; 39; 43; 58; 59; 69-72] and semiconductor nanoparticles,[6; 13; 14; 21; 28; 36; 37; 57; 60; 67; 68; 80; 85] the mechanism of lanthanide luminescence sensitization is still not fully elucidated and does not allow the synthesis of lanthanide-based nanomaterials with predictable properties. The mechanism of Tb^{3+} luminescence sensitization in bulk ZnS has attracted considerable attention. For example, Anderson[2] finds that the process includes (a) a donor level related to Tb^{3+} [$6s^2 5d^1$] that lies 0.4 eV below the conduction band (the $4f^8$ levels were assumed to be located somewhere below the valence band), (b) a hole trap that lies 1.02 eV above the valence band (assumed to be a copper-related site),[40; 47] and (c) that the excitation of the $4f^8$ electronic system occurs during recombination of the electron−hole pair in these traps. Although these efforts provide a useful framework for the current studies, the luminescence sensitization of Tb^{3+} and Eu^{3+} in ZnS nanoparticles is not well understood. Previous studies have been limited by an inability to identify the location of lanthanide ground and excited states with respect to the valence and conduction bands of the semiconductor materials. In this work, the nature of sensitization in the ZnS nanoparticles is discussed in light of the model proposed by Dorenbos, [22-27] for the relative energetics of the lanthanide ions in the host semiconductor.

10.2 MATERIALS AND METHODS

10.2.1 Chemicals

Trioctylphosphine [TOP] (90%), zinc stearate (tech.), octadecene (90% tech.), and tetracosane (99%) were purchased from Sigma-Aldrich-Fluka, St. Louis, MO. Chloroform was purchased from J. T. Baker, Phillipsburg, NJ. Sulfur, toluene, and methanol were purchased from Fisher Scientific, Pittsburgh, PA. Terbium(III) nitrate (99.9%) was purchased from Strem, europium(III) nitrate (99.99%) was purchased from Aldrich, and gadolinium(III) nitrate (99.99%) was purchased from Alfa Aesar, Ward Hill, MA. In all cases, hydrated lanthanide salts were used. *n*-Hexane and 1-octanol were purchased from Acros, and ethyl acetate was purchased from EMD, Gibbstown, NJ. Argon gas was purchased from Valley National, Pittsburgh, PA. All chemicals were used as purchased without purification, except toluene, which was distilled over sodium under nitrogen.

10.2.2 Nanoparticle Synthesis

All ZnS nanoparticle systems were synthesized using a noncoordinating solvent system consisting of octadecene and tetracosane. Zinc stearate and lanthanide nitrate salts were used as cation precursors, and elemental sulfur served as the anion precursor. Tetracosane (4.0 g), octadecene (3.0 mL), and 0.68 mmol of zinc stearate were loaded into a three-neck, round-bottom flask and heated to 350 °C while stirring under nitrogen. The lanthanide stock solution

(0.12 mmol lanthanide nitrate dissolved in a combination of octadecene and trioctylphosphine oxide) was injected after approximately ∼2 h of heating and allowed to stir within the reaction mixture for at least 30 min. The sulfur stock solution (sulfur powder dissolved in octadecene) was injected ∼1 h after the lanthanide stock solution. The reaction temperature was then decreased to between 270 and 300 °C for the duration of nanocrystal growth. Aliquots of sample were removed at varying growth times. The resulting nanoparticles were then redispersed in an appropriate solvent for spectroscopic analysis.

ZnS nanoparticles without lanthanides incorporated were prepared using the methods described above; however, the zinc stearate precursor was increased to 0.80 mmol, and the lanthanide stock solution preparation was omitted.

10.2.3 Steady-State Optical Measurements

Steady-state absorption spectra were obtained on an Agilent 8453 UV−visible spectrophotometer with 1 nm resolution. Steady-state excitation and emission spectra were recorded using a Jobin Yvon Horiba Fluorolog-322 with a 5 nm bandpass; spectra were corrected for excitation and emission (lamp, detector, and monochromator). A 1 cm path length quartz cuvette was used for the measurements. All measurements were performed at room temperature.

10.2.4 Quantum Yields

Absorption spectra were recorded on either a Perkin-Elmer Lambda 9 Spectrometer coupled to a personal computer using software supplied by Perkin-Elmer or on an Agilent 8453 UV−visible spectrophotometer. Quantum yields were recorded by the relative method using references.

Steady-state luminescence quantum yields were measured using quinine sulfate reference solution (solvent H_2SO_4 1 N, $\Phi = 0.546$).[48] Time-gated luminescence quantum yields were measured using [Tb(H_{22}IAM)] reference solution (solvent water, $\Phi = 0.59$).[55] Spectra were corrected for the instrumental response.

The quantum yields were calculated using the following Equation 10.1:

$$\frac{\Phi_x}{\Phi_r} = \frac{A_r(\lambda_r) I(\lambda_r) \eta_x^2 D_x}{A_x(\lambda_x) I(\lambda_x) \eta_r^2 D_r}$$

Equation 10.1

where the subscript r stands for the reference, and x, for the sample; *A* is the absorbance at the excitation wavelength, *I* is the intensity of the excitation light at the same wavelength, η is the refractive index (η = 1.333 in water, η = 1.496 in toluene, η = 1.446 in chloroform), and *D* is the measured integrated luminescence intensity. ZnS systems (λ_{ex} = 315, 320, and 325 nm) were measured in chloroform, whereas ZnSe (λ_{ex} = 315, 320, and 325 nm) and CdSe (λ_{ex} = 300, 305, and 310 nm) systems were measured in toluene.

Lanthanide-centered quantum yields for ZnSe/Ln^{3+} and CdSe/Ln^{3+} were collected with the fluorometer in time-gated mode, whereas the contribution from lanthanide-centered emission was discriminated spectrally from the overall quantum yield. For the ZnS/Ln^{3+} systems, calculations were performed by integrating the narrow emission bands arising from the lanthanide cations in steady-state mode.

10.2.5 Time-Gated Measurements

Time-gated excitation and emission spectra were collected with a Varian Cary Eclipse fluorescence spectrophotometer with 10 and 20 nm bandpass for Tb and Eu samples, respectively. The spectra were acquired with a delay time and a gate time of 0.2 and 5 ms, respectively. Using such a delay time, only lanthanide sharp bands are expected to appear in the spectra without any contribution from shorter lived nanoparticle bandgap emission. Both excitation and emission filters were set in auto mode in the software. All measurements were performed at room temperature.

10.2.6 Time-Resolved Measurements

The time-resolved luminescence decay kinetics was measured using the time-correlated single-photon counting (TCSPC) technique. Samples were excited with the frequency-doubled output (centered at ~300 nm) of a synchronously pumped cavity dumped dye laser (Coherent, Santa Clara, CA, model 599) using rhodamine 6G as the gain medium; emission from the sample was collected at different wavelengths using a monochromator. The instrument response function had a full-width-at-half-maximum (fwhm) of ~40 ps. A 1 cm path length quartz cuvette was used for all the time-resolved measurements. All measurements were performed at room temperature. Experiments were performed with a 1 MHz laser repetition rate. Lifetime values were found to be similar, with 125 (for ZnS/Tb) and 300 kHz (for ZnS/Gd and ZnS) repetition rates; these measurements were performed at selected wavelengths. Lifetime decay traces were fitted by an iterative reconvolution method with IBH DAS 6 decay analysis software.

The Tb^{3+} and Eu^{3+} luminescence lifetime measurements were performed by excitation of solutions in 1 mm quartz cells (NSG Precision Cells, Inc., Farmingdale, NY) using either a Xenon flash lamp or a Nd:YAG Continuum Powerlite 8100 laser (354 nm, third harmonic) as the excitation source. Emission was collected at a right angle to the excitation beam, and wavelengths were selected by means of the Spex FL1005 double monochromator or a Spectral Products CM 110 1/8 m monochromator. The signal was monitored by a Hamamatsu R928 photomultiplier tube coupled to a 500 MHz bandpass digital oscilloscope (Tektronix TDS 620B). Signals from >500 flashes were collected and averaged. Luminescence lifetimes were averaged using samples from several different batches. Luminescence decay curves were imported into Origin 7.0 and analyzed using the Advanced Fitting Tool.

10.3 RESULTS AND DISCUSSION

10.3.1 HRTEM Imaging

High-resolution transmission electron microscopy (HRTEM) images were obtained using a JEOL-2100 CF instrument operating between 120 kV and 200 kV. A representative TEM image is shown in Figure 10.1. The size distribution of ZnS:Tb nanoparticles was calculated using Image J software and found to be 3.3 ± 0.4 nm in average diameter. Both the stoichiometry (lanthanide-to-zinc ratio) and the location of the lanthanides in the nanoparticles are not yet fully

quantified. These data will be reported in a more comprehensive future study that will address the stoichiometry and the relative importance of the lanthanide locations, on the surface or in the bulk of the nanoparticles.

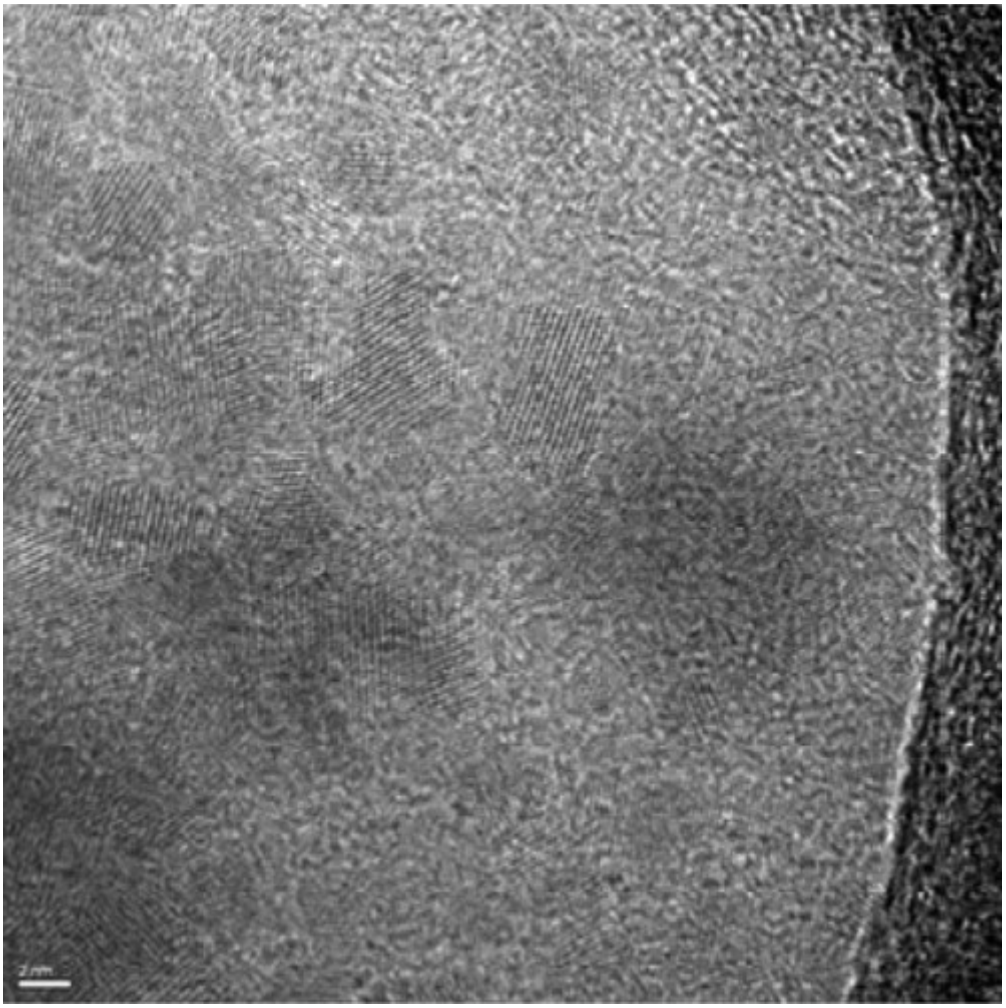

Figure 10.1: Representative HRTEM image of synthesized ZnS/Tb nanoparticles

Representative HRTEM image of synthesized ZnS/Tb nanoparticles. A 2 nm scale bar is shown on the bottom left of the image

10.3.2 Absorption Spectra

Representative absorption spectra of ZnS nanoparticles dissolved in chloroform are shown in Figure 10.2 for two different growth times. The absorption spectra reveal characteristic bands centered at ~290 and ~360 nm. The band with an apparent maximum at ~290 nm shows a small dependence on growth time and is attributed to the lowest energy exciton band of the nanoparticle. The ~360 nm band is probably associated with a transition involving a trap state. The assignment of the ~290 nm band is corroborated by a simple estimation of the nanoparticle band gap using a method proposed by Brus [8] (Equation 10.2), and found to be ~4.2 eV, corresponding to a ~290 nm band gap transition. In this model, the change in bandgap with nanoparticle size is given by

$$E_g(nano) \approx E_g(bulk) + \frac{\hbar^2 \pi^2}{2R^2}\left[\frac{1}{m_e} + \frac{1}{m_h}\right] - \frac{1.8e^2}{\epsilon R}$$

Equation 10.2

assuming E_g(bulk) = 3.6 eV, R = 1.65 nm (see above), m_e = 0.25 m_0, m_h = 0.59 m_0 and ε = 8.3. The effective mass and dielectric constant values were adopted from the work by Murphy and co-workers.[65] We assign the long wavelength tail to the contribution from various surface states of the nanoparticles (vide infra).

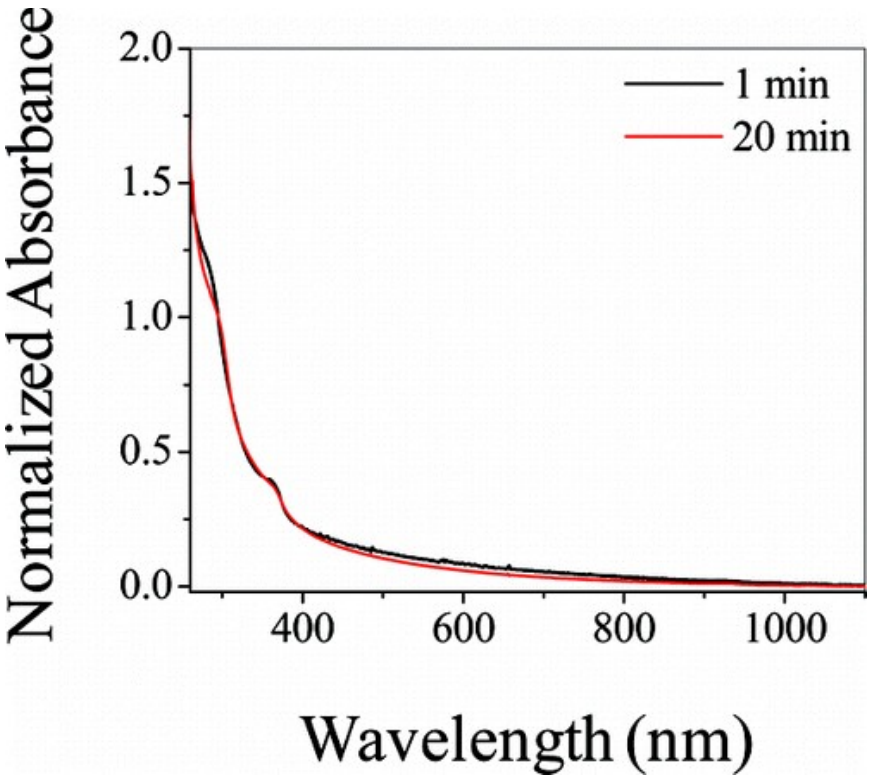

Figure 10.2: Normalized absorption spectra of a ZnS nanoparticle in chloroform

Representative normalized absorption spectra of a ZnS nanoparticle sample dissolved in chloroform obtained with growth times of 1 and 20 min. Spectra were normalized arbitrarily at 295 nm. The band at ~290 nm is associated with the band gap transition (see text).

Figure 10.3 shows steady-state luminescence excitation and emission spectra for the lanthanide incorporated ZnS nanoparticles and for undoped ZnS nanoparticles (NP) without lanthanide ions, in $CHCl_3$. The spectra correspond to ∼20 min NP growth time; the spectra corresponding to the analysis of the samples obtained after 1 min growth times are similar.

10.3.3 ZnS/Tb Spectra

Figure 10.3B shows emission spectra for ZnS/Tb. For λ_{ex} = 300 nm, λ_{em} bands were identified at ∼410 (ZnS band), 490, 545, 585, and 620 nm (Tb^{3+} sharp bands); for λ_{ex} = 375 nm, λ_{em} bands were assigned at ∼455 (ZnS band), 490 (weak Tb^{3+} band), and 545 nm (Tb^{3+} band); and for λ_{ex} = 440 nm, a λ_{em} band was assigned at ∼510 nm (ZnS band). An excitation wavelength dependence (red edge effect) is observed, that is, with an increase in λ_{ex}, the emission band position shifts toward the red.

The excitation spectra (Figure 10.3A) also depend on λ_{em}. For λ_{em} = 410 nm (ZnS emission), the λ_{ex} bands were identified at ∼260 and 350 nm; for λ_{em} = 450 nm (ZnS emission), the λ_{ex} bands were assigned at ∼270 and 375 nm; and for λ_{em} = 545 nm (Tb^{3+} emission), a broad λ_{ex} feature appeared. To examine whether this wavelength dependence reflects size heterogeneity of the sample, efforts were made to improve the sample's size distribution. Thus, centrifugation was performed at 20 000 rpm for 2 h, a chemical purification by solvent precipitation method (see Supporting Information [51]) was used, and the nanoparticle samples were dialyzed. None of these three methods yielded any noticeable change in the excitation wavelength-dependent behavior. On the basis of these studies, the excitation wavelength-dependent emission spectra are taken to reflect the energy distribution of surface states on the nanoparticles.

Sensitization of the lanthanide emission is evident in the steady-state emission spectra. Interestingly, the lanthanide emission intensity displays a wavelength dependence; when exciting the sample at 300 nm, terbium (Tb^{3+}) bands at ~490 and ~545 nm are clearly identifiable, whereas a 375 nm excitation results only in a weak Tb^{3+} emission. Excitation with 440 nm light results in no observable Tb^{3+} sensitization in the steady-state mode; however, a weak Tb^{3+} sensitization can be observed in time-gated mode. This dependence on excitation energy correlates with the energy level mismatch between the donating excited states of ZnS nanoparticles and the accepting levels of Tb^{3+} ions (vide infra).

The broad excitation spectrum, with an absence of any atomlike band upon monitoring the Tb^{3+} emission, clearly indicates that the electronic structure of ZnS nanoparticles act as an antenna for the Tb^{3+} sensitization (and not from direct excitation of the lanthanide cations). Additional evidence for this interpretation has been obtained from the time-gated spectrum (vide infra).

The broad nature of the nanoparticle emission band indicates that the spectrum consists primarily of surface states or results from the combined emission of core states of variously sized nanoparticles. Peng and co-workers [46] have reported that the bandgap photoluminescence of ZnS nanoparticles is often mixed with a deep trap tail; namely, a bandgap photoluminescence at ~310 nm (fwhm of 10−12 nm) and a broad-band, ~380 nm deep trap emission. A similar broad emission from ZnS nanoparticle surface states was also reported by Chen and co-workers. [16] In addition, Murphy and co-workers [65] reported a broad emission band centered at ~435 nm upon excitation of 5 nm ZnS nanoparticles at 270 nm and have attributed that emission to sulfur vacancies, more generally to shallow electron traps. Although the band maximum is

somewhat shifted, this reported blue emission is qualitatively similar to that observed in this study while exciting the sample at ∼300 nm. Although the chemical nature of the surface states remains unclear, it seems evident that they play a significant role in broadening the emission spectrum. The observation that 1 and 20 min growth time samples have identical emission spectra indicates that the surface state distribution does not change with the growth time for the synthetic parameters that were utilized here.

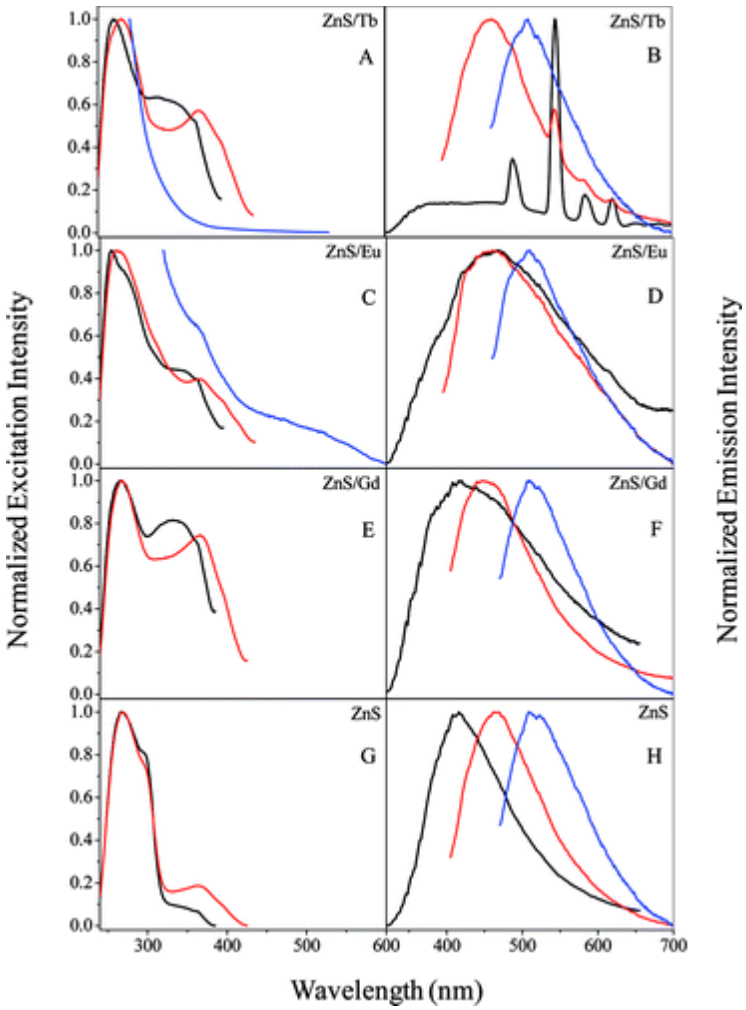

Figure 10.3: Excitation and emission spectra of ZnS nanoparticles

(Left panel) Normalized excitation spectra for λ_{em} = 410 nm (black), 450 nm (red), and 545 nm (blue) (only for ZnS/Tb); and 620 nm (blue) (only for ZnS/Eu). (Right panel) Normalized emission spectra for λ_{ex} = 300 nm (black), 375 nm (red), and 440 nm (blue). All of the spectra are taken in chloroform.

10.3.4 ZnS/Eu Spectra

Figure 10.3D shows the steady-state emission spectra for ZnS/Eu^{3+}. For λ_{ex} = 300 nm, a λ_{em} band was assigned at ~460 nm (ZnS band); for λ_{ex} = 375 nm, a λ_{em} band was found at ~455 nm (ZnS band); and for λ_{ex} = 440 nm, a λ_{em} band was found at ~510 nm (ZnS band). These materials also display a red edge effect. Although this observation is qualitatively similar to the spectral change observed for the ZnS/Tb samples, some differences are evident; in particular, the emission spectrum for λ_{ex} = 300 nm has an emission band maximum similar to that for the spectrum with λ_{ex} = 375 nm. The absence of broad emission with band maximum centered at ~520 nm upon exciting the sample at ~300 nm indicates that the samples under investigation in the present work do not have significant emission from Eu^{2+} (see ref [30] for more details).

Here, we wish to comment on the presence of Eu^{2+} in the ZnS/Eu samples. While working on an extensive tabulation of charge transfer energies to Eu^{3+} in different inorganic materials, Dorenbos could not find any literature information of this data in sulfides.[24] In a previous study, Blasse et al. concluded that for systems in which E_{CT} (Eu^{3+}) < 2.5 eV, Eu^{3+} is not the stable valence state (*Mater. Chem. Phys*. **1987**, *16*, 237−252). The unavailability of this parameter value was taken to be an indication that Eu^{2+} is the stable valence state for Eu compounds where $E_{CT} < E_F$, E_F being the Fermi energy level.[24] However, the possibility of the existence of the Eu^{3+} state in sulfides could not be excluded.[24] The luminescence from

Eu^{3+} ions in sulfide systems is known.[28; 36; 57; 67; 68; 80; 85] The absence of broad emission with band maximum centered at ~520 nm upon exciting the sample at ~300 nm indicates that the samples under investigation in the present work do not display a spectral contribution from Eu^{2+}. With λ_{ex} = 260 nm, Chen and coworkers have reported a broad emission of Eu^{2+} in ZnS/Eu^{2+} nanoparticles with the band maximum located at ~530 nm and assigned it to the allowed $4f^6 5d - 4f^7$ transition.[15] A similar broad Eu^{2+} emission was also observed by Shu-Man and co-workers in Eu-doped ZnS nanoparticles with a band maximum located at ~520 nm (*Chin. Phys. Lett*. **2000**, *17*, 609−611).

Figure 10.3C shows the excitation spectra for ZnS/Eu^{3+}. For λ_{em} = 410 nm (ZnS emission), λ_{ex} bands were identified at ~255, 270, and 350 nm; for λ_{em} = 450 nm (ZnS emission), λ_{ex} bands were assigned at ~260 and 370 nm; and for λ_{em} = 620 nm (attributed to Eu^{3+} emission), a λ_{ex} band appeared at ~360 nm, with a broad excitation band centered at ~510 nm (assigned to a charge transfer transition from anion valence band to Eu^{3+} ions; vide infra).

The luminescence signal from the Eu^{3+} is not clearly evident in the steady-state spectra; however, it becomes prominent in time-gated mode (vide infra). Qualitatively, the less intense Eu^{3+} emission indicates that the ZnS nanoparticles are less efficient in sensitizing Eu^{3+}, as compared with the corresponding Tb^{3+} system. The broad band located on the emission spectrum probably reflects the contribution from surface states, as was discussed previously for ZnS/Tb samples. Similar to the observation found in ZnS/Tb system, no shift in band positions was observed in the emission spectra for 1 and 24 min growth time samples, suggesting that the surface states play an important role.

10.3.5 ZnS/Gd Spectra

Figure 10.3E and F shows the excitation and emission spectra of ZnS/Gd. Other than the lack of Tb^{3+} emission bands, the nanoparticle spectra recorded on ZnS/Gd samples (exclusive of the ions 4f emission bands) were found to be very similar to those recorded for the ZnS/Tb samples in terms of band positions, excitation wavelength dependence and broadness of the spectra, indicating that luminescence sensitization of Tb^{3+} has a negligible impact on the nanoparticle emission in ZnS/Tb samples.

10.3.6 ZnS Spectra

Figure 10.3G and H shows the excitation and emission spectra of ZnS. These spectra show an excitation wavelength dependence (red edge effect) that is similar to that observed for the ZnS/Tb and ZnS/Gd samples, indicating that the red edge effect arises from an intrinsic property of the ZnS nanoparticles and is not caused by the lanthanide ion. The broad nature of nanoparticle emission indicates that the spectrum is strongly influenced by the surface states, as are the samples in which lanthanide ions are incorporated in the nanoparticle.

10.3.7 Time-Gated Excitation and Emission Spectra

Representative time-gated excitation and emission spectra of ZnS/Tb (1 min growth time) and ZnS/Eu (24 min growth time) nanoparticle samples in $CHCl_3$ are shown in Figure 10.4. The attempt to collect spectra for the ZnS/Gd and the ZnS nanoparticles under the same conditions showed only the background signal.

These spectra reveal that the electronic levels of ZnS nanoparticles can be used to sensitize the Tb^{3+} and Eu^{3+} emission. Sharp lanthanide emission bands were clearly visible for both the ZnS/Tb and the ZnS/Eu samples. For the ZnS/Tb sample, the bands with apparent maxima at 490, 545, 585, and 620 nm were assigned to transitions from $^5D_4$ to $^7F_6$, $^7F_5$, $^7F_4$, and $^7F_3$, respectively. For the ZnS/Eu sample, the bands at 590, 616, and 696 nm were assigned to transitions from $^5D_0$ to $^7F_1$, $^7F_2$, and $^7F_4$ respectively.

The excitation spectra, recorded upon monitoring the lanthanide emission, reveal a broad excitation spectrum that is similar to the one recorded for the ZnS nanoparticles upon monitoring their emission at either 410 or 450 nm. These results imply that the same energy route is used to sensitize emission of the ZnS and lanthanide emission, proceeding by energy transfer from the electronic states of the ZnS to the accepting levels of Tb^{3+} or Eu^{3+}. This conclusion is confirmed by the absence of sharp intraconfigurational f−f bands in the excitation spectra, which would indicate direct excitation of lanthanide ions. It is important to note that the energy transfer from the 4f−5d excitation band of Tb^{3+} and the charge transfer band of Eu^{3+} are broad excitation bands and may contribute to the excitation spectrum. The 4f−5d excitation band in Tb^{3+} arises at

~4.8 eV,[23] and for Eu^{3+} (in sulfide compounds), the charge transfer band from the anion valence band to Eu^{3+} occurs at ~2.2 eV.[26] Although excitation at higher energies cannot rule out the possibility of some partial energy transfer from the Tb^{3+} 4f−5d excitation band, the strongest Tb^{3+} and Eu^{3+} luminescence arises from exciting the sample in the 280−350 nm window and argues in favor of the ZnS bandgap excitation being the dominant excitation pathway. However, the luminescence of Tb^{3+} decreases more sharply with increasing wavelength than does that of Eu^{3+} (vide infra, see Figure 10.7 and Table 4S of the Supporting Information [51]), suggesting that the charge transfer excitation from the anion valence band to Eu^{3+} can also play a role in the Eu^{3+} sensitization. It is important to appreciate that the charge transfer band in Eu^{3+} is weak, and its contribution alone cannot account for the sensitization; in particular, that arising from exciting the sample at higher energies.

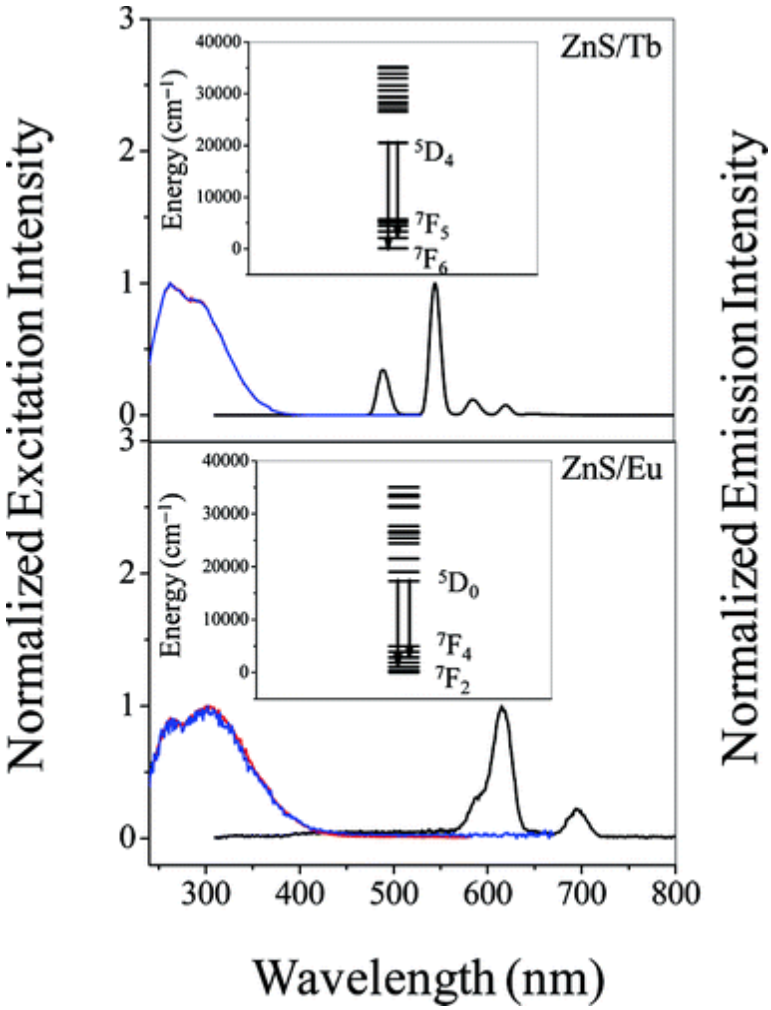

Figure 10.4: Normalized time-gated excitation and emission spectra of ZnS/LnX

Normalized time-gated excitation and emission spectra of ZnS/Tb [λ_{ex} = 300 nm (black), λ_{em} = 490 nm (red), λ_{em} = 545 nm (blue)] (upper panel) and ZnS/Eu [λ_{ex} = 300 nm (black), λ_{em} = 616 nm (red), λ_{em} = 696 nm (blue)] (lower panel) nanoparticle samples in chloroform. Inset shows the electronic transitions associated with the 490 and 545 nm bands for ZnS/Tb, 616 and 696 nm bands for ZnS/Eu.

10.3.8 ZnS Luminescence Lifetime Measurements

Luminescence lifetime parameters for the different systems studied are summarized in Table 1S (see Supporting Information [51]). Table 1S shows values for all parameters in a sum of three exponentials varied in the fitting procedure. To see any obvious trend in the individual lifetime components, the decay data were also fit to a sum of exponentials with lifetime components fixed and varying only the amplitudes (Table 2S; see Supporting Information [51]). This procedure gives rise to somewhat lesser quality fits, as judged by the relative χ^2 value being higher; however, they are adequate and reveal a clear relationship between lifetime components in the different systems. Note that the average lifetime remains relatively unchanged while varying all parameters versus fixing the lifetime components in the fitting procedure. Some representative luminescence decays for 1 min growth time samples are shown in Figure 10.5.

10.3.9 ZnS/Tb Samples

The samples obtained with 1 and 20 min growth time behave similarly in terms of the decay kinetics. The experimental lifetime decays were typically fitted with the sum of three decaying exponentials, with a subnanosecond component that comprises ∼60% of the emission; a 2−3 ns component with ∼30% contribution; and the longest time component (∼10 ns), with an amplitude of ≤∼10%. The average lifetime increases continuously with increasing λ_{em}, which indicates that the emission band shifts with time. Attempts were made to monitor the Tb^{3+} emission by lowering the repetition rate to ∼100 kHz and increasing the full time window to 5

microseconds; in all cases, only the ZnS emission was significant, and no longer time component, which might be related to the Tb^{3+} emission, was observed. At all wavelengths, only the ZnS emission is important. Long-lived Tb^{3+} emission appears as a baseline, as shown in the left panel in Figure 10.5 at 545 nm.

10.3.10 ZnS/Eu Samples

ZnS/Eu behaves differently compared with all other systems. Namely, the longer lifetimes are more dominant in this sample, and the amplitude of the subnanosecond component is much lower. This result suggests that a different energy transfer mechanism may take place. Balandin and co-workers [20] used a theoretical investigation of ZnO quantum dots to predict an increase in the radiative lifetime for a surface-bound ionized acceptor-exciton complex, as compared with the lifetimes of confined excitons and surface-bound ionized donor-exciton complexes. Such a type of complex would give rise to an increase in quantum yield. A comparison of the overall quantum yield of ZnS/Eu^{3+} (0.27 ± 0.02) to that of ZnS/Tb^{3+} (0.12 ± 0.03) corroborates this conclusion. The lack of a long-lived baseline in the ZnS/Eu sample, as compared with the ZnS/Tb sample, reflects the decreased luminescence of the Eu^{3+} bands in the steady-state spectra (Figure 10.3D).

10.3.11 ZnS/Gd Samples

Because of an energy level mismatch between the donating energy levels of the nanoparticles and the Gd^{3+} accepting levels, no Gd^{3+} luminescence is observed. The fact that the ZnS/Gd^{3+} sample's nanoparticle emission is very similar to the ZnS emission of the ZnS/Tb^{3+} shows that the ZnS properties are not sensitive to the presence and nature of the lanthanide cations.

10.3.12 ZnS Samples

The average lifetime of the ZnS sample is comparable to that of the corresponding value in the presence of Tb^{3+} and Gd^{3+}. The ZnS sample's emission lifetime depends on λ_{em} in a fashion that is similar to that found for the lanthanide-containing nanoparticles. Thus, the emission wavelength dependence appears to be an intrinsic property of the nanoparticles and is not associated with the presence of lanthanide ions (Tb^{3+}, Eu^{3+}, and Gd^{3+}) in the system. The origin of the shift might be caused by decays from different donor−acceptor pairs that vary in distance; that is, close pairs emit with faster lifetime at higher energy, and the distant pairs emit at lower energy.[20]

10.3.13 Lanthanide Ion Luminescence Lifetime Measurements

The luminescence lifetimes of the lanthanide cations were recorded using a low repetition rate Nd:YAG laser-based setup. Experimental luminescence signals were fitted best by a biexponential decay for Tb^{3+} and Eu^{3+}. For ZnS/Tb^{3+}, the luminescence lifetime values were found to be 0.92 ± 0.01 and 2.50 ± 0.06 ms, whereas, for ZnS/Eu^{3+}, the corresponding values were 2.0 ± 0.01 and 3.6 ± 0.2 ms. The lifetimes for the Tb^{3+} emission band are similar to those observed for CdSe/Tb^{3+} in a previous study.[19] Two components could arise from different locations of the lanthanide ions in the nanoparticles; for example, Tb^{3+} in the core of the ZnS nanoparticles may be better protected and have a longer luminescence lifetime, whereas the shorter lifetime component may originate from the surface-located Tb^{3+}, which experiences more solvent quenching. Examples of lifetime values for molecular complexes with well-protected Tb^{3+} and Eu^{3+} cation coordination sites are 1.3 and 0.78 ms, respectively.[56] The longer lifetime values recorded in the nanoparticle samples suggest that the lanthanide ions are better protected from quenching through vibrations located in solvent (and in the organic sensitizer for molecular complexes) when in the nanoparticles, as was reported previously by Chengelis et al. for CdSe/Tb^{3+}.[19]

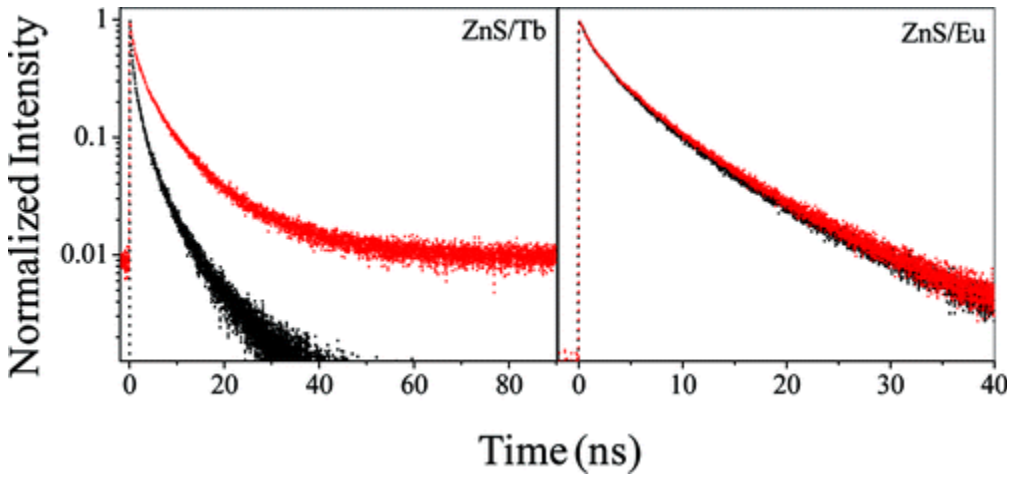

Figure 10.5: Luminescence decay plots are shown for different nanoparticle systems studied in chloroform

Representative luminescence decay plots are shown for different nanoparticle systems studied in chloroform. For ZnS/Tb, the black curve is at λ_{em} = 400 nm (no Tb^{3+} emission), and the red curve is at λ_{em} = 545 nm. For ZnS/Eu, the black curve is λ_{em} = 500 nm (no Eu^{3+} emission), and the red curve is λ_{em} = 618 nm. Luminescence decay parameters are summarized in Tables 1S and 2S of the Supporting Information [51] Supporting Information . The traces have been recorded with a time window that can only give information on nanoparticle electronic structure decay kinetics, as they have shorter emission lifetimes.

10.3.14 A Mechanism for Sensitization of Lanthanide Luminescence

This section considers the possibility of Förster (dipole−dipole interaction) and Dexter (exchange interaction) electronic energy transfer mechanisms in the studied systems, but argues that a different mechanism operates.

The rate of energy transfer under the Förster formulation depends on (a) the spectral overlap of donor and acceptor (J_F), (b) the donor luminescence quantum yield, (c) the donor luminescence lifetime, (d) the relative orientation of donor and acceptor transition dipoles, and (e) the distance between donor and acceptor. Most of the lanthanide transitions (dipolar electric) are formally forbidden and, thus, have a low oscillator strength and a low energy transfer rate by the Förster mechanism. The Förster overlap integral is $J_F \sim 10^{-19}$–10^{-20} M^{-1} cm^3 for the systems studied here, whereas the typical value of J_F for organic fluorophores is on the order of 10^{-13}–10^{-15} M^{-1} cm^3.[82] Assuming a $\Phi_D = 0.2$, one calculates an R_0 of ∼2.5 Å for a lanthanide, which should be compared with a value of $R_0 = 25$ Å for a typical organic fluorophore. The ratio of the rate of energy transfer for organic fluoropohores in comparison with the ZnS/Tb^{3+} nanoparticle samples is $\sim 10^6$. On the basis of this estimate, we conclude that the Förster mechanism is less likely to play a significant role in the energy transfer process for the systems investigated in the present study. More straightforward evidence against the operation of the Förster energy transfer mechanism can be established from a comparison of J_F and R_0 values in the different systems studied (see Table 3S in the Supporting Information [51]). The Förster

model predicts that the Eu^{3+} sensitization should be larger than Tb^{3+} in ZnS nanoparticles for a given distance, by ~3 times; in contrast, the experiments show that Tb^{3+} is at least 2-fold more luminescent than Eu^{3+} (vide infra). In addition, a comparison of the host nanoparticles (ZnS, ZnSe, CdS, CdSe) indicates that the rate of energy transfer to Tb^{3+} should be very similar in ZnS and CdS; however, experiments demonstrate that ZnS is more efficient than CdS in sensitizing Tb^{3+} luminescence (Figure 10.6). It has been assumed that both the nanoparticles have similar luminescence lifetime in absence of acceptors and Tb^{3+} resides at almost equal distance from the nanoparticle sensitizing center.

The rate of energy transfer for the Dexter formulation depends on (a) the spectral overlap of donor emission and acceptor absorption (J_D) and (b) the electronic coupling factor. The Dexter mechanism can account for energy transfer involving forbidden transitions. The fact that the calculated J_D values are very similar in the different systems indicates that the experimental trend in energy transfer rates among the different nanoparticles can only be explained by a concomitant change in the electronic coupling parameter. Although this possibility cannot be excluded, it seems unlikely. Thus, it seems that both the Förster and Dexter energy transfer mechanisms play a negligible role in the energy transfer mechanism of the studied systems.

A number of other plausible mechanisms for luminescence sensitization in rare earth ions in semiconductors have been proposed. For example, Klik et al., in the context of InP/Yb^{3+}, [42] rationalized Yb^{3+} sensitization in InP by this mechanism: (a) excitation of the semiconductor from the valence band to conduction band; (b) capturing of a free electron at a Yb^{3+} related trap; (c) generation of an electron−hole pair on the trap; and (d) nonradiative

recombination of electron−hole pair to excite the Yb^{3+}, thus generating the Yb^{3+} emission. This model was based on earlier studies by Palm et al.,[53] Takahei and co-workers,[73; 82] Thonke et al.,[78] and Needels et al.[52] In molecular systems, Lazarides et al. has discussed a redox-based energy transfer mechanism in the context of molecular d−f complexes.[45] Mechanisms of this type require a detailed knowledge of the dopant energy levels in the host semiconductor.

Although much has been discussed about the lanthanide sensitization in semiconductor materials, considerably less is known about the energy level positions of lanthanide ions in the host material.[54; 62; 75-77] The location of dopant ion energy levels with respect to the valence and conduction bands of the host lattice is of extreme importance because it is useful for predicting the luminescence properties and the charge trapping and detrapping kinetics. Recently, Dorenbos [22-27] addressed the problem of locating lanthanide impurity levels in a host crystal semiempirically and developed a model that relies on three host dependent parameters: (a) the charge transfer energy from the anion valence band to Eu^{3+}, (b) the redshift of the first 4f to 5d transition in appropriate lanthanide ions, and (c) the band gap of the semiconductor material. The fundamental assumptions in this method are that the binding energies of the 4f electrons follow a universal trend and that the charge transfer energy between the anion valence band and Eu^{3+} is equal to the energy gap between the valence band of the host material and the ground state of Eu^{2+}. Once the Eu^{2+} ground state energy level is assigned, all other energy levels can be predicted according to the trend in binding energies.

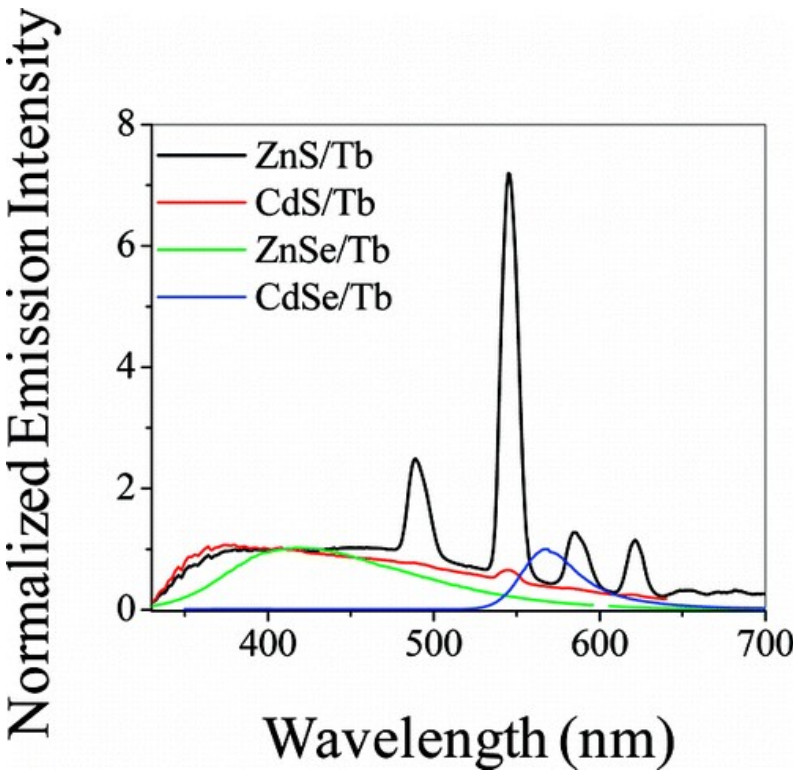

Figure 10.6: Emission spectra of different ZnS/LnX systems studied with $\lambda_{ex} \approx 300$ nm

Emission spectra of different systems studied with $\lambda_{ex} \approx 300$ nm. The ZnS/Tb (black), CdS/Tb (red), and ZnSe/Tb (green) spectra are normalized to unity at 410 nm, and the CdSe/Tb spectrum (blue) is normalized to unity at the band position. These spectra clearly put in evidence the difference in Tb^{3+} luminescence sensitization efficiency by different types of nanoparticles. The ZnSe/Tb spectrum is broken at ~600 nm to eliminate the second order band from the excitation light.

The energy diagram in Figure 10.7 uses this method to predict the energy levels of lanthanide ions in bulk II−VI semiconductor materials. In this diagram, the charge transfer energy was obtained by using Jörgensen's relationship between the charge transfer energy and the Pauling electronegativity of the anions.[38] For sulfides, selenides, and tellurides, we have assumed the charge transfer energy values of 2.17, 2.06, and 0.34 eV, respectively. The value (2.17 eV) for sulfide compounds is in good agreement with the assignment of the charge transfer band (~2.43 eV) in the ZnS/Eu system (vide infra). The parameter values in this scheme were obtained from the work of Dorenbos and co-workers,[25] and the ground state energies of lanthanides were placed in accordance with the systematic trend of 4f electron-binding energies of trivalent lanthanide ions in narrower band gap materials. The energy difference between the 4f ground states of Eu^{3+} and Eu^{2+} was assumed to be 5.70 eV.[26] The higher-lying energy levels of Tb^{3+} and Eu^{3+} were placed from the tabulation of Carnall and co-workers for trivalent lanthanide aquo ions.[12]

The values of the energy levels estimated with this calculation approach compare well with existing data. Wen-lian and co-workers[37] have shown that the Tb^{3+} ground and excited energy levels in ZnS nanoparticles are located at 0.9 eV above the valence band and 0.5 eV below the conduction band, respectively. In a separate study, Chen and co-workers [15] have placed the ground state of Eu^{2+} at 1.6 eV above the valence band of bulk ZnS. Although these values do not match exactly with the values reported in this work, they show sufficiently good qualitative agreement. Considering the typical error of ±0.5 eV, estimated by Dorenbos, the

agreement with the available literature is reasonable. It has to be noted that as long as any systematic error in assigning these energy level values is relatively constant, it should not change the conclusions discussed here.

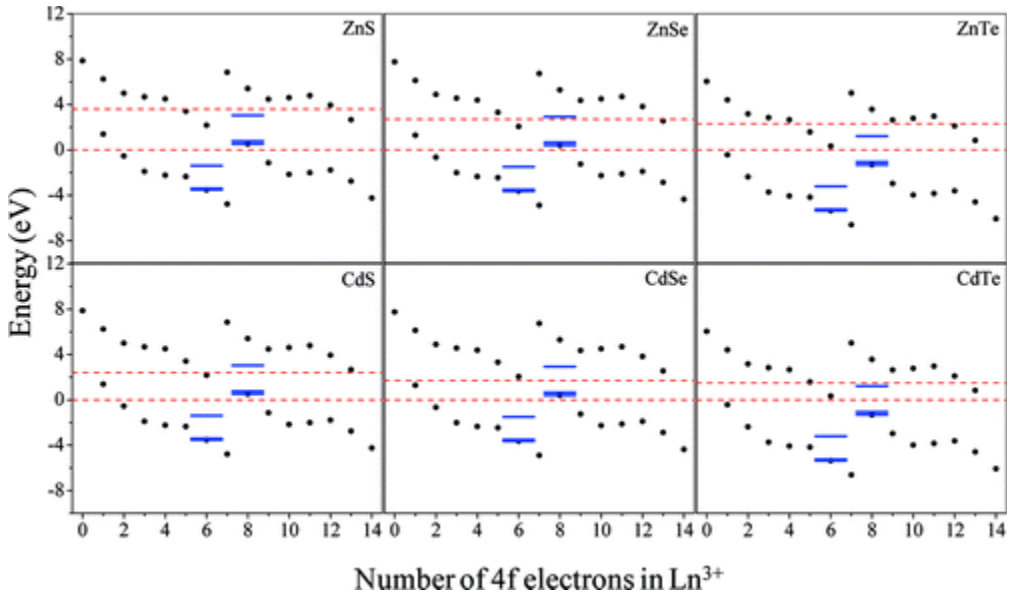

Figure 10.7: Energy level diagram of lanthanide (III) ions in different II−VI semiconductor materials

Energy level diagram of lanthanide (III) ions in different II−VI semiconductor materials based on the method proposed by Dorenbos.[22-27] At each abscissa value, the lower and higher solid circles are the ground state energy of lanthanide (III) and lanthanide (II) ions, respectively. The blue solid horizontal lines at x = 6 and 8 represents the ground and excited states of Eu^{3+} and Tb^{3+} ions. The red dashed lines represent the bulk band gap values; the valence band energy is arbitrarily set at zero. It is worth noting that Tb^{3+} is a potential hole trap in II−VI sulfide and selenide compounds, and Eu^{3+} can potentially act as an electron trap in these compounds.

To determine the charge transfer energy from the anion valence band to Eu^{3+}, the excitation spectra of ZnS/Tb and ZnS/Eu were compared (see Figure 10.8). The band at ~510 nm is assigned to a charge transfer band of Eu^{3+} in the ZnS/Eu system. Note that the red-shifted emission spectrum for ZnS/Eu systems with λ_{ex} = 300 nm could arise from its charge transfer nature. Circumstantial evidence for this assignment in the ZnS/Eu system comes from a comparison of Tb^{3+} and Eu^{3+} emission intensities with different excitation wavelengths (see Table 4S in the Supporting Information [51]). While the intensity of the Tb^{3+} luminescence decreases sharply when exciting the sample with lower energy than the bandgap of the ZnS nanoparticles, the situation is different for the ZnS/Eu system. Considerable luminescence intensity was observed from Eu^{3+} in ZnS nanoparticles, even while exciting the sample at longer wavelength values. Although this observation does not directly prove the existence of a charge transfer band in the ZnS/Eu system, it strongly suggests that some energy level located lower than the bandgap of ZnS nanoparticles exists, and it is involved in the sensitization of Eu^{3+} in the ZnS doped nanoaparticles.

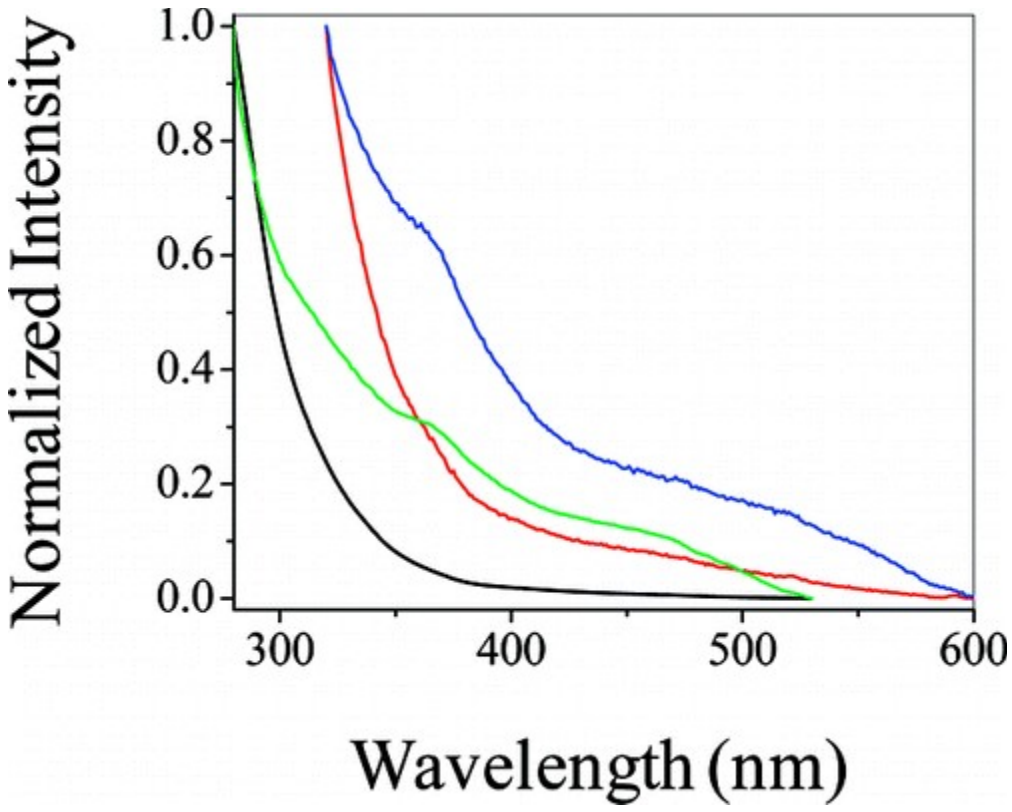

Figure 10.8: Normalized steady-state excitation spectra of ZnS/Tb nanoparticles

Normalized steady-state excitation spectra of ZnS/Tb nanoparticles with λ_{em} = 545 (black) and 620 nm (red). The green and blue curves are the corresponding spectra for ZnS/Eu nanoparticles. Spectra are normalized arbitrarily to the maximum intensity

Several features of the energy level diagram in Figure 10.7 are noteworthy:

1. Both the ground and excited states of Tb^{3+} lie within the band gap of bulk ZnS, an effect that should be more pronounced in nanoparticles because of the quantum confinement and, hence, a higher band gap (~4.2 eV as opposed to 3.6 eV for bulk material). This indicates that the Tb^{3+} can potentially act as a hole trap in ZnS. Moreover, it suggests that the excited electron in the $^5D_4$ level of Tb^{3+} does not undergo ready autoionization. These two conditions result in the enhancement of the Tb^{3+} luminescence in ZnS. It is generally believed that the luminescence efficiency of lanthanide ions is increased when their 3^+ levels act as trap states.[73]
2. The $^5D_4$ level of Tb^{3+} lies above the conduction band of CdSe so that autoionization of the Tb^{3+*} should be efficient, thereby decreasing its luminescence efficiency. Experimentally, the ZnS/Tb^{3+} emission is much stronger than the CdSe/Tb^{3+} emission, for which the overall quantum yields of ZnS/Tb^{3+} and CdSe/Tb^{3+} are 0.12 ± 0.03 and 0.025 ± 0.001, respectively, whereas the Tb^{3+} contribution to the overall quantum yield were found to be 0.05 ± 0.01 and 0.000 015 ± 0.000 003. It should also be noted that the time-gated mode is required to observe the Tb^{3+} emission in CdSe/Tb^{3+},[19] whereas they were readily observable in steady-state mode for ZnS/Tb^{3+} luminescence.
3. The energy level locations of Eu^{3+} are qualitatively different from Tb^{3+} in ZnS, because both the ground and excited states of Eu^{3+} lie below the valence band of ZnS. It is important to note that the ground state of Eu^{2+} lies within the band gap of ZnS, which

makes the system a potential electron trap. On the basis of these considerations, Eu^{3+} can be brought to the excited state by two possible pathways: (1) a bandgap transition of the ZnS host and (2) a ZnS valence band to Eu^{2+} ground state transition. Our observations are consistent with either of these mechanisms.

4. ZnS should be more efficient than ZnSe in sensitizing Tb^{3+} luminescence because as the excited energy level of Tb^{3+} lies close to the conduction band of ZnSe, the excited electrons face a competitive nonradiative path of autoionization. To test this hypothesis, ZnSe/Tb nanoparticles were prepared. The measured Tb^{3+} lanthanide-centered quantum yield value for ZnSe/Tb is 0.000 18 ± 0.000 07 as compared with 0.05 ± 0.01 for ZnS/Tb system, validating this prediction.

5. On the basis of the energy level diagrams, CdS should be more efficient in sensitizing Tb^{3+} luminescence than is CdSe, but similar or less efficient than ZnS. To check this prediction, experiments with the CdS/Tb system were undertaken. Results from these experiments are shown in Figure 10.9. Sharp Tb^{3+} bands are clearly visible at 490 and 545 nm. Interestingly, a band shift in the time-gated excitation spectra with the growth time of nanoparticles is evident and attributed to the effect of quantum confinement. This shift unequivocally points toward the presence of an antenna effect for the Tb^{3+} sensitization. Moreover, on the basis of the ratio of bandgaps and Tb^{3+} emission intensities, it is apparent that the ZnS is more efficient than CdS in sensitizing Tb^{3+} luminescence, which is consistent with the prediction based on the energy level diagrams. The ratio of ZnS bandgap emission to the Tb^{3+} luminescence at ∼545 nm in ZnS and CdS was found to be 1:10:1.4.

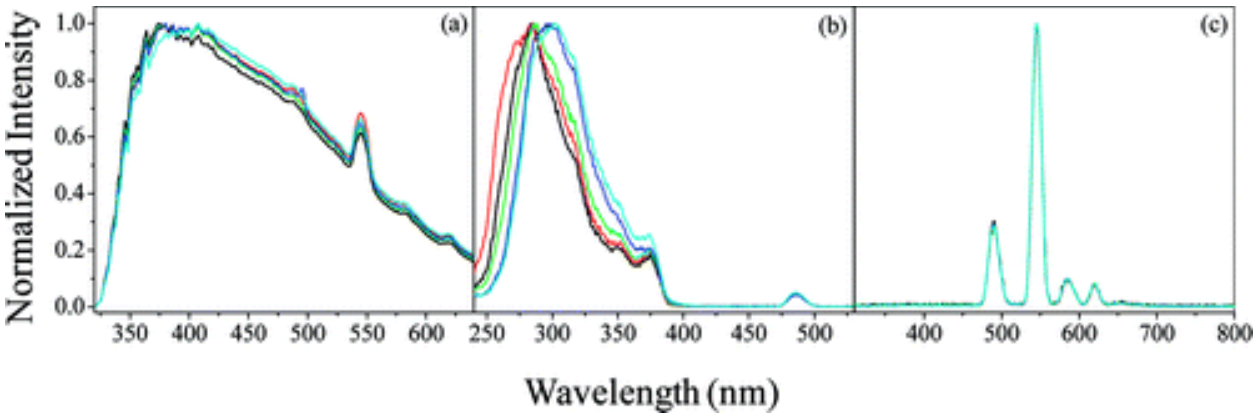

Figure 10.9: Spectra of CdS nanoparticles in chloroform

Normalized (a) steady-state emission with λ_{ex} = 300 nm, (b) time-gated excitation with λ_{em} = 545 nm, and (c) time-gated emission with λ_{ex} = 300 nm of CdS nanoparticles in chloroform with 1 (black), 2 (red), 5 (green), 10 (blue), and 20 min (cyan) growth times. Intensities of the excitation and emission spectra are normalized to the highest intensity of the respective spectra. Sharp Tb^{3+} bands are clearly visible in the steady-state mode. We observe a band shift in the excitation spectra monitoring the Tb^{3+} emission band, which undoubtedly confirms the presence of the antennae effect between the electronic structure of the nanoparticle and Tb^{3+}.

10.4 CONCLUSION

An efficient and less toxic luminescent lanthanide system, consisting of ZnS nanoparticles with incorporated lanthanide ions, has been established. Efficient sensitization was observed for both the ZnS/Tb^{3+} and the ZnS/Eu^{3+} systems. The ZnS/Tb^{3+} nanoparticles appear to be more efficient lanthanide-based emitters, with lanthanide-centered quantum yield values for ZnS/Tb^{3+} and ZnS/Eu^{3+} being 0.05 ± 0.01 and $0.000\,13 \pm 0.000\,04$, respectively. Excitation spectra, while monitoring the lanthanide emission, clearly reveal that ZnS nanoparticles act as an antenna to sensitize the lanthanide luminescence in these systems. Moreover, the absence of observable sharp bands in the excitation spectra indicate that direct excitation of lanthanides has a negligible contribution to the overall sensitization mechanism. These systems represent a significant improvement over the originally proposed system CdSe/Tb^{3+} in their efficiency for lanthanide luminescence sensitization.

The mechanism of lanthanide luminescence sensitization in II−VI semiconductor materials can be rationalized by a semiempirical method proposed by Dorenbos and co-workers. Energy level diagrams indicate that in ZnS, Tb^{3+} can act as a potential hole trap and provide a dramatic increase in sensitization efficiency because its energy levels lie between the nanoparticle band edges. The mechanism of Eu^{3+} luminescence sensitization, on the other hand, follows a different type of mechanism. In ZnS, Eu^{3+} can act as a potential electron trap; hence, the sensitization can be achieved either by direct bandgap excitation or by a valence band to

Eu^{2+} transition. Either mechanism can explain the experimental observations in the ZnS/Eu system. A comparison of lanthanide efficiency in ZnS nanoparticles is made with respect to other II−VI materials. Emphasis is given to Tb^{3+}-doped ZnSe and CdS nanoparticles, both being less efficient than the ZnS nanoparticles in sensitizing the Tb^{3+} luminescence, which is consistent with the predictions based on the energy level positions.

10.5 BIBLIOGRAPHY

[1] **Abiko, Y.; Nakayama, N.; Akimoto, K. and Yao, T.** (**2002**). , Phys. Status Solidi, B 229 : 339.

[2] **Anderson, W. W.** (**1964**). , Phys. Rev. 136 : A556.

[3] **Beeby, A.; Clarkson, I. M.; Dickins, R. S.; Faulkner, S.; Parker, D.; Royle, L.; de Sousa, A. S.; Williams, J. A. G. and Woods, M.** (**1999**). , J. Chem. Soc., Perkin Trans. 2 : 493.

[4] **Bhargava, R. N.** (**1996**). , J. Lumin. 70 : 85.

[5] **Binnemans, K.** (**2009**). , Chem. Rev. 109 : 4283.

[6] **Bol, A. A.; van Beek, R. and Meijerink, A.** (**2002**). , Chem. Mater. 14 : 1121.

[7] **Brennan, J. D.; Capretta, A.; Yong, K.; Gerritsma, D.; Flora, K. K. and Jones, A.** (**2002**). , Photochem. Photobiol. 75 : 117.

[8] **Brus, L. E.** (**1984**). , J. Chem. Phys. 80 : 4403.

[9] **Bünzli, J.-C. G.** (**2010**). , Chem. Rev. 110 : 2729.

[10] **Bünzli, J.-C. G. and Piguet, C.** (**2005**). , Chem. Soc. Rev. 34 : 1048.

[11] Carnall, W. T. and Fields, P. R., **1967**. *Lanthanide/Actinide Chemistry*. American Chemical Society, .

[12] **Carnall, W. T.; Fields, P. R. and Rajnak, K.** (**1968**). , J. Chem. Phys. 49 : 4450.

[13] **Chen, L.; Zhang, J.; Lu, S.; Ren, X. and Wang, X.** (**2005**). , Chem. Phys. Lett. 409 : 144.

[14] **Chen, W.; Joly, A. G.; Malm, J.-O. and Bovin, J.-O.** (**2004**). , J. Appl. Phys. 95 : 667.

[15] **Chen, W.; Malm, J.-O.; Zwiller, V.; Huang, Y.; Liu, S.; Wallenberg, R.; Bovin, J.-O. and Samuelson, L.** (**2000**). , Phys. Rev. B 61 : 11021.

[16] **Chen, W.; Wang, Z.; Lin, Z. and Lin, L.** (**1997**). , J. Appl. Phys. 82 : 3111.

[17] **Chen, Y. and Lu, Z.** (**2007**). , Anal. Chim. Acta 587 : 180.

[18] **Chen, Y. S.; Burgiel, J. C. and Kahng, D.** (**1970**). , J. Electrochem. Soc.: Solid State Science 117 : 794.

[19] **Chengelis, D. A.; Yingling, A. M.; Badger, P. D.; Shade, C. M. and Petoud, S.** (**2005**). , J. Am. Chem. Soc. 127 : 16752.

[20] **Chestnoy, N.; Harris, T. D.; Hull, R. and Brus, L. E.** (**1986**). , J. Phys. Chem. 90 : 3393.

[21] **Dong, L.; Liu, Y.; Zhuo, Y. and Chu, Y.** (**2010**). , Eur. J. Inorg. Chem. : 2504.

[22] **Dorenbos, P.** (**2003**). , J. Phys.: Condens. Matter 15 : 8417.

[23] **Dorenbos, P.** (**2004**). , J. Lumin. 108 : 301.

[24] **Dorenbos, P.** (**2005**). , J. Lumin. 111 : 89.

[25] **Dorenbos, P.** (**2009**). , J. Alloys Compd. 488 : 568.

[26] **Dorenbos, P. and van der Kolk, E.** (**2006**). , Appl. Phys. Lett. 89 : 061122-1−061122-3.

[27] **Dorenbos, P. and van der Kolk, E.** (**2008**). , Opt. Mater. 30 : 1052.

[28] **Ehrhart, G.; Capoen, B.; Robbe, O.; Beclin, F.; Boy, P.; Turrell, S. and Bouazaoui, M.** (**2008**). , Opt. Mater. 30 : 1595.

[29] **Eliseeva, S. V. and Bünzli, J.-C. G.** (**2010**). , Chem. Soc. Rev. 39 : 189.

[30] **Fonoberov, V. A. and Balandin, A. A.** (**2004**). , Appl. Phys. Lett. 85 : 5971.

[31] **Fuhs, W.; Ulber, I.; Weiser, G.; Bresler, M. S.; Gusev, O. B.; Kuznetsov, A. N.; Kudoyarova, V. K.; Terukov, E. I. and Yassievich, I. N.** (**1997**). , Phys. Rev. B 56 : 9545.

[32] **Godlewski, M.; Światek, K. and Monemar, B.** (**1994**). , J. Lumin. 58 : 303.

[33] **Godlewski, M.; Zakrzewski, A. J. and Ivanov, V. Y.** (**2000**). , J. Alloys Compd. 300−301 : 23.

[34] **Gregorkiewicz, T.; Thao, D. T. X.; Langer, J. M.; Bekman, H. H. P. T.; Bresler, M. S.; Michel, J. and Kimerling, L. C.** (**2000**). , Phys. Rev. B 61 : 5369.

[35] **Hildebrandt, N. and Löhmannsröben, H.-G.** (**2007**). , Curr. Chem. Biol. 1 : 167.

[36] **Hou, S.; Yuen, Y.; Mao, H.; Wang, J. and Zhu, Z.** (**2009**). , J. Phys. D: Appl. Phys. 42 : 215105.

[37] **Jing-hua, N.; Rui-nian, H.; Wen-lian, L.; Ming-tao, L. and Tian-zhi, Y.** (**2006**). , J. Phys. D: Appl. Phys. 39 : 2357.

[38] Jörgensen, C. K., **1971**. *Modern Aspects of Ligand Field Theory*. , .

[39] **Kahng, D.** (**1968**). , Appl. Phys. Lett. 13 : 210.

[40] **Kallmann, H. and Luchner, K.** (**1961**). , Phys. Rev. 123 : 2013.

[41] **Kim, Y. H.; Baek, N. S. and Kim, H. K.** (**2006**). , Chem. Phys. Chem. 7 : 213.

[42] **Klik, M. A. J.; Gregorkiewicz, T.; Bradley, I. V. and Wells, J.-P. R.** (**2002**). , Phys. Rev. Lett. 89 : 227401-1−227401-4.

[43] **Krupka, D. C.** (**1972**). , J. Appl. Phys. 43 : 476.

[44] **Kühne, H.; Weiser, G.; Terukov, E. I.; Kusnetsov, A. N. and Kudoyarova, V. K.** (**1999**). , J. Appl. Phys. 86 : 896.

[45] **Lazarides, T.; Tart, N. M.; Sykes, D.; Faulkner, S.; Barbieri, A. and Ward, M. D.** (**2009**). , Dalton Trans. : 3971.

[46] **Li, L. S.; Pradhan, N.; Wang, Y. and Peng, X.** (**2004**). , Nano Lett. 4 : 2261.

[47] **Luchner, K. M.; Kallmann, H. P.; Kramer, B. and Wachter, P.** (**1963**). , Phys. Rev. 129 : 593.

[48] **Meech, S. R. and Phillips, D. C.** (**1983**). , J. Photochem. 23 : 229.

[49] **Montgomery, C. P.; Murray, B. S.; New, E. J.; Pal, R. and Parker, D.** (**2009**). , Acc. Chem. Res. 42 : 925.

[50] **Moore, E. G.; Samuel, A. P. S. and Raymond, K. N.** (**2009**). , Acc. Chem. Res. 42 : 542.

[51] **Mukherjee, P.; Shade, C. M.; Yingling, A. M.; Lamont, D. N.; Waldeck, D. H. and Petoud, S.** (**2011**). *Lanthanide sensitization in II−VI semiconductor materials: A case study with Terbium(III) and Europium(III) in zinc sulfide nanoparticles*, The Journal of Physical Chemistry A 115 : 4031-4041.

[52] **Needels, M.; Schlüter, M. and Lannoo, M.** (**1993**). , Phys. Rev. B 47 : 15533.

[53] **Palm, J.; Gan, F.; Zheng, B.; Michel, J. and Kimerling, L. C.** (**1996**). , Phys. Rev. B 54 : 17603.

[54] Pedrini, C.; Bouttet, D.; Dujardin, C.; Belsky, A.; Vasil'ev, A.; Dorenbos, P. and van Eijk, C. W. E., **1996**. Proc. Int. Conf. Inorg. Scintillators,.

[55] **Petoud, S.; Cohen, S. M.; Bünzli, J.-C. G. and Raymond, K. N.** (**2003**). , J. Am. Chem. Soc. 125 : 13324.

[56] **Petoud, S.; Muller, G.; Moore, E. G.; Xu, J.; Sokolnicki, J.; Riehl, J. P.; Le, U. N.; Cohen, S. M. and Raymond, K. N.** (**2007**). , J. Am. Chem. Soc. 129 : 77.

[57] **Planelles-Aragó, J.; Julián-López, B.; Cordoncillo, E.; Escribano, P.; Pellé, F.; Viana, B. and Sanchez, C.** (**2008**). , J. Mater. Chem. 18 : 5193.

[58] **Przybylinska, H. and Godlewski, M.** (**1987**). , Phys. Rev. B 36 : 1677.

[59] **Przybylińska, H.; Świątek, K.; Stąpor, A.; Suchocki, A. and Godlewski, M.** (**1989**). , Phys. Rev. B 40 : 1748.

[60] **Qu, S. C.; Zhou, W. H.; Liu, F. Q.; Chen, N. F.; Wang, Z. G.; Pan, H. Y. and Yu, D. P.** (**2002**). , Appl. Phys. Lett. 80 : 3605.

[61] **Richardson, F. S.** (**1982**). , Chem. Rev. 82 : 541.

[62] **Sato, S.** (**1976**). , J. Phys. Soc. Jpn. 41 : 913.

[63] **Sato, S. and Wada, M.** (**1970**). , Bull. Chem. Soc. Jpn. 43 : 1955.

[64] **Sivakumar, S.; van Veggel, F. C. J. M. and Raudsepp, M.** (**2007**). , Chem. Phys. Chem. 8 : 1677.

[65] **Sooklal, K.; Cullum, B. S.; Angel, S. M. and Murphy, C. J.** (**1996**). , J. Phys. Chem. 100 : 4551.

[66] Streetman, B. G. and Banerjee, S., **2000**. *Solid State Electronic Devices*. , .

[67] **Sun, L.; Yan, C.; Liu, C.; Liao, C.; Li, D. and Yu, J.** (**1998**). , J. Alloys Compd. 275−277 : 234.

[68] **Sun, X. L.; Zhang, G. L.; Tang, G. Q. and Chen, W. J.** (**1999**). , Chin. Chem. Lett. 10 : 807.

[69] **Świątek, K. and Godlewski, M.** (**1990**). , Appl. Phys. Lett. 56 : 2192.

[70] **Świątek, K.; Godlewski, M. and Hommel, D.** (**1990**). , Phys. Rev. B 42 : 3628.

[71] **Świątek, K.; Suchocki, A. and Godlewski, M.** (**1990**). , Appl. Phys. Lett. 56 : 195.

[72] **Świątek, K.; Suchocki, A.; Przybylinska, H. and Godlewski, M.** (**1990**). , J. Cryst. Growth 101 : 435.

[73] **Takahei, K.; Taguchi, A.; Nakagome, H.; Uwai, K. and Whitney, P. S.** (**1989**). , J. Appl. Phys. 66 : 4941.

[74] **Thibon, A. and Pierre, V. C.** (**2009**). , Anal. Bioanal. Chem. 394 : 107.

[75] **Thiel, C. W.; Cruguel, H.; Sun, Y.; Lapeyre, G. J.; Macfarlane, R. M.; Equall, R. W. and Cone, R. L.** (**2001**). , J. Lumin. 94/95 : 1.

[76] **Thiel, C. W.; Cruguel, H.; Wu, H.; Sun, Y.; Lapeyre, G. J.; Cone, R. L.; Equall, R. W. and Macfarlane, R. M.** (**2001**). , Phys. Rev. B 64 : 085107-1−085107-13.

[77] **Thiel, C. W.; Sun, Y. and Cone, R. L.** (**2002**). , J. Mod. Opt. 49 : 2399.

[78] **Thonke, K.; Pressel, K.; Bohnert, G.; Stapor, A.; Weber, J.; Moser, M.; Molassioti, A.; Hangleiter, A. and Scholz, F.** (**1990**). , Sernicond. Sci. Technol. 5 : 1124.

[79] **Tsimperidis, I.; Gregorkiewicz, T.; Bekman, H. H. P. T. and Langerak, C. J. G. M.** (**1998**). , Phys. Rev. Lett. 81 : 4748.

[80] **Wang, L.; Xu, X. and Yuan, X.** (**2010**). , J. Lumin. 130 : 137.

[81] **White, K. A.; Chengelis, D. A.; Gogick, K. A.; Stehman, J.; Rosi, N. L. and Petoud, S.** (**2009**). , J. Am. Chem. Soc. 131 : 18069.

[82] **Whitney, P. S.; Uwai, K.; Nakagome, H. and Takahei, K.** (**1988**). , Appl. Phys. Lett. 53 : 2074.

[83] **Xueyuan, C.; Wenqin, L.; Yongsheng, L. and Guokui, L.** (**2007**). , J. Rare Earths 25 : 515.

[84] **Yang, C.; Fu, L.-M.; Wang, Y.; Zhang, J.-P.; Wong, W.-T.; Ai, X.-C.; Qiao, Y.-F.; Zou, B.-S. and Gui, L.-L.** (**2004**). , Angew. Chem., Int. Ed. 43 : 5010.

[85] **Yang, H.; Yu, L.; Shen, L. and Wang, L.** (**2004**). , Mater. Lett. 58 : 1172.

[86] **Yassievich, I.; Bresler, M. and Gusev, O.** (**1998**). , J. Non-Cryst. Solids 226 : 192.

11.0 THROUGH SOLVENT TUNNELING IN DONOR-BRIDGE-ACCEPTOR MOLECULES CONTAINING A MOLECULAR CLEFT

Author list: Brittney M Graff, Daniel N. Lamont, Matthew F. L. Parker, Brian P. Bloom, Christian E. Schafmeister, and David H. Waldeck

Author contribution: The author of this dissertation contributed to the photophysical characterization of the molecules, interpretation of the results and the preparation of the manuscript. The author was responsible for the quantum chemistry simulations. This work has been published at J. Phys. Chem. A **2016**, 120, 6004

11.1 INTRODUCTION

Electron-transfer (ET) reactions are essential to many chemical and biological transformations. A nonzero electronic coupling $|V|$ between an electron donor (D) and acceptor (A) unit is a prerequisite for electron-transfer reactions. As detailed by Marcus and others, [18] the strength of the electronic coupling is generally used to categorize ET reactions into a strong coupling or adiabatic charge-transfer regime for which $|V| > >$ kT, an intermediate regime for

which |*V*| is comparable to kT, and a weak coupling/ nonadiabatic regime for which |*V*| < kT; the latter is relevant to the systems discussed herein. In the nonadiabatic limit the ET rate constant may be written as

$$k_{ET} = \frac{2\pi}{\hbar} \cdot |V|^2 \cdot FCWDS$$

Equation 11.1

where FCWDS is the Franck-Condon factor, which contains parameters related to molecular structure and environmental variables. The electronic coupling magnitude may be mediated by covalent and/or noncovalent interactions and depends on the electronic features of the medium through which the electron tunnels. Although often weaker than bond-mediated coupling pathways, electron-transfer involving solvent molecules in the electron tunneling pathway is likely to play an important role for intermolecular electron transfer reactions; consequently, the solvent's electronic structure can play an important role in the ET kinetics.

Over the past three decades the study of well-defined synthetic donor-bridge-acceptor (DBA) systems has led to a better understanding of ET mechanisms and kinetics in nonpolar solvents. Investigations of conformationally restricted linear DBA molecules [12; 16; 32; 34; 43] have demonstrated the distance dependence of bond-mediated coupling. Analogous studies with cleft containing molecules have demonstrated electron tunneling through non-bonded contacts. For C-shaped DBA molecules, in which the D and A units are separated by a solvent-accessible cleft;[8; 30; 35; 45] such coupling appears to be strongest when a single solvent molecule occupies the cleft. The dependence of |V| on the molecular orbital

energetics of the solvent molecule involved in the electron tunneling event has been studied using both C-shaped DBA molecules [30] and U-shaped DBA systems, for which a pendant group is fixed inside the cleft.[6; 31] The U-shaped systems have been used to tune the electronic coupling from the weak (nonadiabatic) limit to the strong (adiabatic) limit and to examine the important role played by solvent dynamics. [7; 25] DBA systems, which demonstrate the influence of macromolecular structural fluctuations on ET rates, have been studied as well.[2; 3; 37] The studies reported here are distinguished from these earlier studies by examining solvent mediated coupling in water and polar solvents.

While early studies examined through solvent coupling in frozen media, conformationally restricted DBA systems provide a way to examine solvent mediated ET in fluid media. The use of rigid C-shaped molecules facilitates the study of solvent-mediated electron transfer by limiting the conformational freedom of the D and A moieties. In many rigid DBA systems, the rate of the DBA systems' structural fluctuations that might affect |V| is fast compared to k_{et}; so that an average value for $|V|^2$ can be used to describe the electronic coupling. In a previous study,[8] the shape of a DBA bis-amino acid oligomer was tailored to produce a well-defined cleft with a line-of-site donor-acceptor distance that was just large enough to accommodate a single water molecule. The observed electron-transfer rate constant in water was significantly higher than in DMSO and was attributed to water molecule(s) in the cleft between the donor and acceptor to mediate the electronic coupling.

This study explores how the photoinduced ET rates of two rigid C-shaped DBA bis-amino acid oligomers are affected by polar solvents. The two compounds have similar donor and acceptor groups but different topologies caused by chiral inversions of two bridge stereocenters. The DBA system D-SSS-A, **1**, forms a molecular cleft with a distance of about 6

Å between the donor and acceptor; whereas the D-RSS-A, **2**, molecule has a more open and flexible cleft (see Figure 11.1 for a molecular structure). These two molecules are similar to the DBA systems reported in a previous study [8], but they display different cleft properties and redox energetics by variation of the acceptor unit. The bis-amino acid bridge units and electron donor moiety, dimethylaniline (DMA), are unchanged from the earlier study. The acceptor unit is attached to the bridge, via a carboxamide moiety, however a methylacetamide substitution is made at the C-6 of the pyrene in an attempt to shift the reaction energetics and modulate the properties of the cleft. This feature allows the reaction Gibbs energy to be extracted from the kinetic data directly and to examine how cleft site polarity affects the solvent mediated electron transfer.

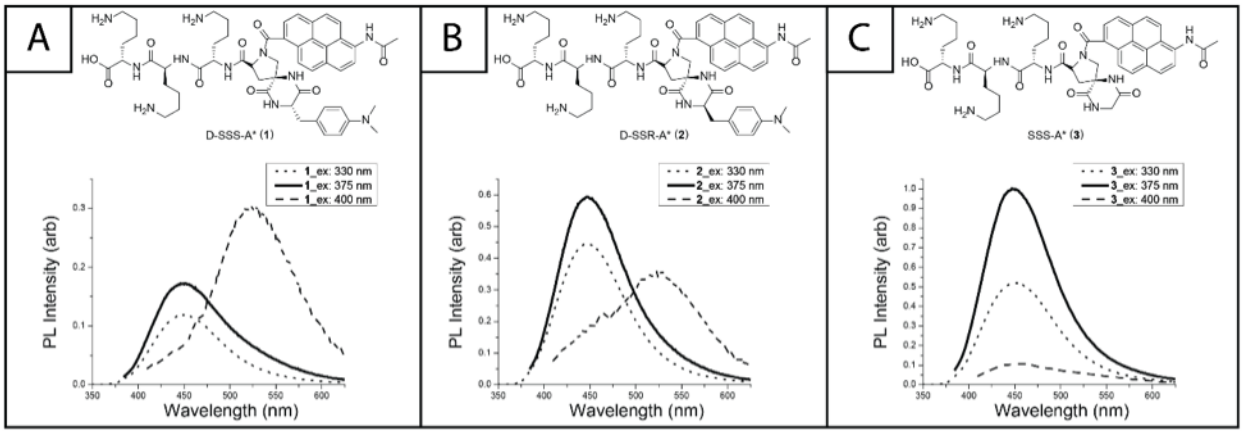

*Figure 11.1: PL spectra and molecular structures of compound **1**, **2**, and **3***

*The figure shows photoluminescence (PL) spectra for aqueous solutions of **1** (A), **2** (B), and **3** (C) at excitation wavelengths of 330 nm (dotted), 375 nm (solid), and 400 nm (dashed). Molecular structures for **1**, **2**, and **3** are shown in the upper portion of each panel. The spectra have been OD corrected and the emission intensity has been scaled for convenience; note that the relative magnitudes of the emission intensity between the panels are accurately reflected by the intensity scale.*

11.2 EXPERIMENTAL

11.2.1 Synthesis

Compounds **1**, **2**, and **3** were prepared using a solid phase peptide chemistry utilizing a 2-chlorotrityl chloride resin similar to that which is described in Chakrabarti et. al.[8] Due to the hydrophilic nature of the compounds, they were liberated from the resin with all protecting groups intact and purified using HPLC, followed by deprotection and subsequent HPLC purification. The final compounds were assessed for identity and purity using NMR and LCMS techniques. The functional pyrene carboxylic acid used to make compounds **1**-**4** was synthesized in 5 synthetic steps and isolated from a mixture of regioisomers. The regiochemistry of the isomer was confirmed using 2D-NMR (See section S3 of the Supplemental Information). All other components used to assemble compounds **1**-**4** were obtained from commercial sources or have been previously described.[6] Compound **4** was prepared using standard solution phase acylation conditions from the same pyrene precursor. See section S1 of the Supplemental Information for more detail on the synthesis and molecule characterization.

Fmoc-Lys(Boc)-OH and Fmoc-Gly-OH were purchased from Novabiochem. O-(7-azabenzo-triazole-1-yl)-N, N,N'N'-tetramethyluronium hexafluorophosphate (HATU) and 2-Chlorotrityl chloride resin were purchased from Genscript. Hexafluoro-2-propanol was purchased from Oakwood. All other reagents were purchased from Sigma Aldrich.

An ISCO CombiFlash Companion was utilized to perform flash chromatography. The cartridges were filled with Bodman 32-63 D grade silica gel. A Waters Xterra MS C18 column (3.5 um packing, 4.6 mm x 100 mm) was utilized with a Hewlett-Packard Series 1200 for HPLC-MS analysis. The solvent system of acetonitrile/water (0.1% formic acid) had a flow rate of 0.8 mL/min. A Waters Xterra column (5um packing, 19 mm X 100 mm) was utilized with the Varian Prostar Prep HPLC system to carry out preparatory scale HPLC purification. The solvent system of acetonitrile/water (0.1% formic acid) had a flow rate of 12 mL/min. A Bruker 500 MHz NMR was utilized to perform NMR experiments. The chemical shifts (δ) reported are relative to the residual solvent peak of the solvent utilized; either DMSO-d_6 or $CDCl_3$. HRESIQTOFMS (high resolution quadrupole time of flight mass spectrometry) analysis was performed at Ohio State University.

11.2.2 Photophysics

Water used in all experiments was purified by a Barnstead Nanopure system, and its resistance was 18.2 MΩ-cm at 25 °C. Dimethyl sulfoxide (99.9+ %), n-methyl-2-pyrrolidone (99.5 %), chloroform (99.8 %), 3-methyl-1-butanol (98+ %), 1-butanol (99.8 %), 1-propanol (99.7 %), ethanol (99.5 %), methanol (99.8 %), citric acid monohydrate (99.0+ %), and sodium phosphate dibasic (99.95 %) were purchased from Aldrich and used without further purification. Samples of **1-3** were readily soluble in DMSO, NMP, methanol, ethanol, and propanol and **4** was readily soluble in chloroform and DMSO. Samples of **1-3** were sonicated and heated to 40 °C for two hours to increase solubility in butanol and 3-methyl-1-butanol.

Samples of **1**, **2**, **3**, and **4** were characterized via absorption and steady-state fluorescence spectroscopy. UV-Vis spectra were collected on a model 8453 Agilent spectrometer and fluorescence spectra were collected on a JY-Horiba Fluoromax-3 spectrofluorometer. Fluorescence spectra were collected at various excitation wavelengths, with 0.34 mm slits and a 0.1 s integration time.

Solutions of **1**, **2**, **3**, and **4** were prepared with an optical density of approximately 0.25 at the absorption peak maximum. All of the solutions, aside from the aqueous solutions, were prepared with molecular sieves in the cuvette. Each solution was freeze-pump-thawed a minimum of three times. The samples were back-filled with argon to reduce evaporation at the higher experimental temperatures and kept moderately above atmosphere by a balloon filled with argon. A temperature cell was constructed from aluminum and controlled using a NESLAB RTE-110 chiller.

Time resolved fluorescence measurements of **1**, **2**, **3**, and **4** were measured using the time correlated single photon counting (TSCPC) technique with a PicoHarp 300 TCSPC module (PicoQuant GmbH).[44] The samples were excited at 375 nm using a picosecond diode laser (PiL037) at a 1 MHz repetition rate. All measurements were made at the magic angle polarization geometry. The data were collected until a maximum count of 20,000 was observed at the peak channel. The instrument response function was measured using colloidal $BaSO_4$, in every case the instrument response function had a full-width-at-half-maximum of ≤96 ps. Emission from the samples was collected on the red side of the emission maximum. The decay curves were fit to a distribution of lifetimes by a convolution and compare method using Edinburgh Instruments fluorescence analysis software technology (FAST).[29]

11.3 RESULTS

11.3.1 Photophysical Model

The donor-bridge-acceptor oligomers in this study form an intramolecular exciplex in polar solvents. The formation of this exciplex is described by a photophysical model that involves a locally excited state and a charge separated state. This model is used to analyze the kinetics and calculate an electron transfer rate.

Figure 11.1 depicts the steady state emission spectra of **1**, **2**, and **3**. Clearly, the spectra of **1** and **2** display a second red-shifted emission that becomes more prominent as the excitation shifts to the red; whereas compound **3** does not. Because **1** and **2** both have the donor (dimethylaniline, DMA) present, but **3** does not, the second red-shifted emission is assigned to the formation of a charge separated state (intramolecular exciplex). While the absorbance spectra of **1**-**3** appear to be the same on the red edge, the excitation spectra show a weak tail on the red edge of the excitation, when the emission is monitored at 525 nm, as compared to 450 nm. Figure S1 depicts these two excitation spectra for a solution of **1** in pH 7 buffer. When exciting at 375 nm (wavelength used in the kinetic studies) the emission from the 'red' species is a small fraction of that observed from the locally excited state; nonetheless both emissions are accounted for in the analysis.

In an effort to confirm exciplex formation, studies were performed to examine the lower energy emission peaks observed in **1** and **2** and rule out excimer formation. Pyrene is known to readily form excimers in solution when the concentration of pyrene is high enough.[17; 36]

Thus, to confirm or exclude excimer formation, **1** and **3** in pH 7 buffer were monitored over a concentration range of 2.3 x 10^{-5} M to 2.2 x 10^{-6} M (see Figure S2). The shape of both the absorbance and emission spectra of **3** did not change with concentration and no red-shifted emission was observed, even in the most concentrated sample of **3**. In contrast, sample **1** displayed a red-shifted emission over the entire concentration range. The intensity of this red-shifted emission did not increase in intensity, nor in proportion to that of the blue (pyrene monomer) emission, at higher concentrations. These data indicate that the red-shifted emission arises from an intramolecular process and is not associated with excimer formation or solute aggregation.

In order to explore whether the red-shifted emission is consistent with charge transfer interactions between the pyrene (acceptor) unit's excited state and the dimethylaniline (DMA) unit (donor), DMA was added to solutions of **3** and to solutions of the N-(6-(pyrrolidine-1-carbonyl)pyren-1-yl)acetamide, denoted **4** (see Figure S3 for the molecular structure) If the charge transfer interaction between the DMA and the pyrene excited state is strong enough, then an intermolecular exciplex can be formed at high enough DMA concentrations.[9; 11; 13; 28] Literature suggests that an exciplex should form when the DMA and pyrene, or similar systems, are in close proximity to one another (approximately between 3 and 8 Å).[4; 24; 33; 41; 42] For deoxygenated solutions of **4** in chloroform (5.6 x 10^{-6} M) an exciplex emission is clearly evident for DMA concentrations in excess of 2.6 x 10^{-4} M (Figure S4). In contrast, DMSO solutions of **4** yielded no resolvable red emission, presumably because the stabilized exciplex is able to dissociate into a solvent separated ion pair, thus quenching the exciplex emission. Note that the excitation spectra for the monomer emission and the exciplex emission are similar, indicating that any ground state association of the pyrene and DMA (Figure

S1) is weak. These data support the assignment of the red-shifted emission in compounds **1** and **2** to the formation of a charge separated state (or intramolecular exciplex); the red tail observed in the excitation spectrum, monitored at 525 nm, suggests that a small percentage of the solution's ensemble of DMA/pyrene conformations may exist in an 'exciplex-like' geometry.

Another feature that supports the formation of a charge separated state is the red shift of the emission peak position (Figure 11.2A) with solvent polarity.[24] Donor-acceptor systems were studied in a series of alcohols, and Figure 11.2B shows a Lippert-Mataga plot made from these data, namely a plot of the solvatochromic spectral shift, $\Delta\upsilon$, versus the Pekar factor Δf. [22; 28] Δf provides a measure of the solvent polarity and is defined by Equation 11.2 [22]

$$\Delta f = \frac{\varepsilon - 1}{2\varepsilon + 1} - \frac{n^2 - 1}{2n^2 + 1}$$

Equation 11.2

where ε is the static dielectric constant and n is the refractive index of the solvent. The plot reveals a roughly linear correlation between the spectral shift and the solvent polarity.[21; 22; 39] The Lippert-Mataga slope can be used to calculate the dipole moment of the donor acceptor system assuming that there is a sphere encompassing the donor and acceptor moieties. If one assumes a 9.2 Å and 8.5 Å radius spherical cavity for **1** and **2** respectively,[23] then the slopes of 19100 cm^{-1} and 37000 cm^{-1} from this plot give an effective dipole moment of 38 D for

1 and 43 D for **2**. This approximation is not always accurate; however the differences between the encompassing ellipsoid and sphere are moderate for **1** and **2** (Supplemental Section 7); *vide infra*.

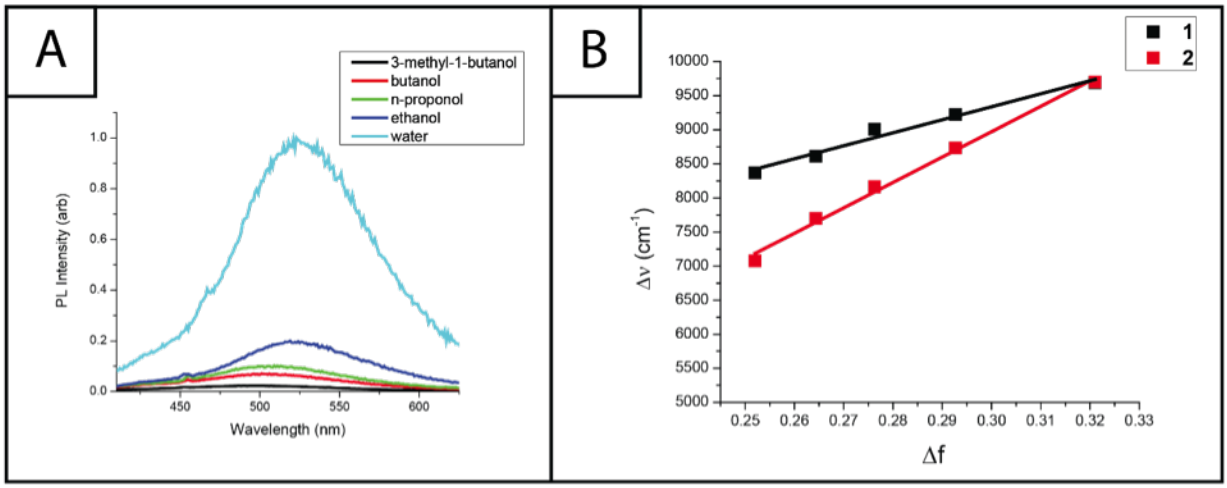

*Figure 11.2: Emission spectra of **1** in different solvents and Lippert-Mataga plot of **1** and **2***

*Panel A shows emission spectra (optical density corrected) of **1** in a variety of different solvents - 3-methyl-1-butanol (black), butanol (red), propanol (green), ethanol (blue), and pH 7 buffer (cyan) . In panel B a Lippert-Mataga plot is shown for **1** and **2** in a series of normal alcohols. An analysis of the correlation between solvent polarity and the emission band red-shift is consistent with a 38 D dipole moment for **1** and a 43 D dipole moment for **2**; see text for details.*

The red-edge emission from **1** is consistent with th e formation of an intramolecular exciplex. The featureless charge transfer band is red-shifted from the pyrene locally excited (LE) state's emission. The intensity and existence of the charge transfer emission relative to the LE state emission is dependent on the presence and concentration of donor (dimethylaniline) when the donor and acceptor are free in solution. When the donor and acceptor are attached as in **1** or **2**, the charge transfer emission is not enhanced relative to the LE state emission by increasing the concentration, which indicates that the charge transfer emission results from intramolecular donor-acceptor interactions. Furthermore, the second emission red-shifts (charge separated state becomes more stable) with solvent polarity.

Interestingly, the charge transfer emission peak of **1** is most prominent in water (Figure 11.2A). In a traditional exciplex reaction scheme, the excited state complex, or contact ion pair, is stabilized as the solvent polarity increases;[14; 21; 22; 27] and it eventually dissociates. For the intramolecular case ion pair dissociation does not occur; rather, the molecule can undergo back electron transfer to the locally excited state or it can relax back to the ground electronic state by either radiative or nonradiative relaxation (Figure 11.3). The charge separated (CS) state is stabilized by solvent polarity (ie., the emission redshifts with increasing solvent polarity). As the CS state energy becomes lower in energy than the locally excited (LE) state, the probability of back electron transfer to the LE state decreases. Thus, stabilization of the CS state relative to the LE state can increase the CS state's quantum yield of emission because the back electron transfer to the LE state is slower; however, the stabilization of the CS state decreases the energy gap to the ground electronic state and increases the internal conversion rate. The balance of these competing effects determines the polarity at which the CS state's emission will be the

strongest. The kinetic scheme shown in Figure 11.3 is consistent with the spectral data and can be used to rationalize the excited state photophysics; below it is used to extract rate constants from the excited state decay law.

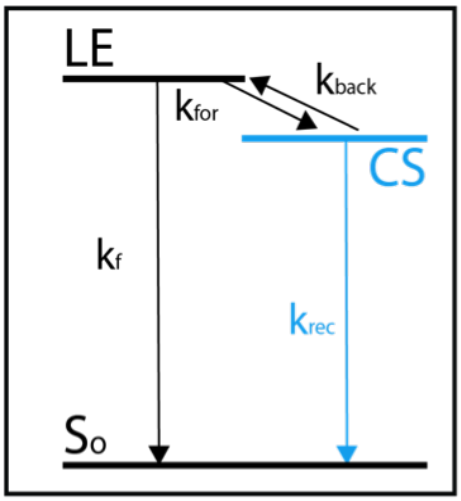

Figure 11.3: Kinetic scheme for charge separated state formation

The diagram depicts the kinetic scheme for the intramolecular exciplex, charge separated state (CS), formation.

11.3.2 Kinetic Analysis

The time-correlated single photon counting method was used to measure the fluorescence intensity decay of molecules 1, 2, and 3 in aqueous buffer at pH=7, dimethylsulfoxide (DMSO), and N-methylpyrrolidone (NMP). All samples were excited by 375-nm radiation. Fluorescence decay profiles were fit using the discrete component analysis, and the distribution of lifetime algorithms provided by the Edinburgh Instruments FAST™ software package. Fluorescence decay profiles of 1 and 2, which were collected at the steady-state LE fluorescence emission maximum, produced discrete exponential fits of three or more distinct components, and lifetime distributions with complex shape. This behavior has been attributed to interactions arising from the bridge pendant groups that are added for solubility purposes (see Supplemental Information, section 6). When the observed fluorescence emission band was red-shifted from the LE emission maximum towards the CS emission, the lifetime distributions displayed a bimodal character and a discrete component analysis consisting of two exponential terms could be used. In addition, single mode lifetime distributions were observed for the bridge-acceptor only compound, 3. For these reasons the observation window was chosen to be 525 nm.

The kinetic scheme proposed in (Equation 11.3) assumes that the photo-excitation of the modified pyrene carboxamide acceptor populates the LE state, the initial population of the CS state is zero, and the observed fluorescence signal arises from a combination of LE $\rightarrow S_0$ and CS $\rightarrow S_0$ radiative emission. In this scheme k_{for} is the forward electron-transfer rate constant, k_{back} is the backward or reverse electron transfer rate constant, and k_{rec} is the rate constant for recombination from the CS state to the ground electronic state. The difference between the assumptions of this model and of the model reported in previous works, [30; 35; 45] , is

the observation of fluorescence originating from two states (see Section S3 of Supplementary Information). Solving the differential equations for this kinetic model, a decay law with a double exponential form is obtained

$$I(t) = I(0)\left[a_{+}\exp(-k_{-}t)+(1-a_{+})\exp(-k_{-}t)\right]$$

Equation 11.3

where a_{+} is the fraction of fluorescence decaying with the fast rate constant k_{+}, k_{-} is the rate constant of the slow fluorescence decay, α is the fraction of fluorescence arising from LE → S_0 emission, and β is the fraction from the CS → S_0. The parameters in this decay law can be used to obtain the primary rate constants

$$k_{for}=\left(a_{+}\left(k_{+}-k_{-}\right)+k_{-}-k_{f}\right)\left[\frac{\alpha}{\alpha-\beta}\right]$$

Equation 11.4

$$k_{back} = \frac{\left(k_{+} - k_{-}\right)^2 - \left[2 \cdot \left(k_{for} + k_f\right) - \left(k_{+} + k_{-}\right)\right]^2}{4\,k_{for}}$$

Equation 11.5

and

$$k_{rec} = k_{+} + k_{-} - k_f - k_{for} - k_{back}$$

Equation 11.6

The intrinsic fluorescence decay rate k_f is the decay rate given by the control molecule, the bridge-acceptor compound **3**, for which the electron transfer pathway is not possible.

In order to relate the predicted decay law to the observed lifetime distributions, a distribution fitting protocol was developed. This protocol splits a bimodal distribution into a short-time distribution and a long-time distribution, and it calculates the distribution statistics used to parametrize the predicted decay law. Two kinds of bimodal distributions were observed for the data (see Figure 11.4). In the first kind, the short-time and long-time distributions are clearly separated. The well separated short-time distributions typically demonstrate a constant positive slope from its onset to 90% of the maximum amplitude value, and a segment of constant negative slope after the maximum amplitude followed by an exponentially decreasing segment. Well separated distributions were observed for molecule **1** at temperatures below 333 K. In the second kind of distribution, the short-time and long-time distribution components overlap with

each other. Here the two segments of constant slope near the amplitude maximum were used to isolate the short-time and long-time distributions. After separation of the two distribution components, normalized distribution amplitudes were used to weight the sampling of each distribution. Short and long time distributions were sampled 1000 times and the 25^{th}, 50^{th}, and 75^{th} percentiles were calculated. The 50^{th} percentile value of the short and long time distributions were used to determine k_+ and k_-, respectively, see Figure 11.5.

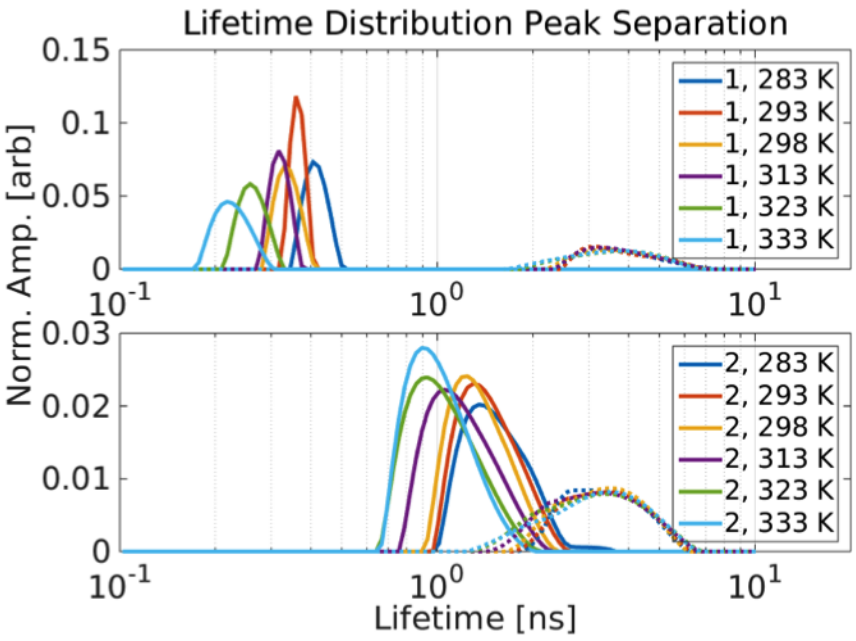

*Figure 11.4: Lifetime distributions of **1** and **2** in pH=7 buffer*

*The top panel shows the lifetime distribution for **1** in pH=7 buffer, and the bottom panel shows the lifetime distribution for **2** in pH=7 buffer. In each case the lifetime distributions could be separated into short-time (solid lines) and long-time (dashed lines) components.*

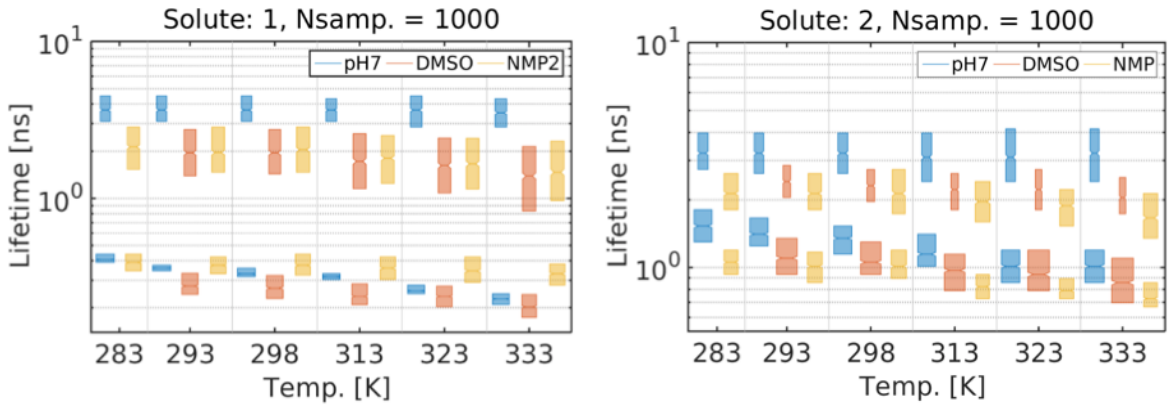

*Figure 11.5: Summary of lifetime decay distributions of **1** and **2***

*This figure shows a box plot representation for separation of the fluorescence decay lifetime distribution into short-time and long-time components. The left panel shows the lifetime distribution for **1**, and the right panel shows the lifetime distribution for **2**. The central line of each box represents the median value. Edges of the boxes represent the 25th and 75th percentiles.*

The temperature dependence of the forward and backward electron transfer rate constants are shown in Equation 11.6. Because of the double exponential character of the excited state decay law, it is possible to determine the reaction Gibbs energy directly from the rate constants as described in Equation 11.7; see Table 4. The free energy of the LE → CS reaction, $\Delta_r G$, is given by

$$\Delta_r G = -RT \ln\left(\frac{k_{for}}{k_{back}}\right)$$

Equation 11.7

Figure S5 plots the reaction free energy as a function of temperature and shows that the dependence on temperature is very weak. In fact, the free energies observed over the temperature range in each solvent are smaller than the spread in the k_+ and k_- caused by the inherent width of the lifetime distributions. In Table 4 $\Delta_r G$ values for each solvent are reported at T = 298 K.

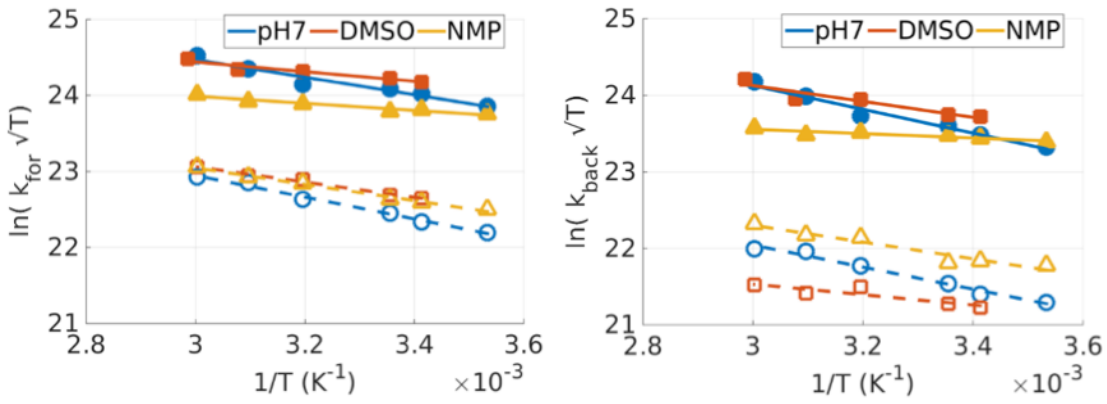

Figure 11.6: Temperature dependence of the forward and back ET rate constants

*The temperature dependence of the forward (left panel and back (right panel) electron transfer rate constant of **1**, DsssA, (filled symbols) and **2**, DsrrA, (open symbols) are shown.*

*Table 4: Reaction free energy for the DBA oligomers **1** and **2** in different solvents, in eV*

Solvent	**ε_s**	**n^2**	**$\Delta_r G$ of 1**	**$\Delta_r G$ of 2**
Water (pH7)	80.1	1.77	-0.013	-0.023
DMSO	46.7	2.19	-0.012	-0.036
NMP	32.3	2.16	-0.008	-0.021

DMSO is dimethylsulfoxide and NMP is N-methylpropionamide

11.3.3 Electron Transfer Rate Analysis

The electron transfer rate constant analysis used a semi-classical version of the Marcus expression.[1; 15; 18; 40; 45] For a single effective quantum mode, the rate constant k_{ET} can be written as

$$k_{ET} = \frac{2\pi}{\hbar}|V|^2 \frac{1}{\sqrt{4\pi\lambda_s k_B T}} \sum_{n=0}^{\infty} e^{-S}\left(\frac{S^n}{n!}\right) \exp\left(\frac{-(\lambda_s + \Delta_r G + n h\nu)^2}{4\lambda_s k_B T}\right)$$

Equation 11.8

where k_B is the Boltzmann's constant, |V| is the electronic coupling matrix element, $\Delta_r G$ is the reaction free-energy, λ_s is the outer-sphere or solvent reorganization energy, ν is the frequency of the effective quantized vibrational mode, and S is the Huang-Rhys factor given as the ratio of the inner-sphere reorganization energy, λ_v, to the quantized mode energy spacing, $\lambda_v / h\nu$. The hν term refers to the energy of a single effective quantized mode associated with the electron transfer reaction; it is specific to the solute vibrational manifold and is not very sensitive to solvent and temperature. Thus, hν and λ_v are fixed at values appropriate for the donor and acceptor, and they are not changed as the bridge, solvent, and temperature change.

The lines of best fit in Figure 11.6 represent fits to the semi-classical electron-transfer rate equation (Equation 11.8). The data reveal that the forward (and backward) electron transfer rate for **1** in the three solvents are significantly higher than that of **2** in the same three solvents.

Given that **1** and **2** have the same donor and acceptor units and the two bridges are diastereomers of one another, the difference in the electron transfer rate occurs because of the different spatial positioning of the donor and acceptor with respect to each other. In this analysis, 1400 cm^{-1} was used as the value for the single effective quantized mode and 0.30 eV for the inner-sphere reorganization energy. These values are the same as those used in previous work on donor-bridge-acceptor systems having the same donor and a similar acceptor group; note that this frequency value is typical of that for carbon-carbon stretching frequencies in aromatic ring systems.[1; 8; 20] While roughly the same values for hν and λ_v were assumed as in Chakrabarti, et. al.[8], these values may have some variation because the pyrene moiety was modified in this set of experiments. Although an error in the internal reorganization energy affects the absolute magnitude of the electronic coupling that is extracted from fits to the semiclassical equation (Equation 11.8), the relative values of the coupling for the same solute in different solvents is not sensitive to the choice of internal reorganization energy.[20] Note that the redox potential of the pyrene is changed by the amide modification, and it is expected to decrease the reduction potential of pyrene.[10; 19]

The slopes of the plots in Figure 11.6 are largely determined by the Gibbs reaction energy and the reorganization energy for the electron transfer, whereas the intercepts depend largely on the electronic coupling. If one considers only the first term (n=0) in Equation 11.8, the classical Marcus expression is obtained and the activation Gibbs energy may be obtained directly from the slope of the graph. The solvent reorganization (λ_s,empirical) and the electronic coupling ($|V|$, empirical) that are obtained from best fits of Equation 11.8 to the data are reported in Table 5, along with the activation Gibbs energy that is extracted from the slope. Note that the electronic coupling values which are obtained by fits of the data to Equation 11.8 are weakly dependent on λ_S; see Figures S6-S12 in the Supplemental Information.

*Table 5: The activation Gibbs energy ($\Delta G^{\ddagger}$), solvent reorganization energy (λ_s), and electronic coupling ($|V|$) of **1** and **2** in different solvents at 298 K*

Sample	**$\Delta G^{\ddagger}$ (eV) classical limit**	**λ_s (eV) empirical**	**λ_s (eV) ellipsoid model**	**$|V|$ (cm^{-1}) empirical**	**$|V|$ (cm^{-1}) ellipsoidal model**
1 pH7	0.10	0.42	0.42	32±8	34
1 DMSO	0.05	0.23	0.23	12±2	9
1 NMP	0.04	0.16	0.16	7±1	5
2 pH7	0.12	0.52	0.53	22±7	26
2 DMSO	0.09	0.40	0.40	12±3	8
2 NMP	0.09	0.40	0.40	13±3	8

Note that the reaction Gibbs energies are reported in Table 4

To assess better the trends observed in the reorganization energy and electronic coupling parameters, the data were analyzed in the framework of a continuum dielectric model. The reorganization energy λ_S was modeled by treating the change in the DBA molecule's electrostatic charge distribution by a dipole moment within a symmetric ellipsoidal cavity; namely

$$\lambda_S = \frac{\Delta\mu^2}{2cb^2}\left(\frac{1}{n^2}-\frac{1}{\varepsilon_S}\right)\sum_{n=1}^{n=\infty} X_n = \frac{\Delta\mu^2}{2cb^2}\left(\frac{1}{n^2}-\frac{1}{\varepsilon_S}\right)\Sigma$$

Equation 11.9

in which c and b are the ellipsoid's radii and $\sum$ is a shape factor that can be evaluated numerically.[5] In order to parametrize this model, the semiempirical molecular orbital package MOPAC2012 was used to study the molecular structures of **1** and **2**. Using the PM7 Hamiltonian, optimized molecular geometries and molecular orbitals were determine for cases in which DBA molecule clefts contained 0, 1, or 2 solvent molecules. The results of these calculations were visualized and analyzed using the three-dimensional chemical structures package Jmol.[26; 38; 46] Prolate spheroids approximately circumscribing the solvent excluded surface of the optimized solvent-DBA systems (see Figures S21 to S27) were used to determine the ellipsoidal radii. Assuming a full charges moves from the donor to the acceptor; the calculated distances between the nitrogen atom of the donor moiety and the carbon atoms of the pyrene ring were used to obtained $\Delta\mu$.

The solvent reorganization energy was calculated using the dipole moments given in Table 6, however the ellipsoid's volume was adjusted to give a good fit with the data; see Figure 11.6. The dipole moments (μ) are calculated using the average distance between the donor ring nitrogen and the acceptor ring carbons, and the μ_{min} were calculated in a similar manner using the minimum distance. The dipole moments calculated using the spheroid model (Table 6) closely mimic the dipole moments that were calculated using the Lippert-Mataga plot (Figure 11.2), which approximate the molecular cleft by an effective sphere of radius r_{sphere} ($V_{sphere} = 4/3\,\pi r_{sphere}^3$) . By keeping the ellipsoid shape fixed (namely the shape factor Σ) but adjusting its volume ($V_{spheriod} = 4/3\,\pi c\, a^2$), to fit the experimental data in Figure 11.6, the solvent reorganization energies reported in Table 5 (as λ_s, ellipsoidal model) were obtained. Using these reorganization energies, one finds the electronic coupling parameters reported as |V|, ellipsoidal model in Table 5. These values are in reasonable agreement with those found by an empirical fit of the data in which the reorganization is varied as a free parameter.

Table 6: Parameters for the CS state dipole moment and solute-solvent complex geometries

Solvent	**Solute**	**r_{sphere} (Å)**	**c (Å)**	**a (Å)**	**V_{sphere} ($Å^3$)**	**$V_{spheriod}$ ($Å^3$)**	**Σ (scale)**	**μ (D)**	**μ_{min} (D)**
H_2O	1	9.2	10.0	7.0	3263	2053	0.86	30.9	28.5
NMP	1	9.0	9.5	7.1	3054	2006	1.20	35.1	31.5
DMSO	1	9.5	9.5	8.1	3591	2611	1.14	42.1	38.2
H_2O*	2	8.0	8.7	8.7	2145	1786	0.91	33.5	24.7
H_2O	2	8.5	9.0	9.0	2572	2235	0.95	39.5	30.5
NMP	2	8.5	9.5	9.5	2572	2421	0.95	41.1	34.0
DMSO	2	8.5	9.3	9.5	2572	2619	0.98	43.5	35.8

** indicated the lowest energy configuration of 2 with two H2O molecules.*

Note that the scaling factor Σ for **1** in water is quite different from the scaling factor for solute **1** in the other solvents (NMP and DMSO) and the "loose-cleft" forming systems, **2**, in all solvents. Water has the most interaction with the cleft, as suggested by the electron transfer data. The solvent water facilitates electron transfer most efficiently in DBA solute **1**, as indicated by the large coupling parameter (see Table 5). Because water has the most interaction with the cleft, particularly in **1**, the scaling factor is less predictable. In system **2** multiple waters can fit into the cleft, thus an individual water molecule does not have as significant interaction with the cleft.

11.4 DISCUSSION

These studies build on the earlier work of Chakrabarti et. al.,[8] by investigating an amide substituted acceptor unit which can interact favorably with a hydrogen bonding solvent. The donor unit used in both systems is the same. Although amide modification has a small effect on the overall molecular volume, the cleft size changes somewhat with the solvent type, *vide infra*. In addition, amide modification causes a red-shift in the absorption spectrum, decreases the excited stated lifetime, and alters the energetics of the electron transfer reaction. In particular, the $\Delta_r G$ for the amide modified pyrene system is significantly smaller than that of the unmodified pyrene system. This decrease in the $\Delta_r G$ facilitates the equilibrium between the locally excited state and the charge separated state and allows for a significant charge transfer emission to be observed; in contrast to the unsubstituted case of Chakrabarti et. al. for which no charge transfer emission could be seen.

The time resolved fluorescence of **1** and **2** was collected at the red edge of the emission spectrum because it displayed a double exponential decay law. The decay law at more blue emission wavelengths had a third component, which was traced to a direct interaction between the solubilizing lysine groups on the bridge and the acceptor (see Supplemental Information). The red edge emission arises from both the locally excited state and the charge separated state; however this could be modeled quantitatively in the kinetic scheme for the reaction. This kinetic scheme, shown in Figure 11.3, was used to extract the $\Delta_r G$ for the reaction directly from the kinetic data.

The $\Delta_r G$ values for **1** and **2** are significantly different from the $\Delta_r G$ that were used to model the electron transfer for the corresponding donor-bridge structure and unsubstituted pyrene acceptor, which were reported to be -0.66 eV and -0.54 eV in water.[8] Most of the shift in the $\Delta_r G$ arises from the amide functionality that has been added to the pyrene. This fact was confirmed by performing ultraviolet photoelectron spectra (UPS) of the bridge-acceptor molecules (see Figure S14), and it is supported by literature data on similar systems.[10; 20] The $\Delta_r G$ for **1** and **2** are the same within experimental error; in contrast the 'tight' and 'loose' cleft molecules reported on by Chakrabarti [8] differed by 0.1 eV. These facts support a view that the amide modification changes both the intrinsic reduction potential of the acceptor and the solvation of the acceptor, as compared to the unsubstituted pyrene system. The amide substitution may open the cleft and reduce the hydrophobic interaction between the donor and acceptor; potentially, allowing it to incorporate multiple solvent molecules.

This view of the cleft is consistent with the difference in solvent reorganization energy found for this system as compared to that reported by Chakrabarti [8] for the unsubstituted case. In the unsubstituted case, the π-π and hydrophobic interactions control the solvation

environment of the cleft, so that a large solvent reorganization occurs upon formation of the charge separated state. For DBA systems **1** and **2** the cleft environment is already somewhat polar. Note that the reaction Gibbs energy and reorganization parameters in the semi-classical equation are highly coupled, and Chakarabarti [8] was unable to experimentally determine $\Delta_r G$ in the donor-bridge-acceptor system; hence the absolute difference in the reorganization energies should not be interpreted too strictly.

In order to examine the features of the molecular cleft more quantitatively, quantum chemistry (PM7) simulations of **1** and **2** with solvent were performed. These calculations showed that the cleft in **1** and **2** was able to adapt to the size of the solvent molecules studied (water, DMSO, and NMP). For the case of DMSO and NMP (see SI) only one solvent molecule was able to fit in the cleft of **2**, and similarly only one solvent molecule could fit in the cleft of **1**. The contact surfaces and the donor to acceptor distances for these cleft/solvent systems were similar, and this finding is compatible with the similar reorganization energies and electronic couplings reported for these systems.

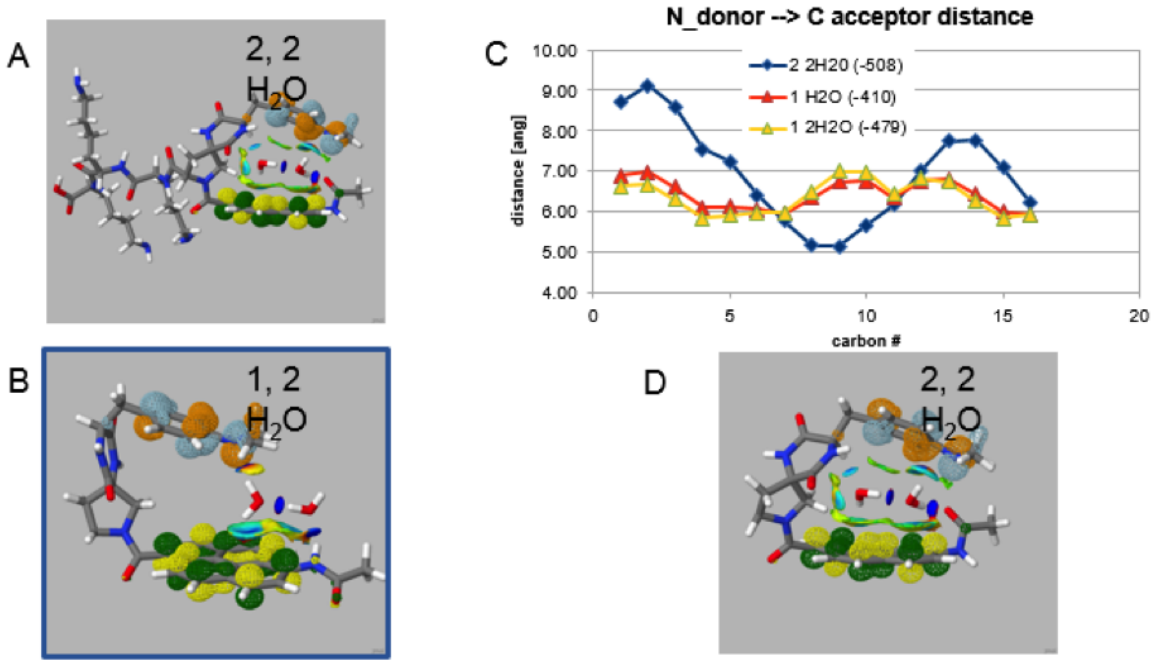

Figure 11.7: HOMO and LUMO molecular orbitals of two DBA molecules

Frontier HOMO(orange/grey) and LUMO(yellow/green) molecular orbitals are shown for the two DBA molecules with water. In panel A the entire DBA structure is displayed. Panel C shows a plot of the distance between the nitrogen atom of the donor and the carbon atoms of the pyrene ring at the optimized geometry. The expanded view in panels (B) and (D) the lysine moieties have been removed to facilitate observation of the DBA cleft region. The interaction surface of the solvent molecules is shown, as well.

Simulations of **1** and **2** with water solvent were performed for both one and two solvent molecules in the cleft (see Figure 11.7 and SI). For both solutes the cleft could accommodate one water molecule; however the loose cleft (**2**) had a better van der Waals contact with two water molecules present than with one. Panel 7b shows the energy minimum for two water molecules in the cleft of **2** and panel 7d shows the energy minimum for two water molecules in the cleft of **1**. The tight cleft does not let the water molecules fill it, whereas the loose cleft does. Panel 7c shows plots of the distance between the donor N atom and the different C atoms of the pyrene acceptor for the tight cleft (**1**) with one and two water molecules and the loose cleft (**2**) with two water molecules; note that the loose cleft with one water molecule had no clear energetic minimum. Note that the tight cleft's distances change only slightly in accommodating more than one water molecule, and that these distances range from 6 to 7 Å depending on ring location. In contrast the loose cleft shows a broader range of distances (5 to 9 Å) and it has some regions of the ring closer to the donor N. These data underscore the different cleft geometries, yet are consistent with the similar electronic couplings that are found for water. Namely, the electron tunneling is controlled by distance and although the loose cleft has a small area of the acceptor placed closer to the donor, most of it is farther from the donor than the distances for the tight cleft. The calculations show that the contact interaction with the solvent controls the donor to acceptor distance. Although **2** has a few 5Å contact interactions, its average contact distance is 7 Å; whereas molecule **1** has an average of 6.4 Å. The net result appears to be a similar coupling for the two cases.

electronic coupling would be higher for the case of water than the other cases, in agreement with the fits to the data; see Table 5. NMP and DMSO both facilitate electron transfer, however the rate constant is smaller because the donor to acceptor distance is larger and hence it has a smaller electronic coupling. Because the cleft spacings are similar for **1** and **2** with DMSO and NMP, the electronic couplings are found to be similar. Thus, the ability of the cleft to accommodate different sizes and numbers of solvent molecules gives rise to a behavior that is more rich than that found for the strictly hydrophobic donor-acceptor system reported by Chakrabarti.[8]

11.5 CONCLUSION

The amide substitution on the pyrene in the donor-bridge-acceptor system changes both the reaction Gibbs energy for the photoinduced electron transfer and the hydrophilicity of the molecular cleft. The less negative $\Delta_r G$ allows one to observe the charge separated emission, under appropriate solvent conditions as compared to the system reported earlier for the unsubstituted pyrene. The increased hydrophilicity of the cleft impacts its ability to accommodate solvent and change the interaction between the donor (DMA) and acceptor (pyrene). As with the earlier study for the unsubstituted pyrene acceptor, in which water was able to lodge in the cleft and mediate the electron tunneling, the amide substituted pyrene forms a cleft that can accommodate water molecules. In contrast to the earlier study, the cleft for **1** and **2** appears to be able to accommodate larger solvent molecules (and multiple water molecules). This feature suggests that substitution of the pyrene ring might be used to tune the cleft's solvation characteristics and the size of the tunneling gap.

11.6 BIBLIOGRAPHY

[1] **Barbara, P. F.; Meyer, T. J. and Ratner, M. A.** (**1996**). *Contemporary issues in electron transfer research*, The Journal of Physical Chemistry 100 : 13148-13168.

[2] **Beratan, D. N.; Skourtis, S. S.; Balabin, I. A.; Balaeff, A.; Keinan, S.; Venkatramani, R. and Xiao, D.** (**2009**). *Steering electrons on moving pathways*, Accounts of chemical research 42 : 1669-1678.

[3] **Bingo l, B.; Durrell, A. C.; Keller, G. E.; Palmer, J. H.; Grubbs, R. H. and Gray, H. B.** (**2012**). *Electron Transfer Triggered by Optical Excitation of Phenothiazine-tris (meta-phenylene-ethynylene)-(tricarbonyl)(bpy)(py) rhenium (I)*, The Journal of Physical Chemistry B 117 : 4177-4182.

[4] **Borsarelli, C. D.; Cosa, J. J. and Previtali, C. M.** (**1992**). *Exciplex formation between pyrene derivatives and N, N-dimethylaniline in aerosol OT reversed micelles*, Langmuir 8 : 1070-1075.

[5] **Brunschwig, B. S.; Ehrenson, S. and Sutin, N.** (**1986**). *Solvent reorganization in optical and thermal electron-transfer processes*, J. Phys. Chem. 90 : 3657–3668.

[6] **Chakrabarti, S.; Liu, M.; Waldeck, D. H.; Oliver, A. M. and Paddon-Row, M. N.** (**2007**). *Competing electron-transfer pathways in hydrocarbon frameworks: Short-circuiting through-bond coupling by nonbonded contacts in rigid U-shaped norbornylogous systems containing a cavity-bound aromatic pendant group*, Journal of the American Chemical Society 129 : 3247-3256.

[7] **Chakrabarti, S.; Liu, M.; Waldeck, D. H.; Oliver, A. M. and Paddon-Row, M. N.** (**2009**). *Solvent dynamical effects on electron transfer in U-shaped donor-bridge-acceptor molecules*, The Journal of Physical Chemistry A 113 : 1040-1048.

[8] **Chakrabarti, S.; Parker, M. F.; Morgan, C. W.; Schafmeister, C. E. and Waldeck, D. H.** (**2009**). *Experimental evidence for water mediated electron transfer through bis-amino acid donor- bridge- acceptor oligomers*, Journal of the American Chemical Society 131 : 2044-2045.

[9] Douglas, K.; Bichenkova, E. and Sardarian, A. (**2003**). *US Patent US 20030108892 A1*.

[10] **Feldman, K. S.; Hester, D. K. and Golbeck, J. H.** (**2007**). *A relationship between amide hydrogen bond strength and quinone reduction potential: Implications for photosystem I and bacterial reaction center quinone function*, Bioorganic & medicinal chemistry letters 17 : 4891-4894.

[11] Gilbert, A. and Baggott, J. E., **1991**. *Essentials of molecular photochemistry*. Wiley-Blackwel, .

[12] **Gilbert, M. and Albinsson, B.** (**2015**). *Photoinduced charge and energy transfer in molecular wires*, Chemical Society Reviews 44 : 845-862.

[13] Gordon, M. and Ware, W., **1975**. *The Exciplex*. Academic Press Inc., .

[14] **Gould, I. R.; Ege, D.; Moser, J. E. and Farid, S.** (**1990**). *Efficiencies of photoinduced electron-transfer reactions: role of the Marcus inverted region in return electron transfer within geminate radical-ion pairs*, Journal of the American Chemical Society 112 : 4290-4301.

[15] Gratzel, M., **1989**. *Heterogeneous photochemical electron transfer*. CRC Press, .

[16] **Gu, Y.; Kumar, K.; Lin, Z.; Read, I.; Zimmt, M. and Waldeck, D.** (**1997**). *Studies into the character of electronic coupling in electron transfer reactions*, Journal of Photochemistry and Photobiology A: Chemistry 105 : 189-196.

[17] **Haedler, A. T.; Misslitz, H.; Buehlmeyer, C.; Albuquerque, R. Q.; Köhler, A. and Schmidt, H.-W.** (**2013**). *Controlling the pi-stacking behavior of pyrene derivatives: Influence of H-bonding and steric effects in different states of aggregation*, ChemPhysChem 14 : 1818-1829.

[18] Jortner, J. and Bixon, M.Prigogine, I. & Rice, S. A. (Ed.), **1999**. *Electron Transfer -- From Isolated Molecules to Biomolecules, Part 1 and Part 2*. John Wiley & Sons Inc, .

[19] **Kerr, C. E.; Mitchell, C. D.; Headrick, J.; Eaton, B. E. and Netzel, T. L.** (**2000**). *Synthesis and photophysics of a 1-Pyrenyl substituted 2'-Deoxyuridine-5-Carboxamide nucleoside: Electron transfer products as CIS INDO/S excited states*, The Journal of Physical Chemistry B 104 : 1637-1650.

[20] **Kumar, K.; Kurnikov, I. V.; Beratan, D. N.; Waldeck, D. H. and Zimmt, M. B.** (**1998**). *Use of modern electron transfer theories to determine electronic coupling matrix elements in intramolecular systems*, The Journal of Physical Chemistry A 102 : 5529-5541.

[21] **Kuzmin, M. G.** (**1993**). *Exciplex mechanism of the fluorescence quenching in polar media*, Pure and applied chemistry 65 : 1653-1658.

[22] Lakowicz, J. R., **2007**. *Principles of Fluorescence Spectroscopy*. Springer US, .

[23] These radii were calculated using the circumscribed sphere (Figures S21 and S24).

[24] **Lewis, F. D.** (**1979**). *Formation and reactions of stilbene exciplexes*, Accounts of Chemical Research 12 : 152-158.

[25] **Liu, M.; Ito, N.; Maroncelli, M.; Waldeck, D. H.; Oliver, A. M. and Paddon-Row, M. N.** (**2005**). *Solvent friction effect on intramolecular electron transfer*, Journal of the American Chemical Society 127 : 17867-17876.

[26] **Maia, J. D. C.; Carvalho, G. A. U.; Mangueira, C. P.; Santana, S. R.; Cabral, L. A. F. and Rocha, G. B.** (**2012**). *GPU linear algebra libraries and GPGPU programming for accelerating MOPAC semiempirical quantum chemistry calculations*, J. Chem. Theory Comput. 8 : 3072-3081.

[27] **Marcus, R.** (**1989**). *Relation between charge transfer absorption and fluorescence spectra and the inverted region*, The Journal of Physical Chemistry 93 : 3078-3086.

[28] Mataga, N. and Kubota, T., **1970**. *Molecular Interaction and Electronic Spectra*. Marcel Dekker Inc., .

[29] **McGuinness, C. D.; Nishimura, M. K.; Keszenman-Pereyra, D.; Dickinson, P.; Campbell, C. J.; Bachmann, T. T.; Ghazal, P. and Crain, J.** (**2010**). *Detection of single nucleotide polymorphisms using a DNA Holliday junction nanoswitch – a high-throughput fluorescence lifetime assay*, Molecular BioSystems 6 : 386-390.

[30] **Nadeau, J. M.; Liu, M.; Waldeck, D. H. and Zimmt, M. B.** (**2003**). *Hole transfer in a C-shaped molecule: Conformational freedom versus solvent-mediated coupling*, Journal of the American Chemical Society 125 : 15964-15973.

[31] **Napper, A. M.; Head, N. J.; Oliver, A. M.; Shephard, M. J.; Paddon-Row, M. N.; Read, I. and Waldeck, D. H.** (**2002**). *Use of U-shaped donor-bridge-acceptor molecules to study electron tunneling through nonbonded contacts*, Journal of the American Chemical Society 124 : 10171-10181.

[32] **Natali, M.; Campagna, S. and Scandola, F.** (**2014**). *Photoinduced electron transfer across molecular bridges: electron-and hole-transfer superexchange pathways*, Chemical Society Reviews 43 : 4005-4018.

[33] **Okada, T.; Fujita, T.; Kubota, M.; Masaki, S.; Mataga, N.; Ide, R.; Sakata, Y. and Misumi, S.** (**1972**). *Intramolecular electron donor-acceptor interactions in the excited state of (anthracene)-(CH 2) n-(N, N-dimethylaniline) systems*, Chemical Physics Letters 14 : 563-568.

[34] **Paddon-Row, M. N.** (**2003**). *Orbital interactions and long-range electron transfer*, Advances in Physical Organic Chemistry 38 : 1-85.

[35] **Read, I.; Napper, A.; Kaplan, R.; Zimmt, M. and Waldeck, D.** (**1999**). *Solvent-mediated electronic coupling: The role of solvent placement*, Journal of the American Chemical Society 121 : 10976-10986.

[36] **Reis e Sousa, A.; Castanheira, E.; Fedorov, A. and Martinho, J.** (**1998**). *Polystyrene cyclization using pyrene excimer formation. Effect of geminate pairs in good solvents*, The Journal of Physical Chemistry A 102 : 6406-6411.

[37] **Skourtis, S. S.; Waldeck, D. H. and Beratan, D. N.** (**2010**). *Fluctuations in biological and bioinspired electron-transfer reactions*, Annual review of physical chemistry 61 : 461.

[38] *MOPAC2012, Version 15.229L*, **Stewart James, J. P.**, Web: HTTP://OpenMOPAC.net

[39] **Van Haver, P.; Helsen, N.; Depaemelaere, S.; Van der Auweraer, M. and De Schryver, F.** (**1991**). *The influence of solvent polarity of the nonradiative decay of exciplexes*, Journal of the American Chemical Society 113 : 6849-6857.

[40] **Van Voorhis, T.; Kowalczyk, T.; Kaduk, B.; Wang, L.-P.; Cheng, C.-L. and Wu, Q.** (**2010**). *The diabatic picture of electron transfer, reaction barriers, and molecular dynamics*, Annual review of physical chemistry 61 : 149-170.

[41] **Verhoeven, J.; Scherer, T. and Willemse, R.** (**1993**). *Solvent effects on the structure of fluorescent'exciplexes' in rigidly-, flexibly-, and nonbridged donor-acceptor systems*, Pure and applied chemistry 65 : 1717-1722.

[42] **Verhoeven, J. W.** (**1990**). *Electron transport via saturated hydrocarbon bridges:'exciplex'emission from flexible, rigid and semiflexible bichromophores*, Pure and Applied Chemistry 62 : 1585-1596.

[43] **Weiss, E. A.; Wasielewski, M. R. and Ratner, M. A.** (**2005**). *Molecules as wires: Molecule-assisted movement of charge and energy*, Top. Curr. Chem 257 : 103-133.

[44] **Yin, X.; Kong, J.; De Leon, A.; Li, Y.; Ma, Z.; Wierzbinski, E.; Achim, C. and Waldeck, D. H.** (**2014**). *Luminescence quenching by photoinduced charge transfer between metal complexes in peptide nucleic acids*, The Journal of Physical Chemistry B 118 : 9037-9045.

[45] **Zimmt, M. and Waldeck, D.** (**2003**). *Exposing solvent's roles in electron transfer reactions: Tunneling pathway and solvation*, The Journal of Physical Chemistry A 107 : 3580-3597.

[46] *JSmol: an open-source HTML5 viewer for chemical structures in 3D.*, Web: http://wiki.jmol.org/index.php/JSmol

12.0 CONCLUSIONS

A brief description of the conclusions of the studies contained within this thesis are described below.

Conclusions of Part I: Scanning Probe Microscopy:

In Chapter 3, we demonstrated ANSOM images of a nanoslit aperture containing interference fringes, which result from superposition of the average detected wavevector and components of the field scattered by the nanoslit. Analysis confirms that such a slit generates two scattered orders launched perpendicular to the slit. Furthermore, fringe patterns can be controlled by changing the orientation of the slit, and thus, the direction of the two scattered orders with respect to the detector or vice versa. The model originally developed by Aubert et al. was extended to account for the two scattered orders present in our system. The resulting calculated fields agreed well with the ANSOM data in several different detector-slit orientations.

Additionally, probe geometry and probe position relative to the slit strongly affect the magnitude of self-homodyning fields exhibited in ANSOM images. For a single slit aperture, sources of homodyning fields include a propagating field transmitted through the slit and reflected by the probe base and/or cantilever body. Sensitivity of self-homodyne amplification to probe geometry suggests that portions of the probe base and cantilever body scatter significant transmitted optical fields.

In Chapter 4 the bending modulus of individual multiwall boron nitride nanotubes (MWBNNTs) was measured *via* AFM bending experiments. Boundary conditions for the beam-bending model were determined by using a force mapping technique. MWBNNTs were found to have excellent mechanical properties with an average bending modulus of 760 ± 30 GPa, which is consistent with the theoretically predicted value for BNNTs. Shear effects were found to be non-negligible, and the Young's modulus and shear modulus were determined to be 1800 ± 300 and 7 ± 1 GPa, respectively. The experimental geometry and the dimensions of the nanotubes were not major contributing factors to the shear effects; rather, it is likely that interwall shearing occurred between crystalline and faceted cylindrical helices in these MWBNNTs.

Conclusions of Part II: Studies of Photonic Crystals

In Chapter 6 we developed a simple, straightforward method to form *non close-packed* ultra-highly-ordered, face centered cubic (fcc) direct and inverse opal silica photonic crystals, which allowed us to independently control the photonic crystal periodicity and size of the basis of the fcc unit cell. We selected the fcc lattice constant by defining the particle number density of this electrostatically self assembled structure. Thus, we independently control the spacing between particles. The particle diameter used determines the wall spacing of the inverse opal photonic crystal and determines the shape of the photonic crystal dielectric constant modulation. This allows us to optimize the diffraction of our photonic crystal structures.

These fcc photonic crystals simply and spontaneously self assemble due to their soft electrostatic repulsion potentials. They showed ordering as good or possibly better than close-packed photonic crystals formed by convective assembly. We showed that colloidal particle size polydispersity has less impact on photonic crystal electrostatic ordering than occured for ordering of close-packed crystals. Point defect induced crystal strains in electrostatically

stabilized CCA anneal within approximately two particle layers. We also showed that charge polydispersity has only a small impact on crystal ordering and that the strains due to defect particles of different charge also anneal out over approximately two particle layers.

In Chapter 7 we developed a novel, simple, and efficient approach to rapidly fabricate large-area 2-D particle arrays on water surfaces. These arrays can easily be transferred onto various substrates and functionalized for chemical-sensing applications. We demonstrated that the ordering of 2-D arrays decreases with the particle size.

Conclusions of Part III: Spectroscopy Studies.

In Chapter 9 we demonstrated that electron transfer and photoluminescence quenching in cadmium selenide / cadmium telluride NP assemblies can be controlled through the interparticle distance, energetics, electric field created by the surface capping group, and particle size. Time-resolved studies indicated that the electron transfer process may involve surface-localized states. The inhibition of electron transfer by the interparticle electric field was significant and may provide an avenue for inhibiting back electron transfer. These findings should be useful for understanding and controlling charge transfer in nanocrystal-based solar cells.

In Chapter 10 efficient sensitization was observed for both the ZnS/Tb^{3+} and the ZnS/Eu^{3+} systems. The ZnS/Tb^{3+} nanoparticles appear to be more efficient lanthanide-based emitters, with lanthanide-centered quantum yield values for ZnS/Tb^{3+} and ZnS/Eu^{3+} being 0.05 ± 0.01 and 0.000 13 ± 0.000 04, respectively. ZnS nanoparticles acted as an antenna to sensitize the lanthanide luminescence in these systems. Moreover, the absence of observable sharp bands in the excitation spectra indicated that direct excitation of lanthanides has a negligible contribution to the overall sensitization mechanism.

The mechanism of lanthanide luminescence sensitization in II−VI semiconductor materials can be rationalized by a semiempirical method proposed by Dorenbos and colleagues. Energy level diagrams indicate that in ZnS, Tb^{3+} can act as a potential hole trap and provide a dramatic increase in sensitization efficiency because its energy levels lie between the nanoparticle band edges. The mechanism of Eu^{3+} luminescence sensitization on the other hand, follows a different type of mechanism. In ZnS, Eu^{3+} can act as a potential electron trap; hence, the sensitization can be achieved either by direct bandgap excitation or by a valence band to Eu^{2+} transition.

In Chapter 11 the amide substitution on the pyrene in the donor-bridge-acceptor system changed both the reaction Gibbs energy for the photoinduced electron transfer and the hydrophilicity of the molecular cleft. The less negative $\Delta_r G$ allows one to observe the charge separated emission, under appropriate solvent conditions as compared to the system reported earlier for the unsubstituted pyrene. The increased hydrophilicity of the cleft impacts its ability to accommodate solvent and change the interaction between the donor (DMA) and acceptor (pyrene). As with the earlier study for the unsubstituted pyrene acceptor in which water was able to lodge in the cleft and mediate the electron tunneling, the amide substituted pyrene formed a cleft that can accommodate water molecules. In contrast to the earlier study, the molecular clefts appeared to be able to accommodate larger solvent molecules (and multiple water molecules). This feature suggests that substitution of the pyrene ring might be used to tune the cleft's solvation characteristics and the size of the tunneling gap.